Searching for electromagnetic signatures of early massive black hole binaries

Léna Arthur

THÈSE en vue d'obtenir le grade de :
Docteure d'Université Paris Cité, Spécialité : Physique de l'Univers

Ecole Doctorale ED560 - STEP'UP
Sciences de la Terre et de l'Environnement et Physique de l'Univers de Paris
Laboratoire APC AstroParticule et Cosmologie
UMR7164 - RSNR n°200512546V

Thèse présentée par :
Léna Arthur

Date de soutenance : 14/05/2024

Searching for electromagnetic signatures of early massive black hole binaries

Directeur: Fabien Casse
Co-encadrant: Alexis Coleiro

Composition du jury :

Simona Mei Professeure des universités, APC-Université Paris Cité	**Présidente**
Olivier Godet MCF-HDR, IRAP-Université Toulouse III	**Rapporteur**
Pierre-Olivier Petrucci DR, IPAG-Université Grenoble Alpes	**Rapporteur**
Delphine Porquet DR, LAM-Université Aix-Marseille	**Examinatrice**
Alessandra Tonazzo Professeure des universités, APC-Université Paris Cité	**Examinatrice**
Fabien Casse Professeur des universités, APC-Université Paris Cité	**Directeur de thèse**
Alexis Coleiro MCF, APC-Université Paris Cité	**Co-encadrant de thèse**

TABLE OF CONTENT

RÉSUMÉ COURT

Ce travail de thèse porte sur les contreparties électromagnétiques de la fusion des binaires de Trous Noirs SuperMassifs (TNSMs) dans les premières étapes de leur fusion. Dans la prochaine décennie, nous pourrions être capables de détecter les Ondes Gravitationnelles (OGs) émises par les fusions de binaires de TNSMs avec les Pulsar Timing Arrays (PTAs) et le Laser Interferometer Space Antenna (LISA). Si l'identification de la source peut être réalisée avant sa fusion finale, cela permettra d'étudier la physique de la matière en accrétion dans des régimes relativistes forts et pourrait aider à comprendre le déclenchement de l'activité des Noyaux Actifs de Galaxie (NAGs). Avant la fusion, les incertitudes sur la localisation de la source dans le ciel associées à la détection par LISA ou PTAs pourraient contenir des centaines voire des milliers de NAGs (Piro et al. 2023; Goldstein et al. 2018). De plus, les detecteurs électromagnétiques peuvent difficilement résoudre les deux TNSMs à ce stade de leur fusion. Il faut donc identifier des signatures électromagnétiques indirectes de la présence d'un binaire, distinctes de l'émission des NAG isolés. Cela peut être fait par des études temporelles et spectrales des observations du centre des galaxies (e.g., la revue D'Orazio & Charisi (2023)). Comme il n'y a pas de détection confirmée de binaires de TNSM dans les dernières étapes de leurs fusions, les simulations sont un outil puissant pour prédire ces signatures électromagnétiques.
Cette thèse se concentre sur les systèmes binaires de TNSMs pendant l'état stationnaire de l'émission d'OG : le rapprochement des deux TNSMs est lent par rapport à la période orbitale. À ce stade, la séparation entre les deux TNSMs est suffisante pour supposer que le disque d'accrétion autour du TNSM le plus massif est encore présent.

Au cours de la première partie de mon doctorat, j'ai travaillé sur des simulations numériques du disque d'accrétion autour de l'un des TNSMs et sous l'influence gravitationnelle du TNSM compagnon. Le but de ces simulations est de comprendre l'impact gravitationnel du TNSM compagnon sur la structure du disque. Les simulations ont été réalisées avec le code MPI-AMRVAC (van der Holst et al. 2012). Le code résout les équations hydrodynamiques classiques. Un défi pour ces simulations dans les premières étapes de la fusion est l'échelle de temps orbitale de la binaire, qui est grand par rapport à l'échelle de temps caractéristique du fluide dans les parties internes du disque et qui fixe le pas de temps de la simulation. Résoudre seulement les équations hydrodynamiques classiques permet d'étudier l'impact du TNSM compagnon pour divers systèmes binaires dans un temps raisonnable. L'influence gravitationnelle du TNSM central sur son disque d'accrétion est prise en compte par un potentiel pseudo-newtonien (Paczyński & Wiita 1980). Cela permet de maintenir le bord interne du disque au niveau de la dernière orbite circulaire stable. Les simulations sont effectuées pour différents systèmes binaires sur une orbite circulaire fixe avec des séparations comprises entre 250 R_s et 3 000 R_s, et un rapport de masse entre 9×10^{-4} et 1.
Les simulations montrent que l'impact gravitationnel du compagnon a trois effets sur le disque d'accrétion.

Premièrement, le TNSM compagnon tronque les parties externes du disque. Deuxièmement, une onde spirale apparaît dans le disque. L'impact des paramètres orbitaux de la binaire sur ces deux effets est présenté au Chapitre 3. Troisièmement, la forme du disque devient elliptique. Les résultats sur la troncature du disque et sa forme elliptique seront publiés dans Casse et al. (in prep, voir Annexe A).

L'impact gravitationnel du compagnon TNSM compagnon sur la structure du disque pourrait changer son emission électromagnétique à un niveau détectable. Pendant la deuxième partie de mon doctorat, j'ai travaillé plus spécifiquement sur le profil de la raie d'émission Kα du fer. L'objectif est d'étudier la détectabilité des changements structuraux du disque dans le profil de la raie du fer.
J'ai développé un code pour calculer le profil de la ligne de fer avec une expansion au premier ordre des équations géodésiques dans une métrique de Schwarzschild, comme présenté dans Hartnoll et Blackman (Hartnoll & Blackman 2000, 2001, 2002). Cette méthode est choisie car elle permet de considérer les effets non axisymétriques dans la structure du disque d'accrétion (l'onde spirale dans le disque et la forme elliptique). La source de photons en rayons X durs (la couronne) est modélisée comme une source ponctuelle (modèle du Lamp-post).
Chacun des trois effets peut être étudié indépendamment sur des modèles analytiques de disques. Nous avons d'abord commencé par la détectabilité de la troncation du disque. En ne considérant que cet effet, les trois paramètres pour calculer le profil de la ligne sont l'angle d'inclinaison du disque par rapport à l'observateur (i_{obs}), la distance entre la couronne et le TNSM (h_s), et le rayon du bord extérieur du disque (r_{max}). Dans une étude préliminaire, une incertitude observationnelle sur le flux dans chaque bin (de largeur 7 eV) est ajoutée à la valeur du flux théorique. La méthode pour trouver r_{max} est de calculer sept rapports de flux dans l'étendue spectrale de la raie de fer et de les comparer à un catalogue de ratios de flux théoriques. Cela donne les valeurs compatibles des trois paramètres ($r_{max},\ i_{obs},\ h_s$).
Les profiles théoriques de la raie du fer ont ensuite été utilisés avec le code Xspec pour modéliser des observations plus réalistes avec le spectromètre X-IFU à bord de la future mission ESA/Athena (Barret et al. 2023). Cela permet de prendre en compte le continuum en loi de puissance et les profils de la raie du fer calculés par la méthode de binning, normalisés à des valeurs physiques du flux intégré entre le continuum et la raie du fer. La détectabilité de la troncation du disque est explorée pour différentes valeurs de la luminosité de la source, du redshift, du temps d'exposition et de la luminosité intrinsèque de la raie de fer. D'après les simulations effectuées, contraindre la valeur de r_{max} semble faisable dans de bonnes conditions, ce qui implique un temps d'exposition suffisamment long ($\gtrsim 500$ ks), une galaxie dans l'univers local ($z \lesssim 0.1$), et une lunminosite intrinseque dans la bande $2-10$ keV supérieure à $\gtrsim 10^{41}$ erg $\cdot$ s^{-1}.

La continuation de ce travail sera d'étudier l'impact de l'onde de densité spirale et de la forme elliptique du disque sur le profil de la ligne de fer. Ensemble, ils peuvent fournir des preuves supplémentaires pour distinguer entre l'émission d'un disque sous l'influence gravitationnelle d'un TNSM compagnon et l'émission d'un NAG isolé. L'étude de l'impact du TNSM compagnon sur les parties internes du disque nécessitera de résoudre les équations de la relativité générale.

Mots clés : Binaires de trous noirs supermassifs, Simulations hydrodynamiques, Disques d'accrétion, Observations en rayons X, Ondes gravitationnelles, Astronomie multi-messagers

ABSTRACT

This thesis focuses on the Electromagnetic (EM) counterparts to the merger of Massive black hole (MBH) binaries in the first stages of their merger.
MBHs designate Black Holes (BHs) with masses ranging between 10^5 $M_\odot$ and 10^{10} $M_\odot$. Since the 1990s, observational evidence has led to the widely spread idea that every massive galaxy harbors a MBH at its center (e.g., Kormendy & Richstone (1995)). When two galaxies — each harboring a MBH at its center — merge, the two BHs sink toward the center of the remnant galaxy by dynamical friction onto the gas and stars (Begelman et al. 1980). This process efficiently brings the two BHs together until they form a gravitationally bound binary. Then, the processes that continue to remove the energy and angular momentum of the binary to bring the two BHs closer are still an open question. Once the separation is small enough, the emission of Gravitational Waves (GWs) is efficient enough to merge the two BHs within the Hubble time.
In the next decade, we might be able to detect the GWs emitted by MBH binary mergers with the PTAs and the LISA. If the identification of the source can be done before the merger, it will allow studying the physics of the accreting matter in strong relativistic regimes and might help to understand the triggering of AGNs. Before the merger, the uncertainties on the localization of the source in the sky associated with the detection by LISA or PTAs might contain hundreds to thousands of AGNs (Piro et al. 2023; Goldstein et al. 2018). Moreover, EM facilities could only hardly resolve the two BHs in the last stages of their merger. Thus, we need to identify EM indirect signatures of the presence of a binary, distinct from the emission of isolated AGNs. This can be done through the temporal and spectral studies of the observations of the center of galaxies (see, e.g., the review by D'Orazio & Charisi (2023)). Since there is no confirmed detection of MBH binaries in the last stages of their mergers, simulations are a powerful tool to predict these EM signatures.

This thesis focuses on MBH binary systems during the steady state of GW emission: the orbital decay is slow compared to the orbital period. At these stages, the separation between the two BHs is sufficient to assume that the accretion disc around the more massive BHs is still present.

During the first part of my Ph.D., I worked on numerical simulations of the accretion disc around one of the BHs and under the gravitational influence of the MBH companion. The simulations aim at understanding the companion's tidal impact on the disc structure. The simulations are performed with the code MPI-AMRVAC (van der Holst et al. 2012). The code solves the classic hydrodynamical equations. One challenge for those simulations in the early stage of the merger is the orbital time scale of the binary, which is tremendously high compared to the dynamical time scale of the fluid in the innermost regions of the disc, which sets the simulation time-step. Thus, solving only the classical hydrodynamical equations allows us to study the impact of the companion for various binary systems

in a reasonable time. The primary MBH gravitational influence on its accretion disc is taken into account in the equations with a pseudo-Newtonian potential (Paczyńsky & Wiita 1980), which allows for maintaining an inner edge to the accretion disc at the Innermost Stable Circular Orbit (ISCO). The simulations are run for different binary systems on fixed circular orbit with separations ranging between 250 R_s and 3 000 R_s, and mass ratio between 9×10^{-4} and 1.
The simulations show that the gravitational impact of the MBH companion has three effects on the accretion disc. First, it truncates the disc's outer parts. Second, a spiral wave appears in the disc. The impact of the binary parameters on these two effects is presented in 3. Third, the disc's shape becomes elliptical. The results on the disc truncation and its elliptical shape will be published in Casse et al. (in prep., see Appendix A).

The gravitational impact of the MBH companion on the disc structure might impact its EM at a detectable level. During the second part of my Ph.D., I worked more specifically on the iron Kα emission line. The aim is to study the detectability of the structural changes in the disc through the iron line profile.
I developed a code to compute the iron line profile with a first-order expansion of the geodesic equations in a Schwarzschild metric, as presented in Hartnoll & Blackman (2000, 2001, 2002). This method is preferred because it allows considering the non-axisymmetric effects on the accretion disc structure due to the gravitational impact of the MBH companion (the spiral wave in the disc and the elliptical shape). The source of hard X-ray photons (the corona) is modeled as a point source (Lamp-post model).
Each of the three effects can be studied independently on analytic models of discs. We first started with the detectability of the disc truncation. Considering only this effect, the three parameters to compute the line profiles are the disc inclination angle relative to the observer (i_{obs}), the distance between the corona and the MBH (h_s), and the disc's outer edge radius (r_{max}). For a preliminary study, an observed uncertainty in the flux in each bin (of width 7 eV) is added around the theoretical flux. The method to find r_{max} is to compute seven flux ratios within the iron line spectral extent and compare them to a catalog of theoretical flux ratios. This gives the compatible values of the three parameters ($r_{max},\ i_{obs},\ h_s$).
The theoretical line profiles were then used with the X-ray fitting code Xspec (Arnaud 1996) to model more realistic observations with the X-IFU spectrometer onboard the forthcoming ESA/Athena mission (Barret et al. 2023). It includes an absorbed power-law continuum and the iron line profiles computed by the binning method, normalized to physical values of the integrated flux between the continuum and the line. The detectability of disc truncation is explored for different values of the source luminosity, the redshift, the exposure time, and the intrinsic luminosity of the iron line. Based on the simulations performed, constraining the r_{max} value seems feasible under good conditions, which implies an exposure time long enough ($\gtrsim$ 500 ks), a galaxy in the local universe ($z \lesssim 0.1$) with a $2-10$ keV X-ray luminosity above $\gtrsim 10^{41}$ erg $\cdot$ s^{-1}.

The continuation of this work will be to study the impact of the density wave spiral and the elliptical shape of the disc on the iron line profile. Together, they can provide additional evidence to distinguish between the emission of a disc under the gravitational influence of a MBH companion and the emission from an isolated AGN. Studying the impact of the MBH companion on the disc inner parts will require solving the General Relativistic (GR) equation.

Key words: Massive black hole binaries, Hydrodynamical simulations, Accretion discs, X-ray observations, Gravitational-waves sources, Multi-messenger astronomy

RÉSUMÉ SUBSTANTIEL

Ce travail de thèse porte sur les contreparties électromagnétiques à la fusion des binaires de TNSMs dans les premières étapes de leur fusion.

Contexte scientifique de ce travail

Les TNSMs désignent des trous noirs dont les masses se situent entre 10^5 $M_\odot$ et 10^{10} $M_\odot$. Depuis les années 1990s, les preuves observationnelles ont conduit à l'idée largement répandue que chaque galaxie massive abrite un TNSM en son centre e.g., Kormendy & Richstone (1995)). Ils peuvent être détectés par leur activité électromagnétiques puissantes lorsqu'ils accrètent suffisamment de matière (e.g., la revue de Padovani et al. (2017)) ou, pour les TNSMs dormants, par leur impact gravitationnel sur les étoiles les plus proches (comme le montre, entre autres, l'étude réalisée par Hees et al. (2017) sur le TNSM au centre de notre galaxie). Lorsque deux galaxies — chacune abritant un TNSM en son centre — fusionnent, les deux TNSMs se rapprochent du centre galactique par friction dynamique sur le gaz et les étoiles (Begelman et al. 1980). Ce processus rapproche efficacement les deux TNSMs jusqu'à ce qu'ils forment une binaire gravitationnellement liée (à une séparation de ~ 1 pc pour une binaire avec une masse totale 10^7 $M_\odot$). Ensuite, les processus qui continuent à extraire l'énergie et le moment angulaire de la binaire pour rapprocher les deux TNSMs restent une question ouverte. Une fois que la séparation est environ inférieure à l'échelle du milli-parsec (pour une masse totale de 10^7 $M_\odot$), l'émission d'OGs est suffisamment efficace pour amener les deux TNSMs à leur coalescence finale. Dans la prochaine décennie, nous pourrions être en mesure de détecter les OGs émises par les fusions de binaires de TNSMs avec les PTAs et le LISA. Ces détections permettront la première observation directe des fusions de binaires de TNSMs et aidera à comprendre l'évolution des TNSMs à l'échelle cosmologique (Agazie et al. 2023b; Amaro-Seoane et al. 2023). De plus, identifier la source de l'émission d'OGs permettra par exemple de donner de nouvelles perspectives sur la coévolution des TNSMs et de leur galaxie hôte (Kormendy & Ho 2013), ou de mesurer indépendamment l'expansion de l'univers. Si l'identification de la source peut être faite avant la fusion, cela permettra d'étudier la physique de l'accrétion dans des régimes relativistes forts et pourrait aider à comprendre le déclenchement des NAGs.

Avant la fusion, les incertitudes sur la localisation de la source dans le ciel associées à la détection des OGs par LISA ou PTAs pourraient contenir des centaines à des milliers de NAGs (Piro et al. 2023; Goldstein et al. 2018). De plus, les observations électromagnétiques ne pourront résoudre que difficilement les deux TNSMs dans les derniers stades de la fusion. Ainsi, nous devons identifier des signatures électromagnétiques indirectes de la présence d'une binaire, distinctes de l'émission de NAGs isolés. Cela peut être fait grâce aux études temporelles et spectrales des observations du centre des galaxies (voir, par exemple, la revue de D'Orazio & Charisi (2023)). Comme il n'y a pas de détection

confirmée de binaires de TNSMs dans les dernières étapes de leurs fusions, les simulations sont un outil puissant pour prédire ces signatures électromagnétiques.

Présentation succincte du travail

Cette thèse se concentre sur les systèmes binaires de TNSMs dans les premières étapes de la fusion, et, plus précisément, pendant l'état stationnaire de l'émission d'OGs : le rapprochement des deux TNSMs est lent par rapport à la période orbitale. À ce stade, la séparation entre les deux TNSMs est suffisamment grande pour supposer que le disque d'accrétion autour du TNSM le plus massif est toujours présent. Pendant la première partie de mon doctorat, j'ai travaillé sur des simulations numériques du disque d'accrétion autour de l'un des TNSMs et sous l'influence gravitationnelle du TNSM compagnon. Le but de ces simulations est de comprendre l'impact gravitationnel du TNSM compagnon sur la structure du disque. Ces simulations montrent que les parties externes du disques sont tronquées, qu'une onde de densité spirale apparait dans le disque et que la forme globale du disque devient elliptique. Ces changements dans la structure du disque peuvent avoir un impact sur son émission électromagnétique à un niveau détectable. Cela permettrait de différencier observationnellement un disque sous l'influence gravitationnelle d'un TNSM compagnon et un disque autour d'un TNSM isolé. Pendant la seconde partie de mon doctorat, j'ai travaillé plus spécifiquement sur le profil de la raie d'émission Kα du fer. J'ai développé un code pour calculer le profil de la raie de fer avec une expansion au premier ordre des équations des géodésiques dans une métrique de Schwarzschild, comme présenté dans Hartnoll & Blackman (2000, 2001, 2002). Cette méthode est choisie car elle permet de prendre en compte les effets non axisymétriques dans la structure du disque d'accrétion dus à l'impact gravitationnel du TNSM compagnon (la spirale et la forme elliptique). Le but est d'étudier la détectabilité des changements dans le profil de la raie du fer.

Etude de l'impact gravitationnel du trou noir compagnon sur la structure du disque

Les simulations numériques étudient le disque d'accrétion autour du TNSM le plus massif de la binaire car son Lobe Roche est le plus grand. La taille des disques d'accrétion autour des NAGs isolés reste une question ouverte. Leur taille approximative peut être comprise entre 1 000 R_s (R_s est le rayon de Schwarzschild du TNSM central) et 1 500 R_s (e.g., Lobban & King (2022)). Par conséquent, la séparation orbitale initiale considérée dans cette étude est 3 000 R_s. Comme la binaire de TNSMs est dans l'état stationnaire de la phase d'émission OGs, la décroissance orbitale peut être négligée sur plusieurs dizaines de périodes orbitales. Nous avons négligé l'excentricité : les deux TNSMs sont sur une orbite circulaire fixe. Cette hypothèse contraint la séparation orbitale à être au-dessus de 250 R_s. Le rapport de masse est compris entre 9×10^{-4} et 1.

Les simulations sont effectuées avec le code MPI-AMRVAC (van der Holst et al. 2012). Le code résout les équations hydrodynamiques classiques. Un défi pour ces simulations dans les premiers stades de la fusion est l'échelle de temps orbitale de la binaire, qui est grand par rapport à l'échelle de temps dynamique du fluide dans les régions les plus internes du disque, et qui fixe le pas de temps de simulation. Ainsi, ne résoudre que les équations hydrodynamiques classiques nous permet d'étudier l'impact du TNSM compagnon pour divers systèmes binaires dans un temps raisonnable. L'influence gravitationnelle du TNSM primaire sur son disque d'accrétion est prise en compte dans les équations avec un potentiel pseudo-newtonien (Paczyński & Wiita 1980), ce qui permet de maintenir un bord intérieur au disque d'accrétion à la dernière orbite circulaire stable, qui est un effet purement relativiste. L'impact gravitationnel du TNSM compagnon est pris en compte par un potentiel newtonien puisque le fluide ne se rapproche pas de sa dernière orbite circulaire stable : il n'y a pas d'effets relativistes à prendre en compte. Les conditions initiales sont l'équilibre du disque autour du TNSM primaire.

Les simulations montrent que l'impact gravitationnel du TNSM compagnon a trois effets la structure du disque. Tout d'abord, le TNSM compagnon tronque les parties externes disque (par exemple, à environ 30% de la séparation orbitale pour des TNSMs de même masse). Deuxièmement, une onde

spirale apparaît dans le disque. Troisièmement, la forme du disque devient elliptique. L'impact des paramètres orbitaux de la binaire sur les deux premiers effets est présenté au Chapitre 3. Les résultats sur la troncature du disque et sa forme elliptique seront publiés dans Casse et al. (in prep, voir Annexe A)

Impact du trou noir compagnon sur le profile de la raie du fer

Pendant la seconde partie de mon doctorat, j'ai écrit un code pour étudier l'impact de ces trois effets sur le profil de la raie d'émission Kα du fer. Cette raie est typique des spectres en rayons X des NAGs. Bien qu'elle soit intrinsèquement étroite, les observations montrent des profiles de raie élargis. Les effets relativistes du Trou Noir (TN) central expliquent de manière cohérente cet élargissement. Le code calcule les géodésiques des photons avec une expansion au premier ordre des équations dans une métrique de Schwarzschild. Cela ne prend pas en compte le spin du TNSM central : le but n'est pas de regarder l'effet du spin mais plutôt l'impact des changements structuraux qui interviennent dans les parties extérieures du disque. La source de photons dans le domaine des rayons X durs — appelée la couronne — qui illumine le disque et excite les atomes et ions de fer froid dans le disque (dont une des voies de dés-excitation est de d'emettre un photon à 6.4 keV, produisant la raie du fer) est modélisée comme une source ponctuelle, appelé le modèle du Lamp-post dans la littérature. Ce modèle est très simpliste, mais aucun des modèles de la couronne existant n'est consistent avec toutes les observations.

La raie de fer est calculée numériquement en utilisant une méthode de *binning* pour une partition du disque sur une grille spatiale. La fréquence observée et le flux associé sont calculés pour les photons émis dans chaque cellule de la grille. Le flux total dans chaque bin de fréquence est la somme des flux observés, émis depuis les cellules de la grille pour lesquelles la fréquence observée se trouve dans le bin considéré. J'ai vérifié les résultats obtenus avec une seconde implémentation numérique. Dans cette seconde méthode, le flux observé de la raie à une fréquence donnée est intégré sur les courbes unidimensionnelles à l'intérieur du disque qui ont émis des photons observés à cette fréquence.

Chacun des trois effets peut être étudié indépendamment sur des modèles analytiques de disques. Nous avons d'abord commencé par la détectabilité de la troncation du disque. En considérant uniquement cet effet, les trois paramètres pour calculer les profils théoriques de la raie du fer sont l'angle d'inclinaison du disque par rapport à l'observateur (i_{obs}), la distance entre la couronne et le TNSM (h_s), et le rayon du bord extérieur du disque (r_{max}). Pour une étude préliminaire, une incertitude observationnelle sur le flux de chaque bin de fréquence (de largeur 7 eV) est ajoutée au flux théorique. La méthode pour trouver la valeur de r_{max} est de calculer sept rapports de flux dans l'étendue spectrale de la raie du fer et de les comparer à un catalogue de rapports de flux théoriques. Cela donne les valeurs compatibles des trois paramètres.

Les profils théoriques des raies ont ensuite été utilisés avec le code Xspec (Arnaud 1996) pour modéliser des observations plus réalistes avec le spectromètre X-IFU de la future mission ESA/Athena (Barret et al. 2023). Cela inclut un continuum de loi de puissance et les profils théoriques de la raie du fer calculés par la méthode de binning et normalisés à des valeurs physiques du flux intégré entre le continuum et la raie. La détectabilité de la troncation du disque est explorée pour différentes valeurs de la luminosité de la source, du redshift, des temps d'exposition et de la luminosité intrinsèque de la raie de fer. D'après les simulations réalisées, il semble possible de contraindre la valeur de r_{max} dans de bonnes conditions, ce qui implique un temps d'exposition suffisamment long ($\gtrsim 500$ ks), une galaxie dans l'univers local ($z \lesssim 0.1$) avec une luminosité dans la bande $2-10$ keV supérieure à $\gtrsim 10^{41}$ erg$\cdot$s^{-1}.

Perspectives succintes

La suite de ce travail consistera à étudier l'impact des deux autres conséquences de l'impact gravitationnel du TNSM compagnon sur la structure du disque (la spirale et la forme elliptique du disque). Cela peut être exploré en calculant les profils théoriques avec la méthode de binning et en simulant

des observations réalistes avec Xspec. Ensemble, ils peuvent fournir des preuves supplémentaires pour distinguer entre l'émission d'un disque sous l'influence gravitationnelle d'un TNSM compagnon et un disque autour d'un NAG isolé.
L'impact du TNSM compagnon sur les parties les plus internes du disque pourra être exploré avec des simulations en relativité générale.

REMERCIEMENTS

Je remercie mes encadrants de thèse, Alexis Coleiro et Fabien Casse, ainsi que Peggy Varniere – mon encadrante pendant le stage de M2 et qui a participé à l'encadrement de cette thèse – de m'avoir permis de travailler sur ce sujet passionnant. Je remercie particulièrement Alexis Coleiro pour son aide dans les dernières semaines de ce travail.

Je remercie aussi l'ensemble de l'équipe MIMOSA au laboratoire APC pour les discussions régulières et très intéressantes sur l'avancée du projet : Jonathon Baird, Fabien Casse, Alexis Coleiro, Fabrice Dodu, Pierre-Alexandre Duverne, Matthias González, Raphaël Mignon-Risse et Peggy Varniere.

Je remercie aussi les membres de mon comité de suivi de thèse pour les discussions au cours de la thèse et leur soutient dans les derniers mois : Andréa Goldwurm et Frédéric Vincent. Je remercie aussi Alessandra Tonazzo (directrice adjointe de l'école doctorale pour son soutient).

Merci beaucoup à l'équipe informatique pour leur disponibilité et leur aide sur l'utilisation du Cluster Dante et des ressources informatiques du laboratoire. Merci beaucoup à Sebastien Zappino.

Je remercie aussi mon jury pour l'évaluation de ce travail. Merci aux rapporteurs Olivier Godet et Pierre-Olivier Petrucci pour les améliorations apportées à ce travail. Merci à Simona Mei, Delphine Porquet et Alessandra Tonazzo pour les discussion lors de la soutenance.

Les discussions avec les autre doctorant·es du laboratoire et leur soutient ont aussi été très importants tout au long de cette thèse. Je remercie particulièrement Anais Wiedmer, Antoine Foisseau, Baptiste Jost, Camille Sironneau, Edwan Preau, Hugo Roussille, Julien Marchioro, Konstantin Leyde, Magdy Morshed, Pilar Iváñez Ballesteros, Simon Biquart, Sruthi Ravikularaman, Théo Boyer, Valentin Nourry.

Je souhaite aussi remercier les postdoctorant·es qui ont été particulièrement important pour comprendre le monde de la recherche et le fonctionnement du laboratoire : Jonathon Baird, Pierre-Alexandre Duverne, Raphaël Mignon-Risse, Giada Peron, Enrico Perretti et Jean-Baptiste Vielfaure.

Merci à Denis Allard, Bruny Baret et Cédric Champion.

Je souhaite aussi remercier les personnes qui m'ont soutenue à l'extérieur du laboratoire. Merci infiniment à mes parents et mon frère. Merci infiniment à Corentin. Merci infiniment à mes ami·es.

LIST OF FIGURES

CHAPTER

1

INTRODUCTION: SCIENTIFIC CONTEXT OF THE STUDY

1.1 Massive black holes and active galactic nuclei

Massive black holes (MBHs) refer to Black Holes (BHs) with masses between 10^5 $M_\odot$ and 10^9 $M_\odot$ ($M_\odot$ is the solar mass). Observational evidence suggests that they lie at the center of most, if not all, galactic bulges and pseudo-bulges of stars (Kormendy & Richstone 1995). They can be detected through their gravitational impact on their environment: on the surrounding gas and stars.

If a MBH accrete enough gas, it emits a powerfull Electromagnetic (EM) signal accross the whole EM spectrum. This is refered to as active galactic nucleus (AGN).
AGNs present a wide variety of observational characteristics from one system to another. They are currently understood through a unification scheme (Antonucci 1993; Urry & Padovani 1995; Heckman & Best 2014). It describes the structure of matter in the MBH environment. The viewing angle and the presence or absence of a powerful plasma jet explain AGNs' main observational characteristics. The current understanding of AGN is a MBH surrounded by an accretion disc. Outside, clouds can produce emission lines (the broad line region). It is further surrounded by a dusty molecular torus. If it exists, the plasma jet is perpendicular to the accretion disc.

1.1.1 Accretion disc

Accretion discs are formed by the accreting matter in the innermost regions of the AGN. Its presence explains the optical/Ultra-Violet (UV) continuum in AGN spectra.
To accrete onto the central MBH, the gas must lose its angular momentum to move onto orbits at smaller radii. The gas can lose angular momentum, e.g., if a magnetic field exerts torques on the disc surface (Balbus & Hawley 1991). Additionally (or alternatively), the angular momentum can be evacuated towards the external parts of the disc: the disc inner parts accrete by transferring their angular momentum to the outer parts. Part (or all of) the gravitational energy released by the accretion can be converted into heat. A fraction (or all) of the heat is radiated away. Thus, the emission spectrum depends on the processes that allow the accreting matter to lose its angular momentum and the radiative processes occurring in the disc. For instance, the main models used to describe the accretion disc physics and explain the observed spectra are summarized in Liu & Qiao (2022).

The standard thin accretion disc model (Shakura & Sunyaev 1973) is geometrically thin and optically thick. Its emission is a combination of black body radiation with different effective temperatures. The

temperature radial profile is computed e.g. in Frank et al. (2002). It is obtained by solving the thermal equilibrium of the disc at each radius.
The relative rotation of the different annuli of gas can redistribute the angular momentum through viscous stresses. However, in astrophysical discs around MBHs, the microscopic viscosity of the gas is too small to be efficient enough to explain the observed luminosities (e.g., King et al. (2007)). Therefore, other processes are involved to remove the gas angular momentum from the disc or redistribute it throughout the disc.
The magneto-rotational instability can generate turbulence and thus angular momentum transport in the disc (Balbus & Hawley 1991, 1992). Even with weak magnetic fields, the differential rotation of the disc annuli amplifies them, which can trigger instabilities and generate turbulence in the disc, resulting in angular momentum transport and energy dissipation.
Self-gravity in the disc can also lead to instabilities. This process is more important in the cooler parts of the disc and globally in more massive discs. It can either lead to angular momentum transport or fragmentation of the disc.
Disc winds also extract angular momentum. The three main mechanisms which can accelerate outflows are:

- Thermal driving mechanisms – In AGNs, vertical gradients of thermal pressure are induced by heating the outer layers of the disc due to irradiation by X-rays (Begelman et al. 1983). The X-rays are produced e.g. in the corona, where a hot plasma of electrons can up-scatter the thermal photons from the disc to X-ray energies by inverse Compton scattering.
- Radiative driving mechanisms – Resonant UV transitions in AGN accretion disc result in line-driven winds (e.g., Murray et al. (1999); Proga et al. (2000)).
- Magnetic pressure – If the poloidal component of the magnetic field is sufficiently inclined compared to the disc rotation axis, the magneto-centrifugal force accelerates winds (Blandford & Payne 1982).

The interaction between the magnetic fieled and the central spinning BH can also extract angular momentum in the disc innermost regions. This is the Blandford-Znajek effect (Blandford & Znajek 1977).

The geometrically thin and optically thick accretion disc model relies on two important assumptions. The gas gravitational energy released by the accretion onto the central mass is converted into heat and radiated, i.e., the radiation timescale is small compared to the accretion time scale. Besides, the radiation does not significantly impact fluid dynamics, i.e., the radiation pressure is small compared to the thermal pressure. These assumptions are not verified at too low or too high accretion rates.
At low accretion rates, the viscous heating primarily affects the ions, while the electrons produce the radiation. Coulomb collision between electrons and ions is inefficient in transferring the ions energy to the electrons. Thus, the cooling time scale through radiation becomes longer than the accretion time scale and part of the energy of the viscous heating is advected rather than radiated. This is the advection-dominated accretion flow (ADAF) (Narayan & Yi 1994, 1995a,b; Abramowicz et al. 1995, 1996). Due to the inefficiency of radiative cooling, the disc plasma becomes hot and thus geometrically thick. As the electron temperature is high, it becomes an efficient source of X-ray emission.
At high accretion rates, the radiation timescale is not negligible compared to the accretion time scale. Physically, the photons cannot escape the disc faster than the accretion. As in the case of the ADAFs, the radiation of the energy released by the accretion becomes inefficient, too. Abramowicz et al. (1988) show that the 'slim'-disc solution is no longer Keplerian, the inner edge of the disc can extend inside the Innermost Stable Circular Orbit (ISCO), and the emitted flux is to be calculated considering the heat advection, as the heat is not radiated at the same radius it is produced.
In the case of a thin disc, the emissivity is computed through a black-body emission at the disc local temperature. When radiation is inefficient, the disc emissivity has to consider the following components (Abramowicz & Fragile 2013). The relativistic electrons in the disc interact with ions and other electrons. This inelastic interaction slows down the electrons and emits a photon (Bremsstrahlung

emission). In a magnetic field, the relativistic electrons can radiate a synchrotron emission. The Bremsstrahlung and synchrotron can also be up-scattered in energy on the relativistic electron via Comptonization.

1.1.2 X-ray emission of active galactic nuclei and the Fe Kα emission line

The thermal emission of the optically thick and geometrically thin accretion disc produces photons from the Infrared (IR) to the optical/UV. The X-ray emission of AGNs is mostly non-thermal. It primarily arises due to the inverse Compton-scattering of the photons emitted by the disc in an optically thin hot plasma called the corona, where the electrons are relativistic (Zdziarski et al. 1994).
While the photons energy is small compared to the electrons rest-mass energy, the interaction can be described with the Thomson cross-section. Blumenthal & Gould (1970) and Rybicki & Lightman (1979) computed the energy loss rate of electrons in the (relativistic) electron rest frame.

$$\frac{dE}{dt} = \frac{4}{3}\,\sigma_T\; c\; U_{rad}\; (\gamma^2 - 1)$$

where σ_T is the Thomson cross-section, U_{rad} is the energy density of the photon radiation in the electron rest frame. γ is the Lorentz factor: $\gamma^2 = 1/(1 - v^2/c^2)$, where v is the (relativistic) speed of electrons.
Blumenthal & Gould (1970) computed the spectrum of inverse Compton radiation:

$$I(\nu)\; d\nu = \frac{3}{16}\;\frac{\sigma_T c}{\gamma^4}\frac{N(\nu_0)}{\nu_0^2}\;\nu\left[2\nu\ln\left(\frac{\nu}{4\gamma^2\nu_0}\right) + \nu + 4\gamma^2\nu_0 - \frac{\nu^2}{2\gamma^2\nu_0}\right]\; d\nu$$

where ν_0 is the constant frequency of the incident photons, and $N(\nu_0)$ is their number density.
To compute the observed spectrum emitted by the corona, the above spectrum must be integrated over the spectrum of incident photons and the speed distribution of the relativistic electrons in the corona. This results in a power-law

$$F_c\left[\text{photon s}^{-1}\ \text{keV}^{-1}\right] \propto E^{-\Gamma}$$

where E is the energy, and Γ is the photon index.

Part of this primary X-ray emission is directly observed as a power-law. Part of it illuminates the accretion disc and the molecular torus, where it is reprocessed through several mechanisms.

The X-ray photons can be Compton-scattered in the optically thick accretion disc, either on the free electrons due to the ionization of the disc material or on the electrons in atom outer layers and ions. Due to the low energy of electrons in the accretion disc, Compton photons with energy > 15 keV lose their energy while interacting in the disc: this produces a 'hump' peaking at approximately 30 keV (Lightman & White 1988; Magdziarz & Zdziarski 1995).
The X-ray photons can also suffer photo-electric absorption: they are absorbed by atoms or ions, which result in the ejection of an electron. The excited system deexcites via the filling of the inner-shell vacancy by an outer-shell electron. The energy released by this process can either be carried away by the emission of a photon, which produces a fluorescent line, or by the ejection of an electron (Meitner-Auger effect). This second process results in the absorption without re-emission of the incident primary X-ray photon.
Several chemical elements in the disc can produce fluorescent lines. The iron Kα emission line is the most prominent because of the higher fluorescent yield (the probability that the deexcitation occurs via the emission of a fluorescent photon instead of the Meitner-Auger effects) and the larger cosmic abundances (Reynolds & Nowak 2003). In the case of the fluorescent iron Kα emission line, the X-ray photon is photo-electrically absorbed by an electron in the iron K-shell. An L-shell electron fills this vacancy. If the deexcitation happens via the emission of a fluorescent photon, its energy is approximately 6.4 keV. Considering the spin-orbit interaction, there are, in fact, two iron lines at 6.391 keV and 6.404 keV ($\Delta E = 23$ eV) (Roseberry & Bearden 1936; Fabian et al. 2000). Since this energy

difference is small compared to the spectral resolution in X-ray observations, the energy of the emitted iron line photons is often supposed to be a single peak at 6.4 keV.

Figure 1 in Fabian et al. (2000) presents a figure from Reynolds (1996) Ph.D. thesis, which was based on similar computations by George & Fabian (1991). They study the reprocessing in the disc of the hard X-ray primary emission from the corona through Monte-Carlo simulations. The disc is supposed to be 'cold' ($T < 10^6$ K), i.e., hydrogen and helium are fully ionized, and the other elements are neutral. Their initial work was followed by new models accounting for the ionization state of the chemical elements, the different sources of hard X-ray radiation, and different vertical density prescriptions (Ross et al. 1999; Nayakshin et al. 2000). For instance, the code `Relxill` (García et al. 2014) resolves the plane-parallel radiation transfer to model the specific intensity of the emitted iron line, considering the emission and absorption process, depending on the abundance and ionization state of the gas (Kallman & Bautista 2001).

The abundance of iron in the disc to fluoresce competes with the photo-electric absorption of the iron line photons by iron L-shell and lower Z elements' K-shell electrons. Fabian et al. (2000) present the equivalent width of the line as a function of the iron abundance in the disc. The equivalent width is a measure of the iron line strength: it corresponds to the spectral extent of the continuum, which contains the same flux as the iron line.

The ionization state of the disc influences the line strength. Matt et al. (1993, 1996) classified it into four regimes depending on the value of the ionization parameter

$$\xi(r) = 4\pi \frac{F_x}{n}$$

where F_x is the X-ray flux received per unit area of the disc and n is the co-moving electron number density. It measures the ratio between the photo-ionization rate due to the X-ray emission proportional to the density and the recombination rate proportional to the square density.

- $\xi < 100$ erg $\cdot$ cm^{-1}: The first low ionization state corresponds to a 'cold' iron line at 6.4keV.
- 100 erg $\cdot$ cm^{-1} $< \xi <$ 500 erg $\cdot$ cm^{-1}: As the ionization increases, the iron ions in the disc can resonantly absorb the iron Kα photons. This resonant absorption can produce a new fluorescent iron line photon or be terminated by the Meitner-Auger mechanism. As the resonant absorption can happen several times, most primary X-ray photons initially producing fluorescent iron line photons are terminated by the Meitner-Auger effect. The iron line is thus weak.
- 500 erg $\cdot$ cm^{-1} $< \xi <$ 5000 erg $\cdot$ cm^{-1}: As the ionization continues to increase, the Meinter-Auger effect cannot happen anymore (Matt et al. 1997). Thus, iron line photons escape the disc. They continue to be resonantly absorbed and re-emitted by iron ions. The iron line frequency is increased due to the decrease in the screening of the nuclear charge from the K-shell electrons (Fabian et al. 2000).
- 5000 erg $\cdot$ cm^{-1} $< \xi$: Finally, the iron line completely disappears if the disc is too highly ionized.

The angle between the direction of emission of the iron line photon and the normal to the disc modifies the amount of reprocessing material that the iron line photons must cross and, thus, the potential scattering and absorption it might suffer. Ghisellini et al. (1994) give the link between the direction of emission of photons and the normal to the accretion disc

$$I(\cos i_e) = \frac{I(\cos i_e = 1)}{\ln(2)} \cos i_e \log\left(1 + \frac{1}{\cos i_e}\right)$$

The spatial extension of the corona remains unknown. It could be a compact source compared to the accretion disc extension. It is thus modeled as a point-source (Haardt & Maraschi 1991) and is

commonly referred to as the lamppost model in the literature. The corona could also be extended (e.g., Eardley et al. (1975); Haardt (1993)), and various models are proposed. Reynolds & Nowak (2003) summarize some of them. The first model separates the corona into two zones: a cool outer disc surrounding a hot inner disc where electrons are sufficiently hot to Comptonize the soft photons emitted by the cool outer disc. Other models explore the possibility for the corona and the disc to exist at the same radii, the corona being either an 'atmosphere' around the disc or clumpy and located only at certain positions.
The simplification to model the corona as a point-source is supported by spectral (see, e.g., Nowak et al. (2011); Szanecki et al. (2020)) and timing studies (see, e.g., Kara et al. (2016)). However, it cannot explain all observations (e.g., Wilkins & Gallo (2015)).

Once the iron line photons leave the outer slab of the accretion disc, they travel towards the observer at infinity. The General Relativistic (GR) influence of the central BH bends photon geodesics and shifts their initial frequency. Fabian et al. (1989) computed the impact of a Schwarzschild BH on the observed iron line as seen by an observer at infinity. Laor (1991) extended the computation for a Kerr metric. The Keplerian motion of the emitters in the disc results in a double peak profile due to the semi-relativistic Doppler effect: the parts of the disc moving outwards from the observer are red-shifted, while the parts of the disc moving towards the observer are blue-shifted. The GR influence of the central BH red-shifts the photon frequency due to the absolute movement of the emitters in the disc and the photons escaping from its gravitational influence. Finally, the GR boosting enhances the flux coming from the blue-shifted parts of the disc and decreases the flux coming from the red-shifted parts of the disc.

The GR impact of the central BHs broadens the iron line, while the intrinsic emission process described above produces narrow lines. The iron lines that have been observed appear broad. This has been known since the observation by ASCA (Tanaka et al. 1995) and the analysis by Nandra et al. (1997), who revealed the extension at low energy. With the *X-ray Multi-Mirror Mission-Newton* (*XMM-Newton*), it was possible to detect and measure the properties of iron lines (for instance, to infer the inclination angle between the accretion disc plane and the observer line of sight or the spin of the central BH, see, e.g., Fabian et al. (2000)). *Chandra* X-ray Observatory offered the highest spatial and spectral resolution but a lower effective collecting area. It was thus less suited for observation of relativistic lines (Reynolds & Nowak 2003).

Even though the broadening of the observed iron line can be attributed to the GR impact of the central BH, other mechanisms have been explored to explain it. Pariev & Bromley (1998) suggested that the hydrodynamic turbulence could also explain the line broadening for thicker discs. Warm absorbers are also suggested as potential contributors (see, e.g., Cappi et al. (1996); Done et al. (2000)). Narrow components to the iron line, which do not present substantial variability, have been observed in many Seyfert galaxies (Yaqoob & Padmanabhan 2004). This suggests that iron line reprocessing material fluoresces from the outer parts of the accretion disc or the dusty torus.

1.1.3 Other components of the AGN emission

Some AGNs can launch powerful jets. The processes to launch them are associated with the vicinity of the MBH and its gravitational effect on the surrounding magnetized accreting material. Liska et al. (2020) summarize the conditions of apparition of a jet: when a rapidly spinning BH has accumulated a sufficient amount of large-scale poloidal magnectic flux in its vicinity. It can either be accreted from large radii (also it is not clear whether the astrophysical discs have the properties to allow such accretion, e.g. Guilet & Ogilvie (2012)) or produced in the vicinity of the central BH through the magnetorotational instability (Balbus & Hawley 1991). At the basis of the jet, electrons are accelerated, which results in a synchrotron radio signal and inverse Compton up-scattering of the thermal photons from the disc at X-ray and γ-ray energies (e.g., King et al. (2017)). At larger scales ($\sim$ 10 kpc), radio

lobes associated with X-ray cavities can be resolved (e.g., Bîrzan et al. (2020)).
The broad line region corresponds to the region where the ionizing emission from the inner regions (the disc, the jet basis, and/or the corona) illuminates dense clouds of gas. It produces strong emission lines that are Doppler-shifted due to gas cloud velocity dispersion around $1\ 000 - 10\ 000\ \mathrm{km \cdot s^{-1}}$ (Blandford et al. 1990). They were initially used to differentiate AGNs from star-forming regions, as both present narrow emission lines associated with forbidden transitions (Kewley et al. 2019). Narrow lines in AGNs are produced in regions orbiting at larger radii from the central MBH (Peterson 2006).
The IR emission is consistent with a thermal emission from dust. It corresponds to the region above the "sublimation radius" from which the dust is no longer destroyed by the ionizing UV/optical radiation from the AGN inner parts. This radius delimits the broad line region from the dusty torus.
Wind and outflows can be launched from the accretion disc or outer regions, creating absorption features. The outflows absorb the underlying emission while moving towards the observer. Thus, if their velocity is sufficient, absorption features are mainly blue-shifted (Blustin et al. 2005).

1.1.4 Quiescent massive black holes

Quiescent MBHs can also be detected through the GR impact they have on their environment: e.g., tidal disruption of stars (see the review by Komossa (2015)), the resolution of the movement of the closest stars (applied to the closest MBH at the center of the Milky Way, SgrA*, Ghez et al. (1998); and other galaxies, Ferrarese & Ford (2005)), the resolution of the immediate vicinity of the event horizon (applied to SgrA*, Event Horizon Telescope Collaboration et al. (2022), and M87, Event Horizon Telescope Collaboration et al. (2019)), or the gravitational lensing of the background sky (e.g., in Abel1201, Nightingale et al. (2023)).

1.1.5 Cosmic evolution of massive black holes

Observational evidence suggests that almost all massive galaxies have a MBH at their center. Moreover, they are known to have a tight connection with the spherical component of their host galaxy (the bulge of stars). In the local Universe elliptical galaxies, the central MBH mass is correlated to the mass of the spheroidal bulge of stars(Magorrian et al. 1998) and stars' velocity dispersion (Ferrarese & Merritt 2000). See a review by Kormendy & Ho (2013). Thus, the evolution of MBHs is thought to be tightly connected to the evolution of their host galaxy. The processes behind this co-evolution have yet to be fully understood.

In the Λ-CDM cosmological paradigm of structure formation, dark matter halos grow through successive mergers across cosmic times (White & Rees 1978). Galaxies form and evolve in these dark matter halos and thus experience successive mergers. In this paradigm, the evolution of MBHs is complex: they grow through the accretion of gas and stars from their galactic environment and merger episodes with other MBHs following a galaxy merger (the timescales of MBH mergers are discussed in section 1.2). In the early 2000s, studies such as Kauffmann & Haehnelt (2000), Volonteri et al. (2003) or Di Matteo et al. (2005), followed the processes of accretion and mergers to explain the growth of MBHs and their co-evolution with their host galaxies through accretion and AGN feedback across cosmic times. However, the triggering of AGNs by galaxy collision, the ratio between growth through merger and accretion, or the secular processes that result in accretion remain to be investigated (e.g., De Rosa et al. (2019) and references therein).

These scenarios also require seeding MBHs at high redshift. The discovery of high redshift quasars (e.g., Fan et al., 2003) constrains the formation of MBHs with large masses ($M \sim 10^9\ M_\odot$) at high redshift ($z > 6$). There are currently two mechanisms to explain the formation of MBH seeds. The seed BHs can be the remnants of the first metal-free massive stars (e.g. Madau & Rees (2001), Haiman & Loeb (2001), or Madau et al. (2014)). In this case, the BH seeds have masses around $100\ M_\odot$ and are frequent. On the other hand, BH seeds can originate from the direct collapse of dense gas, forming seed BH with masses around $10^5\ M_\odot$ (e.g., Loeb & Rasio (1994), Begelman et al. (2006), or Lodato & Natarajan (2006)). In this case, the occupation fraction of seeds in halos at high redshift is smaller.

The detection of MBH binaries merger with the future gravitational wave detectors – the Laser Interferometer Space Antenna (LISA) and the Pulsar Timing Arrays (PTAs) – will give important observational constraints on the population of MBHs and their evolution across cosmic times (see section 1.3.1).

1.2 Formation of massive black hole binaries

After the collision of two galaxies, the two MBHs are isolated from each other in the remnant galaxy. Begelman et al. (1980) first explained the relevant processes to bring the two MBHs together to their final merger. To schematize, the evolution can be divided into three main steps.

1. The large-scale evolution is driven by dynamical friction onto the stars, gas, and dark matter of the remnant galaxy. This process is efficient until the two MBHs form a gravitationally bound binary and the interaction with the background field of stars and gas impacts the binary center of mass but not the separation between the two MBHs.
2. The processes that continue to extract the energy and angular momentum from the binary and bring the two MBHs closer are still an active area of research. Single interactions with stars can contribute to this process: this is referred to as the hardening phase. However, it is not clear whether it is the primary mechanism and whether it can efficiently bring the two MBHs at separation close enough for the third step to begin.
3. Once the two MBHs are close enough, the emission of GWs becomes efficient and can extract the energy and angular momentum of the binary.

The efficiency and timescales associated with each step are important to understand the formation of MBH binaries following galaxy mergers.

Dynamical friction is due to a massive perturber in an environment of collisionless particles with small masses compared to the perturber's mass M. The massive perturber deflects the particles from their unperturbed trajectories. This results in a trailing overdensity, which, in turn, decelerates the massive perturbator. The typical time scale of deceleration of a single MBH towards the remnant galaxy center is Binney & Tremaine (2008)

$$\tau_{DF} = \frac{8\ \mathrm{Gyr}}{\ln\Lambda}\ \left(\frac{r}{1\ \mathrm{kpc}}\right)^2\ \frac{\sigma}{200\ \mathrm{km}\cdot s^{-1}}\ \frac{10^7 M_\odot}{M}$$

where r is the distance between the MBH and the remnant galaxy's center, σ is the velocity dispersion of stars, M is the MBH mass, and $\ln\Lambda$ is the Coulomb logarithm (Chandrasekhar 1943): the logarithm of the ratio between the minimal (b_{min}) and maximal (b_{max}) impact parameters between the stars and the MBH, $\ln\Lambda = ln(b_{max}/b_{min})$.
This initial scenario considers a spherical, power-law, and smooth density profile for the stars' distribution, which is a simplistic view of the star distribution in galaxies. Section 2.2 in Amaro-Seoane et al. (2023) reviews the enrichment of the dynamical friction model to account for additional mechanisms and a more realistic description. This includes the nonsymmetric distribution of stars, the role of gas, and the influence of the AGN feedback on their environment. The qualitative conclusions on the efficiency of the dynamical friction remain unchanged. These studies are motivated by better predicting the MBH binary population that might be detectable with future Gravitational Wave (GW) detectors by specifying the time scales between the galaxy merger and the MBH merger.

Once the two MBHs are in their mutual sphere of influence, dynamical friction does not contribute significantly to bringing them closer to each other. The separation between them is about (Milosavljević

& Merritt 2001):

$$D_{DF\rightarrow hard} \sim 1 \text{ pc} \left(\frac{\sigma}{200 \text{ km} \cdot s^{-1}}\right)^{-2} \frac{10^7 M_\odot}{M}$$

The binary interacts only with a restricted number of stars on centrophilic orbits. These interactions remove the energy and angular momentum from the binary and expel the stars from the galactic center at high velocities. The efficiency of this process to shrink the binary depends on the number of stars in the 'loss cone' (i.e. the region of stars' phase space where the angular momentum is sufficiently low for stars to interact with the MBH binary) and how fast it is refilled (Milosavljevic & Merritt 2003). Considering a spherical distribution of stars, the timescale associated with the binary shrinking due to single interactions with stars is (Colpi 2014):

$$\tau_{hard} \sim 140 \text{ Myr } \left(\frac{1 \text{ mpc}}{D}\right)^2 \frac{10^4 \ M_\odot \text{ pc}^{-3}}{\rho_\star} \frac{\sigma_\star}{200 \text{ km} \cdot \text{s}^{-1}}$$

where D is the separation between the two MBHs and $\rho_\star$ is the star density. This timescale increases with decreasing separation. Thus, the process can become inefficient before the separation is small enough for the emission of GWs to become efficient.

More realistic distributions of the field of stars in the galaxy remnant have been considered. More specifically, the field of stars is not spherical and rotates, which creates a triaxial potential in which the torques exerted on the stars can deflect them towards the 'loss-cone' (e.g., Yu & Tremaine (2002); Merritt & Poon (2004); Khan et al. (2011); Preto et al. (2011); Gualandris & Merritt (2012); Khan et al. (2016)).
Other dynamical mechanisms were explored to find processes that could efficiently refill the 'loss cone'. Perets et al. (2007) study how massive perturbers (gas clouds) can interact with the galactic field of stars and deflect them towards the 'loss cone'. Bortolas et al. (2018) study the influence of stellar clusters in the MBH environment. Ogiya et al. (2020) explore the influence of two individual nuclear stellar clusters around each MBH on the acceleration of their orbital decay. Finally, if the MBH binary remains stalled in the hardening phase, a new galaxy merger can bring a third MBH companion (e.g., Rybicki & Lightman (1979); Bonetti et al. (2019).

The role of gas during this phase is still an active area of research. It was thought since the initial work by Pringle (1981) that the gravitational torque exerted by the binary on the surrounding material prevents it from accreting onto the binary. In the configuration of a circumbinary disc surrounding the binary (see, e.g., Armitage & Natarajan (2002, 2005); Milosavljević & Phinney (2005); Hayasaki (2009); Cuadra et al. (2009)), numerical woks have shown that the exchange of angular momentum is thus due to the viscous forces and results in the binary orbital decay.
However, following studies have shown that the gas can accrete onto the binary (e.g. MacFadyen & Milosavljević (2008); Farris et al. (2014, 2015a,b); Noble et al. (2012); D'Orazio et al. (2013, 2016); Gold et al. (2014); Shi & Krolik (2015); Muñoz & Lai (2016); Miranda et al. (2017)). Therefore, the net torque exerted by the binary does not necessarily shrink the orbital separation. Tang et al. (2017); Miranda et al. (2017); Munoz (2019) explored the global torques exerted by the surrounding accreting environment on the binary, considering the viscous forces, the gravitational interactions, and the accretion onto the binary. They found that the interaction between the circumbinary disc and the central MBH does not necessarily lead to its orbital decay. Their results open the question of the role of gas in the binary orbital evolution. Tiede et al. (2020); Heath & Nixon (2020) explored the impact of the disc's temperature on the net torque. Franchini & Martin (2019) explored the influence of the disc self-gravity. It suggests that a more complete treatment of thermodynamics is required to answer the question of the influence of the gas on the orbital evolution. Therefore, the gas might help the binary to shrink or, on the contrary, impede the orbital decay.

D'Orazio & Charisi (2023) emphasize that our current understanding of the last parsec problem is not to find efficient mechanisms to drive the orbital decay but to evaluate which ones significantly impact

the MBH binary orbital evolution.

Once the MBHs are close enough, the emission of GWs efficiently removes energy and angular momentum from the binary. The typical timescales are (Hughes 2009):

$$\tau_{GW} \sim 1 \times 10^8 \text{ years } \left(\frac{2 \times 10^6 M_\odot}{M}\right)^3 \frac{2}{q(1+q)} \left(\frac{D}{10^{-3} \text{ pc}}\right)^4$$

1.3 Multi-messenger observations of massive black hole binaries

I focus here on the last stages of the merger when the two MBHs form a close and gravitationally bound binary below the parsec scale. These systems are believed to be strong GW emitters during their inspiral phase and merger. They could be detected with future detectors such as LISA and PTAs.

The coalescence of MBHs is often separated into three phases: the inspiral, the merger, and the ringdown (see, e.g., Cattorini et al. (2023)). The inspiral corresponds to the first stages when the emission of GWs occurs in a steady state. The timescale associated with the orbital decay due to the emission of GWs is much longer than the MBH orbital period. The late inspiral and merger correspond to the phase when the two MBHs plunge towards each other and coalesce. The ringdown is the relaxation of the remnant MBHs into a Kerr BH.

1.3.1 Gravitational wave detection

LISA is a space-based interferometer designed to detect GW signals with frequencies between 0.1 and 10 mHz (Amaro-Seoane et al. 2023). The detector is planned for launch in the second half of the 2030s decade. It will be sensitive to the GWs emitted by various astrophysical systems. Not directly linked to the study of MBH binaries, this includes compact stellar-mass binaries in the Milky Way, the inspiral of extreme mass ratio compact objects such as a stellar-mass BH and a MBH, and the GW background. MBH binaries will be detected in the local Universe and at the peak of star formation at $z \sim 2$ for total mass binaries between 10^4 $M_\odot$ and 10^8 $M_\odot$. Besides, the BH mergers forming the local MBH binary populations will be detected up to a redshift $z \sim 20$.
The search for seed BH mergers at high redshift and the capacity to follow their merger across cosmic time is motivated by the remaining open question of the formation and evolution of MBHs and their interaction with their host galaxy during their evolution (see section 1.2).
If the host galaxy can be identified, it will allow to observe the EM counterparts of such systems. This will give more information on the co-evolution of MBH and their host galaxy. The joint observation of the gravitational and EM signals will enable the detection of the luminosity distance of the source and its redshift for constraining cosmological parameters (Tamanini et al. 2016). The time delay between the GW and EM signal will constraint theoretical parameters such as the graviton mass (e.g., Haiman (2017)).
If the identification of the source can be performed before the merger, it will allow monitoring the different phases of the coalescence, merger, and ringdown with multi-messenger observations (e.g., Canton et al. (2019)). The detection of the GW signal with a sufficient number of cycles will allow determining precisely the masses and spins of the MBHs, and the inclination angle of the binary. Therefore, it will provide an interesting laboratory for studying the EM counterparts and, thus, the accretion flows around the MBH binaries. Moreover, this will allow to test the hypothesis of triggering of AGN following major MBH binary mergers.

The PTAs are radio detectors that monitor the radio pulses emitted by galactic millisecond pulsars. The passage of a GW can be detected from the advance and delays of pulses. PTAs are sensitive to GWs with frequencies between 10^{-7} and 10^{-9} Hz (Taylor 2021). The first expected signal from these detectors is the GW background: an incoherent superposition of GWs emitted by the MBH binaries

merging (e.g., Sesana et al. (2008)). Eventually, the signal from close enough and massive enough MBH binaries might be loud enough to be detected above the stochastic noise of the background (Babak & Sesana 2012; Kelley et al. 2018).
Different PTA collaborations work independently and join their efforts in international collaboration: the Indian PTA, the Chinese PTA, the Parkes PTA, the European PTA, and the North American Nanohertz Observatory for GWs (NANOGrav). They jointly found evidence for a GW background, although using different data and analysis (The International Pulsar Timing Array Collaboration et al. (2023)).
Whether not conclusive, the combination of the Indian and European PTA data sets allows the measurement of a common low-GW signal that might be compatible with a population of MBH binary merging (Antoniadis et al. 2023). Other scenarios are also confronted with the data: the consequences of non-linear evolution of a scalar perturbation in the early Universe, or the oscillations of the Galactic potential due to ultra-light dark matter.
If a population of MBH binaries merging explains the signal, the result can constrain the population of MBH binaries. Agazie et al. (2023b) present the total mass, mass ratio, redhsift of emission of the GW signal in the PTA detectability waveband, and redhsift of the galaxy merger.
The combination of the NANOGrav collaboration data is compatible with a population of MBH binary merging (Afzal et al. 2023; Agazie et al. 2023a). The subsequent search for individual sources did not identify plausible candidates (Agazie et al. 2023a).

1.3.2 Electromagnetic counterparts

Resolution of two sources through electromagnetic observations at ~ 0.1 pc

The two sources can be resolved individually at sufficiently high separations between the MBHs. Radio observations can confirm the detection of resolved MBH binaries above the parsec scale (dual AGNs). For instance, the radio galaxy 0402+379, with an orbital separation of 7.3 pc, is the tighter binary found (Rodriguez et al. 2006).
In Breiding et al. (2021), 34 quasars showing broad emission line velocity offset compatible with a close MBH binary scenario were observed with the Very Long Baseline Array (VLBA). No source was resolved with two radio cores, which would have confirmed the binary scenario.
With the next generation of the event horizon telescope, the angular resolution will reach 15 micro-as, which could allow the resolution sources to be separated by ~ 0.1 pc, i.e., in their steady state of gravitational emission Ayzenberg et al. (2023). The expected maximal redshift for these detections is $z \sim 0.5$ (D'Orazio & Haiman 2017).

In the near-IR, Dexter et al. (2020) suggest that the broad line regions associated with the two binaries and the illuminated dusty torus could be resolved with the interferometry instrument Gravity+ on the Very Large Telescope Interferometer. It would target MBH binaries separated by ~ 0.1 pc and detected as MBHs due to their offset, single peak, and moving emission line.

D'Orazio & Loeb (2019) also suggest that the Gaia mission, mapping billions of stars with an astrometric precision of a few micro-as, might be able to detect the orbital motion of the optical broad line region associated with one component of the MBHs. The target systems are MBH binaries with a separation of ~ 0.1 pc and masses around $10^7 - 10^8\ M_\odot$ out to a redshift $z = 0.02$. However, the chances are sparse, as only one source will likely be detected over five years of the mission.

Spectroscopic signatures

Optical emission line offset at ~ 0.01 pc $- 0.1$ pc Shifted optical broad line regions can be interpreted as a kinematic offset due to the orbital motion of the MBH they are attached with (e.g., Dotti et al. (2009)). Along with individual sources studied before 2010, this motivated a systematic search of shifted broad lines in the SDSS spectra of quasars. The scenario of a MBH binary was

subsequently tested against the offset variability expected due to the orbital motion compatible with binary orbital parameters (Eracleous et al. 2012; Decarli et al. 2013; Liu et al. 2014; Runnoe et al. 2015, 2017). A few dozen candidates presented coherent variability (Runnoe et al. 2017; Guo et al. 2019), which allowed for constraining their orbital parameters.
Some spectra present double-peaked broad optical lines. It has been suggested that it could be emitted from two distinct broad line regions, each associated with one MBH of the binary. However, this interpretation was abandoned after follow-up studies (De Rosa et al. 2019). The double-peaked broad line can be explained with AGN discs (Eracleous et al. 2009).
De Rosa et al. (2019) highlight that this diagnostic of MBH binaries is only efficient on a narrow range of orbital separation. If the orbital separation is too small, the broad line region is truncated by the gravitational forces exerted by the companion (Roedig et al. 2014; Runnoe et al. 2015). If the orbital separation is too wide, the spectral shift due to the kinematic offset is not detectable. The analytical study by Pflueger et al. (2018) constrains the orbital separation between ~ 0.01 pc and ~ 0.1 pc for MBH binaries of mass $10^7 - 10^8\ M_\odot$.

Spectroscopic signatures of the accreting environment morphology [Circumbinary disc + cavity + mini discs] In the final stages of the merger, one possible structure of the matter accreting on the binary is extensively studied in numerical works (e.g., Milosavljevic & Merritt (2003); Milosavljević & Phinney (2005); MacFadyen & Milosavljević (2008); Gültekin & Miller¨ (2012); Kocsis et al. (2012); Roedig et al. (2014); Farris et al. (2014, 2015a,b); D'Orazio et al. (2015); Ryan & MacFadyen (2017); Tang et al. (2018); Duffell et al. (2020); Zrake et al. (2021); Combi et al. (2022); Dittmann & Ryan (2022); Gutiérrez et al. (2022); Westernacher-Schneider et al. (2022)). A circumbinary disc surrounds the binary. Matter accretes toward each MBH through ballistic and narrow streams of matter, which form mini-discs around each MBH.
In the advanced stages of the merger, the EM emission can be compared to that of a steady state standard accretion disc around a single AGN (Shakura & Sunyaev 1973). In the hypothesis of a circumbinary accretion disc, theoretical studies have shown that the torques exerted by the MBH binary can open a gap inside the binary (e.g., Milosavljević & Phinney (2005); MacFadyen & Milosavljević (2008); Kocsis et al. (2012). Therefore, if the circumbinary disc size scale is comparable to the size scale of a disc around a single MBH, the missing emitting material might result in missing flux in the thermic black body emission of the disc. This deficit in flux is called a notch (Gültekin & Miller¨ 2012; Roedig et al. 2014).
The optical/UV deficit in the flux thermal component was considered a potential observational signature of binary systems. However, individual targets studied, e.g., by Yan et al. (2015) or Liao et al. (2021), are more consistently explained by dust-reddening (Leighly et al. 2016). Moreover, a systematic search by Guo et al. (2020) in a sample of potential candidates identified by periodic brightness variation results in the same binary selection as in a control sample of quasars. Besides, Farris et al. (2015b) and d'Ascoli et al. (2018) argue that the streams of matter inside the cavity might compensate for the missing emission.
Inside the cavity, accretion might still occur through narrow streams of matter and eventually form persistent mini-discs around each MBH (Farris et al. 2014). The spectral signature at high energy of these mini-discs are studied by Roedig et al. (2014); Farris et al. (2015b); Ryan & MacFadyen (2017); d'Ascoli et al. (2018); Tang et al. (2018); Westernacher-Schneider et al. (2022). It includes an enhancement of the X-ray flux and a hardening of the X-ray spectrum. Saade et al. (2020) confronted these effects with X-ray observations, but no promising candidates were found.

Iron line Yu & Lu (2001); McKernan et al. (2013); Jovanović et al. (2014) explored whether the iron line can be used as a diagnostic of MBH binary systems. Yu & Lu (2001) and Jovanović et al. (2014) focus on the superposition of the two iron lines emitted by the accretion discs around each BH. McKernan et al. (2013) study the iron line profile when a massive satellite is embedded in the accretion disc of a MBH, thus opening a gap or a cavity in it.
No candidates were found in the X-ray Multi-Mirror (XMM)-Newton observations, and the future Advanced Telescope for High ENergy Astrophysics (Athena) is expected to confront this potential EM

signature with observations.

Periodic variability

Relativistic Doppler boost ($\sim 0.001 - 0.01$ pc) The orbital motion of the two MBHs is also expected to cause a periodic Doppler boost in the emission from the regions linked to each MBH. The targeted MBH binary systems must have azimuthal velocities sufficiently high to imprint this Doppler boost ($\sim 10\%$ of the orbital velocity, at least), which results in relatively small separations $\sim 0.001 - 0.01$ pc.
The main studies of the binary scenario tested against the periodic variation of observed optical lights are D'Orazio et al. (2015); Graham et al. (2015); Charisi et al. (2016, 2018); Kelley et al. (2019); Xin et al. (2020). These works assume a fixed circular binary orbit (i.e., the binary is in its steady state of GW emission). They also assume that the optical emission is emitted by the accretion disc surrounding only one of the MBHs and presents no intrinsic variability.
Theoretical models predict a periodic variation of the optical light curve. Assuming that the flux is $F_\nu \propto \nu^{\alpha_\nu}$ in the targeted waveband (where ν is the frequency and α_ν is constant on the targeted waveband), theoretical models (see, e.g., the demonstration in Charisi et al. (2018)) predict the amplitude flux variation

$$A_\nu = (3 - \alpha_\nu)\ \frac{1}{1+q}\sqrt{\frac{G(M_1+M_2)/c^2}{D}}\sin i_{obs}$$

where c is the speed of light, M_1 and M_2 are the two MBH masses, $q = M_2/M_1 < 1$ is the mass ratio, D is the separation between the two MBHs, and i_{obs} is the angle between the binary orbital plane and the observer's line of sight. This expression is used to compare the variability in different wavebands. The two photometric curves show similar variation periods but different amplitudes:

$$\frac{A_{\nu_1}}{A_{\nu_2}} = \frac{3 - \alpha_{\nu_1}}{3 - \alpha_{\nu_2}}$$

These scenario successfully explaines the optical variability of MBH binary candidates. However, if the method is applied to a control sample of aperiodic quasars, the Doppler signature can happen by chance in a significant fraction of them (about 30%, Charisi et al. (2018); Xin et al. (2020)). Moreover, Charisi et al. (2022) show that the intrinsic variability of the accretion disc emission, or the inclusion of both accretion disc emissions, results in a lower flux variation amplitude.
Similar to the UV/optical, the X-ray emission emanating from the innermost region of the disc is also Doppler-boosted. Canton et al. (2019) explore identifying the source of GWs detected with LISA through the periodic emission in X-rays due to Doppler boosting. This signature can be confused with red noise associated with the intrinsic variability of AGNs. Moreover, the Doppler modulation will superpose on the accretion variability of the discs surrounding each MBH or possible variations of the spectral shape with time. This will require more investigation with precise X-ray light curves from GR-Magneto-hydrodynamic (MHD) numerical simulations.

Reverberation mapping ($D < 0.01$ pc) D'Orazio & Haiman (2017); Wang et al. (2018); Ji et al. (2021) suggest that the IR emission emitted by the circumbinary dust torus echoes the periodic variation of the inner Doppler-boosted optical/UV emission. Dotti et al. (2022) explore the variation of the polarization of the flux in this configuration.
This signature has yet to be observed.

Periodic flares through gravitational lensing ($D < 0.01$ pc) D'Orazio & Di Stefano (2018) suggest that the gravitational lensing of the periodic optical/UV emission from the region attached to one of the MBH by its companion generates periodic flares superimposed on the periodic light curve. This magnification can become wavelength-dependent (Davelaar & Haiman 2022). Two quasar candidates for this type of binary EM signature are studied by Hu et al. (2020). One of them is compatible with a periodic Doppler boost and gravitational lensing. Further monitoring is necessary.

Periodic flares in the X-ray bands have also been examined as periodic gravitational lensing associated with the X-ray emission from the inner region around each MBH (Ingram et al. 2021).

Temporal variability of the emission of the accreting environment structure [Circumbinary disc + cavity + mini discs] The temporal variability of MBH binaries in the last stages of their merger is still an active area of theoretical research through simulations.
First, this variability requires the binary to accrete significantly relative to isolated AGNs, which is still debated (e.g., Dittmann & Ryan (2022)).
Duffell et al. (2020) use 2D hydrodynamic simulation to measure the accretion rate (and the torque exerted by the binary) for different values of the MBH binary orbital separation and mass ratio (the binary is expected to be on a circular orbit). Presenting a periodogram of the accretion rate, they show the main periodicities excited by the binary orbital motion in the accretion flow. Below the mass ratio $q = 0.05$, the accretion rate does not present significant periodicity. Between the mass ratio $q = 0.05$ and the mass ratio $q = 0.2$, the variability of the accretion rate is dominated by the orbital period and half the orbital period. Above the mass ratio $q = 0.2$, the variability is dominated by four to five times the orbital period (the value increases with the mass ratio) and approximately twice the orbital period.
D'Orazio & Charisi (2023) summarize the interpretation of this periodic variability. Above the mass ratio $q = 0.2$, the periodicity at half the orbital period is due to the matter accreted by each MBH when it passes near the eccentric inner edge of the accretion disc. The periodicity at $4 - 5$ times the orbital period is due to the coincidence of these accretion events with the position of an over-density at the inner edge called the 'lump'. The physical interpretation of the lump and the conditions in which it appears are still an active area of research (D'Orazio et al. 2013; Noble et al. 2021; Mignon-Risse et al. 2023a).
If the MBH binary orbit is eccentric, an extra absorption occurs at each periapse passage. When the eccentricity increases, the accretion rate modulation has a saw-tooth profile. The profile is a pulse for the highest eccentricities followed by an exponential decrease. Dunhill et al. (2015); Muñoz & Lai (2016); Zrake et al. (2021); Siwek et al. (2023) studied the impact of eccentricity on the time modulation of the accretion rate.
The accretion rate fixes the luminosity in a steady-state standard accretion disc (Shakura & Sunyaev 1973). However, regarding the accretion flows around MBH binaries, the equivalence between the accretion rate and the luminosity modulation remains to be investigated. More specifically, it depends on the cooling and radiative processes. D'Orazio & Charisi (2023) summarized the different hypotheses used in previous numerical works. A first cooling prescription is the standard α-disc model: the viscous heating of the disc is converted into black body radiation. A second cooling prescription is the temperature relaxation towards a reference profile on a prescripted timescale. A third cooling prescription is the relaxation of the entropy towards a reference profile on a prescripted time scale. The radiation is post-processed with the assumption of black body radiation. These different models highlight that converting the accretion rate modulation into a luminosity modulation depends on the time scale of viscous heating and radiative cooling. When the orbital period decreases at small separations, the timescale between changes in the accretion rate and the photon radiation becomes significant and requires further investigation.

Other morphologies of the accretion flow in the last stages of the merger The review by Cattorini et al. (2023) on the GR-MHD simulation in the final stages of the merger stresses that the question of the heating and cooling mechanisms also raises the question of the geometry of the accretion flow around the binary. In addition to the circumbinary disc scenario, the gas cloud scenario has been investigated by several studies. It considers the binary embedded in a hot and tenuous gas cloud, which is geometrically thick and radiatively inefficient (Farris et al. 2010; Bode et al. 2010, 2011; Giacomazzo et al. 2012; Kelly et al. 2017; Cattorini et al. 2023). The periodicity of the mass accretion rate depends on the mass ratio and spin alignment of the MBHs (Cattorini et al. 2022, 2023). Near the merger, the luminosity peaks (Kelly et al. 2017; Cattorini et al. 2022).

Jet morphologies

The previous EM signatures at different stages of the MBH binary merger were presented in roughly chronological order. Another class of EM signatures can be found for radio-loud AGN merging.
If an MBH is involved in a binary and launches a jet, two main effects can be expected (e.g., Krause et al. (2019)). Due to the orbital motion, the jet has a widening helical pattern. The orbital period expected for sub-parsec orbital separation ranges between a year to thousands of years, and the structures are persistent from the parsec scale to kiloparsec scales. Therefore, these signatures could be seen with multi-epoch imaging with the Very Long Baseline Interferometer (VLBI). The geodetic precession of the MBH spin around the binary angular momentum causes a periodic variation of the order of 10^6 years. These signatures are to be looked for in radio maps on hundreds of kilo-parsec scales. These morphological features might be seen in the VLBA radio maps.
These signatures have been confronted to individual jetted AGNs (e.g., Krause et al. (2019)).
However, other scenarios can also explain these phenomena. For instance, if the outer disc is misaligned with the central MBH spin, the Bardeen-Paterson effect (Bardeen & Petterson 1975) will tend to align the inner disc to the MBH spin. The accretion of material from the misaligned outer parts of the disc will then contribute to align the MBH spin perpendicular to the outer disc plane. This alignment provokes a spin precession on timescales comparable to the geodetic precession.

1.4 Context of this study

The work presented in this thesis is about the early stages of merging MBH binaries. It has two main objectives. The first objective is to understand how the accreting environment reorganizes from the situation of accretion discs around each isolated AGN to the structure around close binaries in later phases of the inspiral. Most of the numerical work focusing on the early stages of the binary inspiral considers a situation where the binary is embedded in a circumbinary disc. The binary has opened a gap, and mini-discs might surround each MBH. However, it remains unclear how the accretion discs around each MBH evolve when submitted to the gravitational influence of the MBH companion and how this structure of the accreting environment around the binary forms. Indeed, numerical simulations on the first stages of the merger mainly focus on the circumbinary disc:

- For some numerical simulations, the two MBHs and their individual accretion discs are outside the simulated domain, i.e., inside the simulation inner edge. It is the case in Armitage & Natarajan (2005); MacFadyen & Milosavljević (2008); Cuadra et al. (2009); Shi et al. (2012); Noble et al. (2012); D'Orazio et al. (2013); Rafikov (2016); Muñoz & Lai (2016); Miranda et al. (2017); Mignon-Risse et al. (2023a,b)
- Other numerical simulations consider the two MBHs inside the simulation domain. However, a source term is added to the hydrodynamical continuity equation to remove the fluid progressively inside a fixed radius equal to a fraction of the orbital separation around each BH. Therefore, the mini-discs around each BH are not consistently simulated down to the ISCO. Farris et al. (2014, 2015a,b); D'Orazio et al. (2016); Tang et al. (2017); Duffell et al. (2020) consider a fixed radius of half the separation. Moody et al. (2019) consider a fixed radius of 0.1 times the orbital separation. Zrake et al. (2021) consider a fixed radius of 0.2 times the orbital separation. Dittmann & Ryan (2022) and Westernacher-Schneider et al. (2022) use a torque-free sink prescription (Dempsey et al. 2020).

My thesis work focuses instead on the accretion disc around each MBH (the mini-discs in the context of circumbinary accretion) and studies the gravitational influence of the MBH companion. We do not assume a circumbinary disc at larger scales. This is part of the search for accurate initial conditions for numerical simulations at later stages of the merger.
Chapter 2 presents the hydrodynamical simulations designed to study the gravitational impact of the MBH companion on the accretion disc, while Chapter 3 presents the main outcomes of the numerical study. The article associated with this work is presented in Appendix A.

The orbital separations of these systems correspond to MBH binaries in their steady stage of GW emission: the angular momentum and energy extracted by the emission of GWs shrink the binary orbital separation at a low rate compared to its orbital period. Although some of the systems might have orbital separations large enough and be located close enough to be resolved individually in EM emission (see the first paragraph in section 1.3.2), it remains primordial to identify indirect EM signatures.
The second objective of the numerical simulations is to investigate how the MBH companion's gravitational influence affects the disc EM emission. The aim is to gather additional observational signatures for the presence of a MBH binary, distinct from the emission of isolated AGNs (as, e.g., the thermic emission, the iron line profile, or the periodic variability, see section 1.3.2).

The second part of my Ph.D. was dedicated to studying the iron Kα emission line profile and exploring whether the gravitational influence of the MBH companion on the disc structure impacts it. Using the iron line profile as a diagnostic of binary systems was studied by Yu & Lu (2001); McKernan et al. (2013); Jovanović et al. (2014):

- Yu & Lu (2001) present the iron line profiles due to the superposition of the iron lines emitted by the accreting discs around each MBH. They consider a small accretion disc (compared to the accretion disc size around isolated AGN) extending from the ISCO to an outer radius of 80 Schwarzschild radii of each MBH. They typically envisage systems with a separation of $10^4\ G(M_1 + M_2)/c^2$, corresponding to 0.1 pc for a total MBH mass of $10^8\ M_\odot$.
- At the separations considered by Yu & Lu (2001), the additional constant Doppler shift for each line due to the orbital motion of each MBH can be neglected. Jovanović et al. (2014) conduct a similar study at smaller separations (0.01 pc) and thus add the influence of the Doppler shift.
- McKernan et al. (2013) consider the approach of a satellite embedded in the accretion disc of a MBH. They study how opening a gap between two radii or a cavity inside a radius impacts the line profile.

Thus, the studies by Yu & Lu (2001) and Jovanović et al. (2014) do not consider the gravitational influence of the MBH companion on the accretion disc structure and how it impacts the iron line profile. The systems considered in the study of McKernan et al. (2013) concern either binary systems with smaller mass ratios or the last stages of their coalescence. Therefore, the work on the iron line presented here aims to understand how the changes in the accretion disc structure due to the gravitational influence of the MBH companion impact the iron line profile and whether it can be used to identify MBH binaries in the early stage of their merger.
The method to compute the iron line is presented in Chapter 4. The effects of the truncation of the outer parts of the disc on the iron line profile are presented in Chapter 5.

CHAPTER

2

NUMERICAL SIMULATIONS

This work focuses on the accretion disc around each MBH in the early stages of the merger. More specifically, the MBH binary is in the inspiral phase (see section 1.2). The two MBHs form a gravitationally bound system. It emits gravitational waves at a slow rate compared to the orbital period. Section 2.1 presents the astrophysical characteristics of these systems. The orbital separation between the two MBHs is comparable to the size of the accretion disc around an isolated MBH. Thus, we consider the accretion disc around one MBH under the gravitational influence of its companion. We focus on one of the accretion discs. This chapter presents the numerical simulations conducted to study the gravitational influence of a MBH companion orbiting outside the accretion disc surrounding a MBH. Section 2.2 presents the physical equations which describe the disc. Section 2.3 presents the numerical setup designed.

2.1 Massive black hole binaries in the inspiral phase

Accretion disc size is still an open question. As unresolved with EM observations, it must be measured with indirect methods, such as reverberation mapping (see, e.g., Guo et al. (2022)). This method interprets the temporal lag between the flux variability in different bands as the result of differences in light travel due to varying distances between the emission region and the observer. The density and temperature radial profiles in the accretion disc can be explored by assuming a black body radiation model, which can then be compared to other models, such as the standard disc model (Shakura & Sunyaev 1973). However, the distances between the regions that emit different bands and the theoretical predictions remain incompatible. The distances measured with reverberation mapping are larger than those predicted by theoretical models. Quasar micro-lensing analysis (as described, e.g., in Pooley et al. (2007), Cornachione & Morgan (2020)) also provides disc size measurement through the measurement of the distance between the emitting regions, and the results are also found to be higher than predicted by standard models. This is referred to as the accretion disc size problem.

Goodman (2003) considers the Toomre instability to derive the accretion disc size. In a differentially rotating disc, this criterion measures the radius from which small perturbations of the velocity (which compensate for the central gravitational attraction and pressure forces at equilibrium) will destabilize the disc due to the disc self-gravity. The disc outer edge is estimated to be around 10^{-2} pc using the density and temperature profiles from the standard thin disc model. For a MBH of 10^8 $M_\odot$, this is equivalent to 1 100 R_s, where $R_s = 2GM_1/c^2$ is the Schwarzschild radius of the primary MBH. This theoretical value is coherent with the one given by Lobban & King (2022) using a study by Collin-

Souffrin & Dumont (1990). Lobban & King (2022) compare this value to the maximal echo observed due to the reprocessing of the X-ray emission in the accretion disc. The value of 12 light days is coherent with the above-mentioned theoretical values.
Therefore, to initially allow the two accretion discs to exist around each MBH, the separation should be at least $2\ 000 - 2\ 500\ R_s$. Numerical simulations were conducted up to a separation of $3\ 000\ R_s$.

Studies focusing on the role of gas in the hardening phase have shown that this interaction tends to align the orbital plane of the binary with the circumbinary disc plane of the accreting matter (see, e.g., Nixon et al. (2013); Aly et al. (2015); Moody et al. (2019); Bourne et al. (2023)). Therefore, we will consider that the accretion disc orbits the same plane as the binary.

The simulations aim to understand the early impact of the MBH companion's gravitational influence on the accretion disc. Thus, the simulations are centered on one of the MBHs surrounded by its accretion disc, and the MBH companion lies outside the simulation domain.

Studies on the hardening phase also consider the impact of the gaseous and stellar environment on the binary eccentricity. The interaction with the stars during the hardening phase (e.g., Sesana (2010)) and the binary gaseous environment (e.g., Roedig et al. (2011); D'Orazio & Duffell (2021)) tend to form noncircular binaries. On the contrary, the later emission of GWs tends to circularize these orbits. However, we will first consider non-eccentric binaries. Therefore, the MBH companion orbits a circular orbit outside the primary MBH.

We will study only one of the accretion discs. The more massive the BH is, the more extensive its Lobe Roche is. Thus, the more massive BH accretion disc is more likely to survive the companion's approach. The study will focus on the primary MBH disc.
It has been found that during the hardening phase, the accretion from the circumbinary disc occurs preferentially on the lightest BH, pushing mass ratios towards 1 (see, e.g., Siwek et al. (2022) and references therein). However, whether this preferential accretion is efficient enough to significantly modify the MBH merging population is still being determined. Therefore, we will consider a wide range of mass ratios below unity.

Orbital separations of the system

It is logical to assume that the gravitational interaction between the two MBHs is Newtonian when long distances separate them. Hughes (2009) presents for a 'Newtonian, quadrupole' waveform the temporal evolution of the separation in a BH binary for Newtonian orbital dynamics:

$$D(t) = \left(\frac{256\ G^3\ M_1^3 q(1+q)\ (t_c - t)}{5c^5} \right)^{1/4} \tag{2.1}$$

where t_c is the time of the final coalescence of the BH binary and G is the gravitational constant. The shrinking of orbital separation over one BH binary orbital period T_{orb} is

$$\left[\frac{dD}{D} \right]_{dt=T_{orb}} = -\frac{16\sqrt{2}\pi}{5}\ q\sqrt{1+q}\ \left(\frac{D}{R_s} \right)^{-5/2} \tag{2.2}$$

When the separation is $3\ 000\ R_s$, the separation shrinks by less than $4 \times 10^{-6}\%$ over a binary orbital period. If the initial binary orbital motion is assumed to be circular, there is no reason to consider any evolution of the orbital parameters during the simulations. The simulations compare how the MBH companion impacts the primary's accretion disc, depending on the binary mass ratio and separation. For consistency, the configuration of the simulations must be the same for all systems. The binary orbital motion can be assumed to be circular and constant in time only if the orbital decay due to the emission of GWs expressed in equation (2.2) remains negligible. The orbital separation decay over

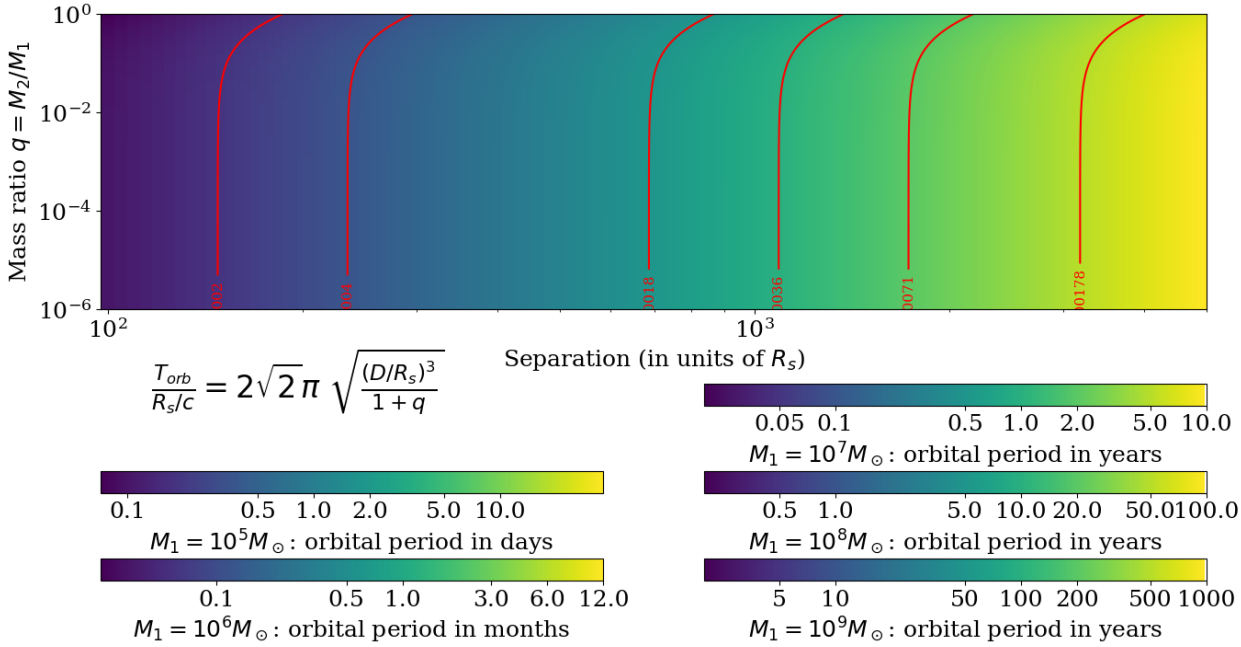

Figure 2.1: **Binary orbital period.**
The term in equation (2.3) brackets is displayed against $(D/R_s,\ q)$. Each color bar corresponds to the conversion in physical units for different values of the central MBH mass. The red curves correspond to the ticks displayed in the color bars for $M_1 > 10^7\ M_\odot$, and thus, the corresponding values of the binary orbital period in units of R_s/c (the units of the code).

one binary orbital period remains below 0.01% if the orbital separation is above $100 - 200\ R_s$. Hence, simulating the system during 100 binary orbital periods will only introduce an error of 1% in the orbital separation.

Orbital period and time to merger

Considering a Newtonian circular orbit, the MBH binary orbital period is

$$T_{orb} = \frac{R_s}{c}\left[2\sqrt{2}\pi \sqrt{\frac{(D/R_s)^3}{1+q}}\right] \tag{2.3}$$

Figure 2.1 displays the orbital period in units of R_s/c against $(D/R_s,\ q)$. The color bars display the conversion in physical units for different values of the central MBH mass. The orbital period almost reaches a millennium for the most massive equal mass binaries, while for the lightest systems, it can be of the order of a month. This significantly impacts the feasibility of the search for periodicities as an EM signature for binary systems. If the orbital period exceeds $50 - 100$ years, following the evolution is impossible due to the lack of observational archives.

The time to merger can be derived using equation (2.1).

$$T_{merger} = \frac{R_s}{c}\left[\frac{5}{32}\ \frac{(D/R_s)^4}{q(1+q)}\right] \tag{2.4}$$

Figure 2.2 displays the time to merger in units of R_s/c against $(D/R_s, q)$ with various color bars indicating the corresponding physical units for different M_1 values, as done in Figure 2.1. The time before the final coalescence varies from months to values exceeding the age of the Universe. These later binaries are stalled, usually called the last parsec problem. Besides the emission of GWs, other

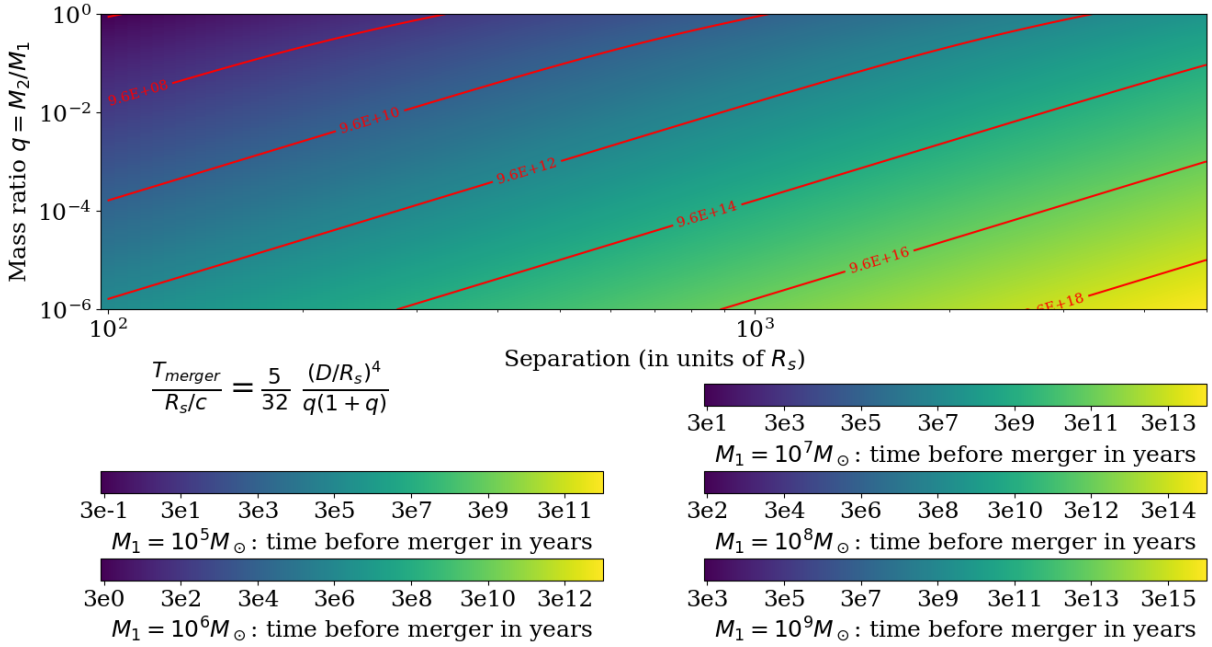

Figure 2.2: **Time to merger.**
The term in equation (2.4) brackets is displayed against $(D/R_s,\ q)$. Each color bar corresponds to the conversion in physical units for different values of the central MBH mass. The red curves correspond to the ticks displayed in the color bars, and thus the corresponding value of the time to merger in units of R_s/c (the units of the code).

mechanisms are required for the MBH binary to merge. The merger is expected for the lightest equal mass binaries within a few months to years. Identifying such a source would enable monitoring a MBH binary merger with multi-messenger observations.

Gravitational waves emitted by the massive black hole binary

The GW frequency equals the inverse of the orbital period. Figure 2.3 displays the inverse of the term in equation (2.3) brackets. The color bars show the corresponding values in Hz for different values of the primary MBH mass. The PTA sensitivity waveband is $10^{-9} - 10^{-7}$ Hz, while the LISA sensitivity waveband is $10^{-5} - 10^{-1}$ Hz. When the primary MBH mass is $10^5\ M_\odot$ or $10^6\ M_\odot$ with separation close to $100 - 200\ R_s$, the GWs emitted by the binary might be detectable with LISA; when $M_1 = 10^7\ M_\odot$ or $M_1 = 10^8\ M_\odot$, the emitted GWs for the considered separation values are within the PTA sensitivity waveband. Only the closest binaries might be detectable with PTA for the highest mass.

2.2 Physical equations

2.2.1 Two-dimensional hydrodynamic equations of a thin accretion disc

The complete description of the accretion disc should solve the MHD equations in a GR framework. Space-time description should consider the metric associated with the MBH binary.
However, the MBH companion is outside the accretion disc in the situation the simulations aim to describe. Therefore, its gravitational impact is stronger in the outer parts of the disc, where the GR effects due to the central MBH are fainter. Hence, the accretion will be studied using a Newtonian framework.

The structure of accretion discs depends on different parameters, such as the accretion rate and the magnetic field. This defines different regimes and coupling between the radiation and matter in the

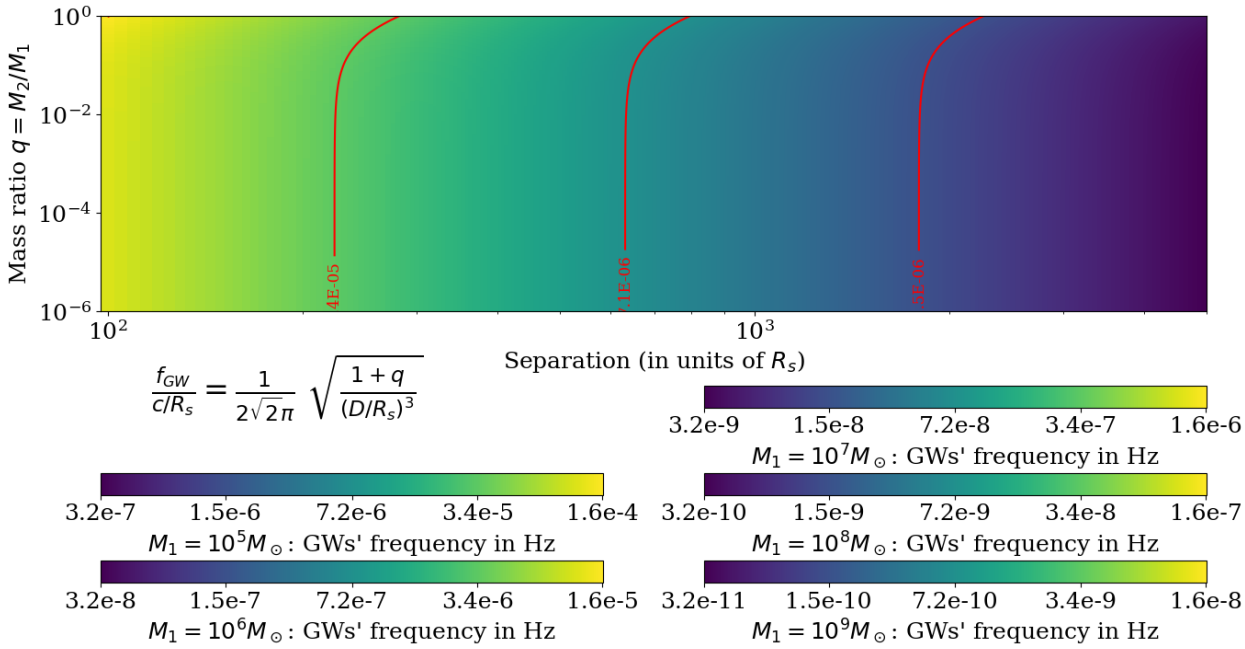

Figure 2.3: **GWs frequency.**
The inverse of the term in equation (2.1) brackets is displayed against $(D/R_s, q)$. Each color bar corresponds to the conversion in physical units for different values of the central MBH mass. The red curves correspond to the middle ticks displayed in the color bars. PTA sensitivity waveband $10^{-9} - 10^{-7}$ Hz. LISA sensitivity waveband $10^{-5} - 10^{-1}$ Hz.

disc (e.g., the different models in Abramowicz & Fragile (2013)).
Here, we will consider the geometrically thin and optically thick accretion disc. The accretion rate is low (less than 10% of the Eddington Luminosity). The radiative pressure is negligible compared to the gas pressure. The energy released by accretion is integrally converted into radiative energy (contrary to the model where a fraction of the energy can be advected).

The magnetic fields in the accretion disc play a key role in the physics of jets (see, e.g., the review by Pudritz et al. (2012)), winds, and angular momentum transport (Hawley & Balbus 1991; Balbus & Hawley 1991; Hawley & Balbus 1992; Balbus & Hawley 1992). These considerations are beyond the scope of this thesis, and we will not consider the impact of magnetic fields on the accretion disc structure.

In this context, the complete equations to describe the accretion disc are the Navier-Stokes equations:

$$\frac{\partial \rho}{\partial t} + \vec{\nabla} \cdot (\rho \vec{u}) = 0 \tag{2.5a}$$

$$\rho \frac{\partial \vec{u}}{\partial t} + \rho \left(\vec{u} \cdot \vec{\nabla} \right) \vec{u} = -\vec{\nabla} p + \rho \vec{f} + \vec{\nabla} \cdot \sigma \tag{2.5b}$$

$$\frac{\partial \rho E}{\partial t} + \vec{\nabla} \cdot ((\rho E + p)\vec{u}) = \rho \vec{f} \cdot \vec{u} + \vec{\nabla} (\sigma \cdot \vec{u}) + ... \tag{2.5c}$$

where ρ is the density, $\vec{u}$ is the velocity field, p is the pressure, $\vec{f}$ represents the volumic forces, σ is the viscous stress tensor, and E is the total energy density:

$$E = e + \frac{\rho u^2}{2}$$

where e is the internal energy. Equation (2.5c) is the energy conservation equation. Additional terms can be added to account for, e.g., radiation, temperature diffusion, and additional external heating

and cooling processes. This system of equations is closed by the equations of state:

$$p = p(\rho, T)$$
$$e = e(\rho, T)$$

where T is the temperature. For an ideal gas with a constant ratio of specific heat γ:

$$p = \frac{\rho \mathcal{R} T}{\mu}$$
$$e = \frac{p}{(\gamma - 1)\rho}$$

where $\mathcal{R}$ is the ideal gas constant, and μ is the gas molar mass.

The angular momentum loss is a key question underlying the description of accretion discs with the Navier-Stockes equations (2.5). As the molecular viscosity is insufficient to explain the accretion rates in usual astrophysical accretion discs, other mechanisms must be found. The turbulent viscosity is a plausible explanation for angular momentum transport in optically thick and geometrically thin accretion discs (Shakura & Sunyaev 1973; Pringle 1981). The magneto-rotational instability is also often used to describe angular momentum transport (Fromang & Lesur 2019). These mechanisms rely on a modeled description of the viscous stress tensor. As we do not aim to describe angular momentum transport through the disc, we will not introduce these model equations in our description of the accretion disc.
Moreover, to simplify the equations, energy conservation will not be considered. Therefore, the equations governing the accretion disc evolution are the Euler equations.

$$\frac{\partial \rho}{\partial t} + \vec{\nabla} \cdot (\rho \vec{u}) = 0 \tag{2.8a}$$
$$\rho \frac{\partial \vec{u}}{\partial t} + \rho (\vec{u} \cdot \vec{\nabla})\ \vec{u} = -\vec{\nabla} p - \rho \vec{f} \tag{2.8b}$$

The equation of state $p = f(\rho)$ closes the systems. The gas motion is considered adiabatic with a barotropic equation of state:

$$p = \kappa \rho^{\gamma} \tag{2.9}$$

with $\gamma = 5/3$ for a monoatomic gas. κ is the adiabatic constant. Its value fixes the sound speed in the accretion flow:

$$c_s^2 = \frac{dp}{d\rho} = \kappa \gamma \rho^{\gamma - 1} = \gamma \frac{p}{\rho} \tag{2.10}$$

As explained in the introduction, the accretion disc around the more massive BH is assumed to be aligned with the orbital plane. Considering that the accretion flow is confined to a narrow layer and the vertical motion can be neglected, the accretion disc can be studied only in two dimensions.

With this assumption, the vertical structure of the disc can be evaluated with the equilibrium of equation (2.8b) projected in the vertical direction, with the assumption that the vertical motion of the disc is negligible:

$$0 = -\frac{\partial p}{\partial z} + \rho \vec{f} \cdot \vec{e}_z = -\frac{\partial p}{\partial z} - \rho \frac{G M_1}{r^2 + z^2} \times \frac{z}{\sqrt{r^2 + z^2}}$$

where (r, ϕ, z) are the cylindrical coordinates centered on the BH with the accretion disc in the equatorial plane. $(\vec{e}_r, \vec{e}_\phi, \vec{e}_z)$ is the associated basis. Therefore,

$$\gamma \kappa \rho^{\gamma - 2} d\rho = -G M_1 \frac{z}{(r^2 + z^2)^{3/2}} dz$$

To evaluate the disc thickness at each radius $H(r)$, this formula can be integrated between the disc mid-plane where the density is $\rho_m(r)$ and the altitude where the density vanishes.

$$-\frac{\kappa\gamma}{\gamma-1}\rho_m^{\gamma-1}(r) = GM_1\left[\frac{1}{\sqrt{r^2+H^2}} - \frac{1}{r}\right]$$

The hypothesis of a thin disc is equivalent to $H/r \ll 1$. Therefore, the second term within brackets can be simplified with a first-order expansion

$$\frac{\kappa\gamma}{\gamma-1}\rho_m^{\gamma-1}(r) = \frac{GM_1}{2r}\left(\frac{H}{r}\right)^2$$

Therefore,

$$\frac{H(r)}{r} \ll 1 \Leftrightarrow \frac{2\kappa\gamma}{(\gamma-1)GM_1}\, r\rho_m^{\gamma-1} \ll 1 \tag{2.11}$$

This relation first implies that

$$\frac{2\gamma}{\gamma-1}\, p \ll \frac{\rho_m(r)GM_1}{r}$$

The pressure term is negligible in front of gravity. This, in turn, limits the sound speed

$$\frac{2}{\gamma-1}c_s^2 \ll \frac{GM_1}{r} = \left(v_\phi^{kepler}\right)^2 \tag{2.12}$$

where $v_\phi^{kepler} = \sqrt{\frac{GM_1}{r}}$ is the angular velocity of Keplerian circular orbits around the central BH.

Moreover, the condition in equation (2.11) also constrains the density profile in the disc mid-plane. If the lengths are scaled to the Schwarzschild radius of the central BH, the speed to the speed of light, and the masses to the central mass M_1, equation (2.11) is

$$\frac{4\gamma}{\gamma-1}\, \kappa^\star\, r^\star {\rho_m^\star}^{\gamma-1} \ll 1$$

where $\kappa^\star$ (respectively $r^\star$, $\phi_m^\star$) are the dimensionless quantities associated with κ (respectively r, ϕ_m). As $\gamma = 5/3$, the first term is of the order of unity. Thus, the condition is

$$\kappa^{\star 3/2}\rho_m^\star \ll r^{\star 3/2} \tag{2.13}$$

Thus, the radial evolution of the density must stay below a power law of $-3/2$ to study an arbitrarily large accretion disc.

2.2.2 Pseudo-Newtonian potential for the primary massive black hole potential

Artemova et al. (1996) present several pseudo-Newtonian potentials. These potentials are not an approximate solution of the GR equation or a fit of the exact solution. They are used to reproduce GR effects in the disc structure simulated with hydrodynamic equations.

The Newtonian potential cannot explain the GR effect of a disc's ISCO. Thus, to simulate the disc down to the ISCO, we describe the gravitational influence of the central MBH on its surrounding disc by a pseudo-Newtonian potential. Using these potentials in numerical simulations allows for maintaining the disc inner edge at the ISCO.
The Paczsynski-Wiita potential is (Paczyńsky & Wiita 1980)

$$V_{PW}(r) = -\frac{GM_1}{r-R_s}$$

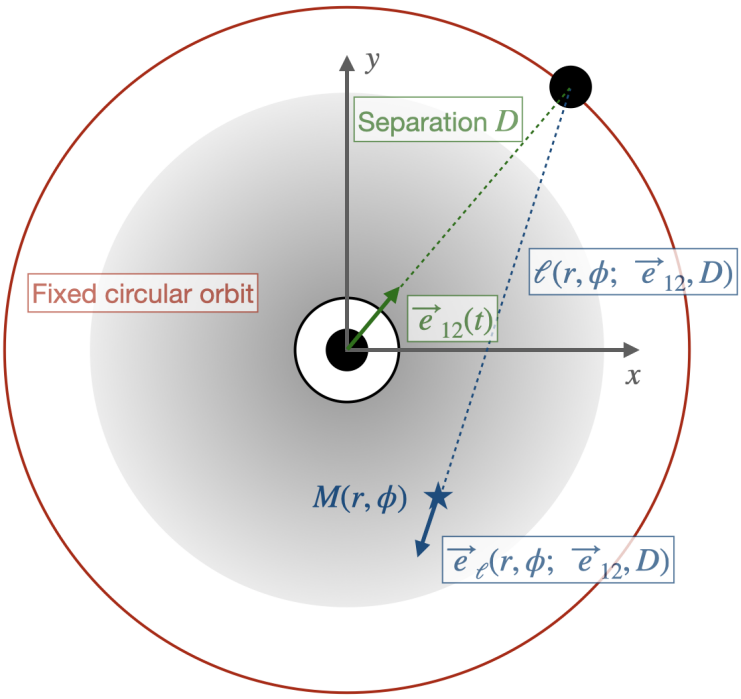

Figure 2.4: **Parametrization of the accretion disc in the frame centered on the primary MBH.**

It accurately reproduces the position of the ISCO and the marginally bound circular orbit. Another potential that accurately produces the radius of these orbits is the one introduced by Nowak & Wagoner (1991).

$$V_{NW} = -\left(\frac{GM_1}{r}\right)\left[1 - 3\frac{GM_1}{rc^2} + 12\left(\frac{GM_1}{rc^2}\right)^2\right]$$

The difference between these two potentials lies in their errors when they are used to compute other quantities compared to the GR solution. The radial profile of the Nowak & Wagoner (1991) potential results in a more accurate radial profile of the angular velocity for circular orbit. However, the Paczyński & Wiita (1980) potential is better at reproducing the specific energy at the ISCO. When the α-disc model (Shakura 1972) is used to compute the emission of the disc, the Paczyński & Wiita (1980) potential results in a smaller overestimation of the overall energy dissipation at each radius than the Nowak & Wagoner (1991) potential. In the work presented here, we used the Paczyński & Wiita (1980) potential as the final aim is to understand the impact of the MBH companion on the emission of the disc.

Therefore, the volumic force exerted by the central MBH on its surrounding disc is

$$\vec{f}_{PW}(r,\phi) = -\frac{GM_1}{(r-3R_s)}\vec{e}_r \tag{2.14}$$

2.2.3 Gravitational influence of the massive black hole companion

The presence of a MBH companion must be considered through two different volumic forces in the Euler equations (2.8). Firstly, due to the orbital motion of the primary MBH, the referential centered on it is not inertial. Secondly, the MBH companion exerts a gravitational force on the accretion disc.

As explained in section 2.1, the binaries studied here are in the first stages of their merger. Therefore, the orbital motion of the MBHs is Newtonian. Moreover, the ellipticity of their orbital motion is

neglected. Therefore, the inertial force density due to the primary MBH orbital motion is

$$\vec{f}_{ie} = -\frac{GM_2}{D^2}\ \vec{e}_{12} \tag{2.15}$$

where $\vec{e}_{12}$ is the elementary vector from the primary MBH to the MBH companion (see Figure 2.4). The axes of the Cartesian coordinates associated with the primary MBH are kept parallel to those in the frame associated with the binary center of mass. Thus, there is no requirement to account for additional Coriolis forces.

The MBH companion is outside the accretion disc and the simulation domain. Therefore, we do not simulate matter near its ISCO. Thus, the force exerted by the MBH companion on the accretion disc can be considered Newtonian. Its density is

$$\vec{f}_{BH_2} = -\frac{GM_2}{\ell^2}\ \vec{e}_{\ell} \tag{2.16}$$

where $\ell = \ell(r, \phi;\ D, \vec{e}_{12})$ is the distance between the fluid cell within the disc to the MBH companion, and $\vec{e}_{\ell} = \vec{e}_{\ell}(r, \phi;\ D, \vec{e}_{12})$ is the elementary vector pointing from the fluid cell to the MBH companion (see Figure 2.4).

$\vec{e}_{12}$, ℓ, and $\vec{e}_{\ell}$ in equations (2.15) and (2.16) depend on the orbital motion of the MBH companion in the primary MBH rest frame. The MBH companion position in polar coordinates around the primary MBH (R_{BH_2}, Φ_{BH_2}) is

$$R_{BH_2} = D \tag{2.17a}$$

$$\Phi_{BH_2} = \frac{2\pi}{T_{orb}} t + \Phi^0_{BH_2} \tag{2.17b}$$

where the binary orbital period is given in equation (2.3), and $\Phi^0_{BH_2}$ is linked to a reference position of the MBH companion. The polar coordinates of $\vec{e}_{12}$ in the primary MBH's frame is

$$\vec{e}_r \cdot \vec{e}_{12} = \cos\left(\Phi_{BH_2}(t) - \phi\right) \tag{2.18a}$$

$$\vec{e}_{\phi} \cdot \vec{e}_{12} = \sin\left(\Phi_{BH_2}(t) - \phi\right) \tag{2.18b}$$

The distance between the fluid cell within the disc and the MBH companion is

$$\ell^2 = r^2 + D^2 - 2rD\cos\left(\phi - \Phi_{BH_2}(t)\right) \tag{2.19}$$

The polar coordinates of $\vec{e}_{\ell}$ in the primary MBH's frame is

$$\vec{e}_r \cdot \vec{e}_{\ell} = \frac{r - D\cos\left(\phi - \Phi_{BH_2}\right)}{\ell} \tag{2.20a}$$

$$\vec{e}_{\phi} \cdot \vec{e}_{\ell} = \frac{D\sin\left(\phi - \Phi_{BH_2}\right)}{\ell} \tag{2.20b}$$

2.3 Numerical setup

2.3.1 Basics of the numerical resolution of hyperbolic equations

The 2D hydrodynamic system of equations (2.8) can be written in the general conservative form

$$\partial_t \mathcal{U} + \nabla \cdot \mathcal{F}(\mathcal{U}) = \mathcal{S}\left(\mathcal{U}, \partial_i \mathcal{U}, \partial_{ij} \mathcal{U}, \vec{x}, t\right) \tag{2.21}$$

$\mathcal{U}$ represents the conservative variables:

$$\mathcal{U} = \begin{pmatrix} \rho \\ \rho\vec{u} \end{pmatrix}$$

$\mathcal{F}$ represents the fluxes:

$$\mathcal{F} = \begin{pmatrix} \rho\vec{u} \\ \rho\vec{u} \otimes \vec{u} - \kappa\rho^{\gamma}\underline{\underline{1}} \end{pmatrix}$$

where $\underline{\underline{1}}$ is the 2×2 identity matrix. The source terms $\mathcal{S}$ are the gravitational terms due to the two MBHs and the inertial force due to the primary MBH orbital motion.

$$\mathcal{S} = \begin{pmatrix} 0 \\ \vec{f}_{BH_1,PW} + \vec{f}_{BH_2} + \vec{f}_{ie} \end{pmatrix} = \begin{pmatrix} 0 \\ -\frac{\rho G M_1}{(r-R_s)^2}\ \vec{e}_r - \rho\ \frac{GM_2}{\ell^2}\ \vec{e}_\ell - \rho\frac{GM_2}{D^2}\ \vec{e}_{12} \end{pmatrix}$$

This equation belongs to the general class of hyperbolic partial differential equations, which can be solved with the code `MPI-AMRVAC` (Keppens et al. 2012; van der Holst et al. 2012). `MPI-AMRVAC` is a versatile code that solves hyperbolic differential equations in different situations. It contains different physics modules (for instance, hydrodynamics and MHD). Various numerical schemes to solve the partial derivative equations are implemented. The code can work in one, two, or three dimensions with different geometries.

As mentionned previously the equations describing the evolution of the disc are in two dimensions and the polar coordinates are used. The adiabatic equations of hydrodynamics are used, with specific source terms that account for the gravitational influence of the two MBHs and the primary MBH orbital motion. I implemented these source terms in a subroutine provided for in `MPI-AMRVAC`.

The conservative quantities are continuous throughout the accretion disc and depend on the position (r, ϕ) and time (t). To solve the equations numerically, space and time must be discretized. The accretion disc is divided into cells, forming the simulation grid together. The radial and azimuthal edges of cells are written $(r_i)_{0\leq i\leq N_r}$, where N_r is the number of cells in the radial direction and $(\phi_j)_{0\leq j\leq N_\phi}$, where N_ϕ is the number of cells in the azimuthal direction. The solution is computed on a list of discrete times t^n.
Equations (2.21) can be integrated over each cell's spatial extent in two dimensions and between two time steps.

$$\int_{t^n}^{t^{n+1}} \iint_{S_{ij}} \left[\partial_t \mathcal{U} + \nabla \cdot \mathcal{F}(\mathcal{U})\right] = \int_{t^n}^{t^{n+1}} \iint_{S_{ij}} \left[\mathcal{S}\left(\mathcal{U}, \partial_i \mathcal{U}, \partial_{ij}\mathcal{U}, \vec{x}, t\right)\right] \tag{2.22}$$

where S_{ij} is the surface of the cell (i, j) (from r_i to r_{i+1} and from ϕ_j to ϕ_{j+1}). The left-hand side of this equation can be simplified since the integrated quantities are expressed as a time derivative or divergence (Green-Ostrogradsky theorem). Before writing the simplified equation, the following quantities are introduced:

$$U_{ij}^n = \int_{r_i}^{r_{i+1}} \int_{\phi_j}^{\phi_{j+1}} \mathcal{U}(r, \phi, t^n)\ r dr d\phi \tag{2.23a}$$

$$[F_\phi]_{ij}^n = \int_{t^n}^{t^{n+1}} \int_{r_i}^{r_{i+1}} \mathcal{F}(r, \phi_j, t^n) \cdot (dr\vec{e}_\phi) \tag{2.23b}$$

$$[F_r]_{ij}^n = \int_{t^n}^{t^{n+1}} \int_{\phi_j}^{\phi_{j+1}} \mathcal{F}(r_i, \phi, t^n) \cdot (r_i d\phi \vec{e}_r) \tag{2.23c}$$

$$S_{ij}^n = \int_{t^n}^{t^{n+1}} \int_{r_i}^{r_{i+1}} \int_{\phi_j}^{\phi_{j+1}} \mathcal{S}(r, \phi, t)\ dt r dr d\phi \tag{2.23d}$$

Equation (2.23a) is the average value of the conservative variable within a single 2D cell. Equations (2.23b) and (2.23c) are the fluxes that cross the edges of the cell during the iteration time step. Equation (2.23d) is the source term exerted on the whole cell over the iteration time step.

Equation (2.22) is equivalent to

$$U_{ij}^{n+1} = U_{ij}^{n} - {F_{r}}_{i+1,j}^{n} - {F_{r}}_{i,j}^{n} - {F_{r}}_{i,j+1}^{n} - {F_{r}}_{i,j+1}^{n} + S_{ij}^{n} \tag{2.24}$$

Thus, the conservative variable value can be computed iteratively from a time step to the following. The numerical solution of the hydrodynamic equations at each time step is U_{ij}^{n}.

To implement these equations, lengths are normalized to the primary MBH Schwarzschild radius R_s, speeds to the speed of light c, and masses to the primary MBH mass M_1. The dimensionless quantities will be written with the symbol $\star$.

The numerical schemes to implement this method have a general philosophy of performing first a reconstruction step (i.e., computing numerically the equations (2.23)), then an evolution step which solves Riemann problems at each cell interface, and finally a projection step to compute the conservative variable at the cell centers from the solution to Riemann problems.

2.3.2 Initial conditions

The numerical simulations are designed to understand the impact of the MBH companion on the accretion disc structure. Therefore, the initial conditions are consistent with the equilibrium of the disc around the isolated primary MBH. The radial velocity is null, the initial density is axisymmetric, and the partial derivatives with respect to time are null. As the equilibrium is defined around the isolated primary MBH, the volumic $\vec{f}$ in the Euler equations (2.8) equals the Paczynski-Wiita volumic force given in equation (2.14). The axisymmetric radial profile for the azimuthal velocity profile can be derived from equation (2.8b) projected on the radial axis.

$$u_{\phi,0}^{\star}(r^{\star},\phi) = u_{\phi,0}^{\star}(r^{\star}) = \sqrt{r^{\star}\ \kappa^{\star}\gamma\ \left(\rho_0^{\star}(r^{\star})\right)^{\gamma-2}\ \frac{\partial \rho_0^{\star}}{\partial r^{\star}}(r^{\star}) + \frac{r^{\star}}{2\left(r^{\star}-1\right)^{2}}} \tag{2.25}$$

where $\rho_0^{\star}(r^{\star})$ is the dimensionless initial condition of density. The centrifugal force compensates for the central MBH's gravitational attraction (the second term under the square root) and the pressure forces (the first term under the square root).

The axisymmetric profile for the initial density condition is the same as in Vincent et al. (2013). Their study also uses the Paczyński & Wiita (1980) potential to describe the MBH's gravitational influence on its surrounding accretion disc.

$$\rho_0^{\star}(r^{\star},\phi) = \rho_0^{\star}(r^{\star}) = \frac{\rho_0^{\star}}{4}\left(1+\tanh\left(\frac{r^{\star}-r_b^{\star}}{\sigma_b^{\star}}\right)\right)\left(1-\tanh\left(\frac{r^{\star}-r_{ext}^{\star}}{\sigma_{ext}^{\star}}\right)\right)\left(\frac{3}{r^{\star}}\right)^{3/2} \tag{2.26}$$

The first term in brackets defines the accretion disc inner edge, while the second term in brackets defines the disc outer edge. $\sigma_b^{\star}$ and $\sigma_{ext}^{\star}$ are homogeneous to length and characterize the sharpness of each disc edge.
Within the disc, the two terms in brackets approach one. Thus, the density profile within the disc is

$$\rho_0^{\star}(r^{\star}) = \rho_0^{\star}\left(\frac{3}{r^{\star}}\right)^{3/2} \tag{2.27}$$

This evolution of the density within the disc ensures that the hypothesis of a thin accretion disc remains valid, as explained in section 2.2.1 (see equation (2.13)).

The parameters (r_b, σ_b) control the location and sharpness of the density drop at the inner edge. These parameters are chosen to place the inner edge of the disc at the ISCO defined by the Paczyńsky & Wiita (1980) potential. Initially, these parameter values were the same as in Vincent et al. (2013): $r_b = 1.3\ R_{ISCO} = 3.9\ R_s$ and $\sigma_b = 0.05\ R_{ISCO} = 0.15\ R_s$.
The outer edge of the accretion disc is characterized by the parameters (r_{ext}, σ_{ext}).

2.3.3 Computational time, azimuthal resolution, limitation of the separation value, and azimuthal boundary conditions

The solution to Riemann problems at each cell interface consists of elementary waves (rarefactions, contacts, and shock waves) propagating from the cell center. If the time step between iterations $(t^{n+1} - t^n)$ is too long, these waves will reach the edges of the cell. Thus, they interfere with the solutions of the Riemann problem propagating from the neighboring cells, which cannot be considered in the formulation (see, e.g., section 6.3.2 in Toro (2009)). Therefore, time steps are limited at each iteration by the velocity of the wave solutions to the Riemann problem. This limitation is commonly known as the Courant–Friedrichs–Lewy (CFL) condition. For the Euler equations, the wave speeds generated by the solution of the Riemann problem can be estimated using the following formula (e.g., Toro (2009))

$$S_{max} = \max_{(i,j)\in[1;N_r]\times[1,N_\phi]} \left(\ |[u_r^\star]_{i,j}| + c_s \ , \ \ \left|[u_\phi^\star]_{i,j}\right| + c_s \ \right)$$

where $\left([u_r^\star]_{i,j},\ [u_\phi^\star]_{i,j}\right)$ are the component of the velocity field at the center of the cell (i, j) The radial velocity is small compared to the azimuthal velocity (the initial condition is the equilibrium of the disc). Moreover, the sound speed is small compared to the Keplerian velocity field (see equation (2.12)). Therefore, the azimuthal velocity can approximate the speed of the solution to Riemann problem at each cell interface. The maximal value of each iteration time step is given by

$$\delta t^\star < \min_{(i,j)\in[1;N_r]\times[1,N_\phi]} \left(\ \frac{[r^\star]_{i,j} \times \delta\phi}{[u_\phi^\star]_{i,j}} \ \right)$$

$[r^\star]_{i,j} \times \delta\phi$ is the size of each cell in the angular direction: $[r^\star]_{i,j}$ is the radius at the center of the cell and $\delta\phi = \phi_{j+1} - \phi_j$ is constant. As the radial profile of the azimuthal velocity increases towards the ISCO, this radius $r^\star_{ISCO} = 3$ imposes the stronger CFL condition. Therefore, the number of time steps to describe one orbit of the MBH is at least:

$$N \simeq \frac{T^\star_{orb}}{\delta t^\star} > \frac{T^\star_{orb}}{\left[\frac{r^\star_{ISCO} \times \frac{2\pi}{N_\phi}}{[u_\phi^\star]_{ISCO}}\right]} \simeq \frac{N_\phi\ D^{\star 3/2}}{\sqrt{6(1+q)}} \tag{2.28}$$

where $[u_\phi^\star]_{ISCO}$ is the angular velocity at the ISCO. Thus, the number of steps is directly proportional to the number of cells in the azimuthal velocity. Furthermore, the length of the cells in the azimuthal direction is $r \times \delta\phi$. Thus, it increases in the outer regions, where the influence of the MBH companion is expected to have a stronger impact. Therefore, the number of cells used in the azimuthal direction is a compromise between the resolution of the simulation and the computation time. It is fixed to $N_\phi = 320$.

The total number of iterations required to compute one orbital period of the MBH companion for the binary orbital parameters $(D = 3\ 000\ R_s, q = 10^{-3})$ is at least 2.2×10^7. This was the binary system with the longest orbital period that was studied. As mentioned in Section 2.1, this orbital separation is sufficient to consider accretion discs with typical astrophysical sizes around each MBH.

The equations (2.23) are solved using a second order spatial numerical scheme implemented in `AMRVAC`. Therefore, two ghost cells are required to compute the evolution of conservative variables in the last two rows of the simulation grid. The boundary conditions are calculated using the primitive variables (and not the conservative variable), as they are independent.
In the azimuthal direction, the conditions are periodic, meaning that the value of the conservative variable in the ghost cells is copied from the two first rows at the opposite end of the grid.

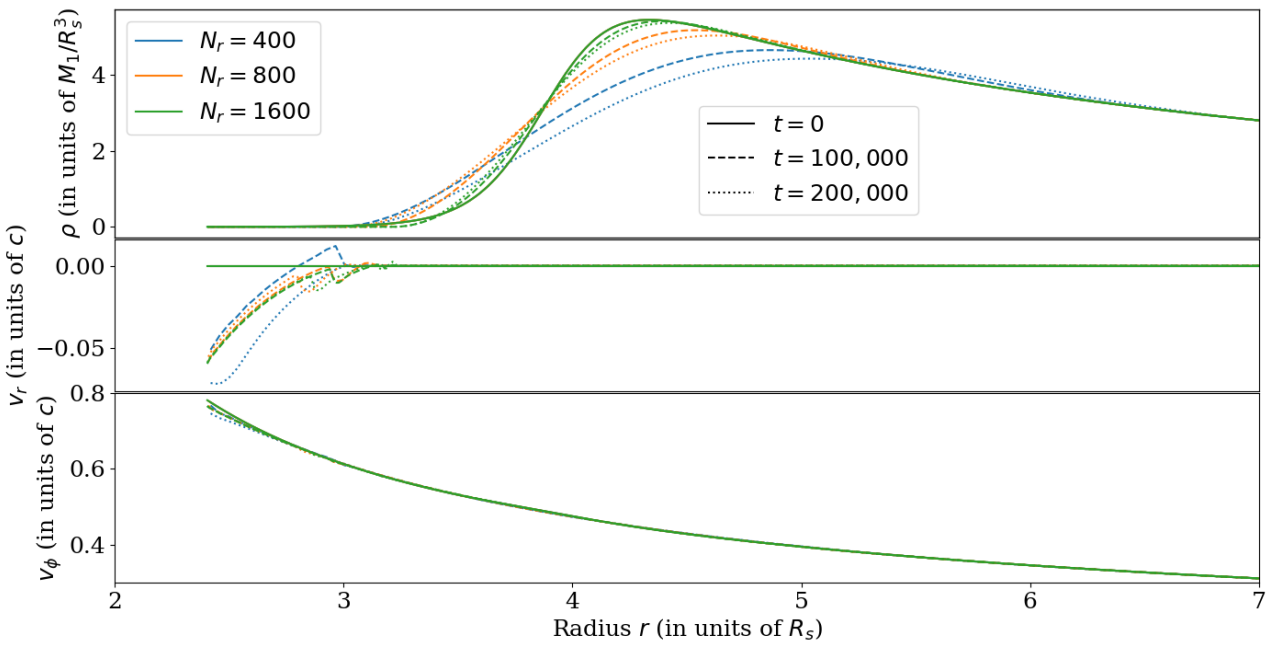

Figure 2.5: **Influence of radial resolution on the disc inner edge**
Simulations are run without considering the influence of the MBH companion: the conservative variables remain symmetric. Each curve corresponds to a radial profile.
Upper panel: density, middle panel: radial velocity, lower panel: azimuthal velocity. Colors represent the radial resolution. Line styles represent the simulation times (in units of R_s/c).

2.3.4 Boundary conditions, radial resolution, and simulation domain

When initially designing the numerical set-up, it became apparent that a suitable number of cells were required to accurately describe the disc inner edge to ensure its stability over long simulations. Figure 2.5 illustrates the impact of the radial resolution on the evolution of the disc inner edge around an isolated MBH companion. More specifically, if the radial resolution is too low, the sharpness of the disc inner edge decreases. The matter from the inner parts of the disc are accreted, as shown by the negative radial velocities.

Increasing the radial resolution of a simulation comes at a higher computational cost: the number of computations to realize each time step is directly proportional to the number of cells in both directions. The `MPI` library allows for parallelization of the code, which can keep the final computation duration the same if more cores are used but which uses higher computational resources.

Due to the need for a high radial resolution in the inner parts of the simulation, the initial plan to explore the influence of the MBH companion was to divide the disc into multiple simulation domains to reduce computational costs. Each domain would encompass a range of radii, forming an annulus inside the disc. The computational cost of each simulation decreases in regions of the disc that are farther from the center for two reasons. Firstly, the angular velocity decreases, causing an increase in each iteration time step due to the CFL condition mentioned earlier (equation (2.28)). Secondly, only the first simulation domain covers the inner edge of the disc, thereby allowing for a reduction in radial resolution for the outer parts of the disc.

When the disc inner edge is inside the simulation domain, the inner radial edge of the grid is inside the ISCO. As a result, the material within is likely to be pulled towards the central MBH. Therefore, the boundary condition requires the material to flow outwards, with negative radial velocity, and maintain

continuous density and azimuthal velocity conditions.

One of the significant challenges in performing these simulations was implementing stable boundary conditions at the outer and inner edges when the accretion disc inner edge is not included in the simulation domain. Ensuring that the accretion disc structure would not be impacted during the long simulation time was crucial in our case. A first naïve attempt was to use the continuity of the primitive variables. Their values in the two ghost cells are copies of their values in the last cell inside the grid. For instance, for the outer boundary condition:

$$x_{\mathrm{gs}_1} = x_{N_r} \tag{2.29a}$$
$$x_{\mathrm{gs}_2} = x_{N_r} \tag{2.29b}$$

where x represents the three conservative variables and the . The grid comprises N_r cells numbered 1 through N_r, with two ghost cells designated gs_1 and gs_2. This formula remains the same for all azimuthal angle values.

This continuous boundary condition leads to a discontinuity in the fluxes at the radial interfaces of the cells (equation (2.3.1)). Another approach was taken to ensure the continuity of the radial fluxes by employing the continuity of the primitive variable derivatives. The formula is again presented at the outer boundary of the disc. The first-order derivative can be approximated by

$$f_x^{(1)} = \frac{x_{N_r} - x_{N_r-2}}{r_{N_r} - r_{N_r-2}} \tag{2.30}$$

Therefore

$$x_{\mathrm{gs}_1} = f_x^{(1)} \times \left(r_{\mathrm{gs}_1} - r_{N_r-1}\right) + x_{N_r-1} \tag{2.31a}$$
$$x_{\mathrm{gs}_2} = f_x^{(1)} \times \left(r_{\mathrm{gs}_2} - r_{N_r}\right) + x_{N_r} \tag{2.31b}$$

The profile of density inside the disc is given in equation (2.27). Thus, the density logarithm is a straight line as a function of the radius logarithm. Hence, the continuity of the first-order derivative can be more accurately computed using:

$$f_{\log}^{(1)} = \frac{\log(\rho_{N_r}) - \log(\rho_{N_r-2})}{\log(r_{N_r}) - \log(r_{N_r-2})} \tag{2.32}$$

The value of equation (2.32) at $t = 0$ is $-3/2$. In the case of the density, its value in the ghost cells is given by:

$$\log(\rho_{\mathrm{gs}_1}) = \left(\log(r_{\mathrm{gs}_1}) - \log(r_{N_r-1})\right) f_{\log}^{(1)} + \log(\rho_{N_r-1}) \tag{2.33a}$$
$$\log(\rho_{\mathrm{gs}_2}) = \left(\log(r_{\mathrm{gs}_2}) - \log(r_{N_r})\right) f_{\log}^{(1)} + \log(\rho_{N_r}) \tag{2.33b}$$

The logarithm can also be used for the azimuthal velocity due to the very low adiabatic constant. However, it is not relevent for the radial velocity, for which the radial profile using the logarithms is not a straight line. These boundary conditions were adequate for the first simulation domain, which includes the accretion disc inner edge.

However, these boundary conditions were no longer adequate when considering outer simulation domains, for instance, from 8 R_s to 22 R_s. In this case, the inner edge of the disc is no longer inside the simulation domain. The errors caused by the boundary condition at each edge of the simulation domain are reflected and amplified. The solver used is a spatial second-order numerical scheme. Therefore, efficient boundary conditions are the continuity of the primitive variables second derivative. I am presenting the formula again at the outer boundary of the disc for clarity:

$$f^{(2)} = \frac{x_{N_r-2} - 2x_{N_r-1} + x_{N_r}}{\delta r^2} \tag{2.34}$$

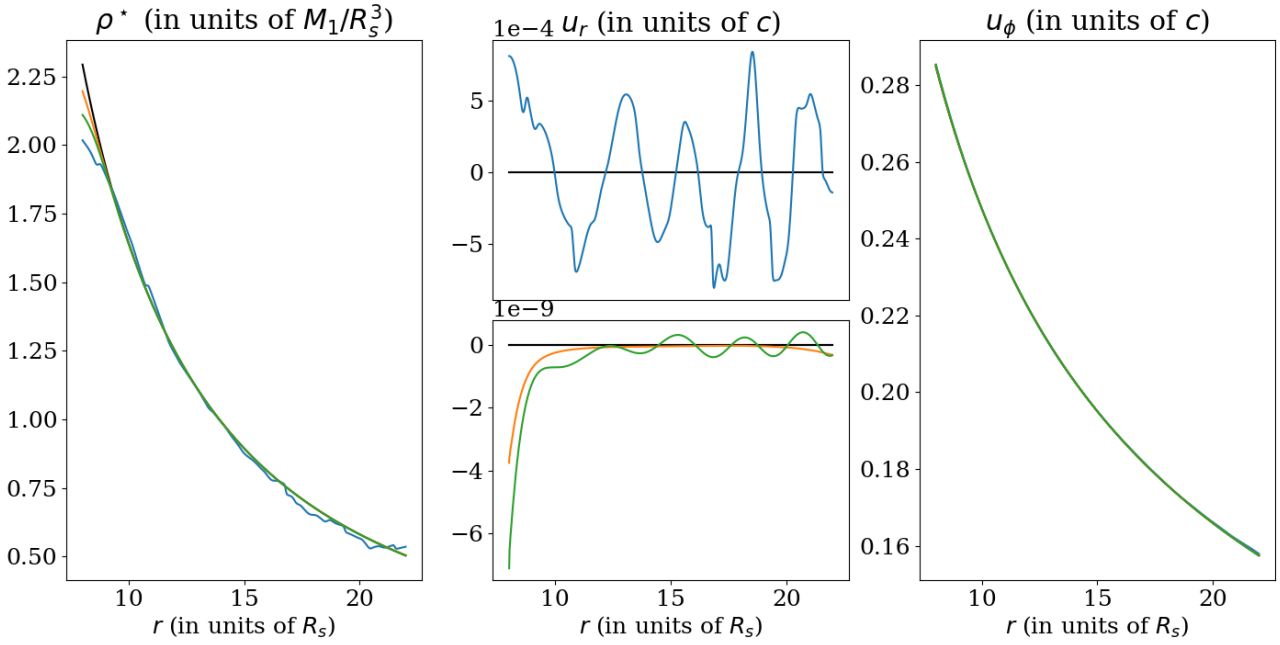

Figure 2.6: **Influence of the choice of the boundary conditions when the inner edge of the disc is not included in the simulation domain.**
Each curve corresponds to a radial profile. The first column is the density, the second is the radial velocity, and the third is the azimuthal velocity.
The black line represents the initial conditions. The blue line corresponds to the boundary condition derived from the continuity of primitive variables first-order derivative (using the logarithm for the density and the azimuthal velocity); see equation (2.33). The orange and green lines correspond to the boundary condition derived from the continuity of primitive variables second-order derivative ; see equation (2.35). The orange line corresponds to a linear radial resolution of 1260 cells, while the green line corresponds to a linear radial resolution of 840 cells.

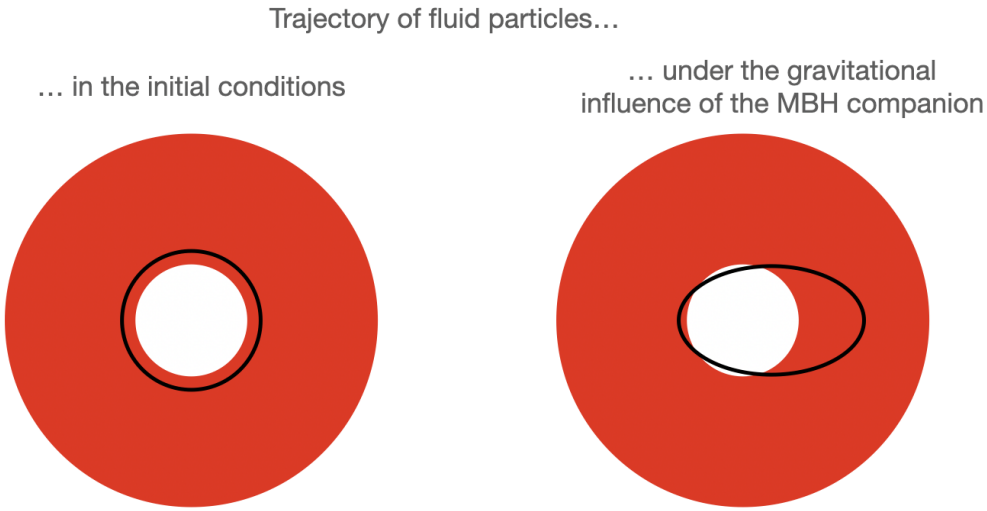

Figure 2.7: **Schematic view of the trajectories of fluid cells**

where δr is the radial extent of cells in the grid. Therefore the primitive variables in the ghost cells are given by

$$x_{\mathrm{gs}_1} = \delta r^2 f^{(2)} + 2x_{N_r} - x_{N_r-1} \tag{2.35a}$$

$$x_{\mathrm{gs}_2} = \delta r^2 f^{(2)} + 2x_{\mathrm{gs}_1} - x_{N_r} \tag{2.35b}$$

Figure 2.6 shows the difference in the radial velocity when the boundary conditions are defined with the first and second-order derivatives. The oscillations in radial velocity caused by the propagation and reflection of errors arising from boundary conditions disappear when we use the continuity of the second-order derivative with a sufficient radial resolution.

The challenge of these boundary conditions is the simulation time required to study the influence of the MBH condition. For instance, Vincent et al. (2013) also studied the accretion disc using a Paczyński & Wiita (1980) potential. Our numerical setup is similar to theirs. The simulation domain extends from $r_{in} = 2.4\ R_s$ to $r_{ext} = 18\ R_s$. The boundary conditions they use are identical to those of Meheut et al. (2010): the continuity of the primitive variables at the disc outer edge. However, they did not have the same problems as us because their simulation time is of the order of several dozen orbital periods at the ISCO. In our case, the ratio between the binary orbital period T_{orb} and the gas period at the ISCO, assuming a Keplerian motion T_{gaz} is

$$\frac{T_{orb}}{T_{gaz}} = \frac{1}{\sqrt{27\ (1+q)}} \left(\frac{D}{R_s}\right)^{3/2} \sim 4\ 300 \times \sqrt{\frac{2}{1+q}} \left(\frac{D}{1\ 000\ R_s}\right)^{3/2}$$

Using the primitive variables second-order derivatives (with the logarithm for the density and the azimuthal velocity) solved this issue.

However, the concept of dividing the disc into different simulation domains was abandoned due to its impracticality when the influence of the MBH companion is also taken into account. The trajectory of the gas fluid cells encoded in the initial conditions is circular. The disc remains axisymmetric if the gravitational influence of the MBH companion is not considered. The impact of the MBH companion causes the gas circular orbits to become elliptical, and they are no longer centered on the (Oz) axis of the polar grid. This leads the fluid particles to cross the inner edge of the simulation, as schematized in Figure 2.7. The disc structure can no longer be described using a polar simulation grid with circular boundaries inside the accretion disc, even with accurate boundary conditions. Therefore, it is necessary to simulate the disc from inside its inner edge to outside its outer edge.

At this stage, Peggy Varniere and Fabien Casse continued to develop the numerical setup for the simulation while I worked on the iron line, which is presented in Chapters 4 and 5.

To reduce the numerical time cost, the initial approach to simulate the complete accretion disc involved adaptative mesh refinement. However, the grid refinement is not adapted in this situation as the brutal resolution changes due to different refinement levels induce too much distortion in the gas. They opted for a logarithmic fixed grid (without refinement), which helped to save computational resources by reducing the radial resolution in the outer regions of the disc. Initially, this solution was not considered while I was working on the numerical setup development because it was expected that the increase of the radial size of the cells with radius would prevent the influence of the MBH companion from developing in the disc outer parts and propagating to the disc inner parts. Despite this logarithmic grid, the gravitational influence of the MBH companion could still propagate from the exterior to the inner parts of the disc. The disc outer edge inside the simulation domain allows the trajectory of fluid particles inside the disc to become elliptical without crossing the simulation outer edge.

To explore the impact of the MBH companion, the numerical set-up for different values of the orbital parameters ($D,\ q$) is kept similar.
One significant effect of the gravitational impact of the MBH companion is to truncate the disc outer parts. The disc outer edge is inside the simulation domain with ($r_{ext} = 0.7\ D, \sigma_{ext} = 0.05\ D$) in the initial condition of density presented in equation (2.26) and with the simulation outer radius $r_{out} = 0.98\ D$. The approximate position of the Lagrangian point $\mathcal{L}_1$ for $q \in [10^{-2};\ 2]$ is (Frank et al. 2002)

$$\frac{r_{\mathcal{L}_1}}{D} = 0.500 - 0.227 \log(q) \tag{2.36}$$

Therefore, the Lagrangian point $\mathcal{L}_1$ is inside the simulation domain and the disc outer edge for the following conditions on the mass ratio.

$$\frac{r_{\mathcal{L}_1}}{D} < 0.98 \Leftrightarrow q > 7.7 \times 10^{-3} \tag{2.37a}$$

$$\frac{r_{\mathcal{L}_1}}{D} < 0.7 \Leftrightarrow q > 0.13 \tag{2.37b}$$

The outer edge condition allows the material to leave the simulation domain due to the gravitational attraction of the MBH condition outside the primary MBH's Roche lobe. The boundary conditions use the continuity of the primitive variables. If matter enters the simulation domain, the density is set close to the density floor value allowed in the simulations ($\rho^\star = 10^{-10}$), and the two components of the velocity are continuous.

At the disc inner edge, the sharpness of the density drop was softened from the initial values (we first used the same values as in Vincent et al. (2013)) $\sigma_b = 0.05\ R_{ISCO} = 0.15\ R_s$ to $\sigma_b = 0.1\ R_{ISCO} = 0.3\ R_s$. Moreover, the position of the disc inner edge was slightly moved back from $r_b = 1.3\ R_{ISCO} = 3.9\ R_s$ to $r_b = 1.5\ R_{ISCO} = 4.5\ R_s$. The simulation inner edge is finally $r_{in} = 2.5\ R_s$ instead of $r_{in} = 2.4\ R_s$.
This configuration allows for a slight relaxation of the constraint on the radial resolution at the disc inner edge. Moreover, as the simulation inner edge radius is higher, the maximal azimuthal velocity is smaller, which relaxes the CFL condition. The ISCO remains inside the simulation domain.
The inner boundary condition is the outflow of the material from the simulation domain falling onto the central MBH. The density is kept at a constant value of 10^{-5} (in the code units M_1/R_s^3).

The numerical simulation setup presented in this section describes the accretion disc orbiting the primary MBH and under the gravitational influence of the MBH companion. Fabien Casse and Peggy Varniere conducted numerical simulations to explore the binary parameter space. The separation ranges between 250 R_s and 3 000 R_s, and the mass ratio values are between 9×10^{-4} and 1. These

simulations aim to characterize the gravitational influence of the MBH companion for different values of the binary orbital parameters. The next chapter presents the influence of the MBH companion on the disc structure.
The draft of the forthcoming article on the numerical simulations designed to study the impact of the MBH on the accretion disc structure is presented in Appendix A. It will be submitted to MNRAS with a companion article on observational consequences.

CHAPTER

3

GRAVITATIONAL INFLUENCE OF THE COMPANION ON THE PRIMARY MASSIVE BLACK HOLE ACCRETION DISC

The numerical set-up to simulate the disc with the code `MPI-AMRVAC` is presented in Chapter 2. As masses are scaled to the primary MBH mass M_1 and lengths to its Schwarzschild radius R_s, the binary orbital parameters are the separation D and the mass ratio $q < 1$. Fabien Casse and Peggy Varniere ran different numerical simulations to explore the gravitational influence of the MBH on the accretion disc structure.
The orbital separation ranges between $D = 250\ R_s$ and $D = 3\ 000\ R_s$, while the mass ratio ranges between $q = 9 \times 10^{-4}$ and $q = 1$. The astrophysical characteristics of these MBH binaries in the early phases of their coalescence are presented in section 2.1.

Figure 3.1 displays the evolution of the disc structure when the orbital parameters are ($D = 1\,000\ R_s$, $q = 1$). Fabien Casse and Peggy Varniere use it as a reference to illustrate the typical evolution of the disc structure under the gravitational influence of the MBH companion. The initial conditions for the accretion disc place the Lagrangian position $\mathcal{L}_1$ of the Roche Lobe inside the accretion disc. At the beginning of the simulation, the gravitational force exerted by the MBH companion pulls away the external parts of the disc from the simulation domain. Over approximately three orbital periods, the outer edge of the accretion disc shrinks from its initial radius settled by the initial conditions outside the primary MBH's Roche lobe to a final stable position. Meanwhile, the accretion disc undergoes some structural changes, including the appearance of a density wave spiral and an elliptical shape. While the density spiral lessens during the simulations, the final elliptic shrunk structure remains stable over 20 binary orbital periods. The figure suggests that the accretion disc outer edge stabilizes at a radius of approximately $r_{max} = 300\ R_s$.
The evolution is comparable for equal mass binaries with different values of the orbital separation.

The MBH companion has three significant effects on the accretion disc structure. First, it causes the outer parts of the disc to be truncated. Second, it results in the formation of an overdense spiral arm in the disc. Third, the overall shape of the accretion disc becomes elliptical.
The first section of this chapter details the impact of the binary orbital parameters on the outer edge radius of the truncated accretion disc. The second section of this chapter focuses on the spiral wave developing in the disc.

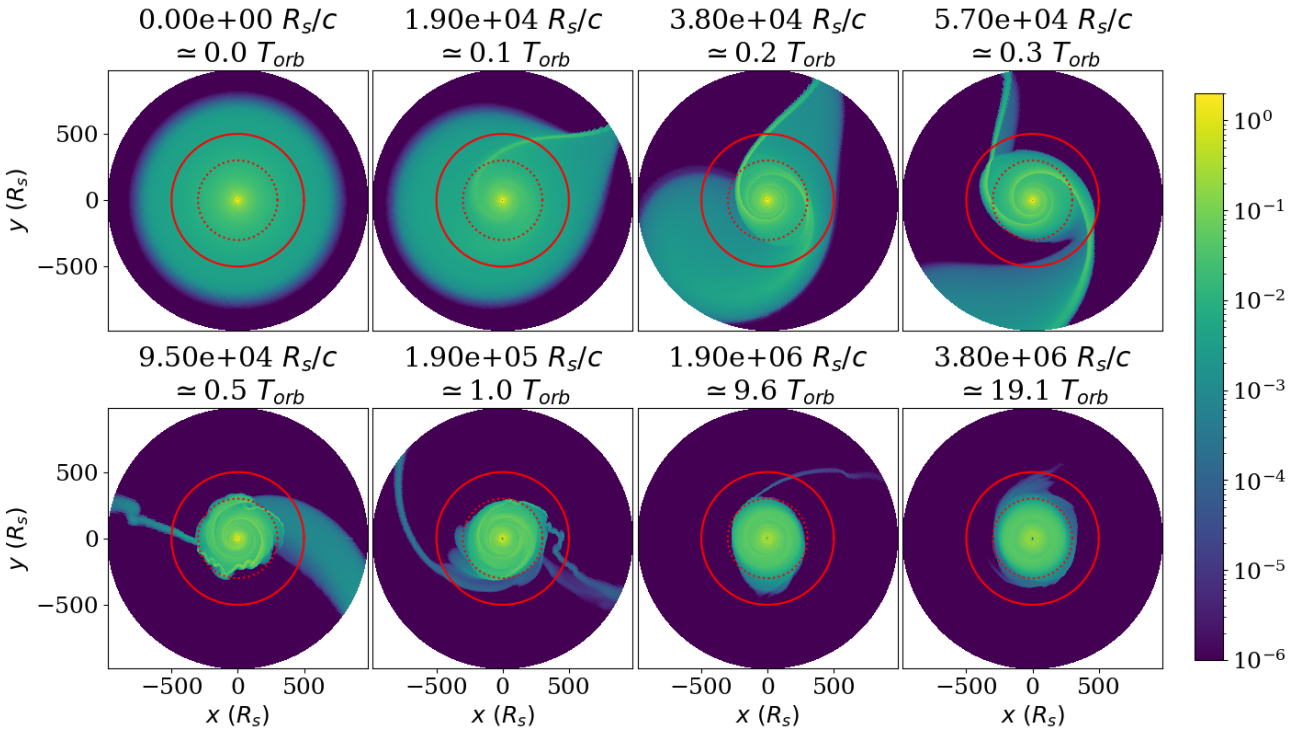

Figure 3.1: **Evolution of the density in the disc for the binary orbital parameters** ($D = 1\ 000\ R_s,\ q = 1$)**.**
Figure adapted from the forthcoming article (see the draft version in Appendix A). The density in the disc $\rho^\star$ is represented in a logarithmic scale from 10^{-6} to 2.
Each panel corresponds to the simulation outputs at a different time. The red solid circle radius equals the Lagrangian point $\mathcal{L}_1$ radius (equation (2.36)). The red dotted circle radius equals 300 R_s.

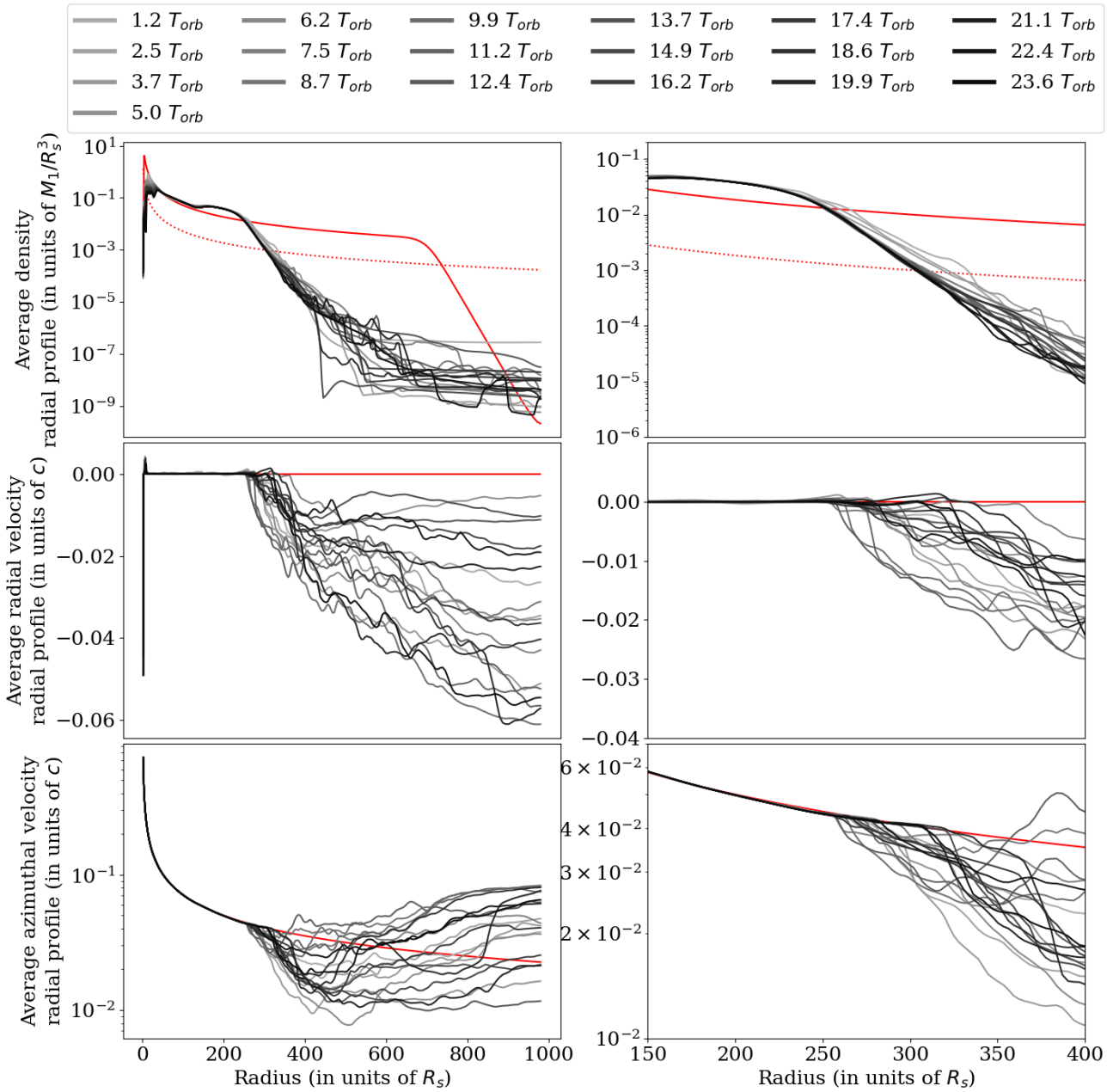

Figure 3.2: **Temporal evolution of the radial profile of the azimuthal average of the density, the radial, and the azimuthal velocities for the simulation with the orbital parameters** ($D = 1\ 000\ R_s,\ q = 1$)**.**
$(\rho^\star, v_r^\star, v_\phi^\star)$ are averaged in the azimuthal direction from the simulation outputs. The red solid lines represent the initial condition. The curves in black and white represent different times, linearly spaced between $t^\star = 0$ and $t^\star = 4.693 \times 10^6$. It corresponds to approximately one curve per orbital period $T_{orb} \simeq 1.97 \times 10^5\ R_s/c$. **The important information here is the convergence of the density profile and the difference between the region which still belongs to the accretion disc after the truncation and the outer parts**. The darker, the more advanced time in the simulation. The right column is a zoom in the plots in the left column. The dotted red line in the first row is the initial radial density profile within the disc ($\rho = \rho_0\,(r/(3\ R_s))^{-3/2}$) divided by ten.

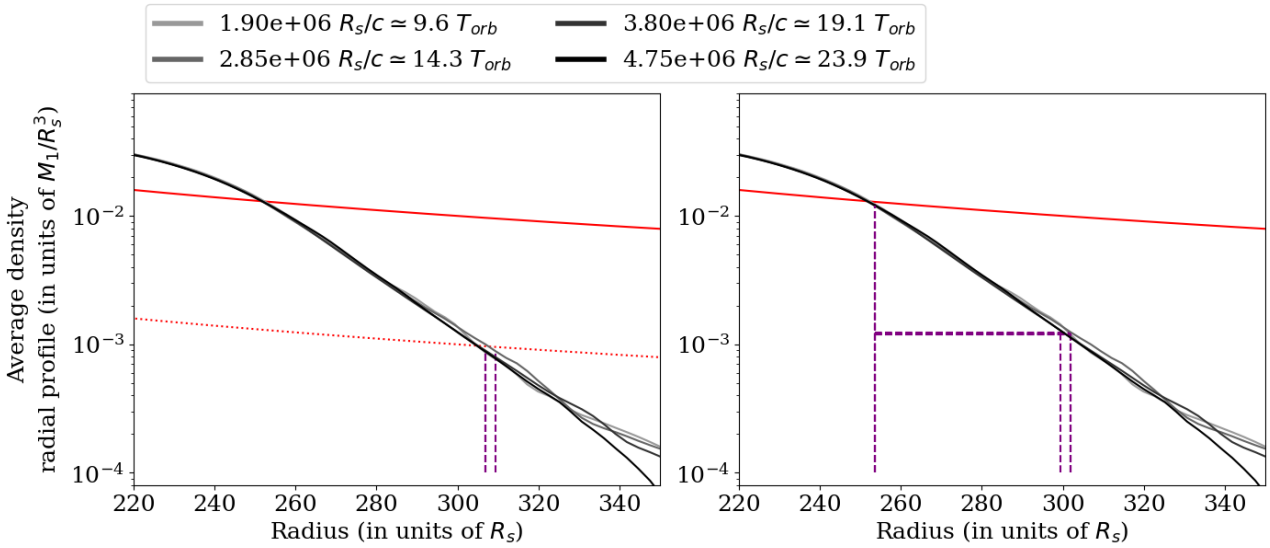

Figure 3.3: **Illustration of the two methods to measure r_{max} for the simulation with the orbital parameters** ($D = 1\ 000\ R_s,\ q = 1$)**.**
Figure adapted from the forthcoming article (see the draft version in Appendix A) to compare the two methods.
Left panel: r_{max} is defined as the radius from which the density drops below one-tenth of the initial density profile.
Right panel: r_{max} is defined as the radius from which the density drops below one-tenth of a reference value defined as the density where the average density profile equals the initial density profile.

3.1 Truncation of the disc outer parts

The density or the radial or azimuthal velocities in the simulation outputs can be used to define the disc outer edge radius, r_{max}. Due to the non-axisymmetric features such as ellipticity and spirals, r_{max} is defined using the mean values averaged over the azimuthal direction. Figure 3.2 displays the temporal evolution of the azimuthally averaged density and components of the gas velocity. The profiles are plotted at 20 simulation times linearly spaced between the initial condition and $t = 4.546 \times 10^6\ R_s/c \simeq 20\ T_{orb}$.

r_{max} can be defined as the radius from which the density falls below a fraction of the initial density axisymmetric profile. This definition is consistent with differentiating the emission of an accretion disc under the gravitational influence of the MBH companion and the emission from an accretion disc surrounding an isolated MBH.
Furthermore, the initial condition is the equilibrium state of the disc around the primary MBH. The radial velocity is null. The azimuthal velocity is set to compensate for the gravitational attraction from the central MBH and pressure forces. The outer regions of the disc are truncated due to the gravitational effect of the MBH companion. Hence, there is no reason for the azimuthal velocity to continue to follow a Keplerian profile outside r_{max} as it corresponds to the matter torn apart from the stable inner accretion disc. Figure 3.2 shows that the average profile of the velocity components differs from the initial condition from radii that approximately correspond to the end of the over-density in the density average profile.
However, the aim is to differentiate the emissions of the accretion disc with and without the impact of the MBH companion. Therefore, it is more relevant to define r_{max} as the radius from which the density drops below a significant fraction of the initial density, corresponding to the unperturbed disc. r_{max} can be defined as the radius at which the density drops below one-tenth of the initial density profile.

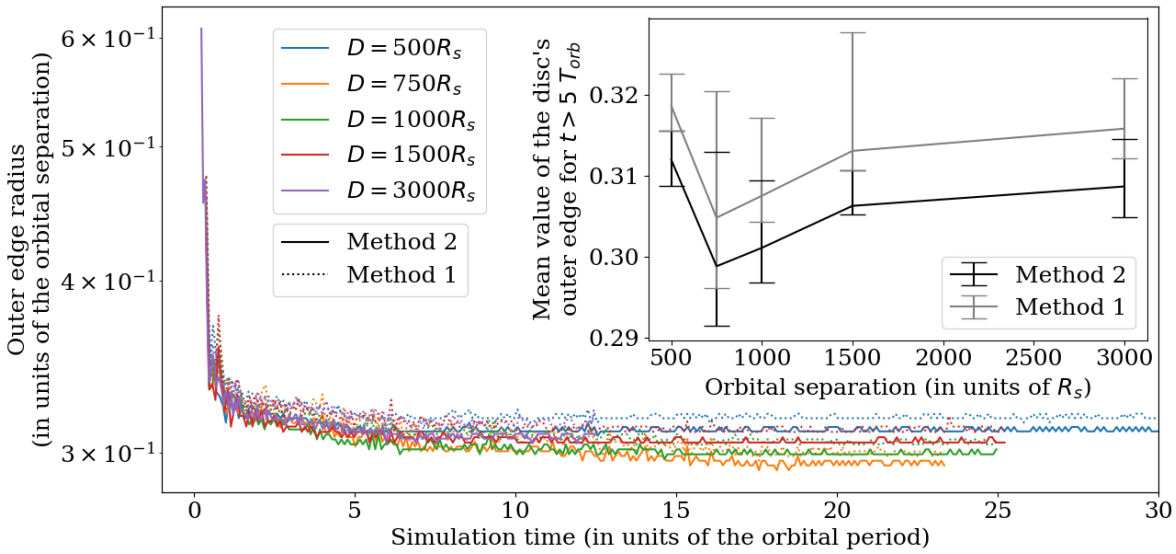

Figure 3.4: **Temporal evolution of r_{max} for equal mass binaries and different values of the orbital separation.**
The main plot illustrates the temporal evolution of r_{max} measured with the two methods described in Figure 3.3. The inside plot displays the average of r_{max} for times above 5 T_{orb}.

Nevertheless, such a definition would lead to difficulties depending on the mass ratio and the abilities of the secondary to create a deep enough groove in the primary's disc. Hence, Peggy Varniere used a well-tested and proven method in lighter systems to follow the evolution of r_{max} in the hydrodynamical simulation in real-time. Following the evolution in real time allowed us to not "overshoot" the duration of the fluid simulations too much beyond the "stable outer edge zone" as those are computationally intensive (some of the simulations take several CPU-months).
The point where the average density profile equals the initial condition determines an intermediate density reference value. r_{max} is defined as the point where the average density profile drops below one-tenth of this reference density. Figure 3.3 illustrates the difference between the two methods, applied to four average density profiles, corresponding to four times linearly spaced between $1.9 \times 10^6\ R_s/c \simeq 9.6\ T_{orb}$ and $4.75 \times 10^6\ R_s/c \simeq 23.9\ T_{orb}$. With the first method on the left plot, the values of r_{max} are between 306.9 R_s and 309.4 R_s, while for the second method on the right plot, the values of r_{max} are between 299.3 R_s and 301.8 R_s. At this radius, the radial size of the cells from the logarithmic grid is $\simeq 2.5\ R_s$. Therefore, each measure of r_{max} is consistent.

Figure 3.4 displays the temporal evolution of r_{max} values, measured with both methods. It compares the results obtained for equal mass binaries and different values of the orbital period. r_{max} values are scaled to the orbital separation because the overall evolution of the disc structure is similar for each case. With the first method, all values of r_{max} are contained between $0.296 \times D$ and $0.328 \times D$, with a mean value of $0.312 \times D$. With the second method, all values of r_{max} are contained between $0.301 \times D$ and $0.313 \times D$, with a mean value of $0.305 \times D$. For each value of the separation, the mean difference between both methods is $0.006 \times D$. The second method shows better stability of the results when scanning the complete temporal evolution of the accretion disc.

Another difference between the two methods is the convergence of r_{max} at smaller mass ratios. Figure 3.5 displays the evolution of the value of r_{max} measured with both methods for the simulations with orbital parameters ($D = 500\ R_s, q = 5 \times 10^{-3}$) and ($D = 1\ 000\ R_s, q = 5 \times 10^{-2}$). The convergence of the method used by Peggy Varniere is faster (in terms of the simulation time) and sharper.

Peggy Varniere used the second method to investigate the impact of the mass ratio on the final value

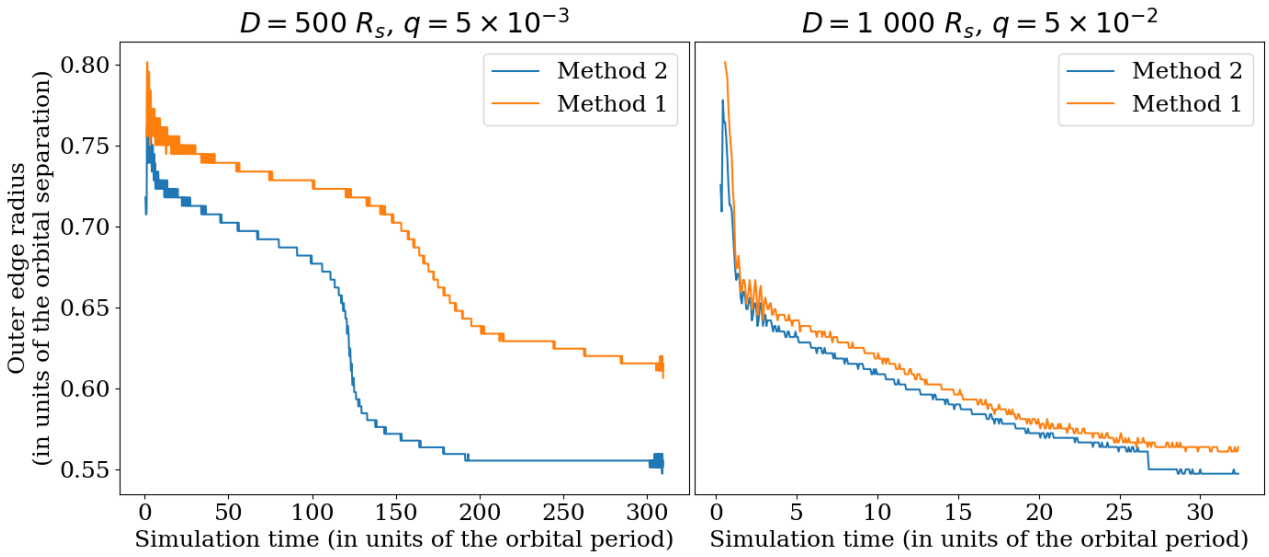

Figure 3.5: **Temporal evolution of r_{max} for unequal mass binaries.**
Method 1: definition of r_{max} as the radius from which the density drops below one-tenth of the initial density profile.
Method 2: definition of r_{max} as the radius from which the density drops below one-tenth of a reference value defined as the density where the average density profile equals the initial density profile.

r_{max} when it has converged and stabilized. Figure 3.6 from the forthcoming article (see Appendix A) displays the ratio r_{max}/D as a function of the mass ratio between 10^{-3} and 1. For equal values of the mass ratio, r_{max}/D is constant. This scaling of the accretion disc structure to the binary orbital separation is also observed when studying the spiral structure (see section 3.2). The relation between r_{max}/D and q can be fitted with the relation

$$\frac{r_{max}}{D} = -0.18\ q^{0.044}\ \log\left[0.019\ q + 6.8 \times 10^{-6}\right] \tag{3.1}$$

This results is presented in the forthcoming article (see Appendix A).

To verify the temporal stability of r_{max}, the Robe Loche radius $r_{\mathcal{L}_1}$ and the radius of the inner Lindblad resonance for small mass ratios ($q \ll 1$) are added in Figure 3.1. These values must be greater than r_{max} to ensure that the position of the disc outer edge remains stable after the end of the simulation time considered here.
Suppose r_{max} exceeds the Robe Loche radius $r_{\mathcal{L}_1}$. In that case, the outer parts of the disc are not gravitationally bound to the central MBH and can be torn apart by the MBH companion.
The Lindblad resonances are radii in the accretion disc where the MBH companion excites resonant waves in the disc. The inner Lindblad resonance corresponds to a negative torque exerted by the MBH companion on the disc. Therefore the matter is unstable and accreted towards the inner parts of the disc. The details on the computation of the linear theory of Lindblad resonance in accretion discs can be found, for example, in Goldreich & Tremaine (1979), Meyer-Vernet & Sicardy (1987), and Artymowicz (1993b,a). For small values of the mass ratio ($q \ll 1$), the radius of the inner Lindblad resonance is

$$\frac{r}{D} = \frac{1}{2^{2/3}} \tag{3.2}$$

As the mass ratio increases, the Robe Loche radius $r_{\mathcal{L}_1}$ gives a tighter constraint on r_{max} than the Lindblad resonance radius.

The truncation of the disc outer parts might be detected through EM observations. As explained in section 2.1, the accretion disc size is expected to be above 10^{-2} pc, corresponding to 1 100 R_s for a BH mass of $M_1 = 10^8\ M_\odot$. The gravitational influence of the MBH companion truncates the disc

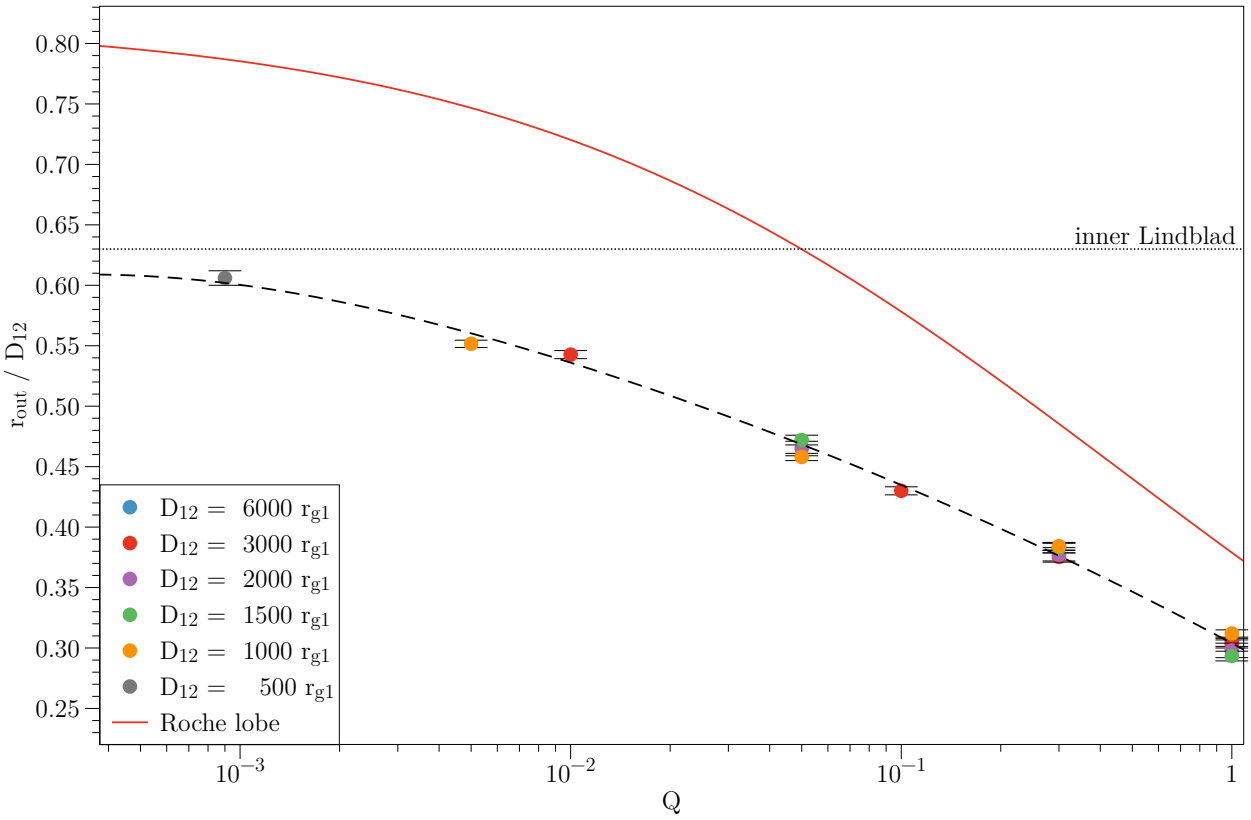

Figure 3.6: **Evolution of the disc outer edge radius with the binary mass ratio for different values of the orbital separation.**
The Figure is from the article in preparation (see the draft version in Appendix A). r_{out} is the outer edge radius (r_{max}). Q is the mass ratio (q). D_{12} is the orbital separation (D). r_{g1} is the primary MBH gravitational radius: $r_{g1} = R_s/2$
r_{max} values are scaled to the values of D. Each color represents a different value of D. The evolution of r_{max}/D as a function of q can be fitted through the relation given in equation (3.1) and is represented in a black dashed line. The red line corresponds to the Robe Loche radius $r_{\mathcal{L}_1}$ (equation (2.36)). The black dotted line represents the inner Lindblad resonance radius computed at small mass ratios ($q \ll 1$) with linearization of the equations (equation (3.2)).

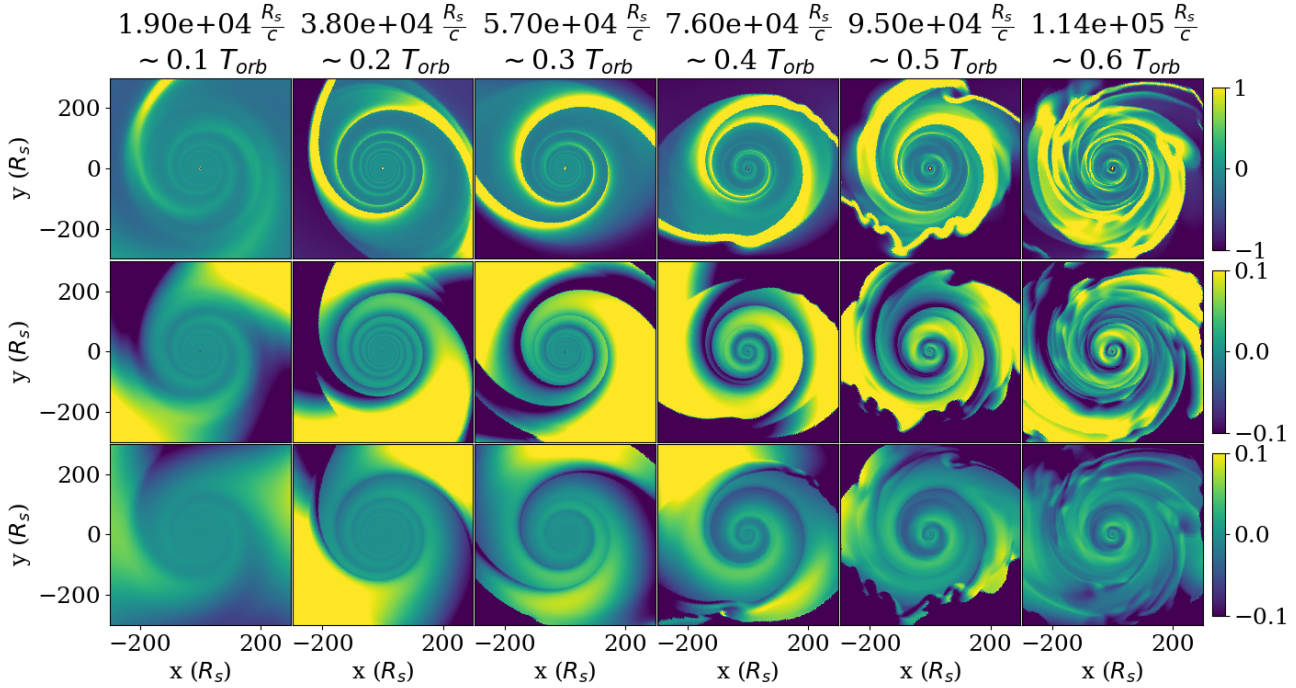

Figure 3.7: **Evolution of the spiral at the beginning of the simulation**
The orbital parameters are ($D = 1000\ R_s,\ q = 1$). Each column corresponds to a different simulation time: $t_i^\star = i \times 1.9 \times 10^4$ ($1 \leq i \leq 6$). The first and third rows correspond to the relative difference from the initial condition for the density and the azimutal velocity. The second row corresponds to the radial velocity divided by the initial value of the azimuthal velocity.

below these values. Therefore, if an abnormally small value of r_{max} is observed, it might suggest the presence of a MBH companion. Such a fact is not conclusive for the presence of a massive companion, as other processes might result in smaller values of the disc outer edge. Nonetheless, it can be useful when combined with other observational clues suggesting the presence of a companion, as highlighted in section 1.3.2.
Fabien Casse and Peggy Varniere used the Gyoto code to explore the disc's black-body emission and analyze the impact of the truncation of the disc outer parts. In the second part of my Ph.D. thesis, I focused on the accretion disc truncation effect on the iron line profile. The method is presented in chapter 4, and the results are shown in chapter 5.

3.2 Density wave spiral

This section aims to understand the phenomenology of the spiral wave that develops in the accretion disc under the gravitational influence of the MBH companion.
Figure 3.7 displays the spiral pattern in the density and the two components of the velocity fields. The density and the azimuthal velocity fields are plotted divided by their initial value, while the radial velocity is plotted divided by the initial value of the azimuthal velocity. The figure shows that the spiral has two arms and rotates within the disc at the same angular speed as the MBH companion around the primary MBH.

Papaloizou & Pringle (1977) study the linear response of the accretion disc to the perturbation by a companion orbiting a Newtonian and circular orbit around the central object. The perturbed velocity field can be written

$$u_r = 0 + u'_r$$
$$u_\phi = u_{\phi,0} + u'_\phi$$

where the first term of each sum is the velocity field associated with the equilibrium of the accretion disc around the central object, and the second term (u'_r, u'_ϕ) is the perturbation. The linearized equations of equations (2.8b) are

$$\frac{\partial u'_r}{\partial t} + \Omega_0(r)\frac{\partial u'_r}{\partial \phi} - 2\Omega_0(r)u'_\phi = \left(\vec{f}_{BH_2} + \vec{f}_{ie}\right)\cdot\vec{e}_r \tag{3.4a}$$

$$\frac{\partial u'_\phi}{\partial t} + \Omega_0(r)\frac{\partial u'_\phi}{\partial \phi} - \frac{\Omega_0(r)}{2}\frac{r-3R_s}{r-R_s}u'_r = \left(\vec{f}_{BH_2} + \vec{f}_{ie}\right)\cdot\vec{e}_\phi \tag{3.4b}$$

where $\Omega_O(r)$ is the Keplerian angular velocity in a Newtonian potential. The gravitational force exerted by the MBH companion is given in equations (2.15),(2.16), and (2.18)-(2.20):

$$\left(\vec{f}_{BH_2} + \vec{f}_{ie}\right)\cdot\vec{e}_r = -\frac{GM_2}{D^2}\cos(\Omega_{bin}t-\phi) - \frac{GM_2\left(r - D\cos(\phi-\Omega_{orb}t)\right)}{\left(r^2+D^2-2rD\cos(\phi-\Omega_{orb}t)\right)^{3/2}}$$

$$\left(\vec{f}_{BH_2} + \vec{f}_{ie}\right)\cdot\vec{e}_\phi = -\frac{GM_2}{D^2}\sin(\Omega_{orb}t-\phi) - \frac{GM_2D\sin(\phi-\Omega_{orb}t)}{\left(r^2+D^2-2rD\cos(\phi-\Omega_{orb}t)\right)^{3/2}}$$

where $\Omega_{orb} = \frac{2\pi}{T_{orb}}$ These terms are periodic in the variable $\xi = \Omega_{orb}t - \phi$. A Fourier decomposition can thus be used. The components of this decomposition are the Laplace coefficients (Papaloizou & Pringle 1977). The Fourier decomposition for each velocity component is:

$$u'_r = \sum_{m=0}^{+\infty} a_m(r)e^{im(\Omega_{orb}t-\phi)} \tag{3.6a}$$

$$u'_\phi = \sum_{m=0}^{+\infty} b_m(r)e^{im(\Omega_{orb}t-\phi)} \tag{3.6b}$$

The complex coefficients $a_m(r)$ and $b_m(r)$ can be computed using equation 3.4.

Papaloizou & Pringle (1977) demonstrate that mode $m = 1$ dominates the disc inner parts while mode $m = 2$ dominates the disc outer parts (inside the inner Lindblad resonance). For each value of m, the modulus of the summed terms determines the spiral amplitude (which depends on the radius), and the complex argument determines its phase. The mode $m = 1$ corresponds to a one-armed spiral while the mode $m = 2$ corresponds to a two-armed spiral.

Binney & Tremaine (2008) present the characterization of spirals in galactic planes that can also be used to describe spirals in accretion discs. The mode m corresponds to a m-arm spiral. The location of each arm is described by

$$m\phi + f(r,t) \equiv \text{cst}\,[2\pi] \tag{3.7}$$

where f is a function of radius and time that describes the spiral shape. The radial wavenumber is

$$k(r,t) = \frac{\partial f}{\partial r}(r,t) \tag{3.8}$$

The sign of the wave number determines whether the spiral is leading or trailing in the disc. Figure 3.7 shows that the spiral is trailing. Thus, $k(r,t) < 0$. The pitch angle α between the spiral arm and a circle of radius r is

$$\tan^{-1}\alpha = \left|\frac{1}{r}\frac{dr}{d\phi}\right| \tag{3.9}$$

The analytic study by Spruit (1987) demonstrates that self-similar shock waves have a constant pitch angle. If $\tan^{-1}\alpha$ is constant, equation (3.9) the spirals have a logarithmic shape.

Figure 3.7 shows that the amplitude of the spiral is stronger in the outer parts of the disc. This is due to the stronger influence of the MBH companion. It increases with time in the first snapshots

displayed in the figure. However, as the disc evolves under the gravitational influence of the MBH companion, the spiral pattern lessens and eventually disappears. Starting from the second column, the regularity of the spiral arms is broken. The linear equations (3.4) used for the analytical work in Papaloizou & Pringle (1977) are not valid anymore: non-linear aspects of the perturbation by the MBH companion's gravitational influence have more impact. Furthermore, Spruit (1987) studies the self-similar solution without explicitly considering the gravitational influence of the MBH companion in the equations. Therefore, with increasing simulation times, the regularity of the logarithmic shape of the spiral disappears.

Accretion discs under the gravitational influence of a perturbator beyond these first analytical considerations can be studied numerically. The nonlinear effects of a gravitational perturbator on the accretion disc have extensively been studied in the literature (see, e.g., Rozyczka & Spruit (1993); Savonije et al. (1994), Larwood et al. (1996), Godon (1997), Armitage & Murray (1998), Murray et al. (1999), Blondin (2000), Makita et al. (2000), Matsuda et al. (2000), Boffin (2001), Kley et al. (2008), Ju et al. (2016), Arzamasskiy & Rafikov (2018), Bowen et al. (2018), Sheikhnezami & Fendt (2018)). These simulations concern the close stellar binaries, those formed by a stellar-mass compact object and a star, and the MBH binaries. They study the non-linear effects on the trailing two spiral arms, which develop in the outer regions of the truncated (and eventually elliptic) accretion disc.

Boffin (2001) presents the profiles of emission lines impacted by the two-arm spiral obtained with SPH numerical simulations designed to study the mass transfer through an accretion disc between two stars forming a closed binary. In the case of MBH binaries, the gravitational influence of the central BH also impacts these emission lines. Hartnoll & Blackman (2002) present the impact of a wave spiral (although not related to a companion's gravitational influence) on the iron Kα line profile computed in the Schwarzschild metric.
This section aims to characterize the tidally induced spiral in the accretion disc simulated with the numerical setup presented in Chapter 2 to study its potential impact on the iron Kα emission line.

To consider all the spiral modes and their coupling due to non-linear effects, the iron line should be computed directly using the simulation outputs. However, the computation of the iron line requires a higher spatial resolution of the discs than the one used for the simulations with `AMRVAC` (see Chapter 4 for more explanations). Therefore, computing the iron line directly from the simulation outputs is impractical. A possible method would be to interpolate the points in the simulation outputs. To start the study of the impact of the spiral on the iron line, its shape and amplitude can be modeled with an analytic formula. This allows computing the iron line with the required spatial resolution for the accretion disc, independently from the spatial resolution in the simulation outputs.

As shown by the analytical and simulation studies in the literature, the dominant mode in the disc outer parts is a logarithmic spiral with $m = 2$. Thus, the location of each arm, as described in equation 3.7, is given by the general formula:

$$2\left(\phi - \Omega_{orb} t_i\right) - k \ln\left(\frac{r}{r_0}\right) = \text{cste } [2\pi]$$

where r_0 is a constant radius, and k is a constant that describes the radial periodicity of the spiral). The spiral radial wave number defined in equation (3.8) is

$$k(r,t) = -\frac{k}{r}$$

The constant pitch angle defined in equation (3.9) is

$$\tan^{-1}\alpha = \left|\frac{1}{r}\frac{dr}{d\phi}\right| = \frac{2}{k}$$

The velocity field – composed of the initial velocity field and the linear perturbation by the spiral mode $m = 2$ – can be written:

$$u_r = u_{\phi,0} \;\; C_r(r) \;\; \cos\left(2\left(\phi - \phi_0 - \frac{2\pi}{T_{orb}}t\right) - k\ln\left(\frac{r}{r_0}\right)\right)$$
$$u_\phi = u_{\phi,0} \;\; \left[1 + C_\phi(r) \;\; \cos\left(2\left(\phi - \phi_0 - \phi_{u_r,u_\phi} - \frac{2\pi}{T_{orb}}t\right) - k\ln\left(\frac{r}{r_0}\right)\right)\right]$$

where ϕ_0 is a constant phase and ϕ_{u_r,u_ϕ} is a phase difference between the two components of the velocity field. C_r and C_ϕ are two functions that are dependent on the radius only. The spiral phase is the argument of the complex coefficients of the Fourier transform of (u'_r, u'_ϕ) defined in equation (3.6). As the linearized equations (3.4a) and (3.4b) are different for each component of the velocity field, their Fourier transform coefficients do not have the same analytical expression as a function of r, the binary orbital parameters, and the Fourier transform coefficients of the gravitational influence of the MBH companion. Therefore, the spiral phase in the two velocity fields can differ by ϕ_{u_r,u_ϕ}.
C_r and C_ϕ are the amplitude of the spiral. It equals the modulus of the Fourier transform complex coefficients.

The spirals are

$$s_r(r,\phi) = \frac{v_r(r,\phi)}{v^0_\phi(\phi)} = C_r\left(\frac{r}{r_1}\right)^n \cos\left(2\left(\phi - \phi_0 - \frac{2\pi}{T_{orb}}t\right) - k\ln\left(\frac{r}{r_0}\right)\right) \tag{3.11a}$$

$$s_\phi(r,\phi) = \frac{v_\phi(r,\phi) - v^0_\phi(\phi)}{v^0_\phi(\phi)} = C_\phi\left(\frac{r}{r_1}\right)^n \cos\left(2\left(\phi - \phi_0 - \phi_{u_r,u_\phi} - \frac{2\pi}{T_{orb}}t\right) - k\ln\left(\frac{r}{r_0}\right)\right) \tag{3.11b}$$

They are the quantities plotted in Figure 3.7. The parameters of the spiral can be fitted to the simulation output.

The temporal evolution of the spiral patterns in Figure 3.7 shows that the non-linear effects perturb the regularity of the mode $m = 2$ with a logarithmic shape from the second snapshot. Thus, we will use the first snapshot to fit the spiral parameters in equation (3.11). Moreover, as explained in Papaloizou & Pringle (1977), the mode $m = 2$ dominates in the outer parts of the disc. However, in the outermost parts of the disc, close to the final truncation radius, the gravitational influence of the disc is already too strong, and the linear mode with a self-similar solution giving a logarithmic spiral shape does not exist. For the binary orbital parameters ($D = 1\ 000\ R_s, q = 1$), the logarithmic spiral $m = 2$ is visible between 40 R_s and 70 R_s.

Figure 3.8 shows the spiral structure for different values of the orbital separation and the same mass ratio $q = 1$ at equivalent simulation times regarding the MBH binary orbital period. The cartesian axes are scaled to the binary orbital separation value. Each disc is plotted between 0.04 D and 0.07 D. This figure suggests the radial dependency of the spiral scale with the separation. Thus, we choose

$$r_0 = D \tag{3.12}$$

This hypothesis is coherent with using the logarithmic shape for the spirals, as it comes from a self-similar solution of waves in the disc (Spruit 1987). If this hypothesis is valid, the value of parameter k obtained from simulations with different separation values should be the same.

The value of the spiral phase parameters $(k, \phi_0, \phi_{u_r,u_\phi})$ can be derived by extracting the points (r, ϕ) corresponding to the minimal and maximal values of s_r and s_ϕ (equation (3.11)) in the simulation output for $t_i = 19 \times 10^3\ R_s/c$. These points satisfy the relation

$$\phi = \phi_0 + \phi_{u_r,u_\phi} + \frac{2\pi}{T_{orb}}t_i + \frac{k}{2}\ln\left(\frac{r}{D}\right) + j\frac{\pi}{2} \tag{3.13}$$

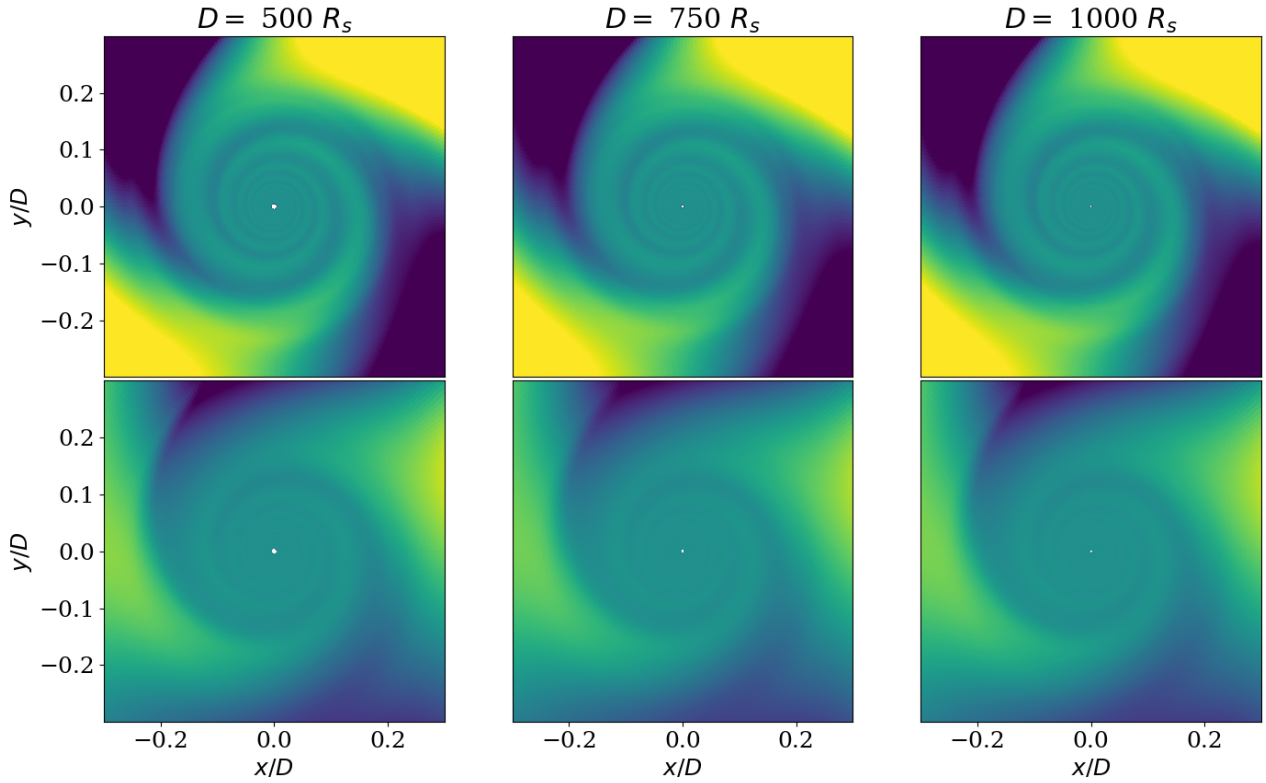

Figure 3.8: **Aspect of the spiral at equivalent times for different values of the separation and a constant mass ratio $q = 1$.**
The first (second) row represents the spiral in the radial (azimuthal) velocity component, as the second and third rows in Figure 3.7. Each column corresponds to a different separation value.
The lengths are scaled to the separation value. For each column, the simulation time is different but corresponds to an approximately constant value of the ratio t^i/T_{orb}. For the first column, $t^i = 7 \times 10^3\ R_s/c \simeq 10.035\ T_{orb}$. For the second column, $t^i = 12 \times 10^3\ R_s/c \simeq 10.755\ T_{orb}$. For the first column, $t^i = 19 \times 10^3\ R_s/c \simeq 10.457\ T_{orb}$.

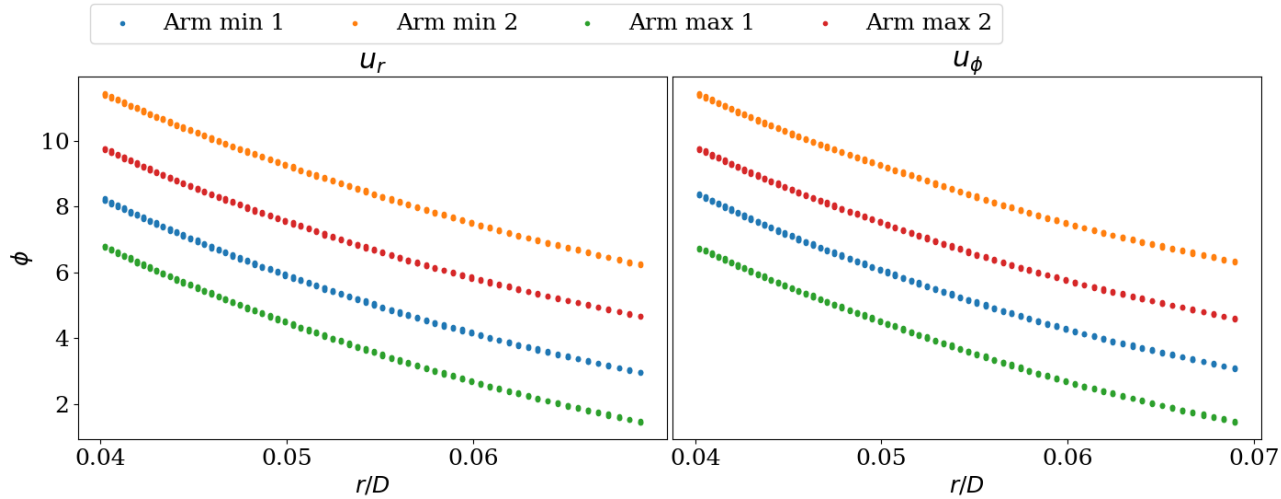

Figure 3.9: **Position of the points where the spiral is minimal or maximal for the simulation with the orbital parameters ($D = 1\ 000\ R_s$, $q = 1$) at $t^\star = 19 \times 10^3\ R_s/c$**
The left (right) plot displays the minima and maxima of the spiral in the radial (azimuthal) velocity component between $0.04D$ and $0.07D$.

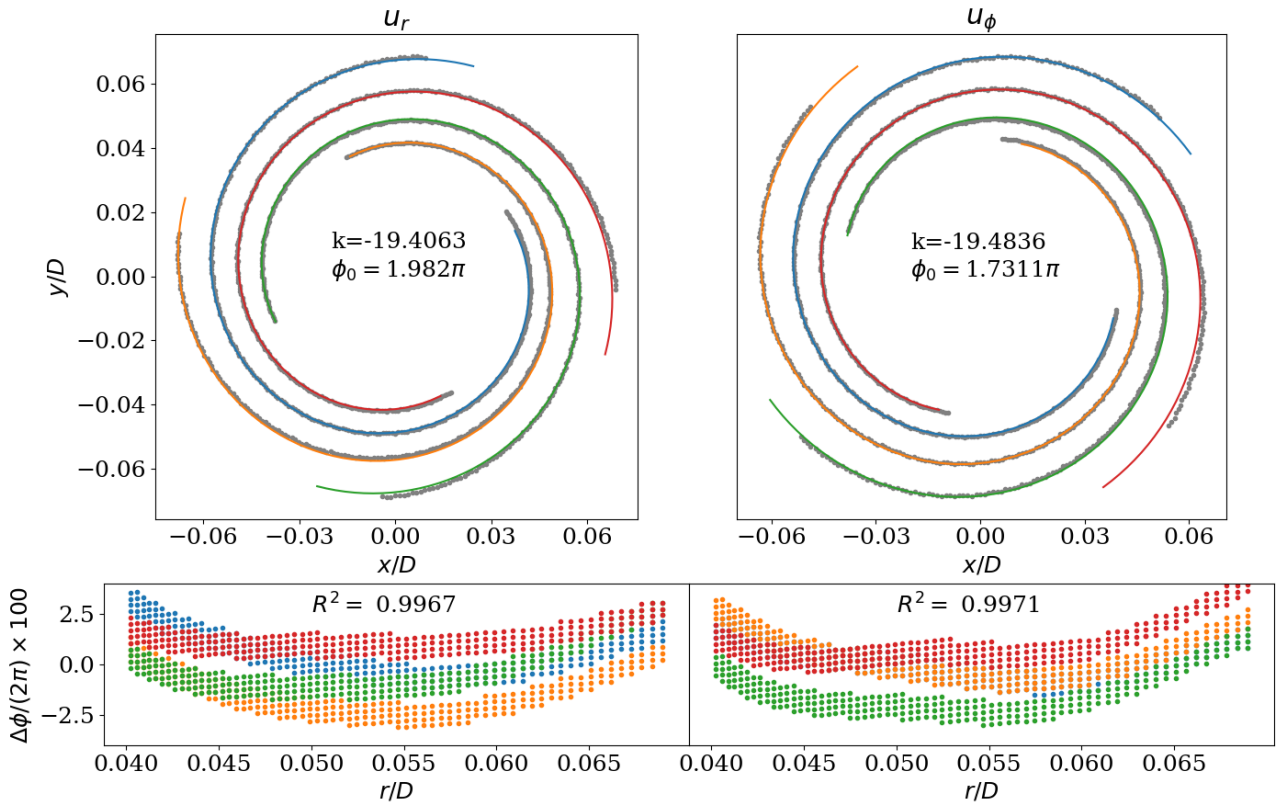

Figure 3.10: **Fits of the position of the minimal and maximal value of the spiral.** The grey line represents the points extracted from the simulation output and presented in Figure 3.9. The color lines represent the model in equation (3.13). The lower panels represent the relative difference of the spiral phase between the simulation outputs and the model in equation (3.13).

where $j = 0$ and $j = 2$ for the maxima, and $j = 1$ and $j = 3$ for the minima. Figure 3.9 displays the position of these points.
Therefore, the spiral phase parameters can be derived by a linear regression $y = ax + b$, where

$$
\begin{aligned}
x &= \ln\left(\frac{r}{D}\right) \\
y &= \phi - j\frac{\pi}{2} - \Omega_{orb} t_i \\
a &= \frac{k}{2} \\
b &= \phi_0 + \phi_{v_r, v_\phi}
\end{aligned}
$$

Figure 3.10 displays the spiral phase obtained with this method.

Figure 3.11 compares the spiral parameters obtained for different values of the binary orbital parameter (q, D). The considered orbital parameters are summarized in Table 3.1. These values were selected among the simulations Peggy Varniere and Fabien Casse ran. The chosen simulations correspond to similar ratio values between the simulation time and the binary orbital period. Therefore, the linear perturbation of the disc, described with a logarithmic spiral $m = 2$, can be compared from one simulation to another. All the linear regression obtained to derive the spiral parameters between $0.04D$ and $0.07D$ have R^2-scores above 0.9966.

We assumed an $m = 2$ spiral, which is the solution of the linear perturbation of the disc by the MBH companion (Papaloizou & Pringle 1977). The logarithmic shape of the spiral comes from the assump-

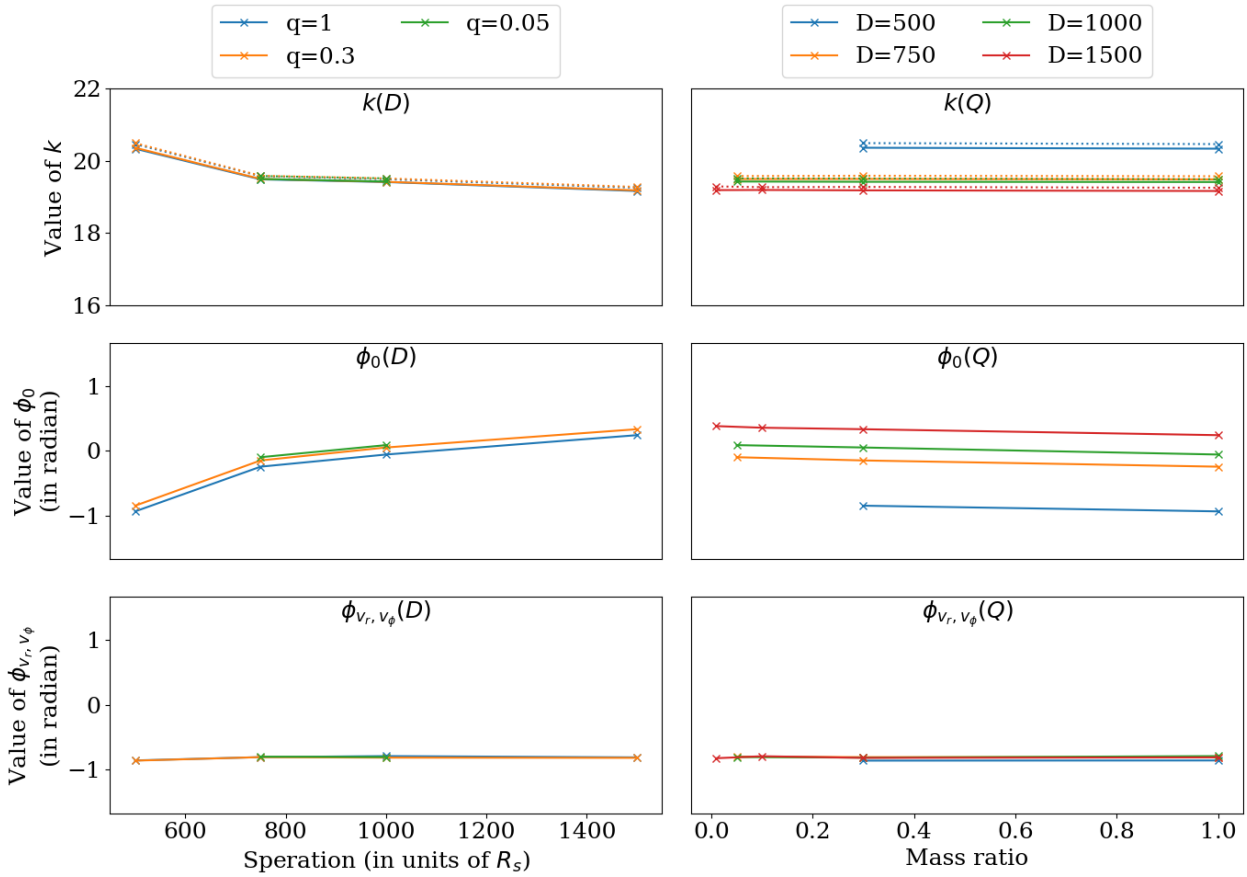

Figure 3.11: **Comparison of the spiral phase parameters for different values of the orbital parameters.**
The left column displays the evolution of the spiral phase parameter with the separation. The different values of the mass ratio are plotted with different colors. The right column displays the evolution of the spiral phase with the mass ratio. The different values of the separation are plotted with different colors. In the first row, the results are plotted with solid (dotted) lines for the spiral associated with u_r (u_ϕ).

Separation	Mass ratio	$t^\star$	T_{orb}/t
500	1	7×10^3	10.035
	0.3		12.447
750	1	12×10^3	10.755
	0.3		13.339
	0.05		14.843
1000	1	19×10^3	10.457
	0.3		12.971
	0.05		14.433
1500	1	35×10^3	10.429
	0.3		12.936
	0.01		14.063
	0.001		14.676

Table 3.1: Simulation orbital parameters and times used to fit the spiral with the model

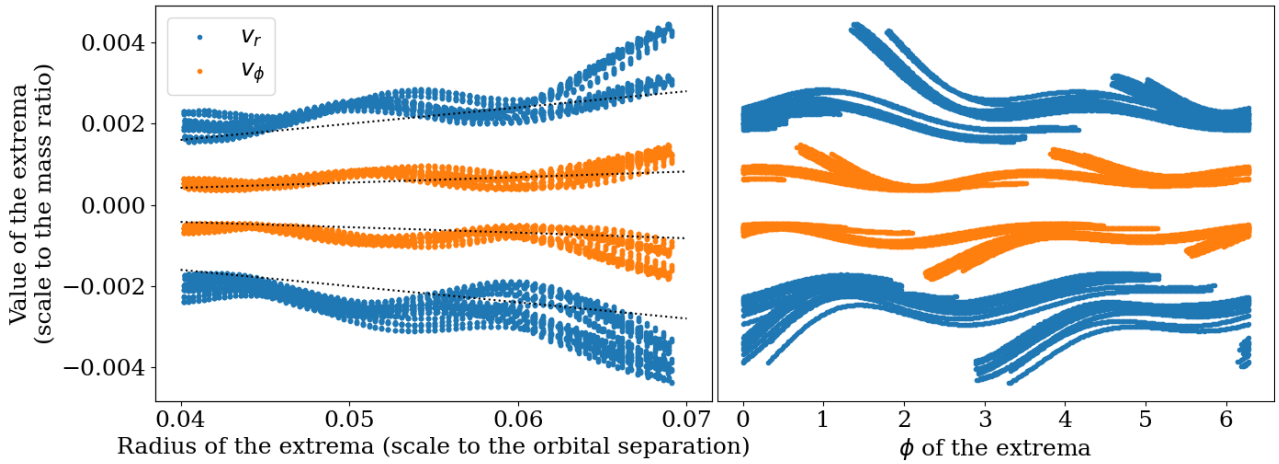

Figure 3.12: **Evolution of the extrema of the spirals in the velocity field of the simulation output as a function of the radius and the azimuthal angle**
The plot combined all the simulations presented in 3.1. The extrema values are scaled to the mass ratio, and the radius is scaled to the binary orbital separation. The colors distinguish between the two components of the velocity field.

tion of self-similar solutions (Spruit 1987). As the spiral is fitted between $0.04D$ and $0.07D$, the spiral phase parameter values should be independent of the separation. The fact that k and ϕ_0 depend on D underlines the difference between the simulated disc, which considers nonlinearities, and the idealized model.

The points where the value of the spirals s_r and s_ϕ are minimal and maximal were used to fit the parameters of the spiral phase in the model. They can also be used to model the spiral envelope as they correspond to the modulus of the Fourier transform components for $m = 2$.
Figure 3.7 shows that the spiral amplitude grows with increasing radius. The gravitational influence of the MBH companion is directly proportional to the mass ratio in the simulations. Thus, the spiral amplitude can scale to the mass ratio. As explained before, the radial dependency is scaled to the separation. Hence, a basic model for the spiral amplitude is

$$C_r(r) = C_r \times q \times \left(\frac{r}{D}\right)^n \tag{3.15a}$$

$$C_\phi(r) = C_\phi \times q \times \left(\frac{r}{D}\right)^n \tag{3.15b}$$

where C_r and C_ϕ are two (non-equal) constants. The linearized equations (3.4a) and (3.4b) are different for each component of the velocity field. Thus, their Fourier transform coefficients do not have the same analytical expression as a function of r, the binary orbital parameters, and the Fourier transform coefficients of the gravitational influence of the MBH companion.

Figure 3.12 displays the evolution of the extremal values of s_r and s_ϕ scaled to the mass ratio as a function of their radius scaled to the separation or azimuthal angle.
The variations of the spiral amplitude with the azimuthal angle suggest that modes other than $m = 2$ are significant in this region. The oscillation of the spiral amplitude with the radius indicates that the model in equation (3.15) is too simplistic.
For a first approximation of the tidal influence of the MBH companion with a logarithmic two-arm spiral, we still keep this model with the values:

$$(C_r,\ n_r) \sim (0.04,\ 1)$$
$$(C_\phi,\ n_\phi) \sim (0.02,\ 1.2)$$

The black dotted line on the left panel of Figure 3.12 shows the model chosen for the amplitude.

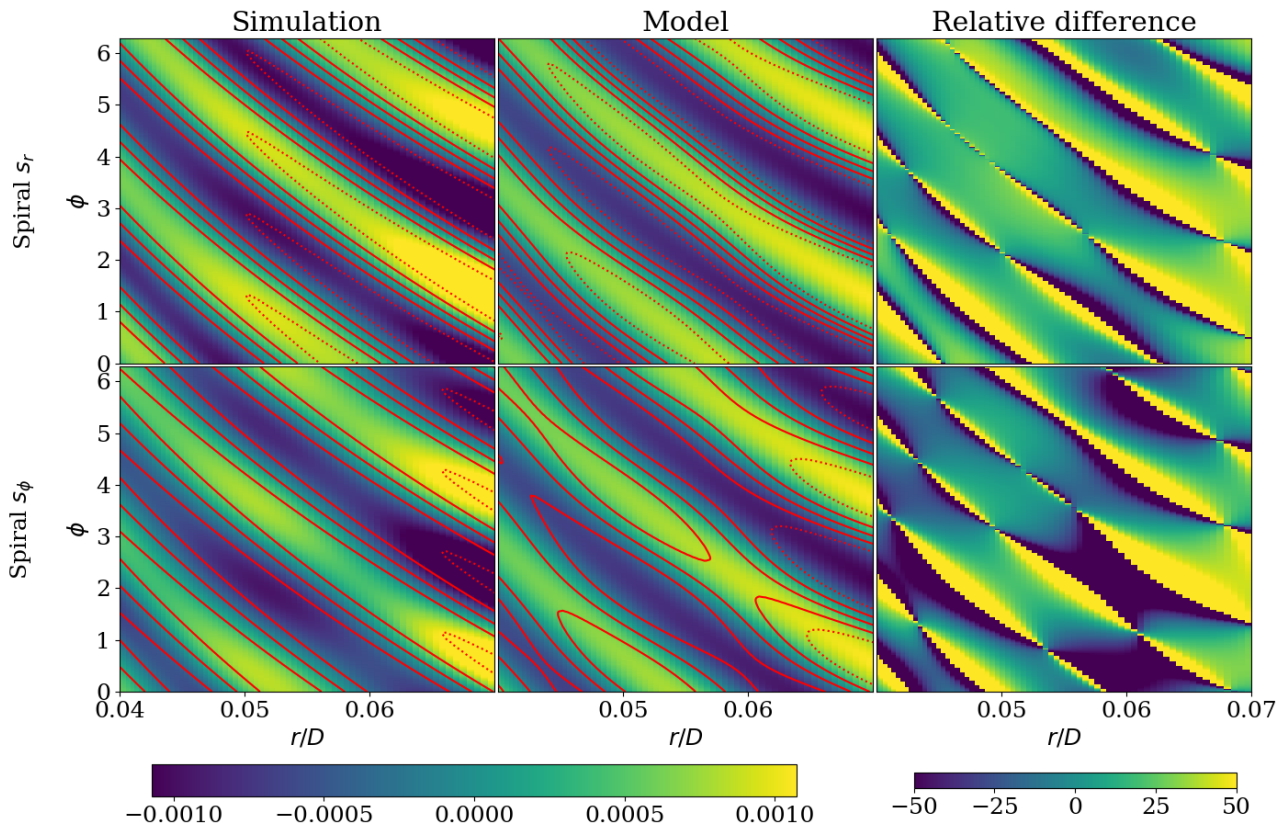

Figure 3.13: **Result of the method to find the spiral parameters applied to the simulation** ($D = 1\ 000,\ q = 1,\ t^\star = 19 \times 10^3$)
The first row represents s_r, and the second row represents s_ϕ. The first column reproduces the simulation output; the second is the result obtained with the model. The lower left color scale is associated with the variations of s_r and s_ϕ. The last column is the relative difference between the simulation output and the model. The lower right color scale is in percentage.
The red lines superimposed on the plot corresponding to the simulation are levels associated with the model and vice versa. For s_r, the dashed lines correspond to the levels ± 0.002 and the solid lines to the levels ± 0.001 and 0. For s_ϕ, the dashed lines correspond to the levels ± 0.001 and the solid lines to the levels ± 0.0005 and 0.

Figure 3.13 compares the spirals obtained with this model and extracted from the simulation output for the simulation ($D = 1\ 000\ R_s, q = 1, t = 19 \times 10^3\ R_s/c$). The relative difference between the two can reach 40%. This is due to the very simplistic model used for the spiral amplitude. The same plots for the other simulations of Table 3.1 are presented in Appendix B.

We did not have time to investigate the spiral pattern further in the simulations because we chose to focus on the effect of the truncation of the disc outer parts on the iron line profile.

CHAPTER

4

IMPACT OF THE MASSIVE BLACK HOLE COMPANION ON THE IRON Kα EMISSION LINE PROFILE

As highlighted by Wilms et al. (1998), computing the GR transport of reflected photons from the outer layer of the disc to the observer at infinity can be done either by computing each geodesic, which is computationally costly, or by using the Cunningham transfer function (Cunningham 1975). These transfer functions convolve the emission, assumed to be isotropic, to a function that encodes all the relativistic effects. This allows fastening the computation of the reflected component from the outer layer in the disc to the observer at infinity once the values are tabulated. Therefore, the impact of the emissivity function on the observed iron line profile can be studied faster. However, it does not account for the emissivity's angular dependency and limits the spatial resolution of the disc to the already computing points (Beckwith & Done 2004). In the work presented here, we chose not to use these transfer functions in order to take into account the non-axisymmetric velocity field of the emitters and the non-axisymmetric elliptic shape of the disc.

4.1 Model to compute the profile of the iron Kα emission line

The observed iron line flux F at the frequency $\tilde{\nu}$ is the sum of the flux contribution from all parts in the disc

$$F(\tilde{\nu}) = \iint I_{obs}(\tilde{\nu}) \ \cos\theta_s \ d\Omega$$

where $I_{obs}(\tilde{\nu})$ is the observed specific intensity at frequency $\tilde{\nu}$, θ_s is the angle from which the observer sees the elementary solid angle $d\Omega$. The disc is assumed to be at infinity: $\cos\theta_s = 1$. For geometrically thin accretion discs, the elementary solid angle is

$$d\Omega = \frac{[\widehat{c}\,(\vec{n}_{obs};\vec{x}) \cdot \vec{n}_d] \ d^2x}{d_{obs}^2}$$

where d_{obs} is the distance between the central BH and the observer, $\vec{n}_{obs}$ is an elementary vector pointing towards the observer at infinity from the central BH, $\vec{x}$ locates the emitting point in the disc from the central MBH, $\widehat{c}\,(\vec{n}_{obs};\vec{x})$ is the direction of emission of iron line photons at the outer layer of the disc so that they reach the observer at infinity, $\vec{n}_d$ is the elementary normal to the disc, and d^2x is the elementary area of the disc.
In the GR framework, Liouville's theorem relates the observed (I_{obs}) to emitted (I_{em}) specific intensity:

$$I_{obs}(\tilde{\nu}) = I_{em}(\nu_{em}) \ \left(\frac{\tilde{\nu}}{\nu_{em}}\right)^3$$

where ν_{em} is the emitted frequency. Therefore, the general formula to compute the iron line flux $F(\tilde{\nu})$ is:

$$F(\tilde{\nu}) = \frac{1}{d_{obs}^2} \iint_{\vec{x}\in\mathcal{D}} \delta\left[\tilde{\nu} - \nu_{obs}(\vec{x})\right] \left(\frac{\nu_{obs}\left(\vec{x}\right)}{\nu_{em}}\right)^3 I_{em}\left(\vec{x}\right) \left[\widehat{c}(\vec{n}_{obs};\vec{x})\cdot\vec{n}_d\right] d^2x \tag{4.1}$$

where $\nu_{obs}(\vec{x})$ is the observed frequency of photons emitted at the position $\vec{x}$ in the disc. $\mathcal{D}$ is the iron line emitting region in the disc. $\delta\left[\tilde{\nu} - \nu_{obs}(\vec{x})\right] = 1$ if $\tilde{\nu} = \nu_{obs}(\vec{x})$, and 0 otherwise.
This formula remains valid if iron line photons are produced solely in a thin accretion disc and experience no absorption from the outer surface of the disc to the observer. Computing this integral requires two steps. The first is to compute the specific intensity of the emission at the outer layer (I_{em}) of the disc. The second step is to compute the transportation of this line from the surface of the disc to the observer at infinity. Section 4.1.1 presents the value of the emitted iron line specific intensity. Section 4.1.2 presents the photon geodesics from the surface of the disc to the observer.

4.1.1 Specific intensity of the emitted iron line

As explained in section 1.1.2, the specific intensity of the emitted iron line at the outer layer of the disc depends on the illumination of the disc by the primary X-ray power law, the chemical composition of the disc, and its ionization state. Its complete computation would require solving the radiation transport equations in the disc.

The truncation of the disc outer parts and its elliptical shape modifies the geometry of the iron line emitting region. The spiral in the velocity field impacts the Doppler semi-relativistic frequency shift between the emitting point and the observer. Therefore, a first exploration of the impact of these effects on the iron line profile can be done without modeling the complex hard X-ray reprocessing in the accretion disc.

In many theoretical computations of the iron line profile, which do not model the complex hard X-ray reprocessing in the accretion disc, the emissivity of the disc is considered to be proportional to r^{-q}, where r is the radius (e.g., Fabian et al. (1989), Bromley et al. (1997), Ni et al. (2016), Bambi et al. (2017)). This hypothesis allows changing the iron line emissivity radial profile to study its impact on the computed iron line profile.

As in Hartnoll & Blackman (2000, 2001, 2002) and Jiang et al. (2015), we suppose the emitted specific intensity is proportional to the received illumination hard X-ray flux produced by a point-source corona located on the central rotation axis of the accretion disc (Lamppost model). We have opted for the Lamppost model as its parameters are easily controlled. The corona is a point-source located at a distance h_s from the central BH on the rotation axis of the accretion disc. The influence of this parameter on the results will be considered in our study.
As the hard X-ray reprocessing processes are not described, the absolute value of the flux emitted by the corona is not significant. We only consider the variation of the illumination flux received by each point in the accretion disc through the impinging angle and distance from the hard X-ray source.

No relativistic effects due to the central MBH are considered from the point-source corona to the accretion disc. This is a simplification since the corona is assumed to be located near the central BH. However, reducing the corona to a point-source is too simplistic to be considered a physical model. Additionally, we have not adequately modeled the hard X-ray reprocessing processes in the accretion disc. Therefore, if we were to add the relativistic effects on the hard X-ray photons from the corona to the accretion disc, it would introduce a level of complexity that would not necessarily significantly improve the model. Dovčiak et al. (2014) explore the impact of the GR effects on the hard X-ray photons from the point-source corona to the accretion disc.

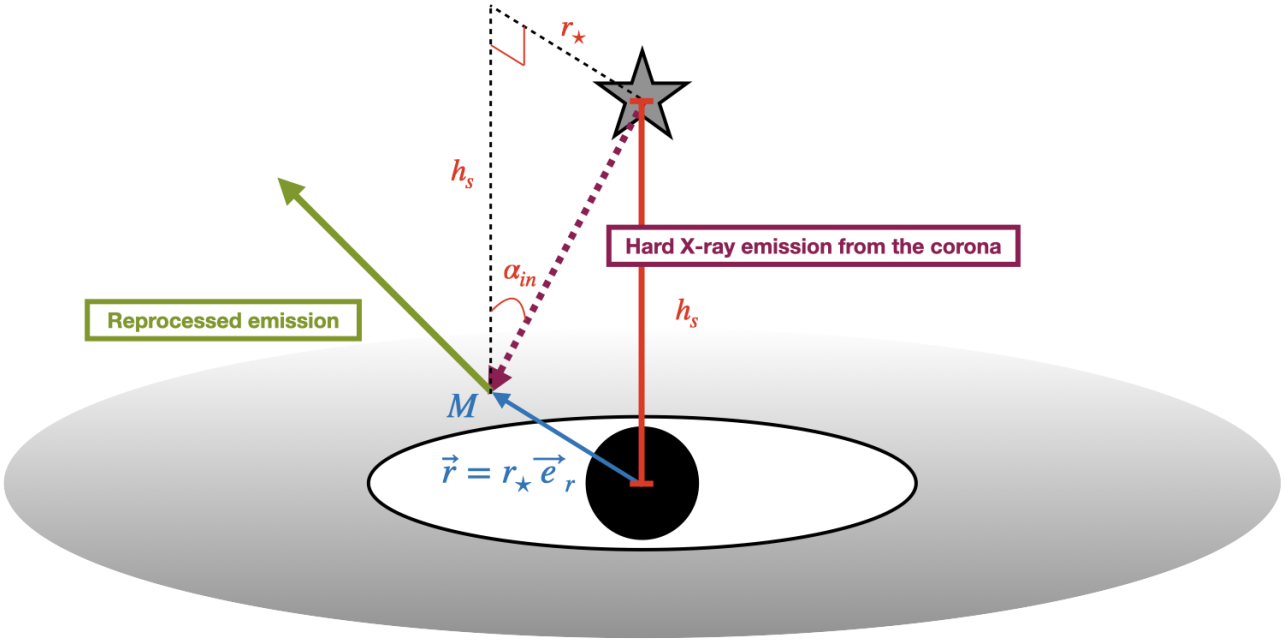

Figure 4.1: **Model of the corona with the Lamppost model** $\vec{r} = r_\star \vec{e}_r$ is the distance from the central BH to the emitting point in the disc. h_s is the distance between the central BH and the point source corona. α_{in} is the impinging angle of hard X-ray photons emitting from the point-source corona to the disc. No relativistic effects are considered on the hard X-ray photons.

The illumination of the disc by the corona is illustrated in Figure 4.1. The specific emitted frequency at each point in the disc is assumed to be proportional the inverse of the square distance between the point in the disc and the point=source corona, and the cosine of the imping angle α_{in}:

$$I_{em} \propto \frac{1}{h_s^2 + r^2} \times \cos \alpha_{in} = \frac{h_s}{(h_s^2 + r^2)^{q/2}} \tag{4.2}$$

where $q = 3$. The introduction of the parameter q in this formula refers to the model of iron line emissivity $I_{em} \propto r^{-q}$ mentioned above.
Most studies controlling the validity of the Lamppost geometry to explain X-ray reflection spectra suggest that the Lamppost corona should remain relatively close to the central BH (e.g., Fabian et al. (2012) or Ursini et al. (2020)): $h_s = 5\ R_s$ (Dauser et al. 2013) or $h_s = 0.65\ R_s$ and $h_s = 2.5\ R_s$ (Niedźwiecki et al. 2016). To test the validity of the numerical computation of the iron line in this chapter, we chose $h_s = 5\ R_s$, as in Hartnoll & Blackman (2002).

4.1.2 Relativistic effects due to the central massive black hole

In this study, we consider that the broadening of the iron line is caused by the GR effects exerted by the central MBH. Therefore, the photons geodesic from their emitting point in the disc to the observer at infinity is computed in the GR framework.

D'Orazio et al. (2015) investigate the effect of the central MBH orbital motion on the iron line. The orbital motion introduces an additional component to the Doppler frequency shift that changes over time. Gravitational lensing might also affect the observed iron line profile if the MBH companion lies between the iron line emitting disc and the observer. This study will not consider these effects: we focus on examining the impact of disc truncation, the elliptic shape of the disc, and the spiral wave in the disc.

These three effects occur in the outer parts of the disc, where the impact of the spin of the central BH on the iron line photons geodesics can be neglected. Using a Schwarzschild metric instead of a Kerr

(1963) metric neglects the effects of the spin of the central BH. Bromley et al. (1997) compare the iron line profiles computed with the Schwarzschild and Kerr metrics. Figure 3 in their article displays iron line profiles observed with an inclination angle $i_{obs} = 30°$ and the emitted specific intensity of the iron line proportional to the inverse of the squared distance between the emitting point in the disc and the central BH. The iron line profile emitted by a disc with an inner edge at 2.25 R_s and an outer edge at 7.5 R_s around a maximally spinning Kerr BH is similar to the line profile obtained in the Schwarzschild case with a disc inner edge at 3 R_s. However, in the case of a maximally spinning Kerr BH, the ISCO is located at a radius of 0.625 R_s. The results on the line profile differ if the inner edge of the disc is at this radius. This suggests that the central BH spin mainly impacts the iron line photons emitted from the disc inner parts. Hence, we neglect the spin and use a Schwarzschild metric to study the influence of the structure changes in the outer parts of the disc.
Thus, we will consider a Schwarzschild (1916) metric to compute the GR effects of the central BH on the iron line photons. The line element ds in the spherical coordinates (t, r, θ, ϕ) centered on the BH is

$$ds^2 = -\left(1 - \frac{R_s}{r}\right) c^2 dt^2 + \frac{1}{1 - \frac{R_s}{r}} dr^2 + r^2 d\theta^2 + r^2 \sin^2\theta d\phi^2 \tag{4.3}$$

As explained in the introduction of this chapter, calculating the photons geodesic from each point in the disc to the observer is a computationally expensive task. However, when studying the effects of a MBH companion in the outer region of the disc, we can use the same approximation as in Hartnoll & Blackman (2000, 2001, 2002). It consists of a first-order expansion of the geodesic equations, which is valid if $R_s/r \ll 1$. This is the case in the outer parts of the disc. This approximation limits the values of i_{obs} that can be studied since only the first order of light-bending is considered. It is also worth noting that Bromley et al. (1997) emphasize that the difference in the iron line profiles between the Schwarzschild and Kerr cases increases with i_{obs}. Therefore, using the Schwarzschild metric instead of the Kerr metric and this approximation is valid only for limited values of i_{obs}.

I will rapidly present the exact equations for the geodesic parameters required to compute the integral in equation (4.1). All the details on how to derive these quantities are shown in Appendix C.1, C.2, and C.3. I will then focus more specifically on the approximations introduced by Hartnoll & Blackman (2000, 2001, 2002) and the first-order expansion of the final geodesic equation. The intermediate steps, which are of little interest to the discussion, are also detailed in Appendix C.4.

In the Schwarzschild metric, the observed frequency is

$$\frac{\nu_{obs}(\vec{n}_{obs}; r, \phi)}{\nu_{em}} = \frac{(\mathbf{p} \cdot \mathbf{v})_{observer}}{(\mathbf{p} \cdot \mathbf{u})_{emitter}} = \frac{\sqrt{1 - \frac{R_s}{r_{em}} - \frac{1}{1 - \frac{R_s}{r_{em}}} \frac{u_r^2}{c^2} - \frac{u_\phi^2}{c^2}}}{1 - \frac{1}{1 - \frac{R_s}{r_{em}}} \widehat{c}_r \frac{u_r}{c} - \widehat{c}_\phi \frac{u_\phi}{c}} \tag{4.4}$$

In the first part of this equation, $\mathbf{p}$ is the photon 4-momentum, $\mathbf{v}$ is the 4-velocity of the observer at infinity, and $\mathbf{u}$ is the 4-velocity of the emitters in the disc. $r_{em} = r'_{em}$ is the radius of the emitting point in the disc (it is the same in the two coordinates systems presented in Figure 4.2). In the second part of this equation, $\widehat{c}_r$ and $\widehat{c}_\phi$ designate the radial and azimuthal components of the initial emission direction of photons projected on the accretion disc plane. The notations are chosen to be consistent with Hartnoll & Blackman (2000, 2001, 2002). The derivation of this formula is presented in Appendix C.2.

A change of coordinate system is used to compute the photons geodesic. The symmetries of the Schwarzschild metric can be exploited to simplify the equations if the photon trajectories lie in the equatorial plane of the spherical coordinates. Figure 4.2 illustrates this change of coordinates. In the initial coordinate system of this transformation, the accretion disc lies in the equatorial plane, and the observer's direction at infinity is in the (Oxz) quadrant. i_{obs} is measured from the (Oz) axis in the direction of the (Ox) axis. In the final coordinate system of this transformation, the photon

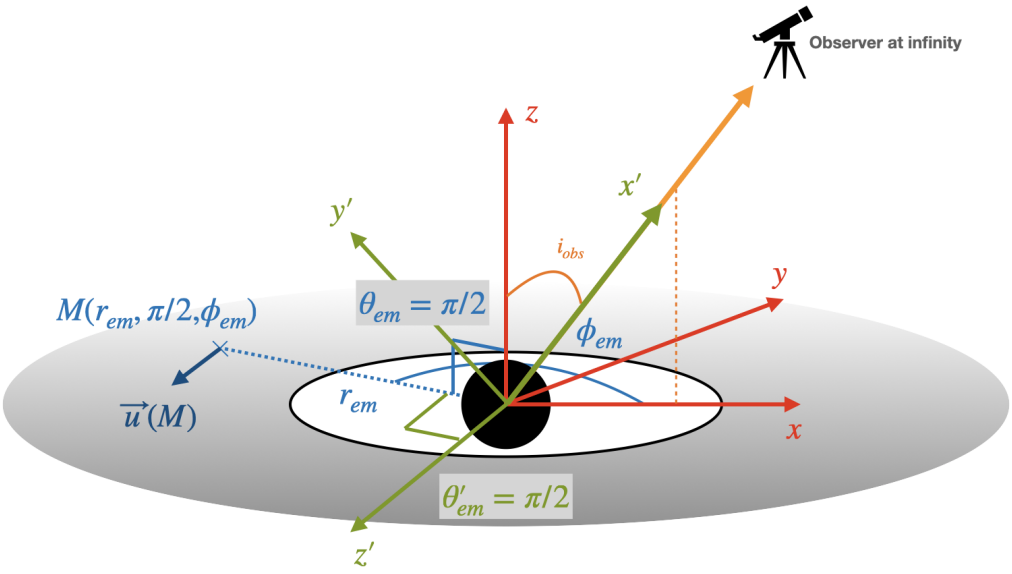

Figure 4.2: **Coordinate substitution to compute photons geodesic**
In red is the coordinate system where the accretion disc lies in the equatorial plane. In green is the coordinate system where the photon geodesic lies in the equatorial plane.

trajectory lies in the equatorial plane, and the (Ox') axis coincides with the observer's direction at infinity. Each photon geodesic from any point on the accretion disc to the observer at infinity requires a unique coordinate substitution. The radius remains unchanged. The spherical coordinates of the emission point change from $(r = r_{em},\ \phi = \phi_{em},\ \theta = \pi/2)$ to $(r' = r = r_{em},\ \phi' = \phi'_{em},\ \theta' = \pi/2)$.

With this coordinates substitution

$$\widehat{c}_r = -\frac{b}{r^2}\left[\frac{dr}{d\phi'}\right]_{em} \tag{4.5a}$$

$$\widehat{c}_\phi = -\frac{b}{r}\left[\frac{d\phi'}{d\phi}\right]_{em} \tag{4.5b}$$

where b is a constant called the impact parameter of the photon geodesic. Its is determined by solving the geodesic equations from the emitting point in the disc to the observer in the direction i_{obs} at infinity.

The relation between ϕ' and ϕ can be computed with the GR coordinate substitution formula

$$\left[\frac{d\phi'}{d\phi}\right]_{em} = \frac{\sin\phi'_{em}\sin i_{obs}}{\sqrt{(\sin\phi'_{em})^2 + (\cos\phi'_{em}\cos i_{obs})^2}} \tag{4.6}$$

where ϕ'_{em} is the polar angle of the emitting point in the disc in the coordinate system $(Ox'y')$ (see Figure 4.2). The derivation of this formula is detailed in Appendix C.1.2. The azimuthal angle of the emitting point in the new system of coordinates is given by

$$\cos\phi'_{em} = \cos\phi_{em} \tag{4.7a}$$

$$\sin\phi'_{em} = \sqrt{1 - \cos^2\phi'_{em}} \geq 0 \tag{4.7b}$$

The cosine value is obtained from equation (C.3). The reason for limiting $\phi'_{em} \in [0;\ \pi]$ is to consider only the photons emitted from the side of the disc that is directly visible to the observer. The photons emitted from the other side suffer a too high deflection to be considered with the approximation of the first-order expansion of the geodesic equations.

The scalar product between the initial direction of emission of photons and the normal to the disc is

$$\widehat{c}(\vec{n}_{obs}; r, \phi) \cdot \vec{n}_d = \frac{1}{\sqrt{\left[\frac{dr}{d\phi'}\right]^2_{em} + r^2_{em}}} \frac{\cos i_{obs}}{\sin \phi'_{em}} \, r_{em} \tag{4.8}$$

This equation is derived in Appendix C.3.

The equations mentioned are exact. To calculate the integral in equation (4.1), the impact parameter b and the azimuthal derivative of radial coordinate $\left[\frac{dr}{d\phi'}\right]_{em}$ must be determined. These values can be obtained by integrating the geodesic equation from the point of emission in the disc to the observer at infinity.
The contravariant coordinates of the photons 4-momentum in the Schwarzschild metric is

$$\mathbf{p}^{\mu'} = \left(c\frac{dt'}{d\lambda'}, \frac{dr'}{d\lambda'}, 0, \frac{d\phi'}{d\lambda'}\right) = e\left(\frac{1}{1-\frac{R_s}{r'}}, \frac{b}{r'^2}\frac{dr'}{d\phi'}, 0, \frac{b}{r'^2}\right)$$

where λ' is an affine parametrisation of the geodesic. The details on the derivation of this formula are presented in Appendix C.2. e is the constant of motion associated with the independence of the Schwarzschild metric elements from the time coordinate (as shown in equation (C.10)). In simpler terms, it represents the energy an observer measures at infinity.
As photon geodesics are null geodesics:

$$0 = \mathbf{p} \cdot \mathbf{p} = e\left(-\frac{1}{1-\frac{R_s}{r}} + \frac{1}{1-\frac{R_s}{r}}\frac{b^2}{r^4}\left(\frac{dr}{d\phi'}\right)^2 + r^2\frac{b^2}{r^4}\right)$$

With the substitution $x = 1/r$, this equation becomes

$$\frac{1}{b^2} = \left(\frac{dx}{d\phi'}\right)^2 + x^2\left(1 - R_s x\right) \tag{4.9}$$

Finally, with the azimuthal derivation of equation (4.9), the geodesic equation becomes

$$\frac{d^2x}{d\phi'^2} = -x + \frac{3}{2}R_s x^2 = -x\left[1 - \frac{3}{2}R_s x\right] \tag{4.10}$$

Hartnoll & Blackman (2000, 2001, 2002) propose the following hypothesis:

$$R_s \times x \ll 1 \Leftrightarrow \frac{R_s}{r} \ll 1 \tag{4.11}$$

This approximation can solve the equation (4.10) using the perturbation theory. The solution is written

$$x(\phi') = x_0(\phi') + x_1(\phi'), \qquad \text{with } x_1 \ll x_0 \tag{4.12}$$

The leading term x_0 is the solution of the leading term in equation (4.10)

$$\frac{d^2x_0}{d\phi'^2} = -x_0 \tag{4.13}$$

And the first-order term x_1 is the solution of the first-order expansion of equation (4.10)

$$\frac{d^2x_1}{d\phi'^2} = -x_1 + \frac{3}{2}R_s x_0^2 \tag{4.14}$$

Details on how to solve these two equations are provided in Appendix C.4. The unknown constants resulting from the resolution can be determined using equation (4.9). The solution is

$$\frac{1}{r(\phi')} = x(\phi') = \frac{\sin\phi'}{b} + \frac{R_s}{2b^2}\left[1 - 2\cos\phi' + \left(\cos\phi'\right)^2\right] \tag{4.15}$$

The leading term is

$$x_0(\phi') = \frac{\sin(\phi')}{b} \Leftrightarrow r\sin(\phi') = b \Leftrightarrow y' = b \tag{4.16}$$

It is a horizontal straight line in the equatorial plane $(Ox'y')$ (see Figure 4.2). The trajectory of the photon is not affected by the GR effect of the central BH, and it reaches the observer on the x'-axis at infinity without being bent.

The value of the impact parameter b is constrained by considering the equation (4.15) at the emitting point $(r = r_{em}, \phi' = \phi'_{em})$.

$$b = \frac{r_{em}}{2}\sin\phi'_{em} + \frac{r_{em}}{2}\sqrt{(\sin\phi'_{em})^2 + \frac{2R_s}{r_{em}}(1-\cos\phi'_{em})^2} \tag{4.17}$$

where $r_{em} = r'_{em}$ is the radius of the emitting point in the disc. The value of the azimuthal derivative of equation (4.15) at the emission point gives $\left[\frac{dr}{d\phi'}\right]_{em}$

$$\left[\frac{dr}{d\phi'}\right]_{em} = -\frac{r_{em}^2}{b}\left(\cos\phi'_{em} + \frac{R_s}{b}(1-\cos\phi'_{em})\sin\phi'_{em}\right) \tag{4.18}$$

As discussed earlier, this calculation aims to study how the MBH companion's influence on the disc outer regions affects the iron line profile. Figures 4.3 and 4.4 can help assess the accuracy of the approximation in equation (4.10) to obtain the equation (4.15). Figure 4.3 presents the minimal value of r/R_s along the geodesic computed with equation (4.15) as a function of the initial position of the emitting point in the accretion disc. The graph shows this value for different values of i_{obs}. Each plot represents the accretion disc in the $(0xy)$ plane (defined in Figure 4.2). Figure 4.4 displays the photon geodesics for several initial positions in the $(Ox'y')$ plane (defined in Figure 4.2). All the geodesics are contained in a different physical plane $(Ox'y')$ but are shown on the same plot for comparison. The results for different values of i_{obs} are presented.

Figure 4.4 shows that for low values of i_{obs}, the coordinate of the emitting point in the $(Ox'y')$ coordinate system is close to $(r_{em}, \phi'_{em} = \pi/2)$; see equation (4.7). The minimal value of r/R_s is r_{em}/R_s, which decreases in the inner parts of the disc. However, for relatively small values of i_{obs}, photons are almost emitted perpendicularly to the disc. The deflection of the light ray is slight. The approximation remains valid.
Figure 4.4 shows that the photons emitted from behind the BH to the observer suffer a higher deflection as i_{obs} increases. Moreover, their geodesic passes closer to the central BH. Figure 4.3 illustrates that the minimal value of r_{em}/R_s diminishes in the parts of the disc where $x < 0$. This weakens the validity of the approximation.

Therefore, the approximation defined in equation (4.11) and the solution derived with a first-order expansion of the geodesic equation can only be used on a limited range of i_{obs} values. We will not consider i_{obs} values higher than 50° when examining the impact of truncating the disc outer parts.

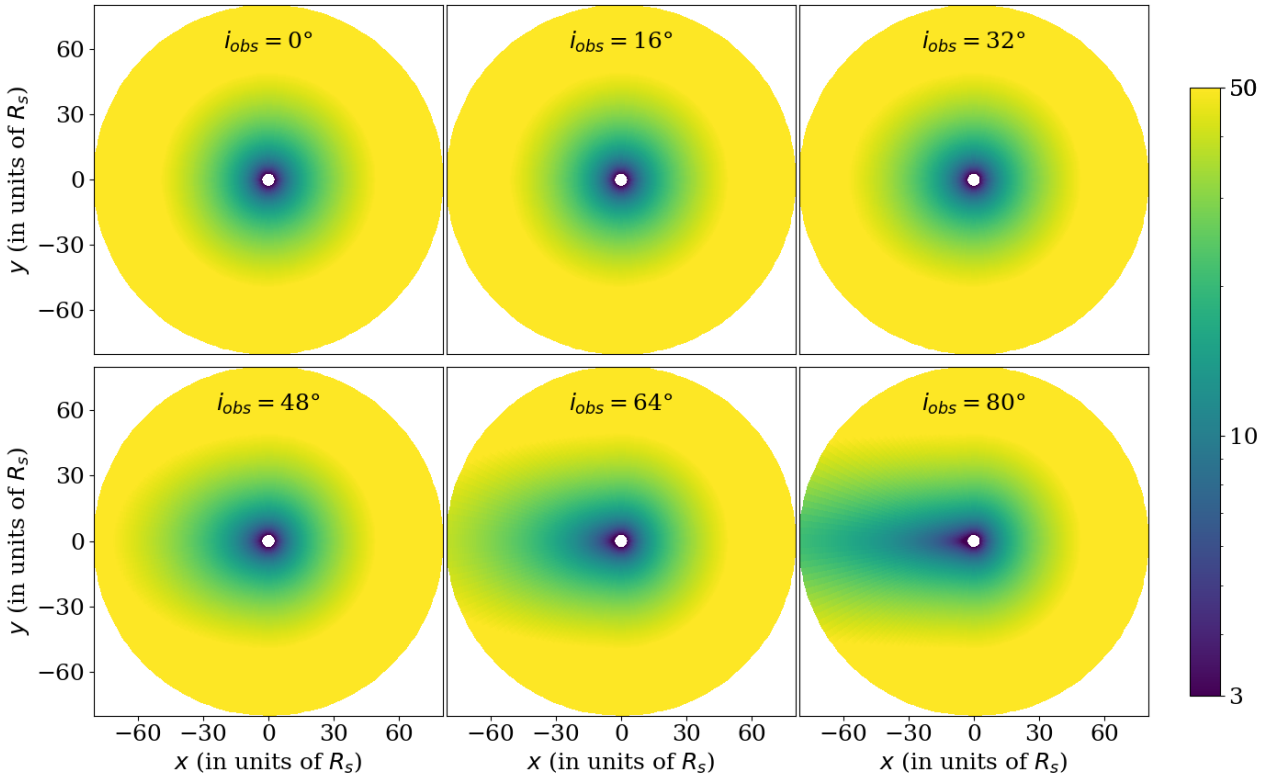

Figure 4.3: **Minimal value of $r(\phi')/R_s$ along photon geodesic (equation (4.15)).** The logarithmic color scale represents the minimal value of $r(\phi')/R_s$ along the geodesic emitted from (r_{em}, ϕ_{em}), plotted on the Cartesian representation of the accretion disc in the (Oxy) plane.

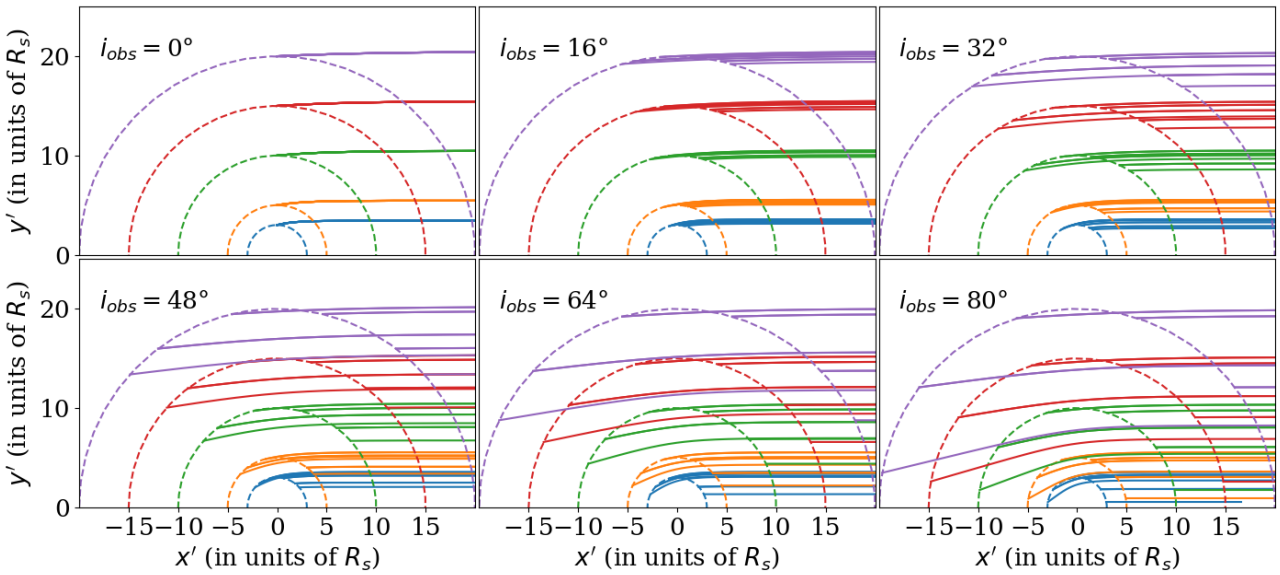

Figure 4.4: **Photon geodesics in the $(Ox'y')$ plane** Representation of the photon geodesic $\phi' \to r(\phi')/R_s$ for the initial conditions $(r_{em}, \phi_{em}) = \{3\ R_s, 5\ R_s, 10\ R_s, 15\ R_s, 20\ R_s\} \times \{i \times \pi/5\}_{0 \leq i \leq 9}$. Geodesics belong to different physical planes $(Ox'y')$ but are shown here on the same plot.

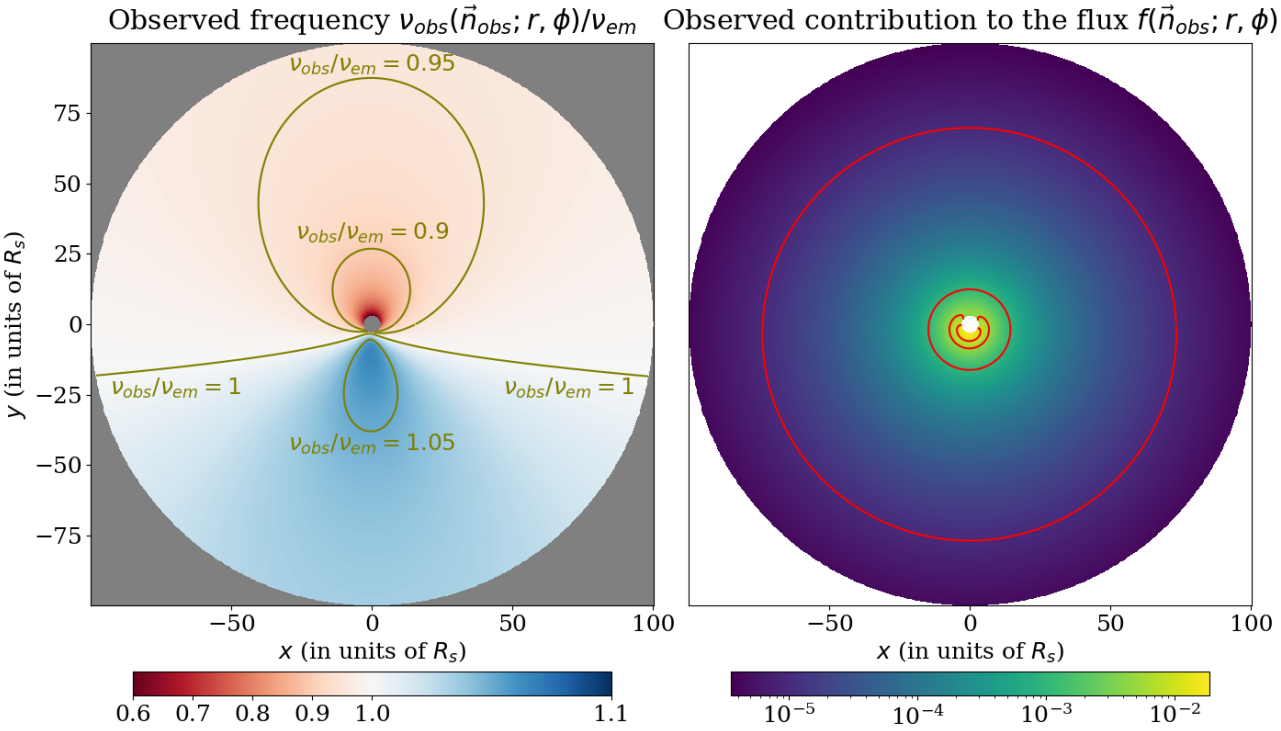

Figure 4.5: **Observed frequency and contribution to the flux from each emitting point of the disc for $i_{obs} = 35°$.**
The iron line emitting region extends from $r = 3\ R_s$ to $r = 100\ R_s$. The velocity field in the disc is Keplerian ($u_r = 0$ and $u_\phi = \sqrt{\frac{GM}{r}}$). The parameters for the disc's illumination by the corona are $q = 3$ and $h_s = 5\ R_s$.
The left panel displays the observed frequency (equation (4.4)) normalized by the emitted frequency ν_{em}. Blue (red) represents blueshifted (redshifted) frequencies. The green lines show the points where the ratio between the observed and emitted frequencies equals 0.9, 0.95, 1, and 1.05.
The right panel displays the observed contribution to the flux (equation (4.20)). The scale is logarithmic. The red lines show the points where the observed contribution to the flux equals 10^{-3}, 5×10^{-3}, and 10^{-2}.

Finally, the elementary surface area in the Schwarzschild coordinate is

$$d^2x = \frac{dr \times r d\phi}{\sqrt{1 - \frac{R_s}{r}}} \tag{4.19}$$

4.1.3 Observed frequency and contribution to the flux from each point in the disc

The observed frequency of photons emitted from each point in the accretion disc is shown in the left panel of Figure 4.5. It is computed using equation (4.4). The observer is in the plane (Oxz), with an angle $i_{obs} = 35°$ measured from the (Oz) axis in the direction of the (Ox) axis (see Figure 4.2 for the definition of the axis).
The semi-relativistic Doppler effect, caused by the motion of the emitters in the disc, results in a blueshift for photons emitted from parts of the disc moving towards the observer ($y < 0$) and a redshift for photons emitted from parts of the disc moving away from the observer ($y > 0$). If only this effect were considered, the red and blue shifts would be anti-symmetric about the y-axis. This symmetry is not preserved when the GR effects are also considered. Firstly, the presence of the central BH causes a gravitational redshift for all the photons escaping its environment towards infinity. Secondly, the movement of the emitters in the framework of general relativity, regardless of the component projected in the line of sight, also causes a redshift.

The observed contribution to the flux from each part of the disc is displayed in the right panel of Figure 4.5. The observed contribution to the flux from each part of the disc is:

$$f(\vec{n}_{obs};\ r,\phi) = \left(\frac{\nu_{obs}\left(\vec{n}_{obs};\ r,\phi\right)}{\nu_{em}}\right)^3 \ \frac{h_s}{\left(h_s^2+r^2\right)^{q/2}} \ \left[\widehat{c}\left(\vec{n}_{obs};r,\phi\right)\cdot\vec{n}_d\right] \ \frac{r}{\sqrt{1-\frac{R_s}{r}}} \tag{4.20}$$

It is the function to be integrated over the disc in equation (4.1).

In the outer part of the disc, the different components of the observed contribution to the flux can be approximated to:

$$\begin{aligned}
\frac{\nu_{obs}(\vec{n}_{obs};r,\phi)}{\nu_{em}} &\sim 1 \\
\frac{h_s}{\left(h_s^2+r^2\right)^{q/2}} &\sim h_s r^{-q} \\
\widehat{c}\cdot\vec{n}_d &\sim \cos i_{obs} \\
\frac{r}{\sqrt{1-\frac{R_s}{r}}} &\sim r
\end{aligned}$$

Thus, for $q = 3$, the radial decrease of the flux is proportional to the inverse of the squared radius and independent of the azimuthal coordinates in the outer parts of the disc.

In the inner part of the disc, the flux is not axisymmetric anymore. First, the flux is proportional to the cosine of the angle between the direction of photons emission and the normal to the disc. This angle is symmetric relative to the x-axis. Moreover, in the parts of the disc where $x > 0$, the presence of the central BH "behind" the photon trajectories requires a higher angle between the direction of photon emission and the normal to the disc relative to the classical case (i.e. without considering the GR effects). On the opposite, in the parts of the disc where $x < 0$, the presence of the central BH between the emission point and the observer requires a smaller angle between the direction of photon emission and the normal to the disc relative to the classical case. Second, the observed contribution to the flux depends on the non-axisymmetric observed frequency. The emission from the blue-shifted parts of the disc is boosted, while the observed flux from the red-shifted part of the disc is fainter.

4.2 Numerical computation of the iron Kα emission line profile

Two numerical methods can be employed to calculate the observed iron line profile using the two-dimensional integral in equation 4.1. The first method is presented in section 4.2.1. The results obtained were verified with a second method presented in section 4.2.2.

4.2.1 *Binning* method

The *binning* method computes the iron line flux in frequency bins defined as

$$b_\nu = [\nu, \nu + \Delta\nu[\tag{4.22}$$

The output is a histogram.
The accretion disc is divided into elementary cells. The observed frequency (equation (4.4)) and the contribution to the flux (equation (4.20)) are calculated at the center of each cell. The observer bein located at infinity, the observed flux in a particular frequency bin is the sum of the flux contributions from every cells where the observed frequency falls within the frequency width of the bin. This is why the method is called the *binning* method.

As the formula presented in section 4.1.3, the numerical computation of the iron line profile is done in the polar coordinates associated with the accretion disc. Writing $x_{i,j} = (r_i, \phi_j)$ the coordinates of the middle of each cell, the observed frequency and contribution to the flux associated with the emission of each cell are $\nu_{obs}^{i,j} = \nu_{obs}(x_{i,j})$ and $f^{i,j} = f(x_{i,j})$. For an observer at infinity, the observed flux F_{b_ν} in a bin defined in equation (4.22) is

$$F_{b_\nu} = \frac{1}{\Delta\nu} \sum_{i=1}^{N_r} \sum_{j=1}^{N_\phi} \delta_{b_\nu}(\nu_{obs}^{i,j})\ f^{i,j}\ (\Delta x)^{i,j} \tag{4.23}$$

where the function $\delta_{b_\nu}(\nu_{obs}^{i,j})$ is equal to 1 if $\nu_{obs}^{i,j} \in b_\nu$ and 0 otherwise ; and $(\Delta x)^{i,j}$ is the spatial extent of the cell at $x_{i,j}$.

The observed frequency and contribution to the flux of each cell can be computed independently. Therefore, the computation can be parallelized. The total time required to calculate the iron line emitted by the entire accretion disc is directly proportional to the number of cells used to discretize the disc.

The most critical point of the *binning* method is the spatial resolution of the disc compared to the spectral resolution. The observed frequency and flux are computed in the middle of the cells, and their values are considered constant over the entire cell. To the first order, this is equivalent to making an error on the flux and the observed frequency on the edges of the cell of

$$\Delta f^{i,j} = \left| \frac{\partial f}{\partial r}(r_i, \phi_j)\ \frac{\Delta r}{2} + \frac{\partial f}{\partial \phi}(r_i, \phi_j)\ \frac{\Delta \phi}{2} \right| \tag{4.24a}$$

$$\Delta \nu_{obs}^{i,j} = \left| \frac{\partial \nu_{obs}}{\partial r}(r_i, \phi_j)\ \frac{\Delta r}{2} + \frac{\partial \nu_{obs}}{\partial \phi}(r_i, \phi_j)\ \frac{\Delta \phi}{2} \right| \tag{4.24b}$$

where Δr is the radial extent of the cell and $\Delta\phi$ is its angular extent. Figure 4.5 indicates that the frequency and flux contribution emitted from the disc inner regions exhibit the highest variations. Thus, higher spatial resolution in those regions is necessary. For this reason, the cells in the radial direction are spaced logarithmically to enable correct resolution of the inner parts of the disc while keeping the number of cells at a reasonable level in terms of computation time.

The study of the impact of the spatial resolution used to discretize the disc is presented below. As in Hartnoll & Blackman (2002), the velocity field in the disc is Keplerian. In the following, I use $q = 3$. From equation (4.2) this means that the hard X-ray flux is directly proportional to the impinging angle and inversely proportional to the square distance between the point-source corona and the emitting point in the disc, h_s. Unless explicitly stated, $h_s = 5\ R_s$, consistent with Hartnoll & Blackman (2002). The inclination angle used is $i_{obs} = 30°$. It is an intermediate value in the range of $[0°;\ 50°]$, which will be explored in the study of the impact of the truncation of the disc outer parts on the iron line profile. The spectral resolution used to compute the iron line is 2.5 eV, which is the expected value at 6 keV for the X-ray integral field unit spectrometer (X-IFU) onboard the future ESA observatory Athena (Barret et al. 2016) (this resolution is the targeted value before the design-to-cost exercise that is going on during the redaction of this manuscript). The frequency bins are linearly spaced between $\nu_{min} = 0.5\ \nu_{em}$ and $\nu_{max} = 1.1\ \nu_{em}$. N_{bin} designates the number of bins to cover this frequency range with a resolution of $\Delta\nu$. The critical point about the spatial resolution resides in the inner part of the disc. Thus, the iron line emitting region is between $r_{min} = 3\ R_s$ (the Schwarzschild ISCO) and $r_{max} = 100\ R_s$ to study the link between the spatial and spectral resolutions. To summarize, the

values of the iron line parameters are

$$u_r = 0, \qquad u_\phi = \sqrt{\frac{GM}{r}} = c\sqrt{\frac{r}{2R_s}} \tag{4.25a}$$

$$r_{min} = 3\ R_s, \qquad r_{max} = 100\ R_s \tag{4.25b}$$

$$h_s = 5\ R_s \qquad q = 3 \tag{4.25c}$$

$$i_{obs} = 30^\circ \tag{4.25d}$$

$$\nu_{min} = 0.5\ \nu_{em} = 3.2 \text{ keV}, \qquad \nu_{max} = 1.1\ \nu_{em} = 7.04 \text{ keV}, \qquad N_{bin} = 1536, \qquad \Delta\nu = 2.5 \text{ eV} \tag{4.25e}$$

General study of the impact of the spectral resolution on the iron line flux in each frequency bin

Studying the impact of the truncation of the disc outer parts requires the computation of many of iron line profiles (see Chapter 5). Thus, exploring ways to minimize the numerical noise while minimizing the computation resources is essential.

Figure 4.6 presents the influence of the spatial resolution on the iron line profile. The lower spatial resolution corresponds to the resolution used for the simulation with `AMRVAC` presented in Chapter 2 ($N_r = 720,\ N_\phi = 320$).
The upper left panel demonstrates that an increase in the spatial resolution (a decrease in the disc cell size) leads to a decrease in the numerical noise on the flux. This noise is caused by errors in the observed frequency and the contribution to the flux made in each cell by considering only the values of the two functions at the center of the cell (as mentioned in equation (4.24)).
The three panels on the lower left are presented to quantify the numerical noise. Since the integral in equation (4.1) can only be calculated numerically, there is no theoretical value for comparing the noise from each line. However, the upper left panel indicates that the iron line profiles converge when the spatial resolution increases. Hence, the highest spatial resolution ($N_r = 1\ 000\ 000$ and $N_\phi = 24\ 000$) is taken as the reference in computing the relative differences. It is assumed that its numerical noise is negligible compared to the ones at lower spatial resolution. The numerical noises are displayed in three different panels because their order of magnitude is significantly different.
The right panel measures this decrease in numerical noise as spatial resolution increases ($N_r \times N_\phi$). The maximum absolute relative difference is irregular as it is sensitive to abnormal bins (the maximum values occur in bins with low flux values). A smoother relationship between the logarithm of the average absolute difference in the 1536 energy bins, $< |\epsilon| >$, and the total number of cells can be seen. This relationship has been modeled by linear regression.

$$\begin{aligned} \log\left(< |\epsilon| >\right) &= \alpha\ \log\left(N_r \times N_\phi\right) + \beta \\ \alpha &= -0.805, \qquad \beta = 5.41 \end{aligned} \tag{4.26}$$

If the number of cells is doubled in both directions, the total computation time is quadrupled, while the average absolute relative error is divided by three.

Furthermore, for a constant total number of disc cells, the ratio between the number of cells in the radial and azimuthal directions impacts the level of numerical noise. Figure 4.7 illustrates the evolution of numerical noise with a fixed total number of cells $N_r \times N_\phi = 1.2 \times 10^9$ and varying distribution of cells between the radial and azimuthal directions. The RAM needed for this computation is 192 GB, corresponding to the memory available on one node (40 cores) on the DANTE platform, APC, France. Each iron line can be computed at once, simplifying the catalog construction to study the truncation of the disc outer parts.
Figure 4.7 shows that the optimal choice to minimize numerical noise in the flux in each bin is

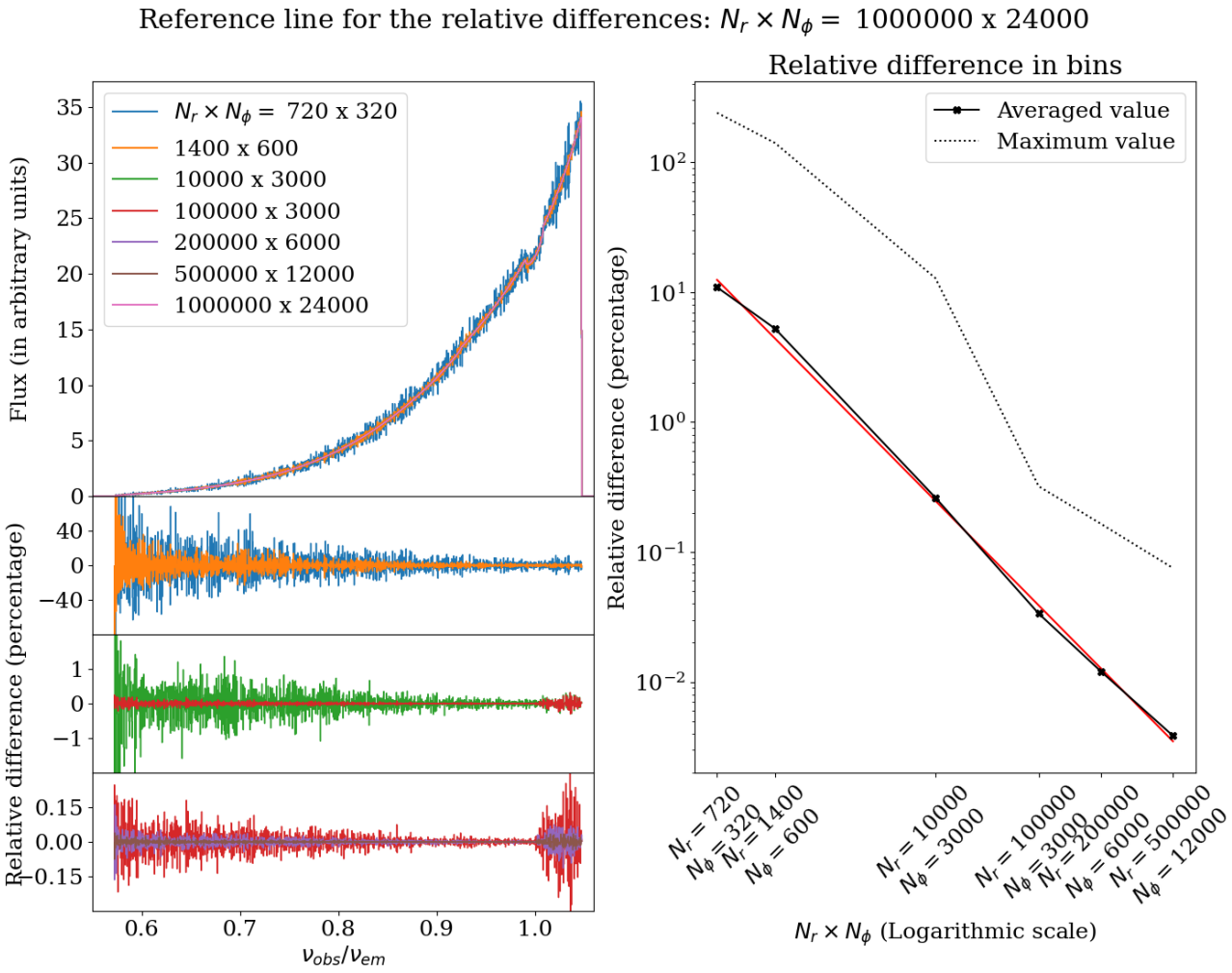

Figure 4.6: **Influence of the spatial resolution on the computation of the line profile.**
Line parameters are given in equations (4.25).
The upper left plot shows the iron line profile for different spatial resolutions. The three plots below indicate the relative difference of the flux in each bin compared to the line computed with the highest resolution.
The right panel shows the maximum and average relative difference values as a function of the logarithm of the total number of elementary cells. The red line is a linear regression of the average relative difference. $\log(<|\epsilon|>) = \alpha \log(N_r \times N_\phi) + \beta$, with $\alpha = -0.805$, $\beta = 5.41$.

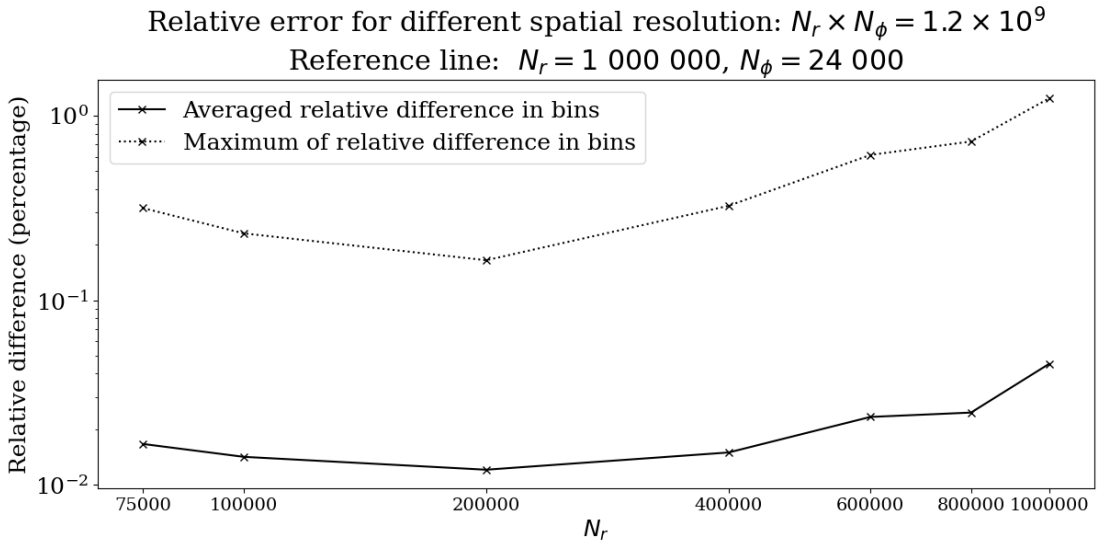

Figure 4.7: **Influence of the spatial resolution on the computation of the line profile for a constant number of total cells 1.2×10^9 corresponding to a RAM of 192 Gb for the calculation with the *binning* method.**
Line parameters are given in equation (4.25).

$N_r = 200\ 000$ and $N_\phi = 6\ 000$. Thus, this resolution will be used to compute the iron line catalog for the study of the impact of the truncation of the disc outer parts on the iron line profile.

For $N_r = 200\ 000$ and $N_\phi = 6\ 000$, the averaged numerical noise of about 0.01%. This numerical noise level is sufficiently low not to perturb the exploration of the potential signature of the MBH companion on the iron line profile. Indeed, the observational errors on the flux expected with instruments such as X-IFU are significantly higher (Barret et al. (2016), and see, e.g., Porter & Fukumura (2020), Barret & Cappi (2019)).

When examining the impact of truncating the disc outer regions, modifying the other iron line parameters is necessary since different parameter combinations can lead to indistinguishable iron line profiles. More specifically, the study of the impact of the outer edge radius, r_{max}, will consider different values of i_{obs} and h_s. As mentioned above (equation (4.24)), the numerical error is influenced by the variations of the observed frequency and contribution to the flux in each cell. Varying the parameters (h_s, i_{obs}) could raise the variation of these quantities and increase the numerical noise. Figure 4.8 shows that the variations of h_s do not significantly affect the numerical noise. On the other hand, increasing i_{obs} from 0° to 50° smoothly increases the numerical noise. The high value of the numerical noise for the iron line profile at $i_{obs} = 0°$ is due to the axisymmetry of the observed frequency and contribution to the flux. Thus, the numerical error is the same for each cell in the azimuthal direction at a fixed radius. Therefore, the final error is multiplied by the number of cells in the azimuthal direction.

Due to its need for high spatial resolution, the *binning* method is unsuitable for calculating the iron line profile emitted by the disc directly on the simulation outputs (the spatial resolution is $N_r = 720$, $N_\phi = 320$). However, the impact of the gravitational influence of the MBH companion on the iron line profiles computed using the *binning* method can still be explored. Indeed, the gravitational influence of the MBH companion truncates the outer parts of the disc, gives an elliptic shape to the disc, and creates a spiral wave in the disc. Each of these effects can be modeled with an analytic formula, allowing the study of their impact on the iron line profile with an accretion disc described by any spatial resolution. The influence of the accretion disc truncation on the iron line profile is presented in Chapter 5.

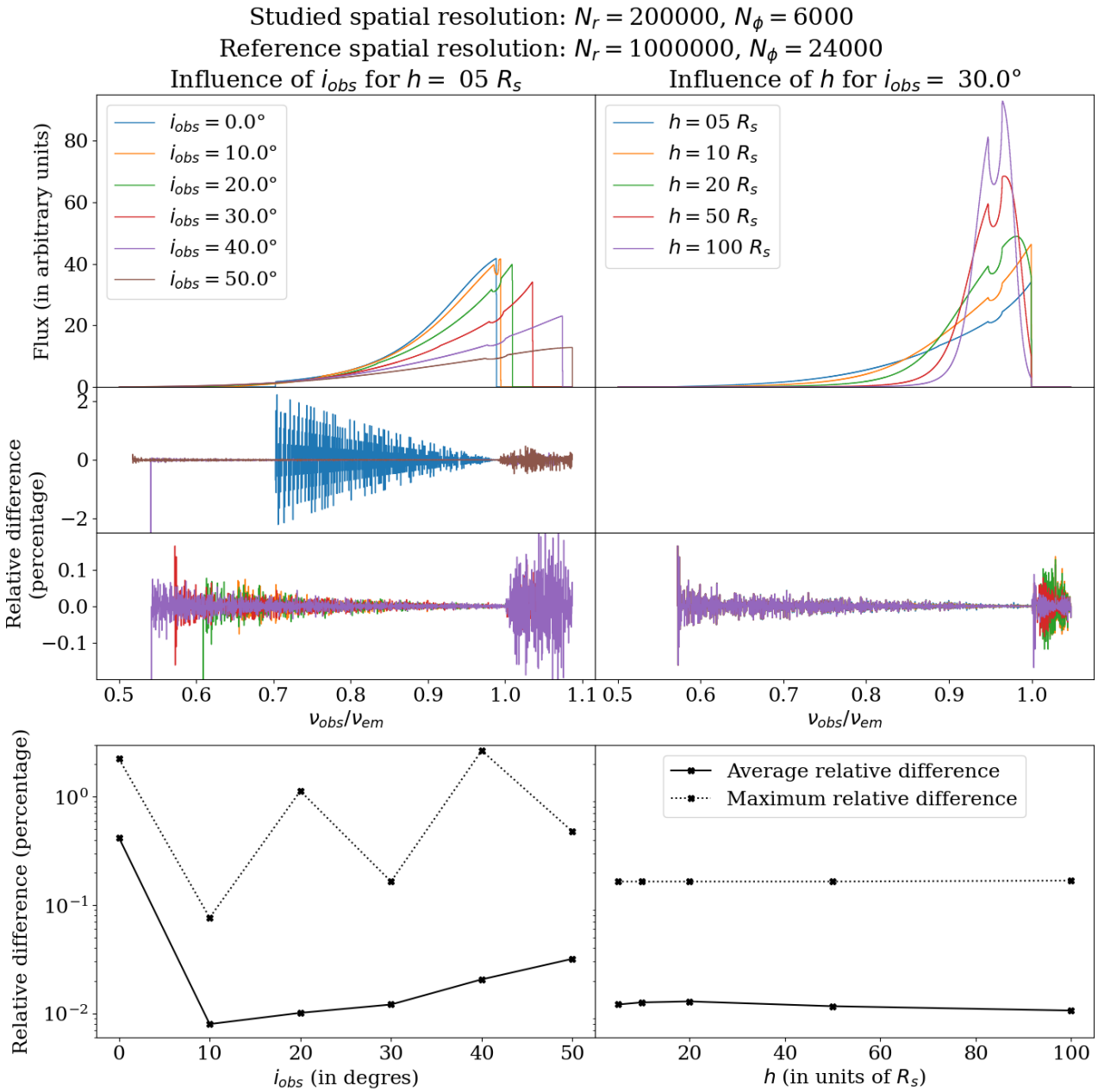

Figure 4.8: **Influence of i_{obs} and h_s on the numerical noise.**
Line parameters are given in equations (4.25). The left panels present the influence of i_{obs} while the right panels present the influence of h_s. The first line present the iron line profile. The second and third lines present the numerical noise as a function of frequency: the relative difference of the flux in each bin between the studied spatial resolution ($N_r = 200\ 000$, $N_\phi = 6\ 000$) and a reference high spatial resolution ($N_r = 1\ 000\ 000$, $N_\phi = 24\ 000$). The third line presents the influence of i_{obs} and h_s on the averaged and maximum value of the numerical noise.

The iron line profiles computed with the *binning* method can be compared to those presented in Hartnoll & Blackman (2002) to verify the numerical implementation. However, unexplained differences were found between the profiles in Hartnoll & Blackman (2002) and the results computed with the *binning* method (see section 4.3.1). Therefore, a second independent method to calculate the iron line flux was implemented to verify the results obtained with the *binning* method. This second method is detailed in the next section.

4.2.2 Second method to verify the results obtained with the *binning* method

The second method is different from the *binning* method in the way it computes the iron line flux given in the double integral in equation (4.1). Instead of dividing the accretion disc into cells, the locations of the disc where $\nu_{obs}(\vec{n}_{obs};\ r,\phi) = \tilde{\nu}$ are idenitified (see the curves in the left pannel of Figure 4.5). To calculate the final flux produced by the disc at frequency $\tilde{\nu}$, the second method integrates the contribution to the flux on the one-dimensional curve where the observed frequency equals $\nu_{obs}(\vec{n}_{obs};\ r,\phi) = \tilde{\nu}$. Unlike the *binning* method that produces a histogram, the second method generates a list of points $(\tilde{\nu}, F(\tilde{\nu}))$ as its output.

Mathematically, the spatial coordinates of each point in the disc are substituted in the integral by a new set of coordinates.

- The first coordinate is a parameter to move along the one-dimensional curves where the observed frequency remains constant. Writing $\mathcal{C}_{\nu_\star}$, the one-dimensional curve along which the observed frequency is equal to $\nu_\star$, and λ, the parameter to describe this one-dimensional curve, the set of integration for the first coordinate is

$$\mathcal{S}_{\nu_\star} = \{\lambda,\ \text{so that } \vec{x} = \vec{X}_{\nu_\star}(\lambda) \in \mathcal{C}_{\nu_\star}\}$$

  where $\vec{X}_{\nu_\star}$ are the coordinates of the points in the disc for which the observed frequency equals $\nu_\star$

- The second coordinate is the observed frequency, which varies continuously in the observed frequency range of photons emitted from the disc.

This substitution is described by the function Ψ defined by:

$$\begin{array}{rrcl} \Psi: &]\nu_{min};\nu_{max}[\times \mathcal{S}_\nu & \rightarrow & \mathcal{D} \\ & (\nu,\lambda) & \rightarrow & \Psi(\nu,\lambda) = \vec{X}_\nu(\lambda) \end{array} \tag{4.27}$$

where $\mathcal{D}$ is the spatial extension of the iron line emitting region.

With this coordinate substitution, the integral to compute the iron line flux is

$$\begin{aligned} F\left(\tilde{\nu}, \vec{n}_{obs}\right) = \int_{\nu\in]\nu_{min};\nu_{max}[} \int_{\lambda\in\mathcal{S}_\nu} [& \\ & \delta\left[\tilde{\nu} - \nu_{obs}(\vec{n}_{obs};\Psi(\nu,\lambda))\right]\ f(\vec{n}_{obs};\Psi(\nu,\lambda))\ \left|\det(\mathbb{J}(\Psi(\nu,\lambda))\right| \\ &]\, d\lambda d\nu \end{aligned} \tag{4.28}$$

where $|\det(\mathbb{J}(\Psi(\nu,\lambda))|$ is the absolute value of the Jacobian determinant for the function Ψ (equation (4.27)). It measures the change in the elementary area for the integration. f is the observed contribution to the flux (equation (4.20)).

Since $\nu_{obs}(\vec{n}_{obs};\Psi(\nu,\lambda)) = \nu$, the term with the Dirac delta distribution is independent of the coordinate λ and can be used to obtain the one-dimensional integral:

$$F\left(\tilde{\nu}, \vec{n}_{obs}\right) = \int_{\lambda\in\mathcal{S}_{\tilde{\nu}}} f(\vec{n}_{obs};\Psi(\tilde{\nu},\lambda))\ \left|\det(\mathbb{J}(\Psi(\tilde{\nu},\lambda))\right|\ d\lambda \tag{4.29}$$

Equation (4.29) is the one-dimensional integration of the observed flux contribution over the curve $\mathcal{C}_{\tilde{\nu}}$, where the observed frequency equals $\tilde{\nu}$.

The second method was implemented with two coordinate substitutions based on the radial and azimuthal coordinates. These substitutions apply to circular discs (with eventually a non-axisymmetric velocity field).

$$\begin{array}{rccc} \Psi_1: &]\nu_{min};\nu_{max}[\times]0;2\pi[& \rightarrow & \mathcal{D}=]r_{min};r_{max}[\times]0;2\pi[\\ & (\nu,\phi) & \rightarrow & (R(\nu,\phi),\phi) \end{array} \tag{4.30}$$

and

$$\begin{array}{rccc} \Psi_2: &]r_{min};r_{max}[\times]\nu_{min};\nu_{max}[& \rightarrow & \mathcal{D}=]r_{min};r_{max}[\times]0;2\pi[\\ & (r,\nu) & \rightarrow & (r,\Phi(r,\nu)) \end{array} \tag{4.31}$$

where the function R (respectively Φ) are defined so that the emitting points in the disc with polar coordinates $(R(\nu,\phi),\phi)$ (respectively $(r,\Phi(r,\nu))$) emits photons that are observed at infinity with the frequency $\nu_{obs}=\nu$.

With the first coordinate substitution Ψ_1 given in equation (4.30), the iron line flux given in equation (4.29) is

$$F(\tilde{\nu})=\int_{\phi\in]0;2\pi[}\sum_{i_{root}}\frac{f\left(\vec{n}_{obs};R_{\phi_\star,i_{root}}(\tilde{\nu}),\phi\right)}{\left|\frac{\partial\nu_{obs}}{\partial r}(\vec{n}_{obs};R_{\phi_\star,i_{root}}(\tilde{\nu}))\right|}d\phi \tag{4.32}$$

where the sum over i_{root} is the sum over the roots of

$$r\rightarrow\nu_{obs}(\vec{n}_{obs},r,\phi_\star)-\tilde{\nu} \tag{4.33}$$

for each value of $\phi_\star$, written $R_{\phi_\star,i_{root}}(\tilde{\nu})$.

With the second coordinate substitution Ψ_2 given in equation (4.31), the iron line flux given in equation (4.29) is

$$F(\tilde{\nu})=\int_{r\in]r_{min};r_{max}[}\sum_{i_{root}}\frac{f\left(\vec{n}_{obs};r,\Phi_{\phi_\star,i_{root}}(\tilde{\nu})\right)}{\left|\frac{\partial\nu_{obs}}{\partial\phi}(\vec{n}_{obs};r,\Phi_{\phi_\star,i_{root}}(\tilde{\nu}))\right|}dr \tag{4.34}$$

where the sum over i_{root} is the sum over the roots of

$$\phi\rightarrow\nu_{obs}(\vec{n}_{obs},r_\star,\phi)-\tilde{\nu} \tag{4.35}$$

for each value of $r_\star$, written $\Phi_{r_\star,i_{root}}(\tilde{\nu})$. The derivation of these equations can be found in Appendix D.

The computation of the iron line profile can be parallelized because the iron line flux values for different frequency values can be computed independently.

To compute equation (4.32) (or equation (4.34)) for each frequency value, the interval $]0;2\pi[$ (or the interval $]r_{min};r_{max}[$) is discretized linearly into N_ϕ points (or logarithmically into N_r points). For each value of $\phi\in]0;2\pi[$ (or $r\in]r_{min};r_{max}[$), the roots of the function defined in equation (4.33) (or in equation (4.35)) are found. This is the most critical step of the method since all the function zeros must be found. The value of the observed contribution to the flux at the root position is computed. The radial (or azimuthal) derivative of the observed frequency is calculated numerically:

$$\frac{\partial\nu_{obs}}{\partial r}(\vec{n}_{obs},r,\phi)=\frac{\nu_{obs}(\vec{n}_{obs},r+dr,\phi)-\nu_{obs}(\vec{n}_{obs},r-dr,\phi)}{2\times dr} \tag{4.36a}$$

$$\frac{\partial\nu_{obs}}{\partial\phi}(\vec{n}_{obs},r,\phi)=\frac{\nu_{obs}(\vec{n}_{obs},r,\phi+d\phi)-\nu_{obs}(\vec{n}_{obs},r,\phi-d\phi)}{2\times d\phi} \tag{4.36b}$$

The final contribution to the flux at the frequency $\tilde{\nu}$ is computed using the Simpson integration method implemented in the `Scipy` package of `Python` (Virtanen et al. 2020).

The values of dr, $d\phi$, N_r, and N_ϕ are initially chosen to be coherent with the spatial resolution used in the *binning* method.

$$dr \sim r_{min}\left[\left(\frac{r_{max}}{r_{min}}\right)^{1/N_r} - 1\right] \tag{4.37a}$$

$$d\phi = \frac{2\pi}{N_\phi} \tag{4.37b}$$

The second method is also used to compare the iron line profiles with those presented in Hartnoll & Blackman (2002). Both substitutions can be used to compute the iron line flux in the case of a Keplerian velocity field (Figure 4, lower left panel in Hartnoll & Blackman (2002)). However, when a spiral wave is present in the velocity field, the second substitution is more suitable as it makes it easier to search for the roots of the function defined in equation (4.35). The iron line parameters are the same as in Hartnoll & Blackman (2002)

$$r_{min} = 3\ R_s, \qquad r_{max} = 30\ R_s \tag{4.38a}$$

$$h_s = 5\ R_s, \qquad q = 3 \tag{4.38b}$$

Algorithm to find the roots of the observed frequency with the substitution defined in equation (4.30)

Figure 4.9 shows the observed frequency radial profiles for a Keplerian velocity field. It is either bijective on the typical radial size of the disc [3 R_s; 1 500 R_s] or can become so by restricting the radial intervals to at most two sub-intervals. The observed frequency is bijective if its radial derivative does not vanish on the interval [3 R_s; 1 500 R_s]. If the observed frequency radial derivative vanishes on the interval [3 R_s; 1 500 R_s], writing r_0 the cancellation radius, the observed frequency is bijective on [3 R_s; r_0] and [r_0; 1 500 R_s].

Thus, the search for the potential zeros of the function in equation (4.33) can easily be implemented numerically. First, the product between the observed frequency radial derivatives at $r_{min} = 3\ R_s$ and $r_{min} = 1\ 500\ R_s$ is computed:

$$\frac{\partial \nu_{obs}}{\partial r}(\vec{n}_{obs}; r_{min}, \phi_j) \times \frac{\partial \nu_{obs}}{\partial r}(\vec{n}_{obs}; r_{max}, \phi_j) \tag{4.39}$$

If the quantity defined in equation (4.39) is positive, the radial derivative does not vanish on the radial interval [3 R_s; 1 500 R_s]. Thus, the observed frequency is bijective, and there can be only one point on this interval where it matches the observer's fixed frequency. The product between the observed frequency at $r_{min} = 3\ R_s$ and $r_{min} = 1\ 500\ R_s$ is computed:

$$\nu_{obs}(\vec{n}_{obs}; r_{min}, \phi_j) \times \nu_{obs}(\vec{n}_{obs}; r_{max}, \phi_j) \tag{4.40}$$

If the quantity defined in equation (4.40) is positive, the function defined in equation (4.33) does not vanish. If it is negative, there is one zero, that standard numerical methods can find.

If the quantity defined in equation (4.39) is negative, the observed frequency radial derivative becomes zero once on the radial interval [3 R_s; 1 500 R_s]. The value of this radius (r_0) is determined via

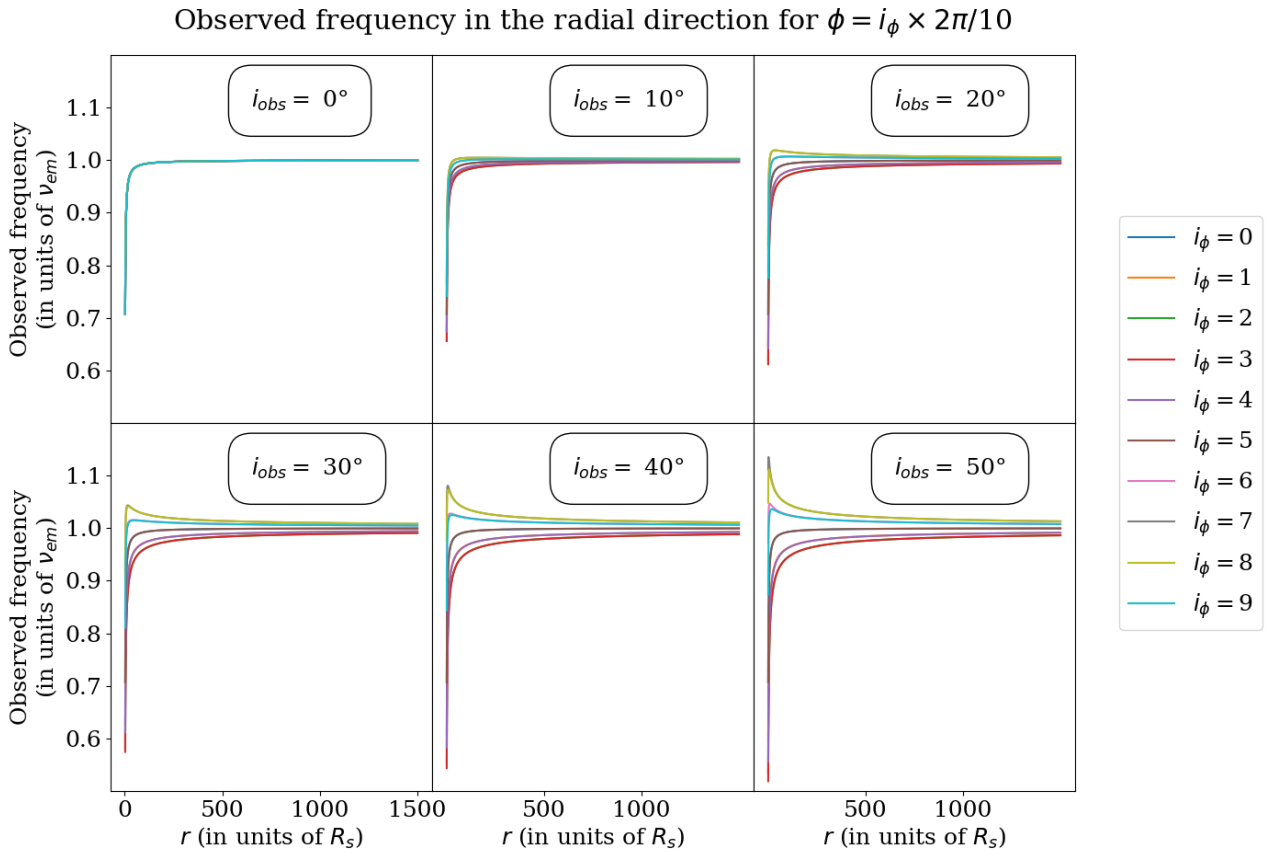

Figure 4.9: **Radial profiles of the observed frequency from each emitting point in the disc.**
The velocity field is Keplerian. Colors represent different values of the emitting point azimuthal angle ϕ_{em}. Each panel correspond to a different value of the inclination angle i_{obs}.

standard numerical methods. The observed frequency is bijective on the sub-intervals [3 R_s; r_0] and [r_0; 1 500 R_s]. In each sub-interval, at most, one point exists where the observed frequency equals the observer's fixed frequency. To find this point, the product in equation (4.40) is computed in both cases, replacing the limit of the higher or lower interval with r_0. If this product is negative, the usual numerical methods can be applied to find a function zero for the function in equation (4.33), which is restricted to the sub-interval.

To ensure a robust algorithm to find the zero of the function, I decided to use the Brent method (Virtanen et al. 2020) is used. This method combines

- the bisection method (which can be applied to monotonic functions that are known to change sign an odd number of times on the root searching interval, this method is robust but relatively slow)
- the secant method (which uses a finite-difference approximation of the Newton method)
- the inverse quadratic interpolation (which uses a quadratic interpolation to infer the inverse of the function to iterate towards the root)

Therefore, the Brent method can only be applied to functions that become zero an odd number of times on a given interval, but the method ensures convergence. It is used in the different sub-intervals so that the algorithm can determine the zero, one, or two roots of the function defined in equation (4.33).

Figure 4.10 compares the iron line profile obtained with this method to the *binning* method. The fluxes for the second method are computed using the frequency at the middle the energy bins used to calculate the fluxes with the *binning* method. This figure shows that the two methods are perfectly coherent. I will now present the impact of the numerical integration method and the number of point to discretize the angular direction on the resulting iron line profile.

Figure 4.11 briefly presents the influence of the integration method for different numbers of points to discretize the azimuthal set $[0; 2\pi]$. It shows that the numerical integration method should be at least of the second order: the trapezoid or the Simpson integration methods should be preferred. The Simpson method has a higher numerical cost than the trapezoid method. In section 4.3, I only compute the dozen iron line profiles presented in Hartnoll & Blackman (2002). Thus, I use the Simspon method. The balance between the numerical cost of both methods and the errors associated should be further investigate to compute more iron lines.

Figure 4.12 displays the influence of the number of points used to discretize the azimuthal set $[0; 2\pi]$. The absolute relative error is calculated with a reference line computed with $N_\phi = 1\ 000\ 000$. As the number of points increases, the relative difference with the reference line decreases, indicating the convergence of the method. Inside the frequency band [0.805 ν_{em}; 0.94 ν_{em}], the error rapidly converges to the value of 10^{-5}% for $N_\phi = 200\ 000$, while outside this frequency band, the convergence is much slower. I do not have a final explanation for this behavior.
However, the two boundaries of the frequency band 0.805 ν_{em} and 0.94 ν_{em} correspond respectively to a change in the slope of the iron line profile and the peak of the iron line profile. Moreover, they correspond to the frequencies for which the one-dimensional curves along which the observed frequency is constant hit the inner and outer edge of the disc (see the left panel of Figure 4.5). Between $\tilde{\nu} = 0.805\ \nu_{em}$ and $\tilde{\nu} = 0.94\ \nu_{em}$, these curves form a closed circle-like feature. For each value of the azimuthal angle, there is one and only one zero for the function defined in equation (4.33). I verified the numerical implementation to confirm that the cases when no root is found do not pollute the result. As the second method was developed to verify the consistency of the *binning* method results, I do not investigate this further.

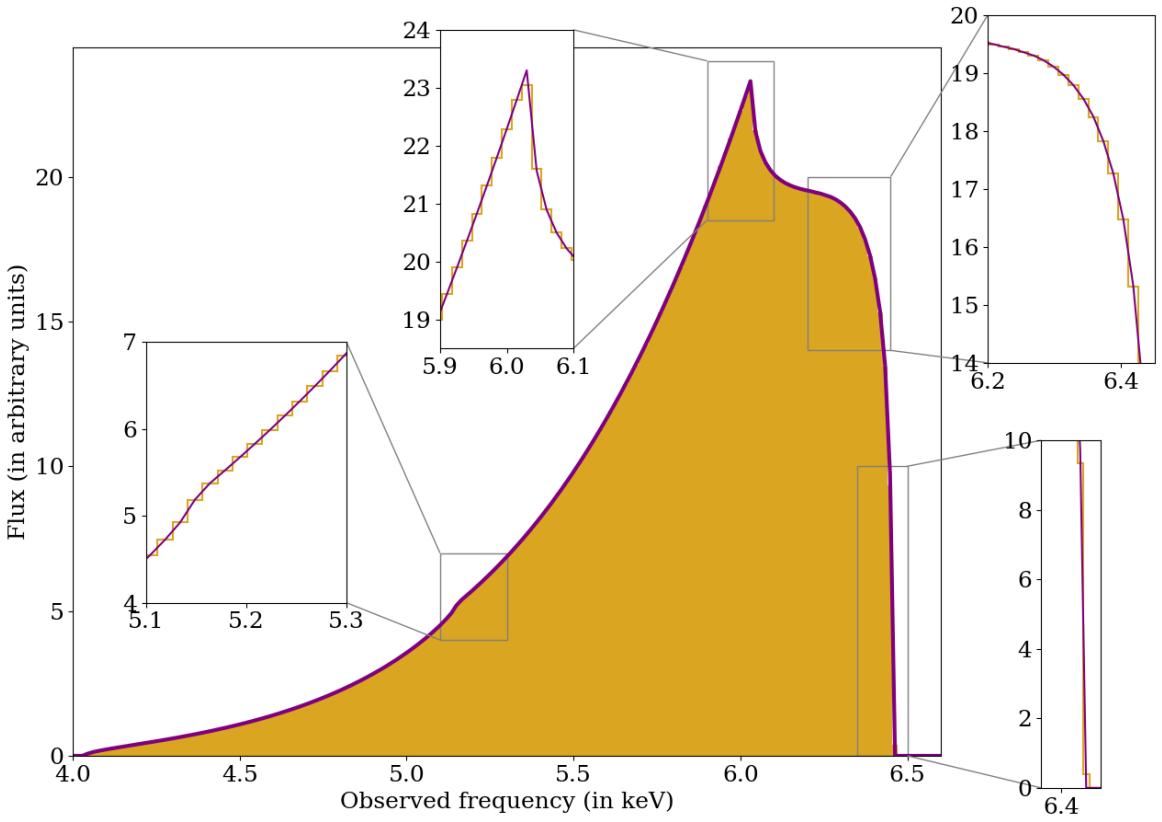

Figure 4.10: **Comparison between the binning and the second method using equation (4.32)**
$N_r = 200\ 000$ and $N_\phi = 6\ 000$ for the *binning* method. For the second method, $dr = 10^{-5}\ R_s$ (equation (4.37)), and N_ϕ is kept the same.
The iron line parameter are the same as the on in Figure 4 lower left panel in Hartnoll & Blackman (2002): see equation (4.38) and $i_{obs} = 15°$.

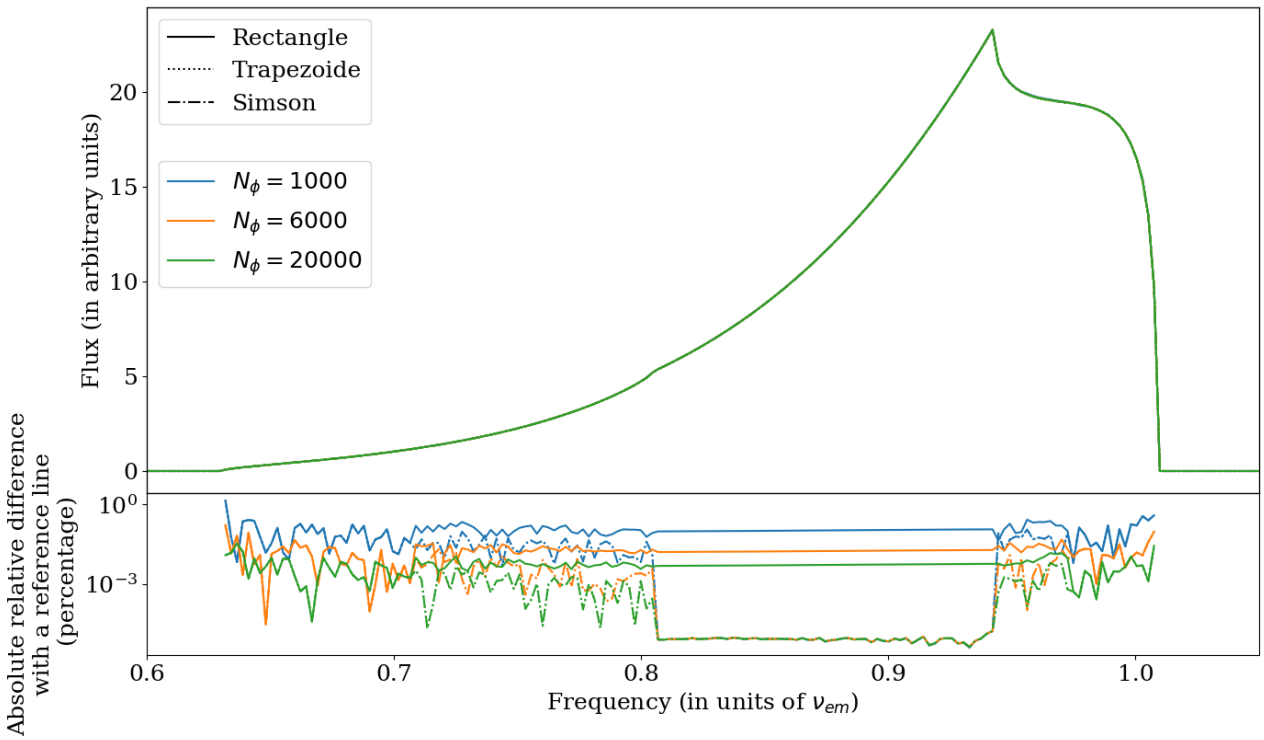

Figure 4.11: **Influence of the integration method used to compute the iron line flux with equation** (4.32)
The iron line parameters are the same as in Figure 4.10. For the reference line (lower panel): $N_\phi = 200\ 000$

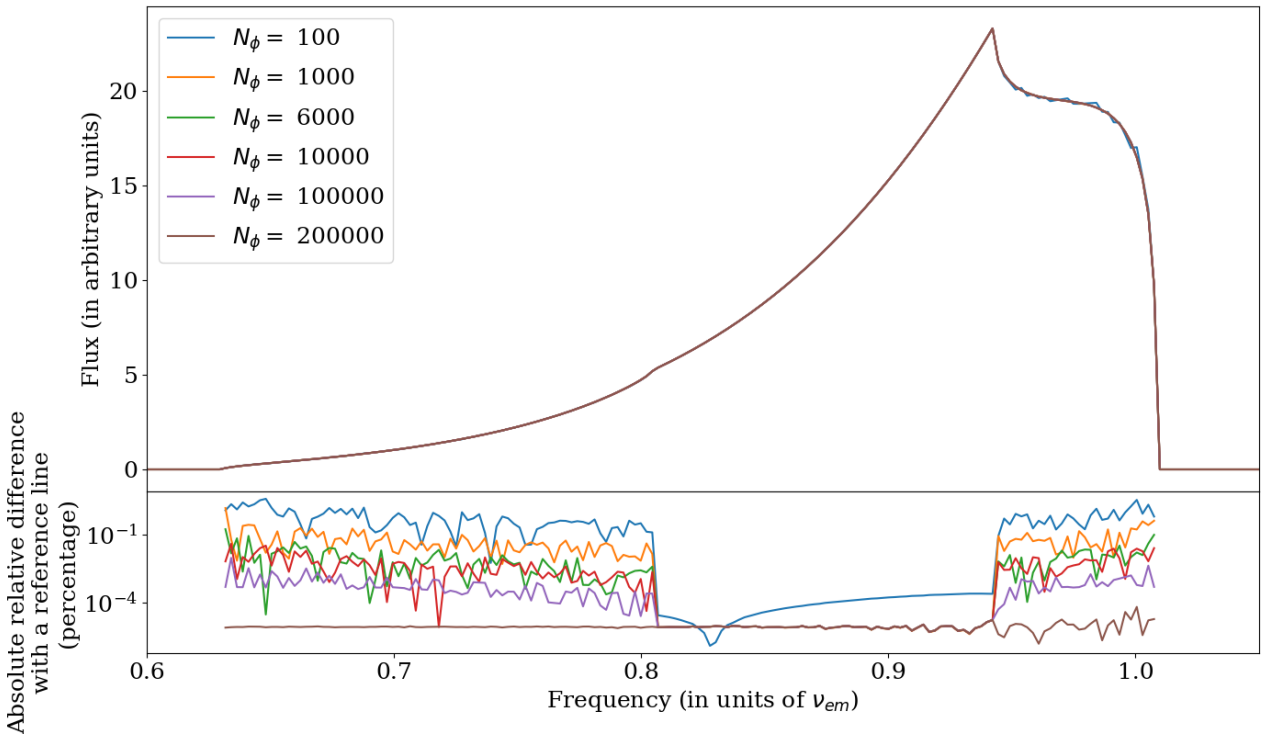

Figure 4.12: **Influence of the number of points used to discretize** $[0; 2\pi]$ **to compute the iron line flux with equation** (4.32)
The iron line parameters are the same as in Figure 4.10. For the reference line (lower panel): $N_\phi = 1\ 000\ 000$

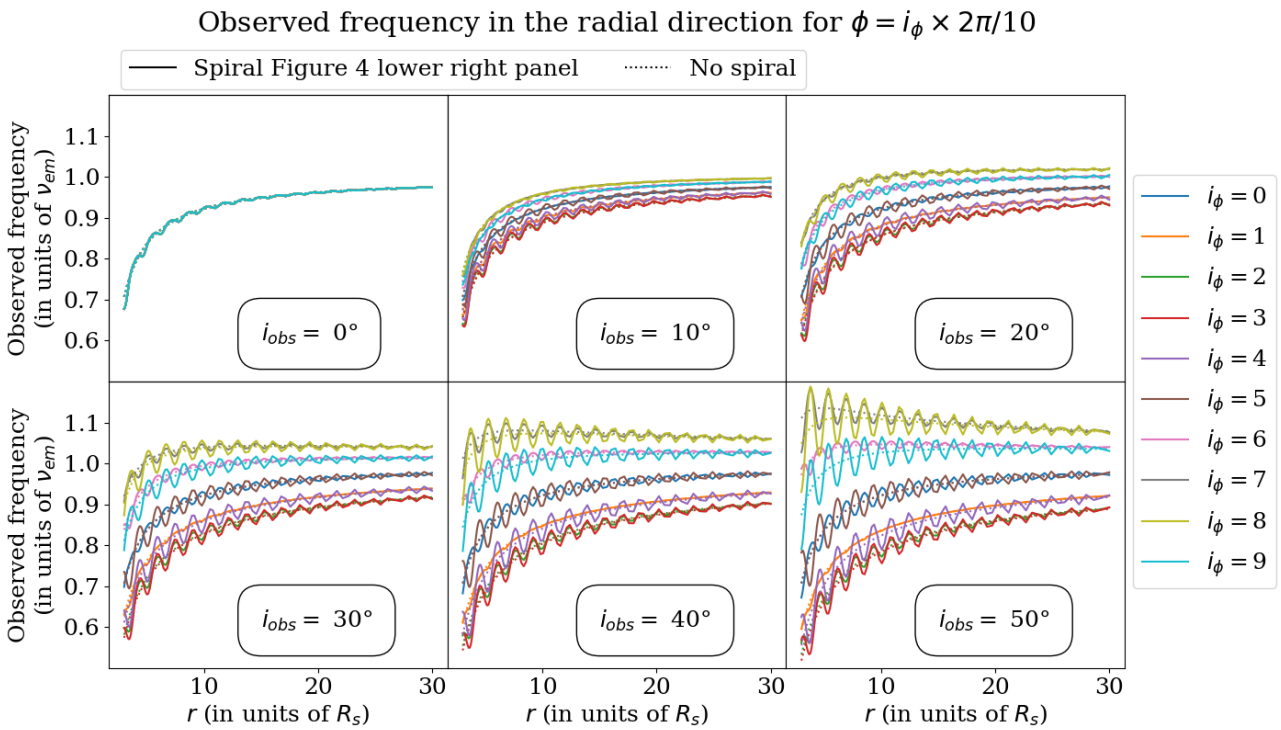

Figure 4.13: **Radial profiles of the observed frequency when a spiral is present in the disc velocity field**
The velocity field is given in equation 4.41 with $m = 1$, $\Delta = 0$, $\epsilon_r = \epsilon_\phi = 0.2$, $r_0 = 7.5\ Rs$, $k = 4\ R_s^{-1}$. (Corresponding to the spiral used in Hartnoll & Blackman (2002) - Figure 4, lower left panel)

Computation with the substitution defined in equation (4.35)

When a spiral is present in the disc velocity field, the radial profiles of the observed frequency are more irregular, and the algorithm presented above can not be used anymore. The number of zeros increases, and there is no easy way to anticipate it to implement the research with the Brent method.

In Hartnoll & Blackman (2002), the spiral waves are modeled with the velocity components:

$$\frac{u_r}{c} = \sqrt{\frac{R_s}{2r}}\ \epsilon_r\ e^{-(r-r_{min})/r_0}\ \cos(m\phi - kr) \tag{4.41a}$$

$$\frac{u_\phi}{c} = \sqrt{\frac{R_s}{2r}}\ \left[1 + \epsilon_\phi\ e^{-(r-r_{min})/r_0}\ \cos(m\phi - kr + \Delta)\right] \tag{4.41b}$$

In these equations, the first term $\sqrt{R_s/(2r)}$ represents a Keplerian velocity field in the azimuthal direction. The amplitudes of the spiral in the radial and azimuthal directions are denoted by ϵ_r and ϵ_ϕ, respectively. $\epsilon_r^2 + 2\epsilon_\phi^2 < 6$ to ensure that the velocity does not exceed the speed of light at the inner edge of the disc. The spiral waves in the models developed by Hartnoll & Blackman (2002) aim to simulate the impact of MHD instabilities on the iron line profile in non-self-gravitating discs. Therefore, the spiral waves are expected to be stronger in the inner parts of the disc (unlike the spiral wave due to the influence of the MBH companion presented in Chapter 3, that are stronger in the outer parts of the disc). The second term represents the fall-off of the wave amplitude in the radial direction from the inner parts of the disc, where r_0 determines the strength of this decrease. Δ represents the phase shift between the radial and azimuthal velocity components. The parameter k denotes the radial periodicity of the spiral, while m represents its azimuthal periodicity, which is equal to the number of arms in the spiral.

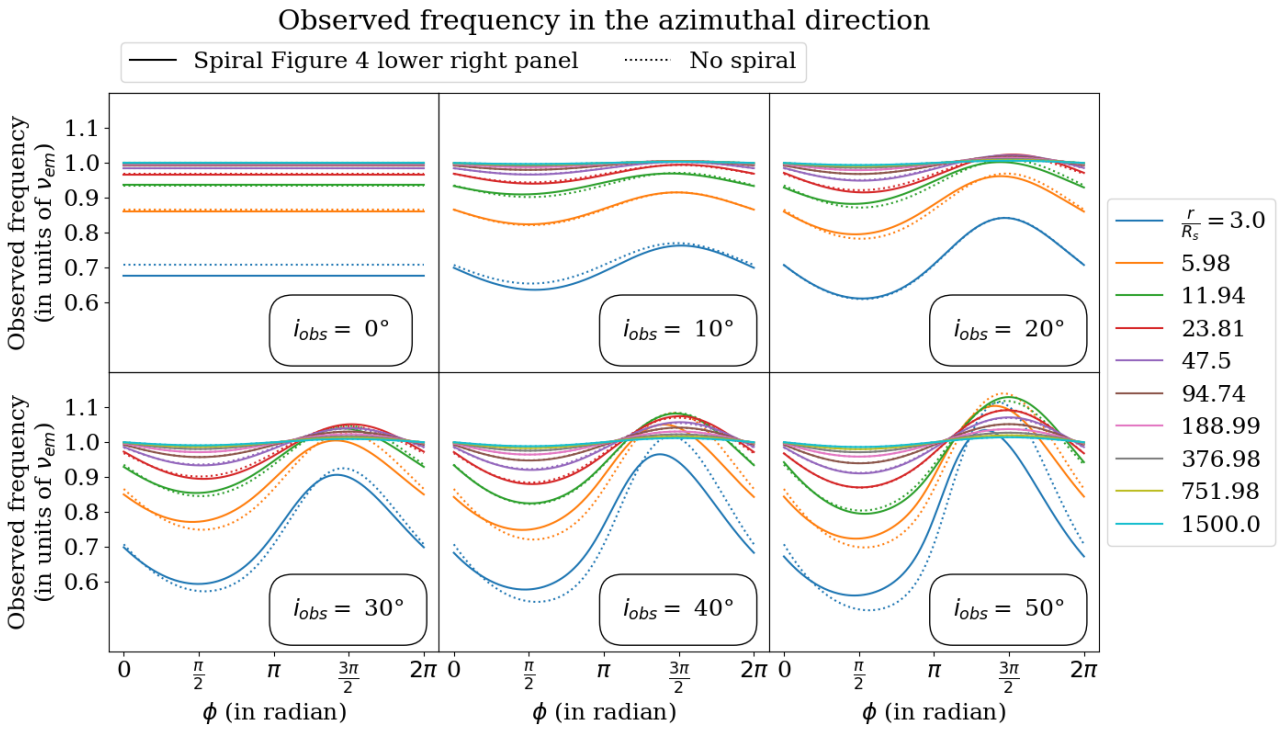

Figure 4.14: **Azimuthal profiles of the observed frequency when a spiral is present in the disc velocity field**
The velocity field is given in equation 4.41 with $m = 1$, $\Delta = 0$, $\epsilon_r = \epsilon_\phi = 0.2$, $r_0 = 7.5\ R_s$, $k = 4\ R_s^{-1}$. (Corresponding to the spiral used in Hartnoll & Blackman (2002) - Figure 4, lower left panel)

Figures 4.13 and 4.14 display the radial and azimuthal profiles of the observed frequency for one example of a velocity field with a spiral taken from the profiles presented in Hartnoll & Blackman (2002). The radial profiles exhibit oscillations that prevent using the algorithm presented earlier. However, the azimuthal profiles are more regular. Therefore, by substituting the coordinates with the transformation Ψ_2 (equation (4.31)) instead of Ψ_1 (equation (4.30)), an algorithm equivalent to the earlier one can be applied to determine the zero in the azimuthal direction instead of the radial direction.

This second method and the two coordinate substitutions were implemented to verify that the differences between my results and the iron line profiles presented in Hartnoll & Blackman (2002) are not due to numerical errors. Figure 4.10 shows that the binning method is consistent with the second method using the first coordinate substitution. Figure 4.15 aims to verify that the two coordinate substitutions are coherent and that the choice of one or the other cannot explain the differences with the iron line profiles presented in Hartnoll & Blackman (2002). Therefore, Figure 4.15 compares the iron line fluxes obtained with the two coordinate substitutions if there is no spiral wave in the disc velocity field (the only case for which the two methods can be used). The relative difference between both methods is compared to the flux uncertainty extracted from Hartnoll & Blackman (2002). The flux values were retrieved with the tool `Webplotdigitizer`[1]. A non-negligible error is associated with these flux values, displayed in green the lower panel of Figure 4.15.
The numerical parameters used to compute the line profiles presented in Figure 4.15 are

$$dr = 10^{-9}\ R_s, \qquad N_\phi = 24\ 000 \tag{4.42a}$$

$$d\phi = \frac{2\pi}{24\ 000}, \qquad N_r = 1\ 000\ 000 \tag{4.42b}$$

They were chosen to increase the precision of both methods when comparing them to ensure that the differences with the iron line profile in Hartnoll & Blackman (2002) are not due to a lack of precision.

[1] https://apps.automeris.io/wpd/

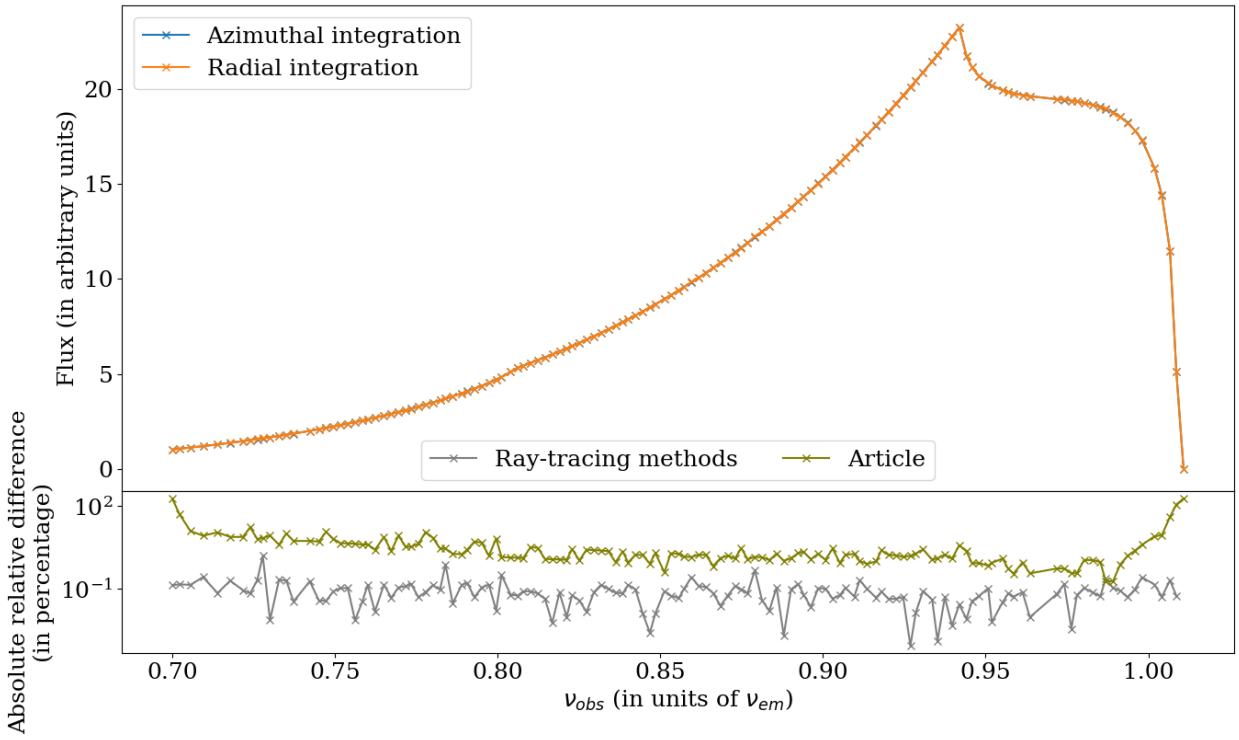

Figure 4.15: **Comparison of the iron line profiles obtained with the two substitutions Ψ_1 (equation (4.30)) and Ψ_2 (equation (4.31)) to implement the second method.**
The velocity field in the disc is Keplerian. The numerical parameters to compute the iron lines are given in equation (4.42). The relative difference between the two methods (in grey) is compared to the uncertainty of the flux retrieved from the article on the lower panel (in green).

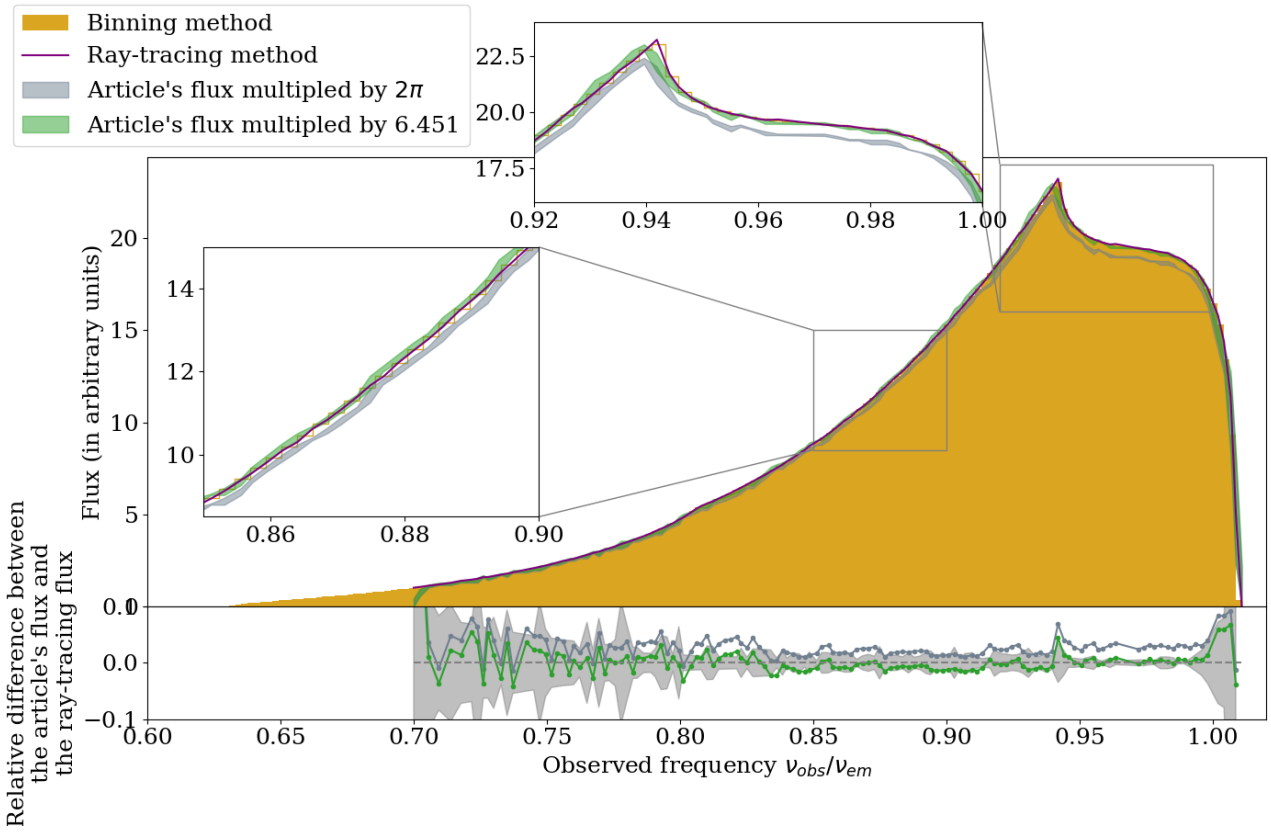

Figure 4.16: **Comparison of the iron line fluxes emitted by a Keplerian disc computed with the two methods implemented and the results presented in Hartnoll & Blackman (2002).**
A multiplicative constant normalizes fluxes from the article.
Fluxes computed with the *binning* method are computed with $N_r = 200\ 000$ and $N_\phi = 6\ 000$.
Fluxes computed with the second method and the first substitution (equation (4.30)) are computed with $N_\phi = 6\ 000$, $dr = 10^{-5}\ R_s$

It shows that the difference between both substitutions is below the uncertainty in the plot by Hartnoll & Blackman (2002). Therefore, the difference between our results and the article's fluxes cannot be attributed to the choice of one substitution over the other.
Hartnoll & Blackman (2002) do not specify whether they use a *binning* method or this second method. Due to the numerical resources at their time, it is more likely that they used this second method. However, the numerical implementation and the substitution they used are not detailed.

4.3 Comparison with the existing literature

4.3.1 Comparison with Hartnoll & Blackman (2002)

The iron line profiles computed with the two numerical methods can be compared with the iron line profiles presented in Hartnoll & Blackman (2002).

Comparison in the Keplerian case

Figure 4.16 compares the iron line profiles for a Keplerian velocity field. The figure compares the results obtained through the *binning* and the second methods and the fluxes retrieved from Hartnoll & Blackman (2002). At first glance, the fluxes acquired from our implementations and the iron line profiles depicted in Hartnoll & Blackman (2002) seem to differ by a constant factor of 2π. Hence, the fluxes from Hartnoll & Blackman (2002) are adjusted by this constant. However, Figure 4.16 demon-

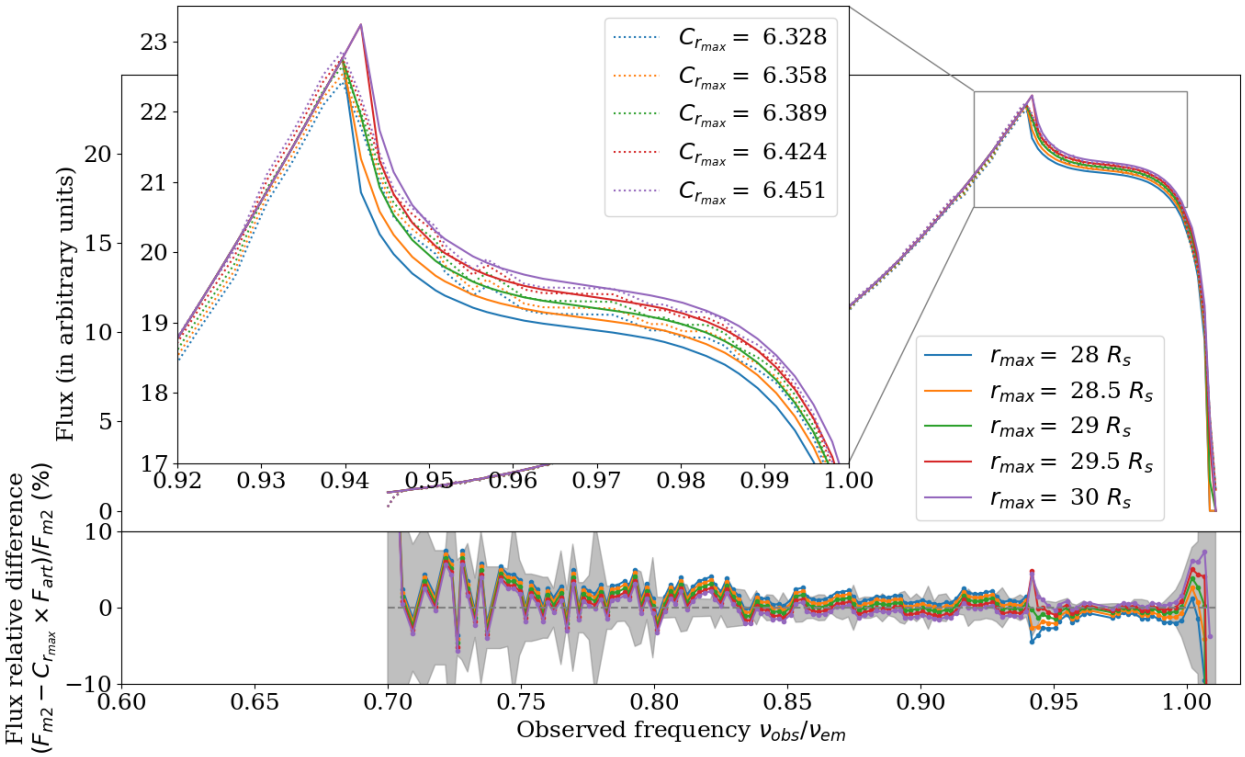

Figure 4.17: **Comparison between the second method and Hartnoll & Blackman (2002) in the Keplerian case: influence of the radius of the disc outer edge**
Numerical parameters are the same as in Figure 4.16.
The upper panel displays the flux computed with the second method (F_{m2}) for different values of r_{max} and the flux retrieved from Hartnoll & Blackman (2002) (F_{art}) multiplied by a constant $C_{r_{max}}$. $C_{r_{max}}$ minimizes the error between $F_{m2}(r_{max})$ and $C_{r_{max}} \times F_{art}$ on the frequency band $[0.74\nu_{em};\ \nu_{em}]$.
The lower panel displays the relative error between $F_{m2}(r_{max})$ and $C_{r_{max}} \times F_{art}$. The grey area corresponds to the uncertainty on the flux retrieved from Hartnoll & Blackman (2002).

strates that despite this re-normalization, the discrepancies between the fluxes from Figure Hartnoll & Blackman (2002) and the fluxes calculated using the two methods are more significant than the uncertainties related to the flux values obtained from Hartnoll & Blackman (2002). Therefore, we attempted a different normalization. Th constant is chosen to minimize the difference between the fluxe values. However, Figure 4.16 shows that the iron line peak remains slightly blue-shifted for the *binning* method and the second method.

Figure 4.17 presents different iron line profiles for different values of r_{max}. A multiplicative constant normalizes the iron line profiles to minimize the difference between the iron line fluxes computed with the second method and the fluxes from Hartnoll & Blackman (2002). The line obtained with $r_{max} = 29\ R_s$ seems closer to the normalized flux from Hartnoll & Blackman (2002). Therefore, we considered that the results obtained with our two methods to compute the iron line for the Keplerian disc are in good agreement with the results presented in Hartnoll & Blackman (2002). Only a question of normalization and exact value of r_{max} remains. In the following comparison, the fluxes from Hartnoll & Blackman (2002) will be multiplied by the constant obtained in the Keplerian case.

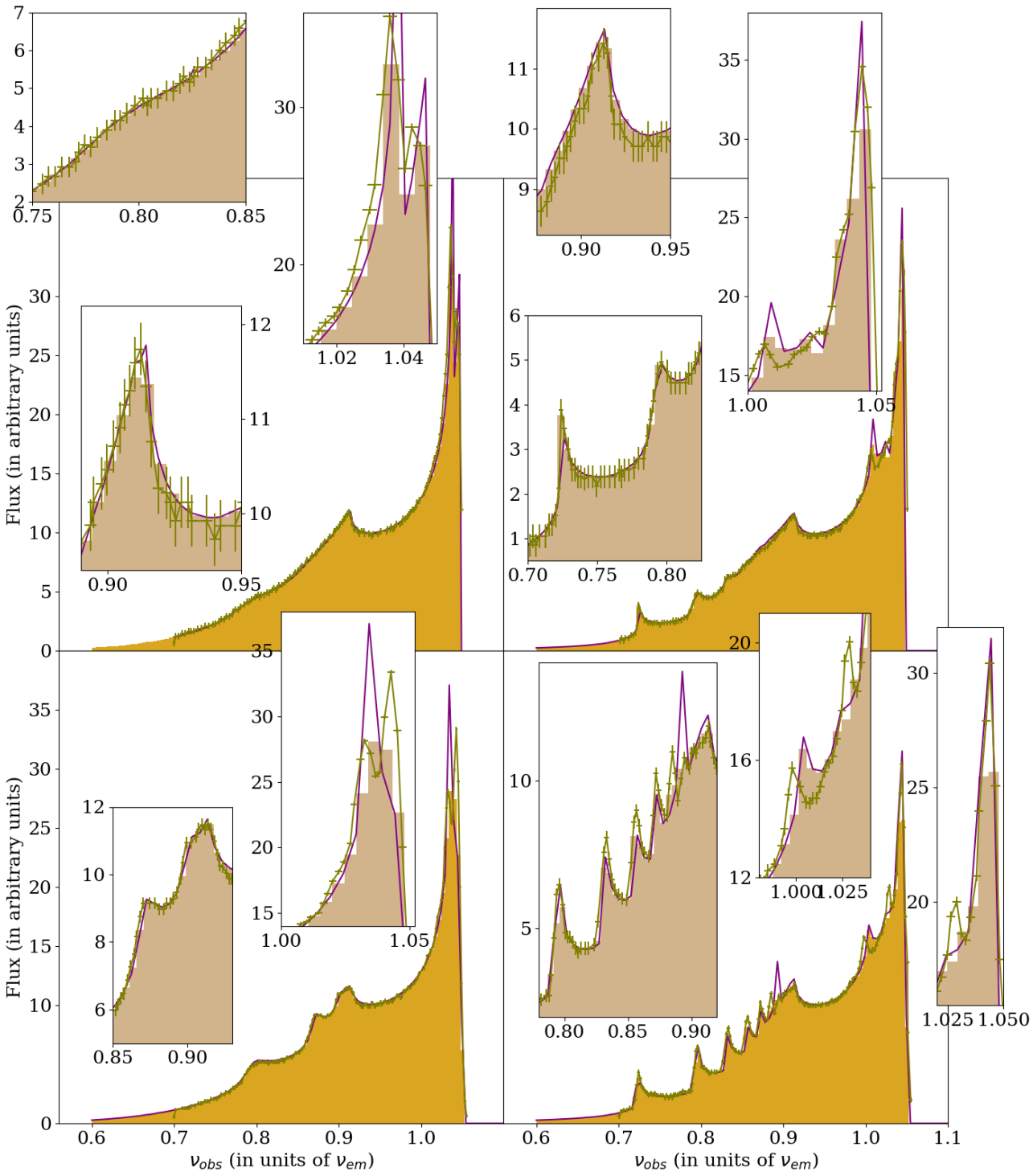

Figure 4.18: **Comparison between the iron line profiles in Figure 3 of Hartnoll & Blackman (2002) and the fluxes computed with our two methods**
The yellow/brown histograms are the *binning* method. The purple curves are the fluxes obtained with the second method. The green curves are the normalized profiles from Hartnoll & Blackman (2002) normalized by 6.451 (the constant obtained to minimize the flux difference in the Keplerian, see Figure 4.16). A spiral is present in the velocity field, defined in equation (4.41) with $m = 1$ and $\Delta = 0$
For the upper left panel: $\epsilon_r = \epsilon_\phi = 0.3$, $k = 0.8\ R_s^{-1}$, and $r_0 = 10\ R_s$.
For the upper right panel: $\epsilon_r = \epsilon_\phi = 0.3$, $k = 2.4\ R_s^{-1}$, and $r_0 = 10\ R_s$.
For the lower left panel: $\epsilon_r = \epsilon_\phi = 0.2$, $k = 0.8\ R_s^{-1}$, and $r_0 = 30\ R_s$.
For the lower right panel: $\epsilon_r = \epsilon_\phi = 0.2$, $k = 2.4\ R_s^{-1}$, and $r_0 = 30\ R_s$.

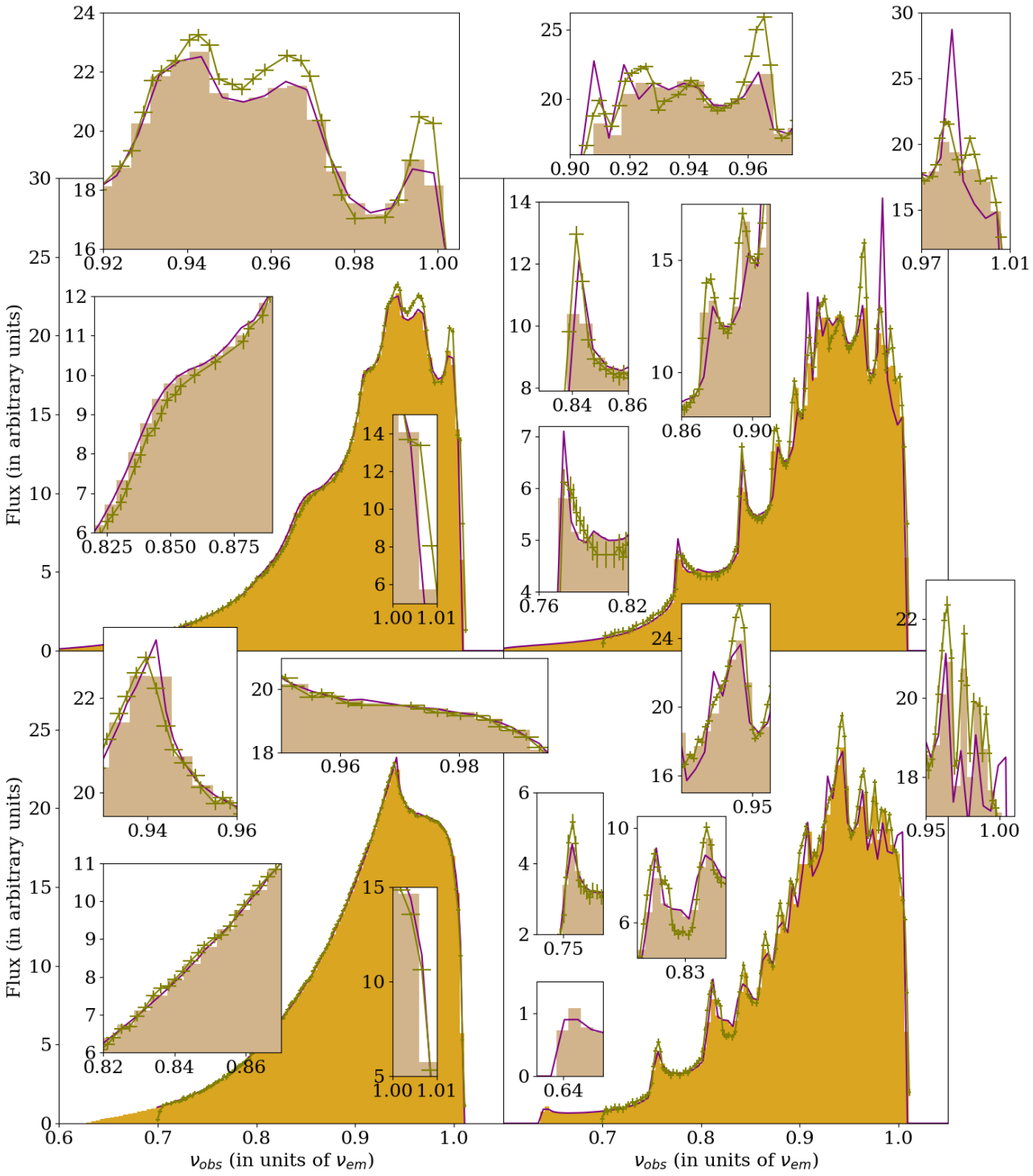

Figure 4.19: **Comparison between the iron line profiles in Figure 4 of Hartnoll & Blackman (2002) and the fluxes computed with our two methods**

The yellow/brown histograms are the *binning* method. The purple curves are the fluxes obtained with the second method. The green curves are the normalized profiles from Hartnoll & Blackman (2002) normalized by 6.451 (the constant obtained to minimize the flux difference in the Keplerian, see Figure 4.16). Except for the lower left panel, a spiral is present in the velocity field, defined in equation (4.41), with $m = 1$, $\Delta = 0$, $\epsilon_r = \epsilon_\phi = 0.2$, and $r_0 = 7.5\ R_s$ for the four plots. For the upper left panel: $k = 0.8\ R_s^{-1}$. For the upper right panel: $k = 2.4\ R_s^{-1}$. For the lower right panel: $k = 4.0\ R_s^{-1}$.

The lower left panel is the Keplerian disc without a spiral.

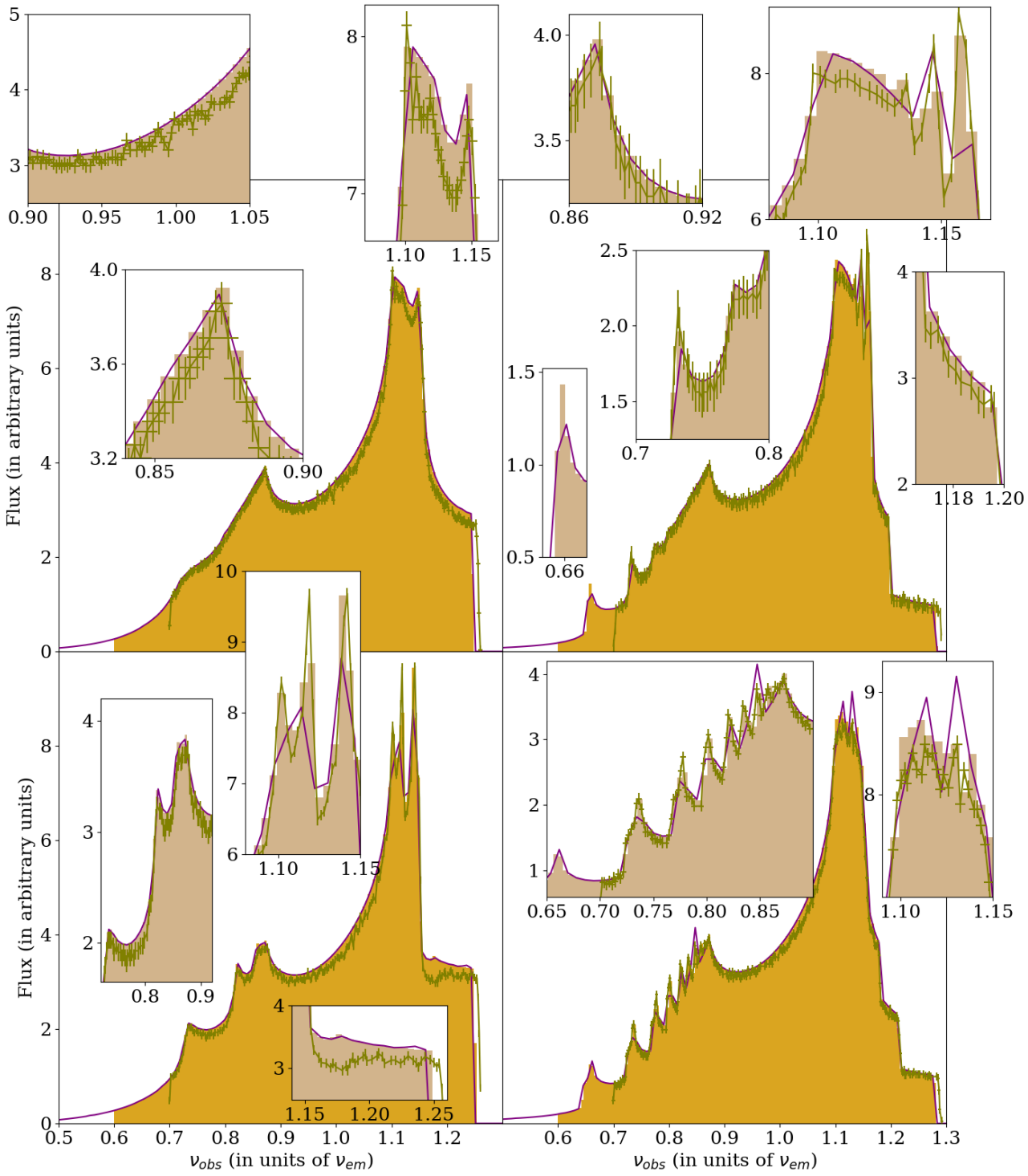

Figure 4.20: **Comparison between the iron line profiles in Figure 5 of Hartnoll & Blackman (2002) and the fluxes computed with our two methods**
The yellow/brown histograms are the *binning* method. The purple curves are the fluxes obtained with the second method. The green curves are the normalized profiles from Hartnoll & Blackman (2002) normalized by 6.451 (the constant obtained to minimize the flux difference in the Keplerian, see Figure 4.16). A spiral is present in the velocity field, defined in equation (4.41) with $m = 1$ and $\Delta = 0$
For the upper left panel: $\epsilon_r = \epsilon_\phi = 0.3$, $k = 0.8\ R_s^{-1}$, and $r_0 = 2.5\ R_s$.
For the upper right panel: $\epsilon_r = \epsilon_\phi = 0.3$, $k = 2.4\ R_s^{-1}$, and $r_0 = 2.5\ R_s$.
For the lower left panel: $\epsilon_r = \epsilon_\phi = 0.2$, $k = 0.8\ R_s^{-1}$, and $r_0 = 7.5\ R_s$.
For the lower right panel: $\epsilon_r = \epsilon_\phi = 0.2$, $k = 2.4\ R_s^{-1}$, and $r_0 = 7.5\ R_s$.

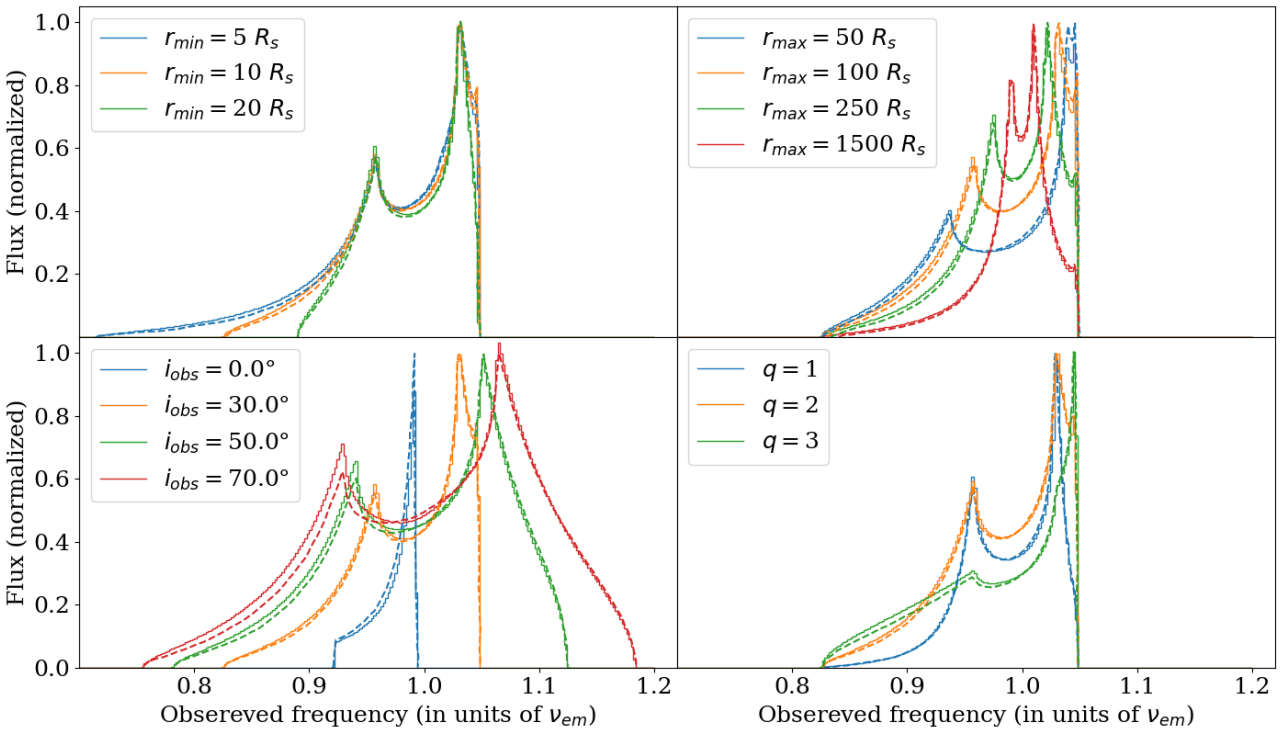

Figure 4.21: **Comparison of the iron line profiles in Fabian et al. (1989)**
The solid lines represent the iron line computed with the *binning* method, while the dotted lines are the flux values retrieved from Fabian et al. (1989). When not explicitely stated in each panel, the other iron line parameters are $r_{min} = 5\ R_s$, $r_{min} = 100\ R_s$, $i_{obs} = 30°$, and $q = 2$.

Comparison when a spiral exists in the velocity field

Figures 4.18, 4.19, and 4.20 compare the iron line profiles from Figures 3, 4, and 5 in Hartnoll & Blackman (2002) with the fluxes computed with the *binning* method and the second method (using the coordinate substitution Ψ_2 in equation (4.31).
For most frequencies, flux values are in good agreement. The different zooms in the Figures display some differences beyond the uncertainty associated with the flux values from the article. As shown in the Keplerian case, it might come from the normalization or a slightly different domain where to look for the points emitting photons at the given frequency.
Our two methods also show different results for a few frequencies. The spiral in the accretion disc steepens the variations of the observed frequency and contribution to the flux. Thus, for the *binning* method the error from the center to the edge of the cells in equations (4.24) raises. For the second method with the substituion Ψ_2 in equation (4.31), a higher number of points N_r is also required to describe more precisely the disc. This explains the differences between the resulting iron line profiles.

4.3.2 Comparison with Fabian et al. (1989)

Figure 4.21 compares the iron line profiles obtained with the *binning* method with those presented in Fabian et al. (1989). In their article, the geodesics are also computed using the Schwarzschild metric. However, they do not use the first-order expansion of the geodesic equations to compute the iron line photons emitted by the inner parts of the disc. In the inner parts of the disc ($r < 10\ R_s$), they integrate the complete geodesic equations while in the outer parts of the disc ($r > 10\ R_s$) they consider the photon trajectories as straight lines. Therefore, comparing the iron line profiles with the profiles presented in Fabian et al. (1989) enables to control the impact of the first-order expansion of the geodesic equations.

The iron line profiles in Fabian et al. (1989) are normalized so that the maximal flux value equals

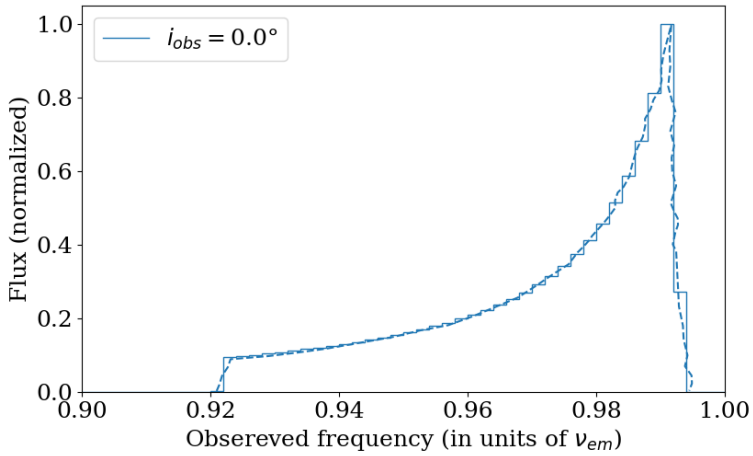

Figure 4.22: **Comparison of the iron line profiles in Fabian et al. (1989) for $i_{obs} = 0°$** The solid line represents the iron line computed with the *binning* method, while the dotted line is the flux values retrieved from Fabian et al. (1989). Unlike in Figure 4.21, the normalization of the iron line profile computed with the *binning* method is done with the maximal flux value.

one. Instead of normalizing the iron line profiles computed with the *binning* method by the maximal flux value, I normalize the fluxes obtained with the *binning* method by a constant that minimizes the flux differences with the values in Fabian et al. (1989) on the frequency interval $[0.95\ \nu_{em};\ 1.05\ \nu_{em}$. This interval corresponds to the less shifted frequencies emitted from the disc outer parts, where the approximation is more valid.

Fabian et al. (1989) computed the iron lines with a different radial profile of the specific intensity. Instead of equation (4.2), the emissivity of the disc is

$$I_{em} \propto \frac{1}{r^q} \tag{4.43}$$

This difference was considered to compute the iron line profiles in Figure 4.21.

The upper left panel displays the evolution of the iron line profiles with the value of the disc inner edge (r_{min}). It shows that the discrepancies between the two iron line profiles increases in the redshifted tail as r_{min} increases. Indeed, using the first-order expansion of the geodesic radial equation introduces more errors in the inner parts of the disc.

The upper right panel displays the evolution of the iron line profiles with the value of r_{max}. It shows that the discrepancies between the two iron line profiles increases as r_{max} decreases. As r_{max} decreases, the flux from the inner parts of the disc has more weight in the final value of the flux in each bin. This highlights that the first-order expansion can be used only to study differences that occur in the outer parts of the disc.

The lower left panel displays the influence of i_{obs} on the iron line profiles. It shows that the discrepancies between the two iron line profiles increases as i_{obs} increases from 30° to 70°. Indeed, the photons emitted behind the central BH suffer a higher light bending as i_{obs} increases. The computation of their geodesic parameters is less accurate with the first-order expansion of the geodesic equations. For the iron line profile observed face-on ($i_{obs} = 0°$), the larger differencies between the two iron line profiles are due to the method used to compute the constant to multiply the profile obtained with the *binning* method. If the iron line profile calculated with the *binning* method is divided by its maximal value, the two computations correspond perfectly, as shown in Figure 4.22.

The lower right panel displays the influence of parameter q in the equation of the disc's illumination by the corona (equation (4.43)). The differences between the two iron line profiles increases with q. Indeed, the emitted iron line flux is proportional to equation (4.43). The ratio of this term between the accretion disc inner and outer parts decreases as q increases. Thus, the differences due to the approximation in the inner parts of the disc has more weight in the final flux value in each bin as q rises.

4.4 Conclusions

This work investigates the impact of the MBH companion on the iron line profile. In Chapter 3, its three main dynamic effects on the accretion disc structure were discussed, which include the truncation of the disc outer edge, the elliptical shape of the disc, and the spiral wave in the disc. Analytic formulas can model each of these effects. Therefore, their impact on the iron line profile can be studied independently using the *binning* method. Chapter 5 explores the effects of the truncation of the disc outer parts on the iron line profile.
The *binning* method was preferred to the second method because there is no risk of missing some of the iron line emitting points in the disc. In the case of the emitter velocity field used in Hartnoll & Blackman (2002), the presented algorithm allows finding all the roots of $\nu_{obs}\left(\vec{x}\right) - \tilde{\nu}$. However, the two algorithms remain dependent on the velocity field in the disc.

It is challenging to compute the iron line profile directly from the `MPI-AMRVAC` simulation outputs using the *binning* method due to the higher spatial resolution required. Figure 4.23 displays the numerical noise of the iron line computation at the `MPI-AMRVAC` simulation spatial resolution. The right panel shows that for the numerical noise to be less than 1%, the spectral width of each bin should be above 30 eV.

The second method would also suffer from the relatively small spatial resolution of the `AMRVAC` simulation output. As the velocity field is only known in the middle of each cell, their values should be interpolated in two dimensions to find the one-dimensional curves where the observed frequency is constant and integrate the observed contribution of the flux along them.

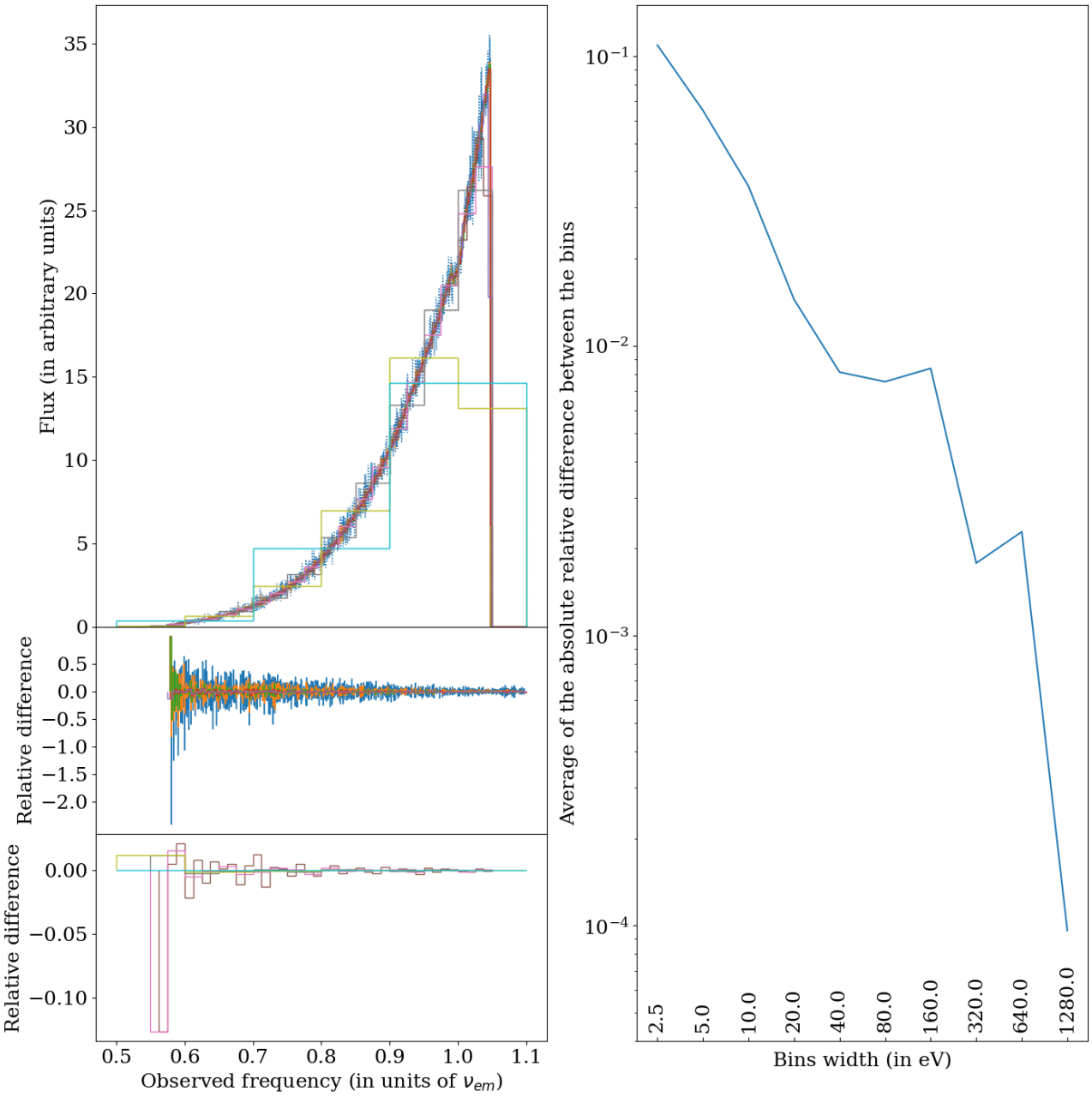

Figure 4.23: **Influence of the spectral resolution on the iron line at the spatial resolution of the hydrodynamical simulations with `AMRVAC`.** For all lines, $r_{min} = 3\ R_s$ to $r_{max} = 100\ R_s$, the velocity field in the disc is Keplerian ($u_r = 0$ and $u_\phi = \sqrt{\frac{GM}{r}}$), $i_{obs} = 30°$, $q = 3$, and $h_s = 5\ R_s$. Two spatial resolutions are considered: the spatial resolution of the hydrodynamical simulation with the code `AMRVAC` ($N_r = 720$ and $N_\phi = 320$) and a high spatial resolution ($N_r = 1\ 000\ 000$ and $N_\phi = 24\ 000$), which serves as a reference.
The iron line is computed between $\nu_{obs} = 0.5\nu_{em}$ and $\nu_{obs} = 1.1\nu_{em}$ using a linear binning N_{bin}.
The upper left panel shows the different iron line profiles. The two lower left panels show the relative difference between the fluxes computed with the two spatial resolutions in each bin. The right panel shows the evolution of the average relative difference between the bins, with the number of bins.

CHAPTER

5

LOOKING FOR MBH THROUGH ITS IMPACT ON THE IRON Kα EMISSION LINE

Chapters 2 and 3 were dedicated to the numerical simulations of the accretion disc surrounding a MBH. The simulations were conducted to study the gravitational influence of a MBH companion on the accretion disc during the initial stages of their coalescence. The simulations showed that compared to the accretion disc around an isolated AGN, the disc outer parts are truncated, a spiral wave can appear, and the overall shape of the disc becomes elliptical. This chapter explores whether the truncation of the disc impacts the iron line profile at a detectable level. If it does, it could be used as corroborating evidence, along with other EM wavelengths, to assert the presence of a MBH binary at the center of a galaxy.

The simulations presented in Chapter 3 show that the MBH companion's gravitational influence truncates the disc outer parts. Section 3.1 discusses the impact of the binary orbital parameter on the disc outer edge radius. The study does not consider the non-axisymmetric features of the disc, such as the ellipticity of the overall shape of the disc and spiral waves within the disc. The disc outer edge radius is defined using an azimuthal average of the density.
The outer edge radius scales with the orbital separation (D) for binary systems with equal mass ratio: $r_{max}/D \sim 0.3$. The influence of the mass ratio (q) on the ratio between the the outer edge radius (r_{max}) and the D was given in equation (3.1):

$$\frac{r_{max}}{D} = -0.18\ q^{0.044}\ \log\left[0.019\ q + 6.8 \times 10^{-6}\right]$$

The disc outer edge gets truncated within a few orbital periods, a short timescale compared to the orbital evolution timescale of a MBH binary.
A study by Fabian Casse and Peggy Varniere explores the impact of disc truncation on its thermal emission, investigating whether the missing emission from the outer parts of the disc can be detected in the IR. It will be published in a companion article to the article on numerical simulations and the impact of the binary orbital parameters on the disc outer edge radius and the ellipticity of the disc (see appendix A). This chapter presents how disc truncation can affect the iron line profile at a detectable level.

5.1 Fixed and variable parameters of the study

Iron line parameters, such as the inclination angle (i_{obs}), vary from one system to another. Some other parameters, such as the inner radius of the iron line region (r_{min}) or the distance between the

corona and the central BH in the Lamppost model (h_s), are either unknown or inherently variable between systems or with time. Furthermore, iron line profiles obtained with different sets of iron line parameters can be degenerated. Therefore, studying the truncation of the disc while varying the other iron line parameters is essential.

This study assumes that the iron line emitting region extends from the inner to outer edges of the accretion disc, written r_{min} and r_{max}.
r_{min} will be kept constant. As highlighted in the comparison of the iron line profiles with the study by Fabian et al. (1989), using the approximation of Hartnoll & Blackman (2000, 2001, 2002) to solve the geodesic equation by a first-order expansion prevents describing correctly the photons emitted in the inner parts of the disc. Therefore, this study will not consider the influence of r_{min}: it will remain at the ISCO around a Schwarzschild BH $r_{min} = 3\ R_s$.
The disc outer radius will vary between $r_{max} = 200\ R_s$ and $r_{max} = 1\ 500\ R_s$ in this study to explore the impact of the truncation of its outer parts.
First, the numerical simulations presented in Chapters 2 and 3 were designed to study MBH binary in the first stages of their merger, when their orbital evolution is slow compared to their orbital period. Therefore, the orbital separation must be above $\sim 100 - 200\ R_s$. Furthermore, the comparison of the iron line profiles obtained with the first order expansion to solve the geodesic equations with a first-order expansion (Hartnoll & Blackman (2000, 2001, 2002)) and the profiles presented by Fabian et al. (1989) highlighted that the disc outer parts must remain large. Otherwise, it would enforce the weight of the contribution to the flux emitted by the inner parts of the disc in the line profiles, which are not very well described when using the first order expansion of the geodesic equations.
In Chapter 2, it was explained that measuring the size of AGN discs using EM observations is still an active area of research. The various theoretical criteria converge around a value of 10^{-2} pc $= 3{\times}10^{16}$ cm (see Lobban & King (2022) using Collin & Huré (2001), or Hawkins (2007) using Goodman (2003) and Lyubarskii (1997)). For a central MBH mass of $10^8 M_\odot$, this is roughly equivalent to $\sim 1\ 100\ R_s$. Lobban & King (2022) found a light echo lasting up to 12 light days, also corresponding to approximately $\sim 1\ 100\ R_s$ for a central MBH mass of $10^8 M_\odot$. Therefore, we will study the impact of the value of r_{max} below $1\ 500\ R_s$.

The specific intensity of the emitted iron line at the outer layers of the disc was assumed to be proportional to the flux received from the corona (see section 4.1.1). $q = 3$ in equation (4.2) describes a flux proportional to the distance between the corona and the emitting point in the disc and the impinging angle of hard X-ray photons. As highlighted in Figure 5.2, the value h_s impacts the iron line profile. Therefore, it will vary in this study between 5 and 100 R_s. The minimal value is consistent with the observational study by Ursini et al. (2020): the point source-corona must be above 5 R_g for a non-spinning BH.

Finally, i_{obs} will vary between $= 0°$ and $50°$. As explained in Figure 4.4 and highlighted in the comparison with the iron line profiles presented by Fabian et al. (1989), the approximation used to derive the geodesic parameters cannot describe the geodesics that suffer high deflection by the central BH. Therefore, it limits the i_{obs} values that can be studied.

This study only focuses on disc truncation, ignoring other effects of the MBH companion's gravitational influence on the disc structure. Therefore, the velocity field in the disc is kept simple and follows Kepler laws.

To summarize, the iron line parameters considered in this study are

$$u_r = 0, \quad u_\phi = \sqrt{\frac{GM}{r}} \tag{5.1a}$$

$$r_{min} = 3\ R_s \tag{5.1b}$$

$$q = 3 \tag{5.1c}$$

$$r_{max} \in [200\ R_s;\ 1\ 500\ R_s] \tag{5.1d}$$

$$i_{obs} \in [0°;\ 50°] \tag{5.1e}$$

$$h_s \in [5\ R_s;\ 100\ R_s] \tag{5.1f}$$

As explained in the presentation of the *binning* method, the spatial resolution used to divide the accretion disc into elementary cells is fixed by the spectral resolution. The spatial and spectral resolution that will be used in this study are

$$N_r = 200\ 000 \tag{5.2a}$$

$$N_\phi = 6\ 000 \tag{5.2b}$$

$$\nu_{min} = 0.5\ \nu_{em} = 3.2\ \text{keV} \tag{5.2c}$$

$$\nu_{max} = 1.2\ \nu_{em} = 7.68\ \text{keV} \tag{5.2d}$$

$$(\Delta\nu)_{bin} = 7\ \text{eV} \tag{5.2e}$$

As this study aims to explore the MBH companion that could be detected in X-ray observations, the chosen spectral resolution is of the order of capabilities by X-IFU onboard the satellite Athena (the expected spectral resolution before the design-to-cost exercise was 2.5 eV, Barret et al. (2016)).
Studying the truncation of the disc outer parts will require the computation of an extensive catalog of profiles. Therefore, as mentioned in the presentation of the *binning* method, an optimized choice of spatial resolution is defined by equations (5.2a) and (5.2b).

5.2 Impact of the outer edge radius on the iron line

Figure 5.1 displays the influence of the disc outer radius on the iron line profile. The gravitational redshift due to the central BH and the frequency shift due to the semi-relativistic effect decrease towards the outer parts of the disc. Therefore, the outer edge radius shapes the iron line profile only at frequencies close to the emitted frequency. Removing iron line emitting material in the outer parts of the disc results in a more prominent trough on a larger frequency band around the emitted frequency. However, the trough is not centered on the emitted frequency. This is because while the semi-relativistic Doppler effect on the iron line profile is symmetric, the central BH GR effects only redshift photons.

When $r_{max} < 1\ 500\ R_s$, the iron line flux drops within a spectral band around the emitted frequency. This spectral feature can be characterized by 1) the spectral range where the two fluxes differ and 2) the difference in the flux values. The spectral interval where the fluxes differ from the untruncated case is

$$I_{h_s,i_{obs}}(r_{max}) = \left[\nu^{min}_{h_s,i_{obs}}(r_{max});\ \nu^{max}_{h_s,i_{obs}}(r_{max})\right] \tag{5.3}$$

The relative difference of the iron line fluxes within this spectral band $I = I_{h_s,i_{obs}}(r_{max})$ is

$$\frac{F_I(r_{max} = 1\ 500\ R_s) - F_I(r_{max})}{F_I(r_{max} = 1\ 500\ R_s)} \tag{5.4}$$

It is easier to determine the value of r_{max} when the difference in the line profile occurs over a wider spectral band, and the flux values are more dissimilar.

i_{obs} and h_s strongly impact the iron line profile, as shown in Figure 5.2.

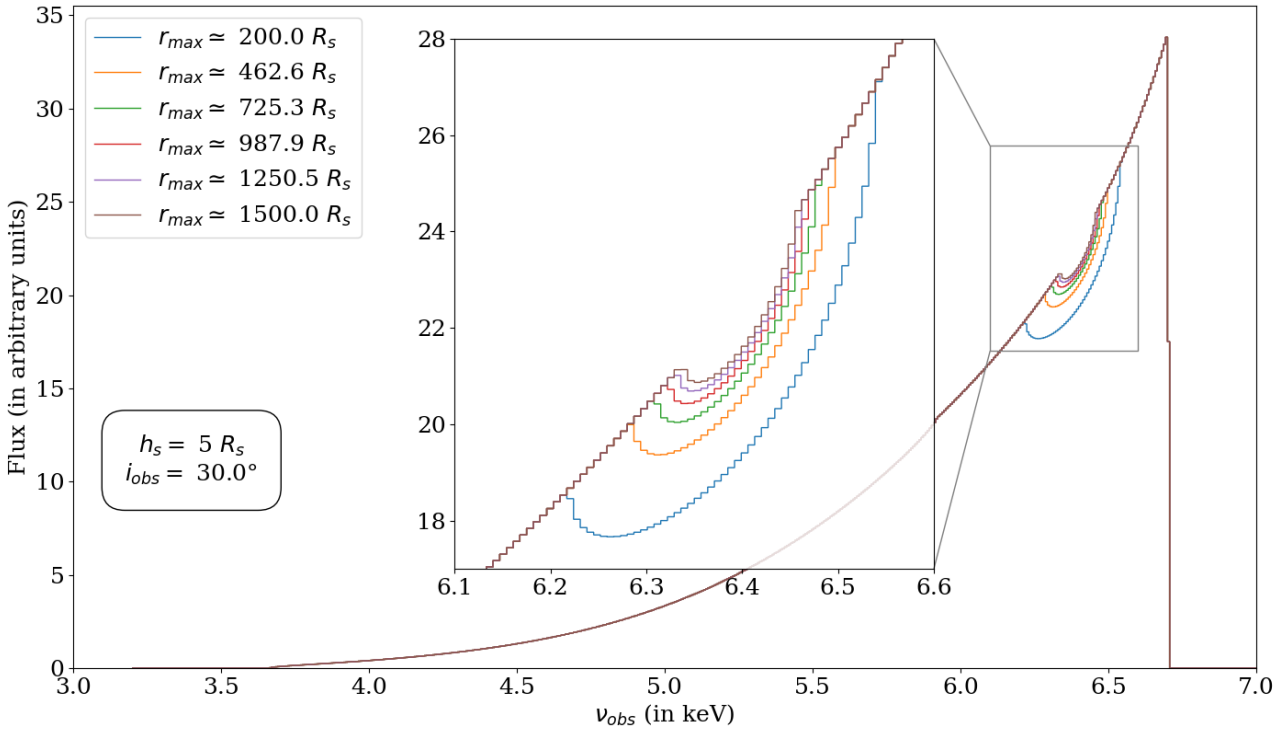

Figure 5.1: **Influence of r_{max} on the iron line profile.**
Parameters of the line are summarized in equations 5.1 and 5.2.

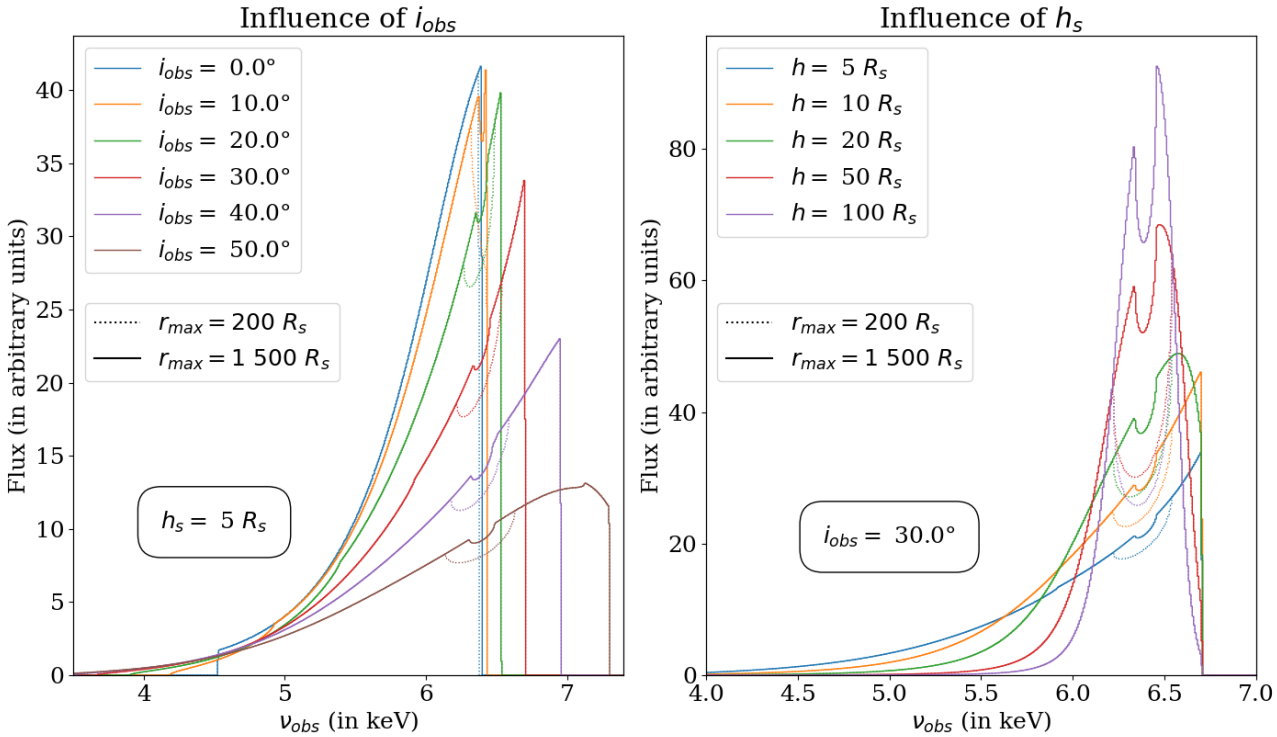

Figure 5.2: **Influence of (i_{obs}, h_s) on the iron line profile.**
Parameters of the line are summarized in equations 5.1 and 5.2.

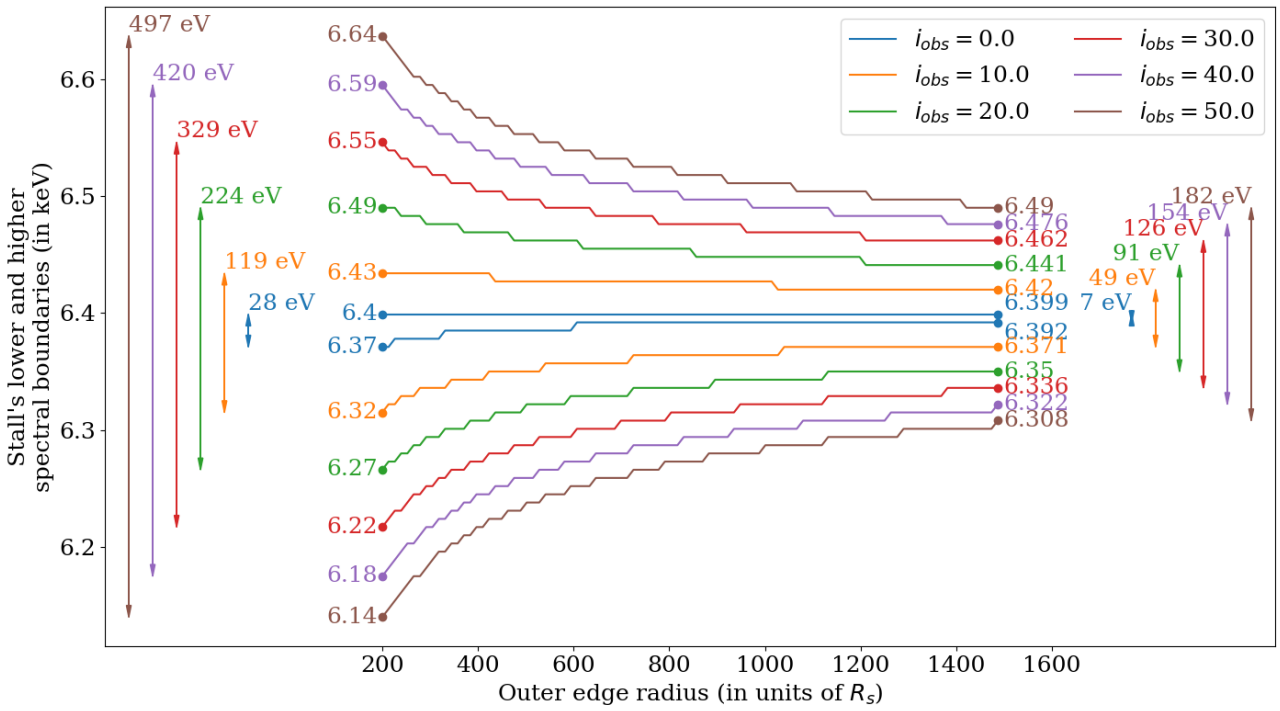

Figure 5.3: **Evolution of the spectral extent of the flux diminution due to the disc truncation (equation (5.5)): influence of i_{obs}**
Each color represents a different value of i_{obs}. Two curves are plotted: the two limits of the spectral interval where the flux differs. The plot shows the evolution of these values with r_{max}. Their spectral extents for $r_{max} = 200\ R_s$ (resp. $r_{max} = 1\ 500\ R_s$) are plotted on the left (resp. on the right).

Evolution of the spectral extent of the flux diminution due to the disc truncation (equation (5.3)): influence of the inclination angle

The value of h_s does not impact the observed frequency of photons emitted by each point in the disc. Therefore, the spatial extent of the flux diminution due to the disc truncation only depends on $(r_{max},\ i_{obs})$. The notations in equation (5.3) are

$$I_{i_{obs}}(r_{max}) = \left[\nu^{min}_{i_{obs}}(r_{max});\ \nu^{max}_{i_{obs}}(r_{max})\right] \tag{5.5}$$

The left panel in Figure 5.2 shows that as the value of i_{obs} increases, the iron line's red wing extends to lower frequencies and the blue wing to higher frequencies. This is due to the semi-relativistic Doppler effect. As the value of i_{obs} increases, the angle between the direction of emission of photons and the velocity of the emitters decreases. Therefore, the photons emitted in the disc moving towards the observer are more blue-shifted, and the ones emitted in the disc moving outwards from the observer are more red-shifted.

Figure 5.3 illustrates the evolution of equation (5.5) with r_{max} for different values of i_{obs}. As i_{obs} increases and r_{max} decreases, the spectral extent grows, making detecting disc truncation easier.
However, if the spectral extent is essential to resolve the spectral bands where the flux varies, the variation of the flux also constrains the potential detection. If it is too low, observations will not be able to distinguish between several r_{max} values.
Furthermore, Figure 5.3 shows that the intervals are degenerated, highlighting the importance of varying the different iron line parameters.

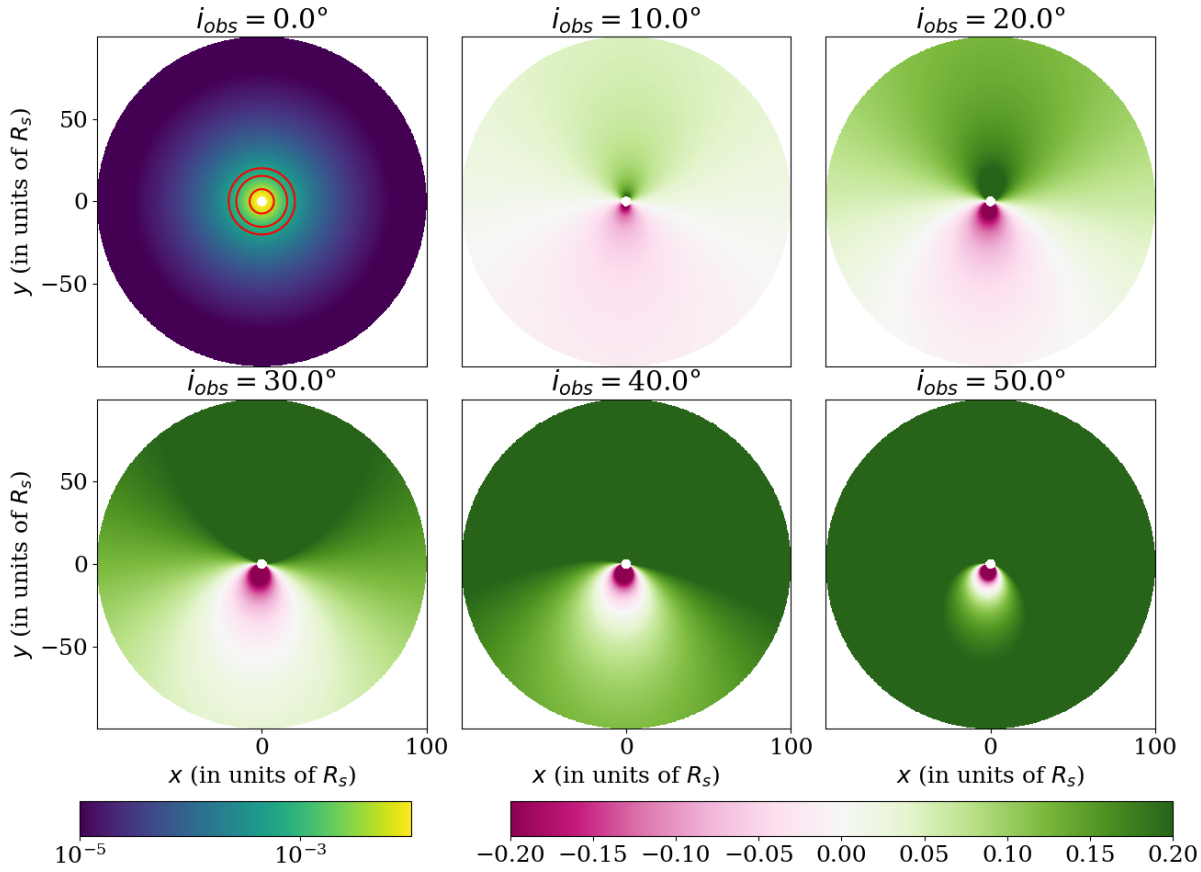

Figure 5.4: **Influence of i_{obs} on the observed contribution to the flux from each point of the disc.**
Parameters to compute the iron line profile are summarized in equation (5.1) and $h_s = 5\ R_s$.

Evolution of the relative flux difference due to the disc truncation (equation (5.4)): influence of the inclination angle and the distance between the central BH and the corona

The observed contribution to the flux (equation (4.20)) is influenced by the values of (i_{obs}, h_s):

$$f(\vec{n}_{obs}; r, \phi) \propto \left(\frac{\nu_{obs}(\vec{n}_{obs}; r, \phi)}{\nu_{em}}\right)^3 \frac{h_s}{(h_s^2 + r^2)^{3/2}} \left[\widehat{c}(\vec{n}_{obs}; r, \phi) \cdot \vec{n}_d\right] \frac{r}{\sqrt{1 - \frac{R_s}{r}}}$$

Figure 5.4 illustrates the influence of i_{obs} on the contribution to the flux. The first term in the observed contribution to the flux is affected by the value of i_{obs}: fluxes associated with blue-shifted frequencies are boosted. In contrast, fluxes associated with red-shifted frequencies are attenuated. Moreover, the value of i_{obs} impacts the angle between the direction of emission of photons and the normal to the disc. If light-bending is neglected, the direction of emission of photons is i_{obs}. Therefore, it moves away from the normal to the disc as the value of i_{obs} increases. As the first-order light bending is considered for computing the iron line profile, the position of the central BH relative to the emitting point in the disc influences the initial direction of emission of photons. Photons emitted from behind the BH will undergo a stronger deflection and are thus emitted in a direction closer to the normal to the disc.

It was assumed that the specific intensity of the emitted iron line is directly proportional to the distance between the corona and the emitting point in the disc and the impinging angle of hard X-ray photons. Therefore, as h_s increases, the distance between the corona and the emitting point in the disc increases (attenuating the flux). However, the impinging angle is closer to the normal to the disc (increasing the

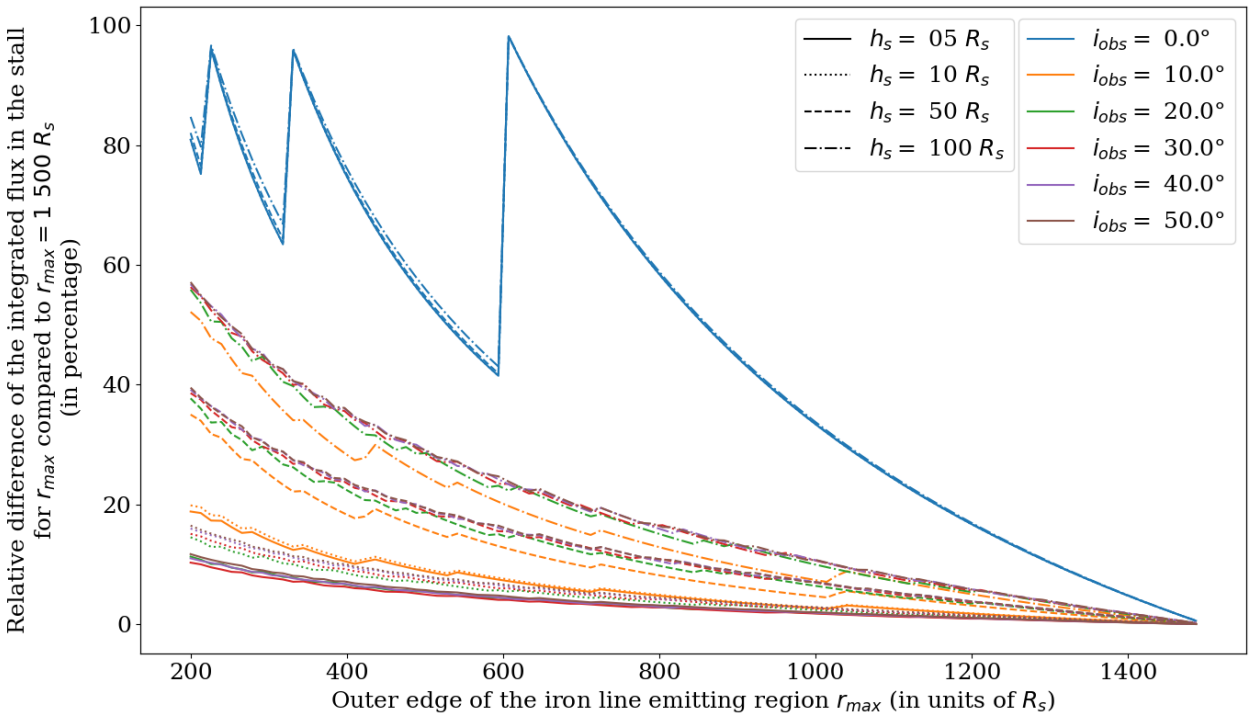

Figure 5.5: **Evolution of the relative difference of the flux in the stall due to the disc truncation (equation (5.4)): influence of** $(i_{obs}\ , h_s)$ The relative difference (equation (5.4)) is plotted against the value of r_{max} for different values of $(i_{obs}\ , h_s)$.

flux). As

$$\frac{\partial}{\partial h_s}\left(\frac{h_s}{(h_s^2+r^2)^{3/2}}\right) = \frac{-2h_s^2+r^2}{(h_s^2+r^2)^{5/2}}$$

the observed contribution to the flux decreases as h_s increases for $r < \sqrt{2}h_s$ but increases for $r > \sqrt{2}h_s$. This results in the attenuation of the red and blue wings of the line. On the other hand, the flux around the less shifted frequencies, which comes from the outer parts of the disc, gets enhanced. This is illustrated in the right panel in Figure 5.2.

Figure 5.5 shows the influence of r_{max} on the relative flux variation (equation (5.4)) for different values of $(i_{obs}\ , h_s)$. Except for the curves with $i_{obs} = 0°$, the qualitative behavior is similar for all values of i_{obs} and h_s.
As r_{max} decreases, the relative flux difference increases, facilitating the detection. When the value of r_{max} is high, the difference in flux is relatively small, regardless of the values of i_{obs}. So, it is nearly impossible to detect even if the flux difference occurs over a broad frequency range (as shown in Figure 5.3 for a large value of i_{obs}).
As h_s increases, the contribution to the flux from the parts where $r < \sqrt{2}h_s$ decreases, and the contribution from the part where $r > \sqrt{2}h_s$ increases. As a result, the outer parts of the disc contribute more significantly to the final flux, making the truncation easier to detect.

The curves in Figure 5.5 display a sawtooth profile (which is more pronounced for $i_{obs} = 0°$). This is caused by the spectral resolution used to calculate the iron line profile through the binning method. Each break corresponds to the flux differences impacting a new bin. This is not a problem for the following study since it will use spectral bands wider than 28 eV.

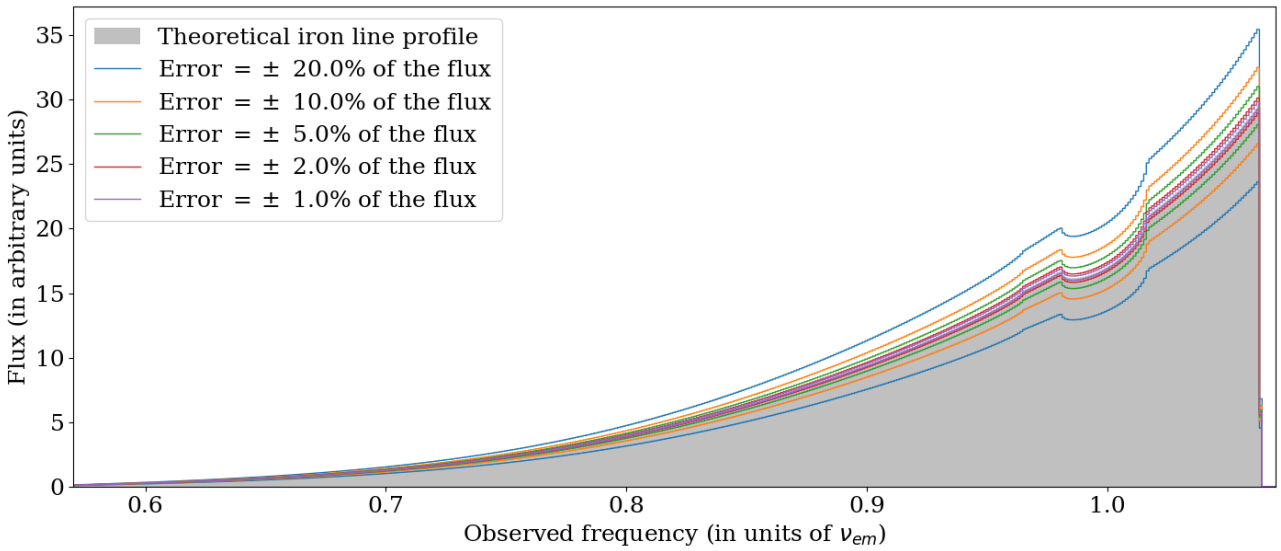

Figure 5.6: **Theoretical iron line profile and error.**
The grey histogram is the theoretical iron line profile computed with the *binning* method. The colored lines indicate the lower and upper limits of the flux in each bin, with the observed uncertainty equal to a constant fraction of the flux in each bin (see equation (5.6)).
Parameters to compute the line are summarized in equations (5.1) and (5.2), with $r_{max} = 502\ R_s$, $i_{obs} = 34.5°$, and $h_s = 8\ R_s$.

5.3 Presentation of the method

Section 5.2 presented a theoretical study of how disc outer edge radius affects the iron line profiles for different values of i_{obs} and h_s.
The iron line profile emitted by accretion discs with different values of r_{max} (and values of (i_{obs}, h_s)) were computed with the binning method. There is no analytical formula to derive the iron line profiles directly from the 'physical' iron line parameters listed in equation (5.1). Therefore, estimating r_{max} with a minimization method like the least square method would be computationally expensive. This is beyond the scope of this thesis study. Our goal here is to present a rapid diagnostic method using the iron line profiles computed with the binning method.

The method consists of calculating flux ratios between two frequency bands. Considering observational uncertainty in the flux in each bin, it defines an interval of possible values for the flux ratio. The interval is measured against a grid of theoretical values derived from 22 000 iron line profiles. These profiles cover the parameter space of the iron line, including r_{max}, i_{obs}, and h_s. The observed flux ratio interval defines a set of compatible values for the three parameters.

Observational error in the flux in each bin

An error is associated with the flux in each bin f^i to model an observed uncertainty on the flux in each bin $u(f^i)$:

$$u(f^i) = x \times f^i \tag{5.6}$$

where x is a constant used in each bin. Figure 5.6 shows an example of a line profile for different uncertainty values x.

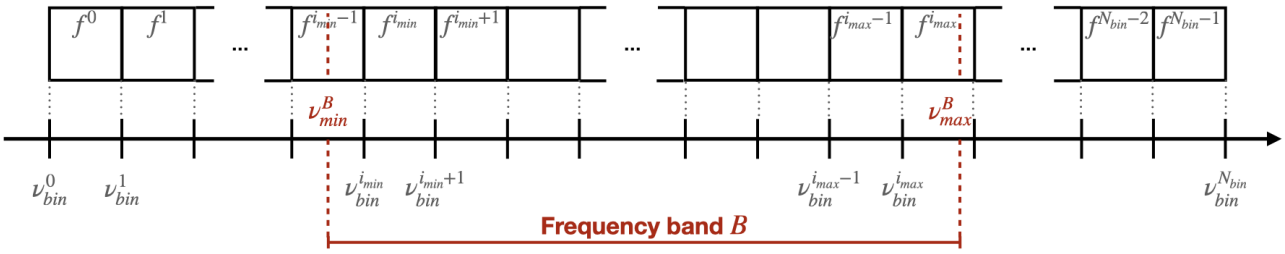

Figure 5.7: **Computation of the flux in a frequency band from the iron line profile obtained with the *binning* method.**
The axis represents frequency, while the squares represent the bins. Each bin covers the spectral interval $[\nu^i_{bin};\ \nu^{i+1}_{bin}]$ with a constant flux f_i.

Flux ratio in two frequency bands

The flux ratio between two frequency bands B_{num} and B_{max} is

$$r = \frac{F_{B_{num}}}{F_{B_{denom}}} \tag{5.7}$$

where the flux F_B in a frequency band $B = [\nu^B_{min};\ \nu^B_{max}]$ is computed with

$$F_B = \frac{1}{\nu^B_{max} - \nu^B_{min}} \left[(\Delta\nu)_{bin} \sum_{i=i_{min}}^{i_{max}-1} f^i + \left(\nu^{i_{min}}_{bin} - \nu^B_{min}\right) f^{i_{min}-1} + \left(\nu^B_{max} - \nu^{i_{max}}_{bin}\right) f^{i_{max}} \right] \tag{5.8}$$

where i_{min}, i_{max}, $\nu^{i_{min}}_{bin}$, and $\nu^{i_{max}}_{bin}$ are defined in Figure 5.7. $(\Delta\nu)_{bin}$ is the spectral width of each bin. The first term in brackets is the flux in the bins entirely inside the frequency band B, and the two last terms are the flux in the bins only partially in the frequency band B.

Using equation (5.6), the error in the flux on the frequency band B is

$$\begin{aligned} \frac{u(F_B)}{F_B} &= \frac{1}{\nu^B_{max} - \nu^B_{min}} \left[(\Delta\nu)_{bin} \sum_{i=i_{min}}^{i_{max}-1} \frac{u(f^i)}{f^i} + \left(\nu^{i_{min}}_{bin} - \nu^B_{min}\right) \frac{u(f^{i_{min}-1})}{f^{i_{min}-1}} + \left(\nu^B_{max} - \nu^{i_{max}}_{bin}\right) \frac{u(f^{i_{max}})}{f^{i_{max}}} \right] \\ &= \frac{x}{\nu^B_{max} - \nu^B_{min}} \left[(\Delta\nu)_{bin} \sum_{i=i_{min}}^{i_{max}-1} 1 + \left(\nu^{i_{min}}_{bin} - \nu^B_{min}\right) + \left(\nu^B_{max} - \nu^{i_{max}}_{bin}\right) \right] \\ &= x \end{aligned} \tag{5.9}$$

and the error in the flux ratio is

$$\frac{u(r)}{r} = \sqrt{\left(\frac{u\left(F_{B_{num}}\right)}{F_{B_{num}}}\right)^2 + \left(\frac{u\left(F_{B_{denom}}\right)}{F_{B_{denom}}}\right)^2} = \sqrt{2}\ x \tag{5.10}$$

Therefore, accounting for observational uncertainty, the interval of possible values for the flux ratio is:

$$I_{comp} = \left[r\left(1 - \sqrt{2}x\right);\ r\left(1 + \sqrt{2}x\right) \right] \tag{5.11}$$

We compare this range with the predicted flux ratios for 22 000 iron line profiles. Iron line parameters for which the theoretical flux ratio falls within the range defined in equation (5.11) are consistent with the observed iron line profile.

This grid of theoretical iron line profiles is defined by three parameters: r_{max}, i_{obs}, and h_s. The range of these parameter values that will be considered in the study is explained in section 5.1. r_{max} has

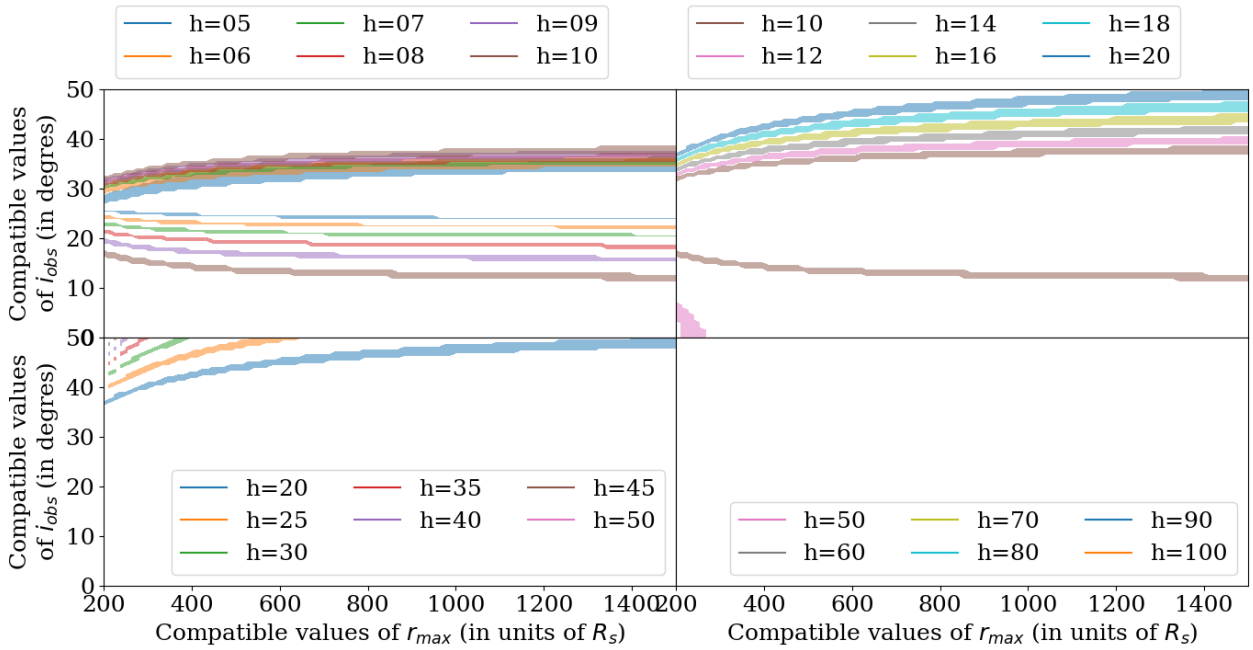

Figure 5.8: **Compatible values of (r_{max}, i_{obs}, h_s) with the observed flux ratio interval defined in equation (5.11).**
Equation (5.12) defines the flux ratio. Figure 5.6 presents the observed line, with the observational uncertainty defined in equation (5.6): $x = 1\%$.
In each panel, the x-axis represents the tested theoretical values of r_{max}, while the y-axis represents the tested theoretical values of i_{obs}. The different tested values of h_s are separated into the plot's four panels. The colored parts of each plot correspond to the sampled values of (r_{max}, i_{obs}) that are compatible with the observed flux ratio interval in equation (5.11) for each tested h_s value.

100 linearly spaced values between 200 R_s and 1 500 R_s. i_{obs} values range from 0 to 50, with values every half degree. h_s is spaced every one Schwarzschild radius between 5 R_s and 10 R_s, every two Schwarzschild radii between 10 R_s and 20 R_s, every five Schwarzschild radii between 20 R_s and 50 R_s, and every ten Schwarzschild radii between 50 R_s and 100 R_s.

For instance, the method can be applied to the theoretical iron line profile presented in Figure 5.6 and the observational uncertainty defined in equation (5.6) with $x = 1\%$. The flux ratio is computed between the two frequency bands:

$$B_{num} = [\nu_{min}^{B_{num}} = 5.76 \text{ keV} = 0.9\ \nu_{em};\ \nu_{max}^{B_{num}} = 6.08 \text{ keV} = 0.95\ \nu_{em}] \tag{5.12a}$$

$$B_{denom} = [\nu_{min}^{B_{denom}} = 6.14 \text{ keV} \simeq 0.959\ \nu_{em};\ \nu_{max}^{B_{denom}} = 6.63 \text{ keV} \simeq 1.036\ \nu_{em}] \tag{5.12b}$$

The denominator band corresponds to the larger spectral extent of the stall $I_{h_s,i_{obs}}(r_{max})$ (equation (5.5)) for the catalog of iron line profiles with all the values of $(r_{max},\ i_{obs},\ h_s)$ (see Figure 5.3). The numerator band is used as a reference at lower frequencies. Figure 5.8 presents the iron line parameter values $(r_{max},\ i_{obs},\ h_s)$ compatible with the flux ratio interval. The range of compatible values for h_s extends from 5 R_s to 50 R_s. Since h_s is unknown, all cases need to be considered. Figure 5.9 displays the combination of all panels shown in Figure 5.8. The value of r_{max} is not constrained, as it can take any of the tested values from the catalog. It is worth noticing that if one of the two parameters, i_{obs} or h_s, can be constrained independently, the other parameter is constrained by this method.

Combining two flux ratios

The parameters used for the tested observed line (Figure 5.6) correspond to a narrower spectral band on which the iron line flux differs from the untruncated disc (displayed in Figure 5.3) than the denominator

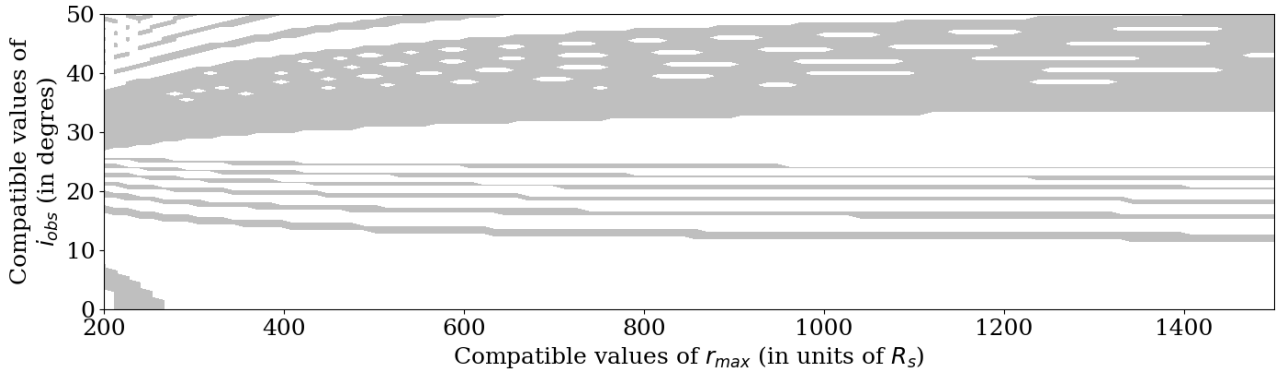

Figure 5.9: **Combination of all plots in each panel of Figure 5.8**
The grey region is the union of all colored areas in Figure 5.8. It shows all the values of (i_{obs}, r_{max}) compatible with the flux ratio interval.

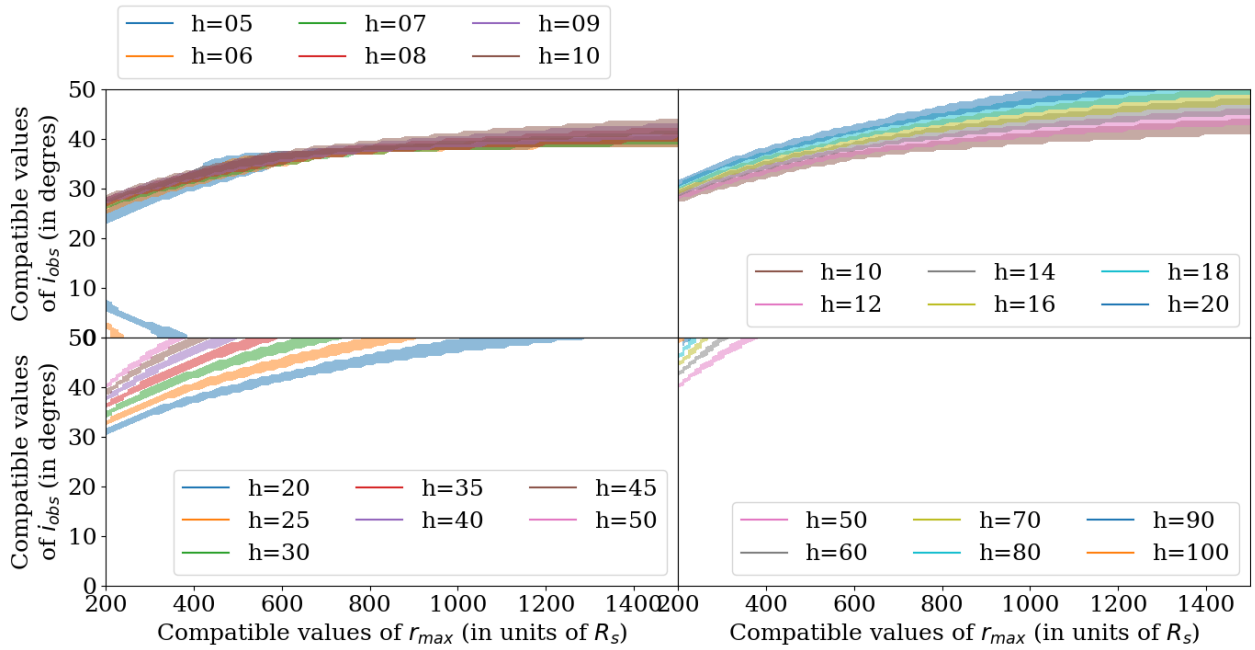

Figure 5.10: **Compatible values of (i_{obs}, r_{max}, h_s) with the observed flux ratio interval defined in equation** (5.11) **and computed with the frequency bands defined in** (5.13)**.**
The Figure is the same as Figure 5.8. Only the frequency bands on which the flux ratio is computed change from equation (5.12) to equation (5.13).

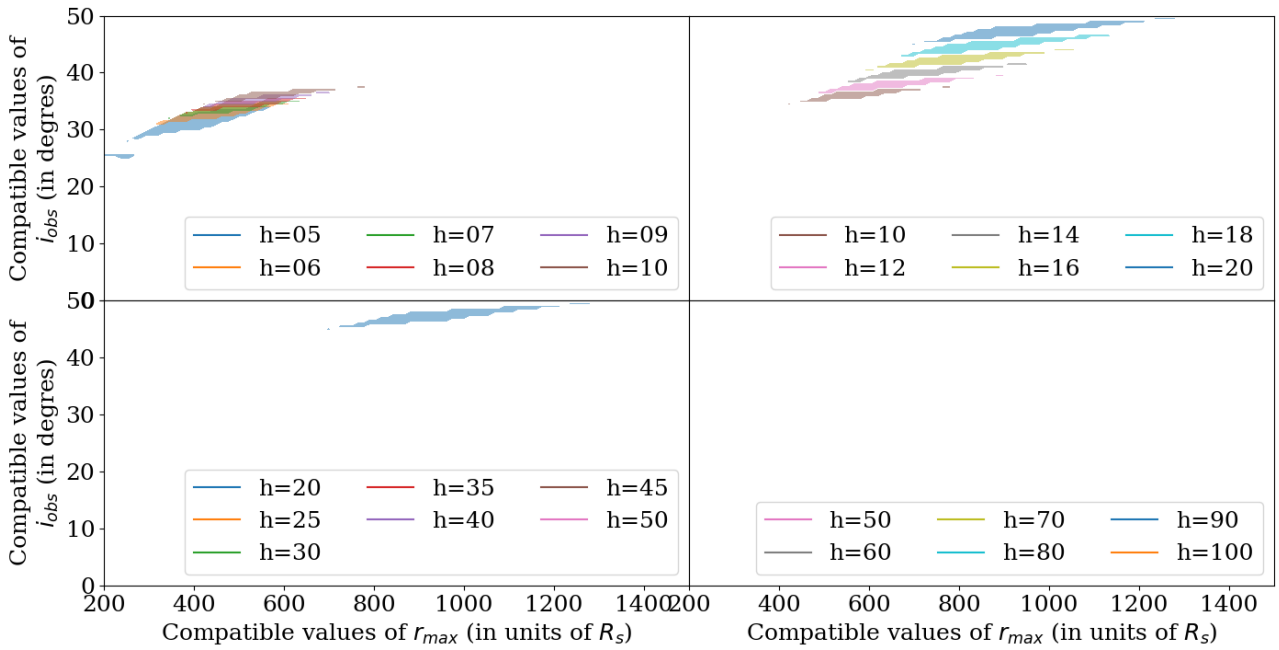

Figure 5.11: **Compatible values of (r_{max}, i_{obs}, h_s) with the two observed flux ratio intervals defined in equation (5.11), with the two frequency bands defined in equations (5.12) and (5.13)**
The Figure is the same as Figures 5.8 and 5.10, but the colored areas in this figure correspond to the intersection of the equivalent colored regions in the two previous figures.

frequency band (equation (5.12b)) used to compute the flux ratio interval. The frequency bands used to define the flux ratio can be updated to

$$B_{num} = [\nu_{min}^{B_{num}} = 5.76 \text{ keV} = 0.9\ \nu_{em};\ \nu_{max}^{B_{num}} = 6.272 \text{ keV} = 0.98\ \nu_{em}] \tag{5.13a}$$

$$B_{denom} = [\nu_{min}^{B_{denom}} = 6.272 \text{ keV} = 0.98\ \nu_{em};\ \nu_{max}^{B_{denom}} = 6.4 \text{ keV} = \ \nu_{em}] \tag{5.13b}$$

The results are displayed in Figure 5.10. Changing the pair of frequency bands does not significantly impact the restriction of the compatible iron line parameters. Nonetheless, the compatible values of $(r_{max},\ i_{obs},\ h_s)$ are slightly altered. The values of $(r_{max},\ i_{obs},\ h_s)$ that are compatible with the observed iron line must result in flux ratios that are compatible with the observed flux ratio intervals defined for the two pairs of frequency bands (equations (5.12) and (5.13)). Combining the results obtained with the two pairs of frequency bands allows for the restriction of the compatible values for $(r_{max},\ i_{obs},\ h_s)$. Figure 5.11 depicts the results obtained by combining the two flux ratios. The compatible values of h_s are more constrained. The lowest values of i_{obs} are discarded. Finally, the compatible values of r_{max} are now constrained below 1 200 R_s. Figure 5.11 also reveals that if the values of i_{obs} and h_s are more closely defined, the potential values for r_{max} can be further restricted. The use of supplementary frequency bands can be helpful in this regard.

Flux ratio in a set of frequency bands: choice of a set

Equations (5.12) and (5.13) define two flux ratios that, when used together, enhance the constraint on the iron line parameters of the observed line profile shown in Figure 5.6. Using additional flux ratios can enhance the constraint.
Furthermore, the capability of a given flux ratio to constrain a tested iron line profile may vary depending on the line profile. Figure 5.12 displays the constraints obtained on the iron line parameters for different tested lines in the four panels. While the truncation of the disc is evident for $(r_{max} = 200\ R_s,\ i_{obs} = 2.5°,\ h_s = 45\ R_s)$ displayed in the upper left panel and $(r_{max} = 763.4\ R_s,\ i_{obs} = 48.5°,\ h_s = 30\ R_s)$ displayed in the lower left panel, it remains ambiguous for

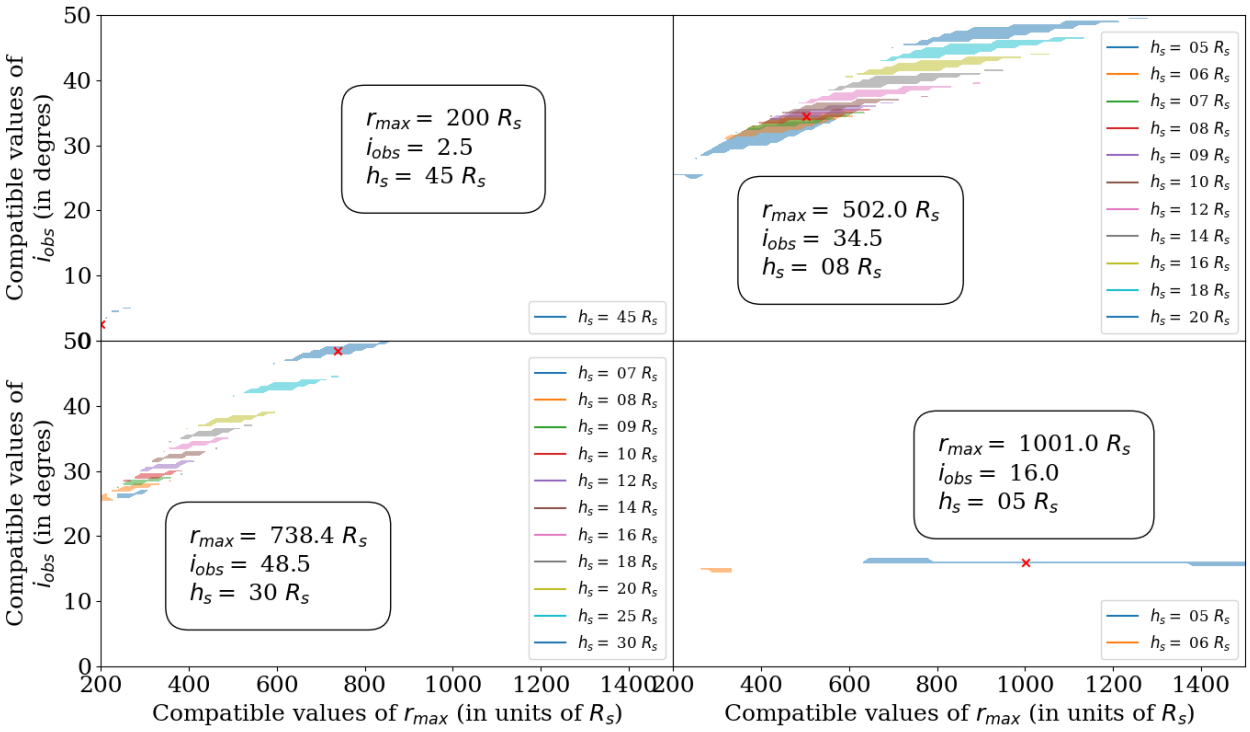

Figure 5.12: **Compatible values of $(r_{max},\ i_{obs},\ h_s)$ with the two observed flux ratio intervals defined in equation (5.11) and computed with the two sets of frequency bands in equations (5.12) and (5.13) on different observed iron lines.**
The Figure is the same as Figure 5.11 but for different initial values of $(r_{max},\ i_{obs},\ h_s)$ to compute observed iron lines (represented with a red cross in each plot). The observational uncertainty in the flux in each bin is still $x = 1\%$.

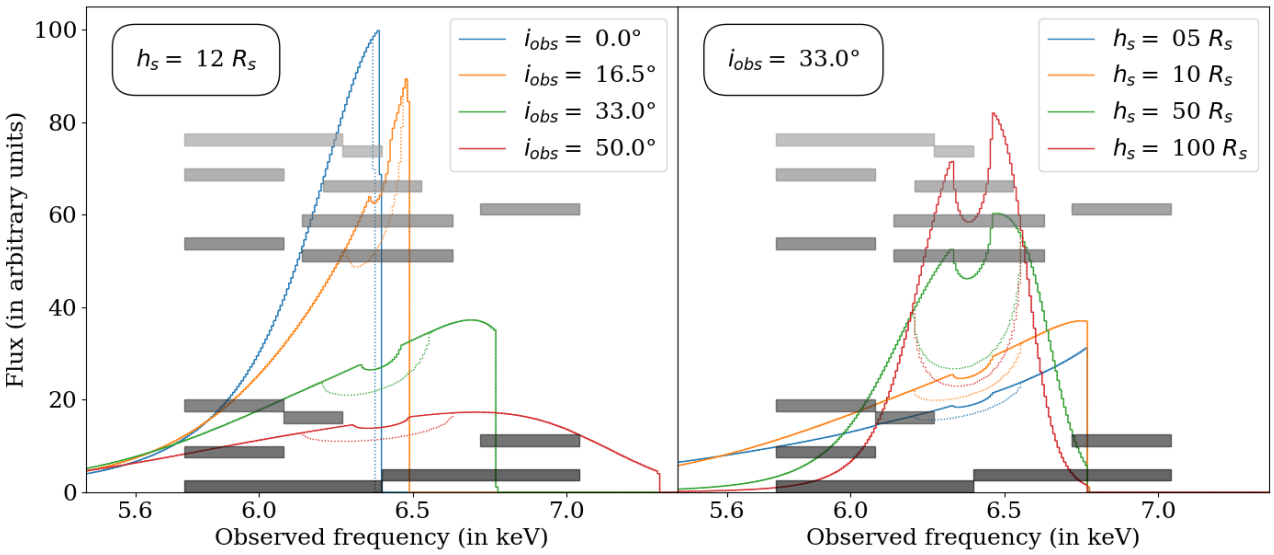

Figure 5.13: **Seven flux ratios chosen to infer the values of** (r_{max}, i_{obs}, h_s)**.**
Grey rectangles represent the frequency bands used to define flux ratios. Each shade of grey corresponds to a distinct flux ratio. For each flux ratio, the top rectangle corresponds to the numerator, and the bottom rectangle to the denominator. The lighter and upper group of flux ratios aims to constrain r_{max}, whereas the darker and lower group of flux ratios aims to constrain i_{obs}.
Equations (5.1) and (5.2) summarize the iron line parameters. For the solid line $r_{max} = 1\ 500\ R_s$, and for the dashed lines $r_{max} = 200\ R_s$.

$(r_{max} = 502\ R_s,\ i_{obs} = 34.5°,\ h_s = 8\ R_s)$ displayed in the upper right panel. Nothing can be concluded for $(r_{max} = 1001\ R_s,\ i_{obs} = 16°,\ h_s = 5\ R_s)$. Therefore, to constrain the outer radius of the iron line in different setups using this method, additional flux ratios are necessary.

While for the tested line $(r_{max} = 502\ R_s,\ i_{obs} = 34.5°,\ h_s = 8\ R_s)$ (upper right panel of Figure 5.12), the constraint on r_{max} could be improved by better characterizing i_{obs}, the constraint on r_{max} from the tested line $(r_{max} = 1001\ R_s,\ i_{obs} = 16°,\ h_s = 5\ R_s)$ (lower right panel of Figure 5.12) requires flux ratios that better characterize the outer edge. New constraints with additional flux ratios could improve the situation depending on the tested line initial parameters. Therefore, Figure 5.13 displays other flux ratios. The lighter grey flux ratios in the upper part of the figure are meant to constrain the outer edge radius. Each ratio has a frequency band extending inside the stall due to the disc truncation. The bands have differing widths and positions to characterize the stall for different values of $(r_{max},\ i_{obs},\ h_s)$. The darker grey flux ratios in the lower part of the figure are intended for constraining the value of i_{obs}. For low i_{obs} values, there is no blue tail in the iron line profile. The first flux ratio differentiates between the low i_{obs} values. The blue tail only extends to a high observed frequency at the highest i_{obs} values. The second flux ratio distinguishes between high values of i_{obs}. The third flux ratio discriminates between intermediate values of i_{obs}, with an increasing flux in the blue-shifted frequency band.
I manually tested the given set of flux ratios to enhance the constraint on the disc outer edge radius. Ultimately, the study has concluded that the seven flux ratios depicted in Figure 5.13 should be employed. Figure 5.14 shows for the four tested lines in Figure 5.12 the constraints obtained by combining these seven flux ratios. The constraint on (h_s, i_{obs}, r_{max}) is precise for the three first lines. However, r_{max} is not constrained for the tested line $(r_{max} = 1001\ R_s,\ i_{obs} = 16°,\ h_s = 5\ R_s)$. The later line corresponds to the smallest possible values of h_s considered in this study. It was highlighted earlier that with small values of h_s, the relative weight of the flux emitted by the inner parts is increased, therefore hiding the contribution of the outer parts.
This particular set of flux ratios was used as an example to investigate the extent to which the disc truncation can be ascertained. The following section will examine the constraints this set of flux ratios

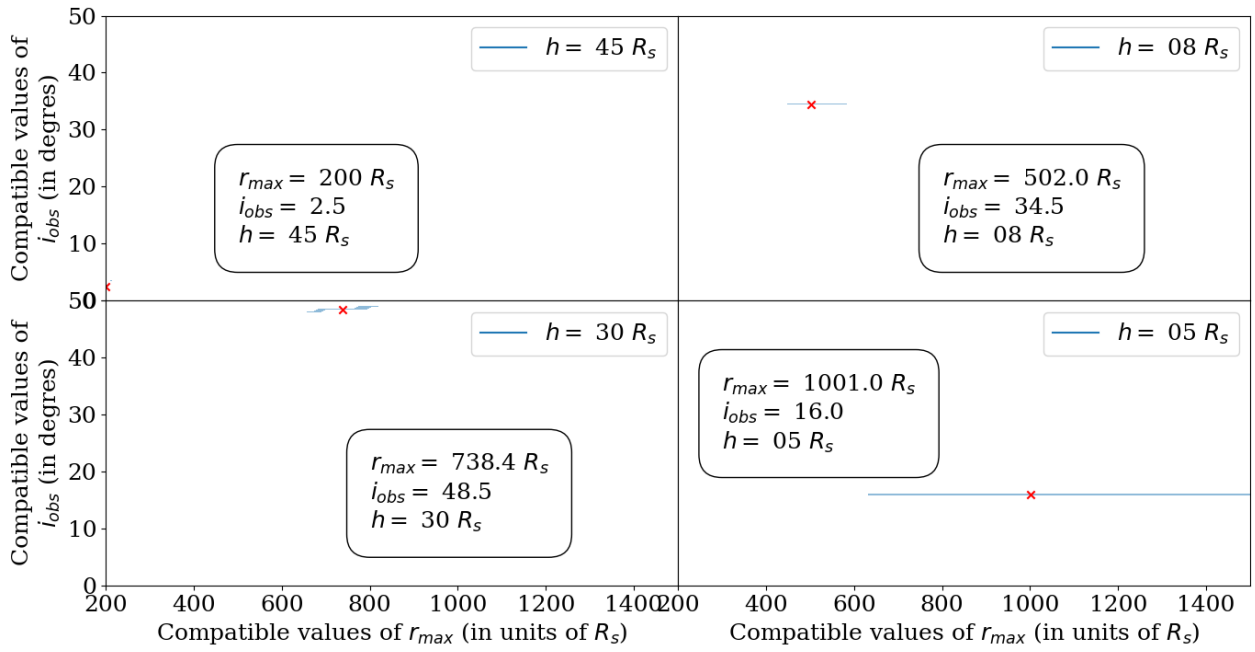

Figure 5.14: **Compatible values of (r_{max}, i_{obs}, h_s) with the seven flux ratio intervals defined in equation (5.11) and computed with the set of frequency bands displayed in Figure 5.13.**
The Figure is the same as Figure 5.12, but all of the seven flux ratios are used, not only the ones defined in equations (5.12) and (5.13).

provides on the parameters of the grid of iron line profiles, now used as test lines.

5.4 Theoretical results

In the previous section, I presented a method for constraining the parameters of an observed iron line to determine the disc outer edge. Additionally, this method limits the value i_{obs} and h_s. The results for the three parameters can be explored before focusing on the detectability of the accretion disc truncation in the context of MBH binary mergers.

For each value of the error in the flux in each bin (x), the method output is a non-necessarily continuous three-dimensional region:

$$\bigcup_{i=1}^{N} (r^i_{max},\ i^i_{obs},\ h^i_s) \tag{5.14}$$

where $(r^i_{max}, i^i_{obs}, h^i_s)$ are the parameters of the N theoretical iron line profiles for which the seven flux ratios are compatible with the observed iron line profile.

This three-dimensional region is defined for each observed line profile. Four parameters characterize the observed line profiles tested here. These include the three parameters (r_{max}, i_{obs}, h_s) for calculating the theoretical flux in each bin using the *binning* method and the parameter x in equation (5.6) to determine the observational uncertainty. The three-dimensional region of compatible iron line parameters defined in equation (5.14) can be computed using the 22 000 theoretical iron line profiles, with different values of the parameter x.

The easiest way to analyze the result is by examining the amplitude of the constraint on the three parameters. It is defined as the difference between the minimum and the maximum of the compatible

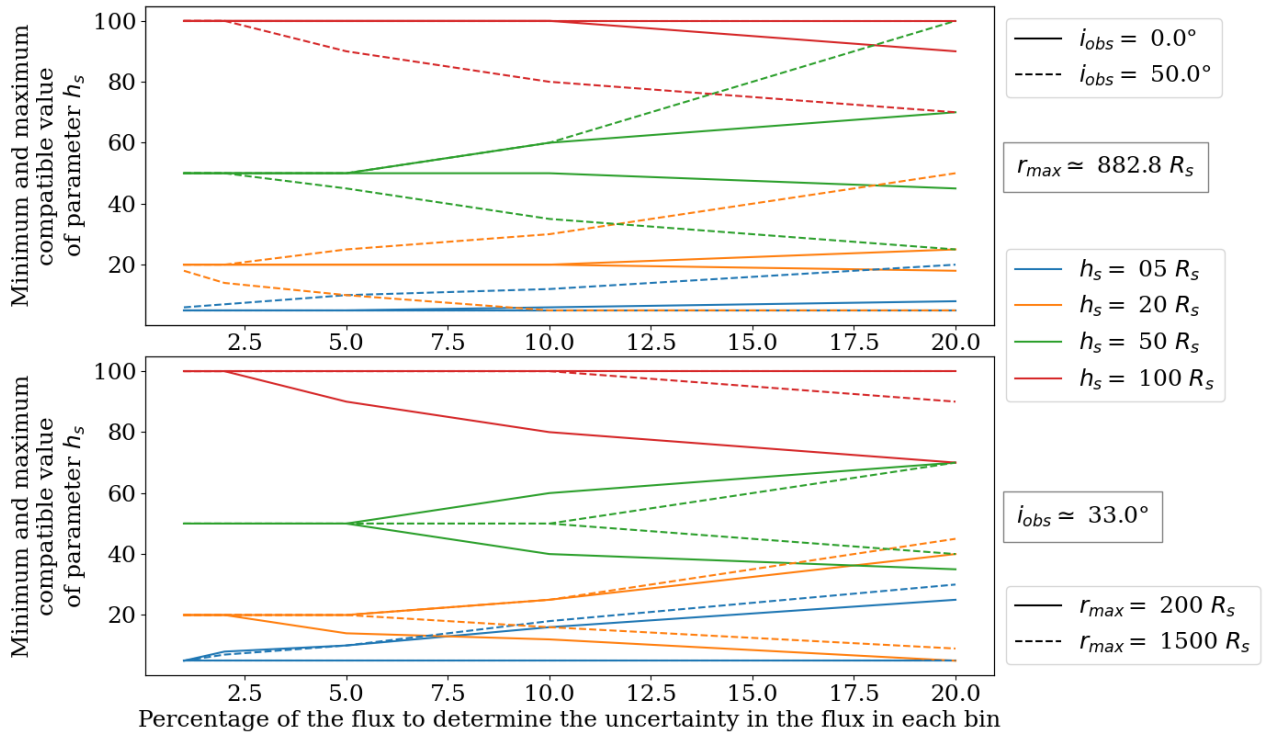

Figure 5.15: **Evolution of the amplitude of the constraint on h_s as a function of x for different initial values of (r_{max}, i_{obs}, h_s).**
The y-axis represents the compatible values for h_s, while the x-axis represents the value of x. Several initial values of the parameters (r_{max}, i_{obs}, h_s) to compute the theoretical profiles with the *binning* method are explored. Line colors represent the values of h_s, and the legend is common for the two panels. Each line style shows different i_{obs} or r_{max} values. Each line in the plots is doubled: the upper one corresponds to the maximum compatible value of h_s, and the lower one corresponds to the minimum compatible value of h_s.

value of each parameter defined in equation (5.14):

$$\Delta r_{max} = \left(\max_i r^i_{max}\right) - \left(\min_i r^i_{max}\right) \tag{5.15a}$$

$$\Delta i_{obs} = \left(\max_i i^i_{obs}\right) - \left(\min_i i^i_{obs}\right) \tag{5.15b}$$

$$\Delta h_s = \left(\max_i h^i_s\right) - \left(\min_i h^i_s\right) \tag{5.15c}$$

This definition of the amplitude does not account for any potential discontinuities in the three-dimensional area defined in equation (5.14). Moreover, the catalog of 22 000 theoretical iron line profiles has unevenly spaced values of h_s. The value of the ampltiude of the constraint for each parameter depends on the four parameters of the observed iron lines.

I first investigate the ampltiude of the constraint on h_s. Figure 5.15 displays the evolution of this amplitude as a function of x for different values of $(r_{max},\ i_{obs})$. As expected, the amplitude of the constraints grows with the increase of x. The right panel in Figure 5.2 shows that the flux in each bin evolves in a complex manner with h_s. Hence, the evolution of the minimum and maximum compatible values is not symmetric around the theoretical value. It is worth noticing that the minimum and maximum tested values are $h_s = 5\ R_s$ and $h_s = 100\ R_s$, respectively. If the curves reach these points, it is only a partial and weak condition.
Figure 5.16 presents the amplitude of the constraint on h_s against all possible values of r_{max} and

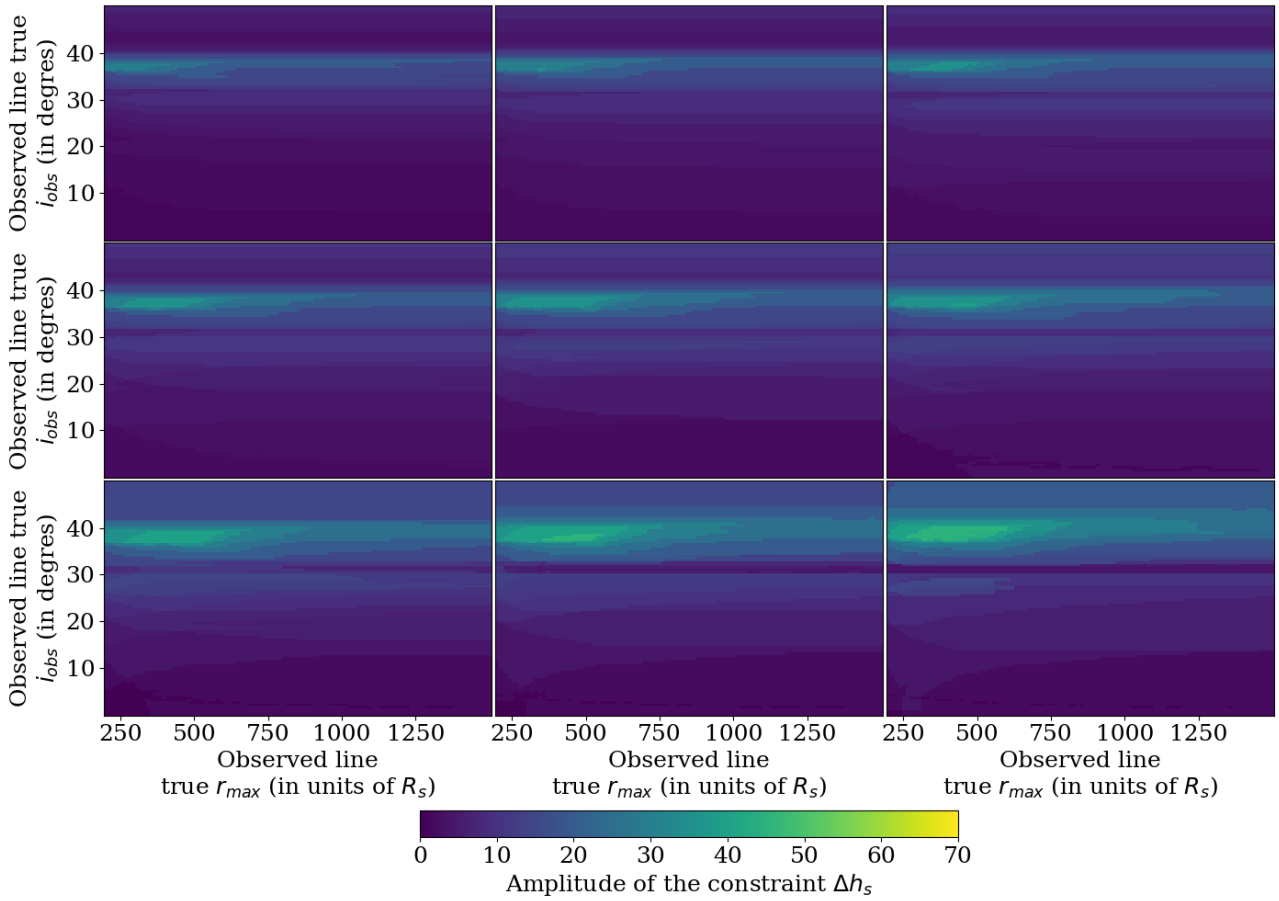

Figure 5.16: **Evolution of the amplitude of the constraint on h_s against the initial values (r_{max}, i_{obs}) of the observed line for different initial values of h_s and $x = 10\%$.**
The x-axis represents the initial value of r_{max}. The y-axis represents the initial value of i_{obs}, and each panel represents a different initial value of h_s. These three parameters are used to compute the observed iron line profiles. The panels are ordered by increasing values of h_s: $h_s = 5\ R_s$, $h_s = 7\ R_s$, $h_s = 10\ R_s$, $h_s = 14\ R_s$, $h_s = 20\ R_s$, $h_s = 30\ R_s$, $h_s = 50\ R_s$, $h_s = 80\ R_s$, and $h_s = 100\ R_s$.

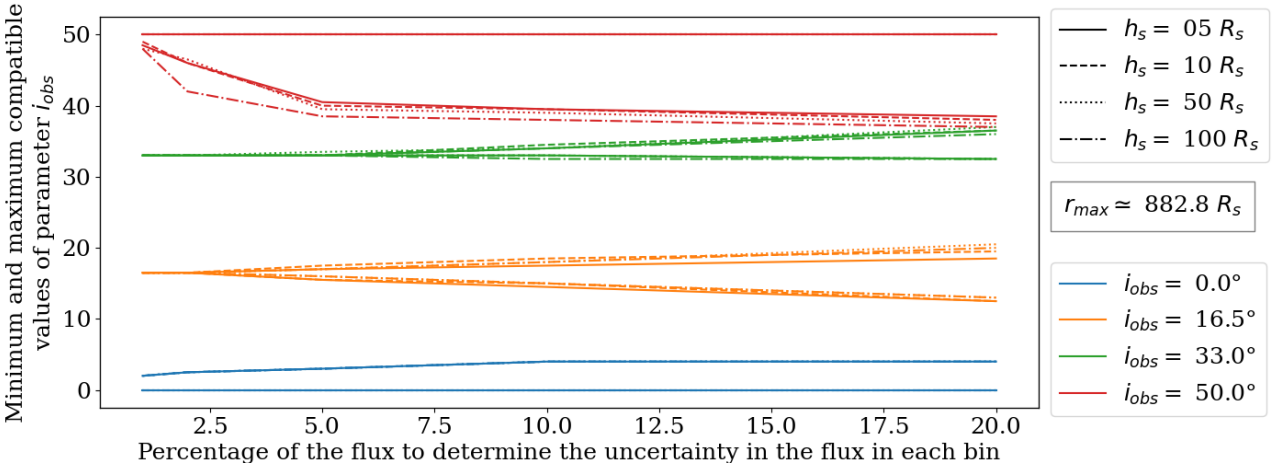

Figure 5.17: **Evolution of the amplitude of the constraint on parameter i_{obs} with the error in the flux in each bin defined in equation (5.6) for different observed iron line profiles.**
The plot is the same as Figure 5.15, but it displays the compatible values of i_{obs} for different observed iron line profiles along the y-axis. Each line color represents a value of i_{obs}, and each line style indicates different values of h_s. The initial value of r_{max} remains constant.

i_{obs} and nine values of h_s and $x = 10\%$. This second representation of the results indicates that the amplitude of the constraint on h_s is influenced firstly by the value of i_{obs} (and then by the value of r_{max} and h_s). The upper panel of Figure 5.15 indicates that the amplitude of the constraint on h_s deteriorates with the increase of i_{obs}. Figure 5.16 shows that, in fact, the weaker constraints are obtained for $i_{obs} \simeq 35° - 40°$.
The lower panel of Figure 5.15 reveals that the constraint on h_s is better when r_{max} is larger, provided the corona is at the highest tested distance. Figure 5.2 shows that the iron line profiles with a higher value of h_s are more distinct with a higher value of r_{max} than a lower value.

The same study can be conducted on the ampltide of the constraint on i_{obs}. Figure 5.17 displays the compatible values of i_{obs} presented in the same way as the upper panel of Figure 5.15 and Figure 5.18 in the same way as Figure 5.16.
Figure 5.17 shows that the constraint on i_{obs} for $r_{max} \simeq 882.8\ R_s$ is independent of the value of h_s used to compute the observed iron line profile. These results remain independent of h_s for other values of r_{max}.
At low values of i_{obs}, the constraint remains constant (a few degres for $i_{obs} =)°$). It does not depend on the initial value of r_{max} and x. This is because the difference between the observed line profiles is confined to a very narrow spectral band close to 6.4 keV (see the left panel in Figure 5.2). The frequency bands considered in this method are too broad to capture these differences (see the frequency bands plotted on the iron line profiles in Figure 5.13).
For i_{obs} values close to 50°, the constraint is more sensitive to the value of x than for the intermediate values i_{obs}. Only two different frequency bands are considered in the iron line profile's blue-shifted wing, which appears only for the most inclined discs. Additional frequency bands at high blue-shifts should be considered to improve this constraint.
The constraint on i_{obs} only slightly depends on the initial value of r_{max}. There are enough frequency bands outside the spectral extent where the outer edge affects the iron line profile.

Figure 5.19 displays the compatible values of r_{max}, presented in the same manner as in Figure 5.15. It reveals that the range of compatible values for r_{max} is heavily influenced by the initial values of (r_{max}, i_{obs}, h_s). The amplitude of the constraint on r_{max} increases faster with x than the amplitude of constraint on h_s and i_{obs}. The impact of r_{max} on the iron line profile is limited to a smaller frequency

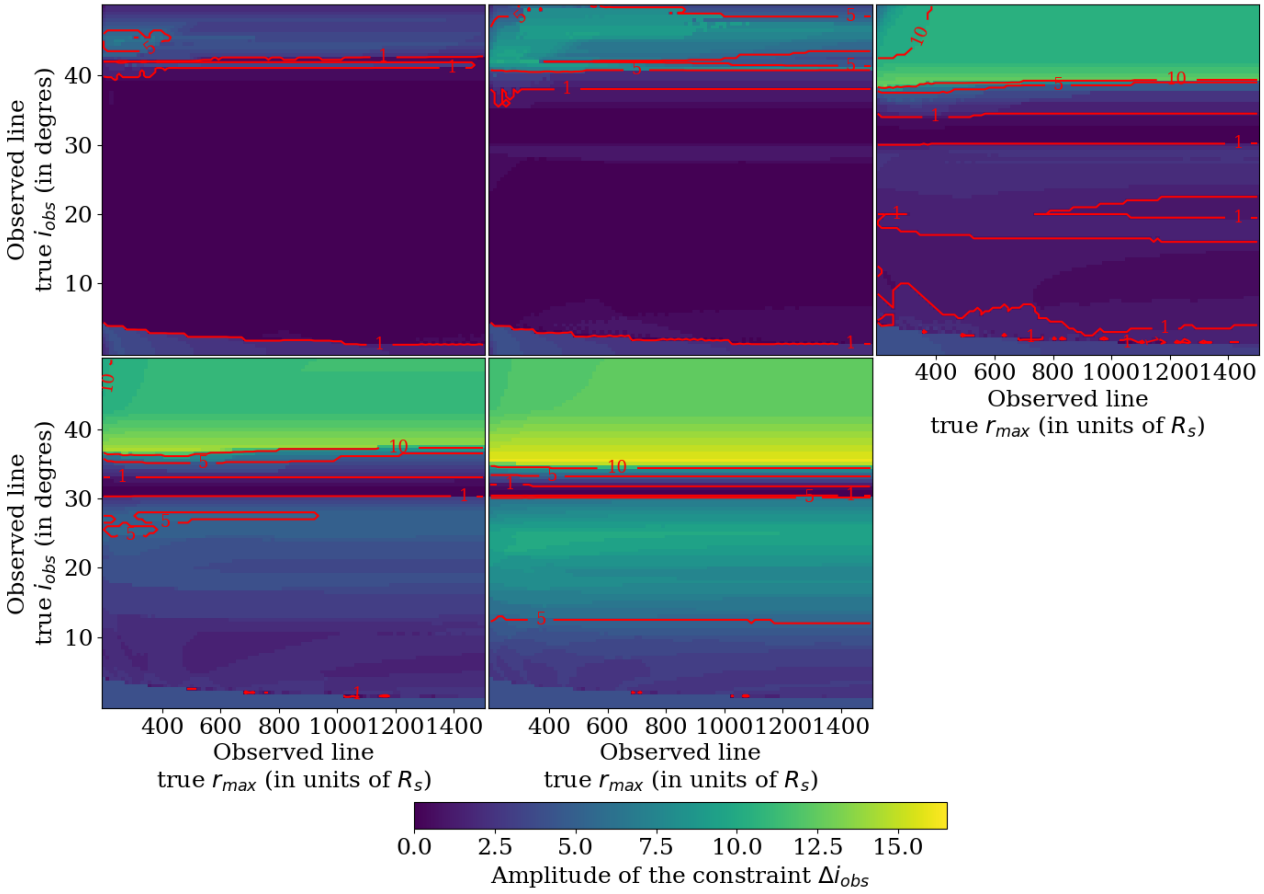

Figure 5.18: **Evolution of the amplitude of the constraint on i_{obs} against the initial values of (r_{max}, i_{obs}) of the observed line for different initial values of x and $h_s = 10\ R_s$.**
The figure is the same as Figure 5.16, but each panel represents a different value of x. From the upper left panel to the lower right panel: $x = 1\%$, $x = 2\%$, $x = 5\%$, $x = 10\%$, and $x = 20\%$. The red curves correspond to constant Δi_{obs} (in degres).

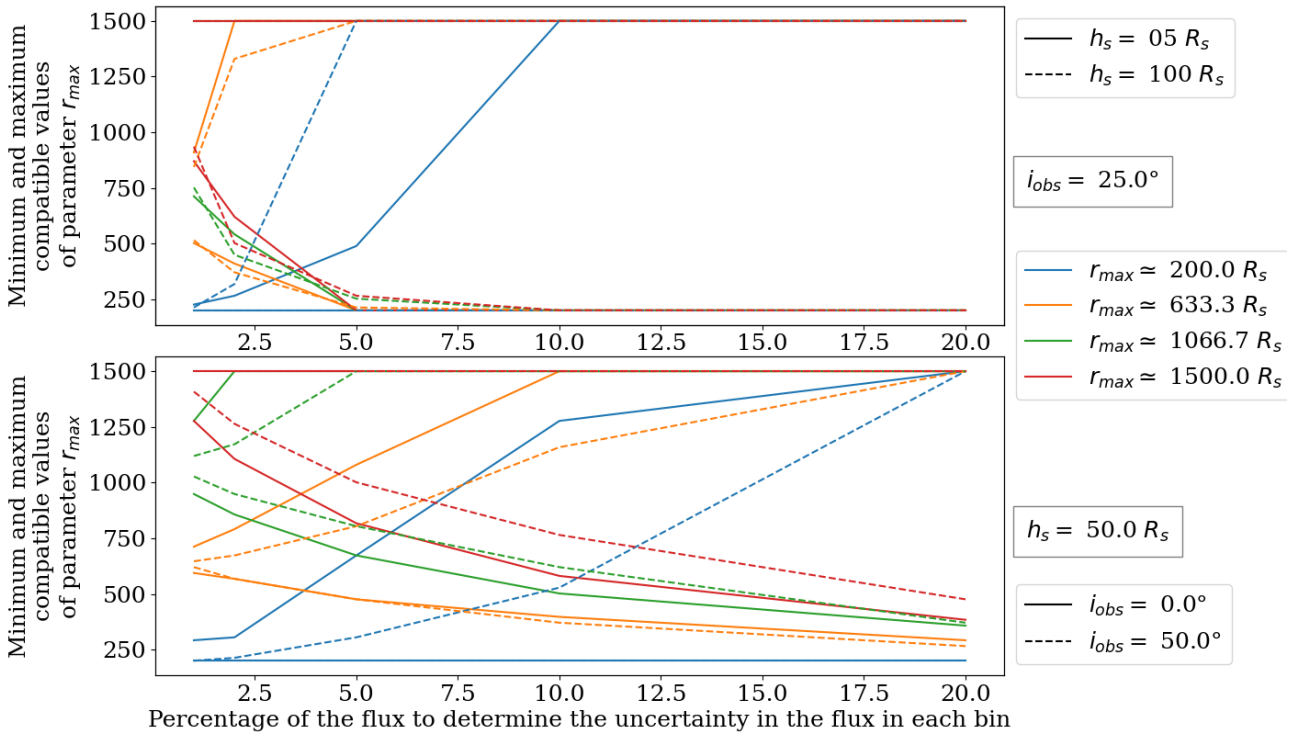

Figure 5.19: **Evolution of the ampltiude of the constraint on r_{max} as a function of x for different initial values of $(r_{max},\ i_{obs},\ h_s)$.**
The plot is the same as Figure 5.15, but the y-axis shows the compatible values for r_{max}. The colors represent different initial values of r_{max}, and each line style indicates different values of h_s or i_{obs}.

range compared to the two other parameters considered in this study. Thus, it is more challenging to constrain.
Figure 5.20 displays the amplitude of the constraint on r_{max} divided by the initial value of r_{max}. The relative amplitude of the constraint is shown against the initial values of $(r_{max},\ i_{obs})$, as in Figures 5.16 and 5.18. Each panel corresponds to different initial values of h_s and x.
As the value of h_s increases, constraining the value of r_{max} becomes easier. This is illustrated in the left panel in Figure 5.2, which shows that the value of r_{max} has a more significant influence on the iron line profile as the value of h_s increases. However, this global decrease of the amplitude of the constraint is not continuous across all the values of the parameter h_s.
When i_{obs} is low, relative amplitude of the constraint stays high. This is because the value of r_{max} affects the iron line profile only within a narrow frequency range in this case. The frequency range of the stall caused by the truncation of the outer parts of the disc for different values of i_{obs} is displayed in Figure 5.3.

Can we estimate the radius of the disc outer edge?

The study investigated the possibility of detecting the truncation of the outer parts of the disc. The objective is not necessarily to determine the exact value of r_{max} but rather to be able to detect the disc truncation.
As explained earlier, the reference value for an untruncated accretion disc outer edge value was $r_{max} = 1\ 500\ R_s$. As highlighted in section 5.1, theoretical values are around $\sim 1\ 100\ R_s$, but the question is still an active area of research. Figure 5.20 presents the relative amplitude of the constraint on r_{max}. This section aims to determine the precision in the flux that the X-ray observations should reach to conclude that the disc is truncated. Therefore, Figure 5.21 presents the maximum value of the error in the flux in each bin for which the maximum compatible values of the disc outer edge radius is below $1\ 200\ R_s$.

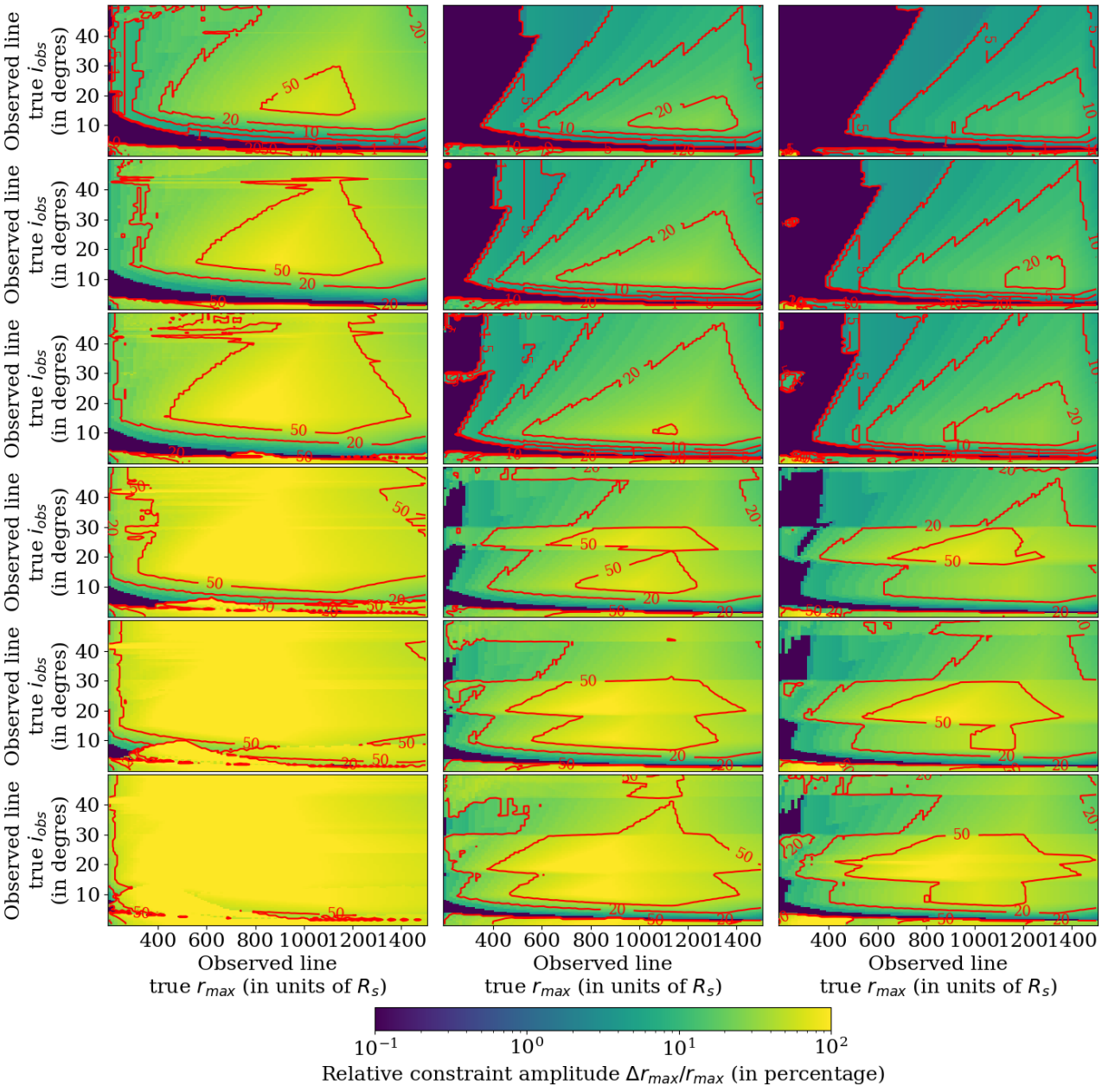

Figure 5.20: **Evolution of the relative amplitude of the constraint on r_{max} against the initial values of (r_{max}, i_{obs}) for different values of x and h_s.**
The plot is the same as Figures 5.15 and 5.18, but the value of x varies in each line, and the value of h_s varies in each column. First line: $x = 0.5\%$, second line: $x = 0.75\%$, third line: $x = 1\%$, $x = 2\%$, and fourth line: $x = 2.5\%$. Left column: $h_s = 5\ R_s$. Middle column: $h_s = 50\ R_s$. Right column: $h_s = 100\ R_s$. The color map illustrates the amplitude of the constraint on parameter r_{max} divided by the initial value of r_{max} used to compute the observed iron line profile. The color scale is a logarithmic percentage. Red contours correspond to constant value of $\Delta r_{max}/r_{max}$: 5%, 10%, 20%, and 50%.

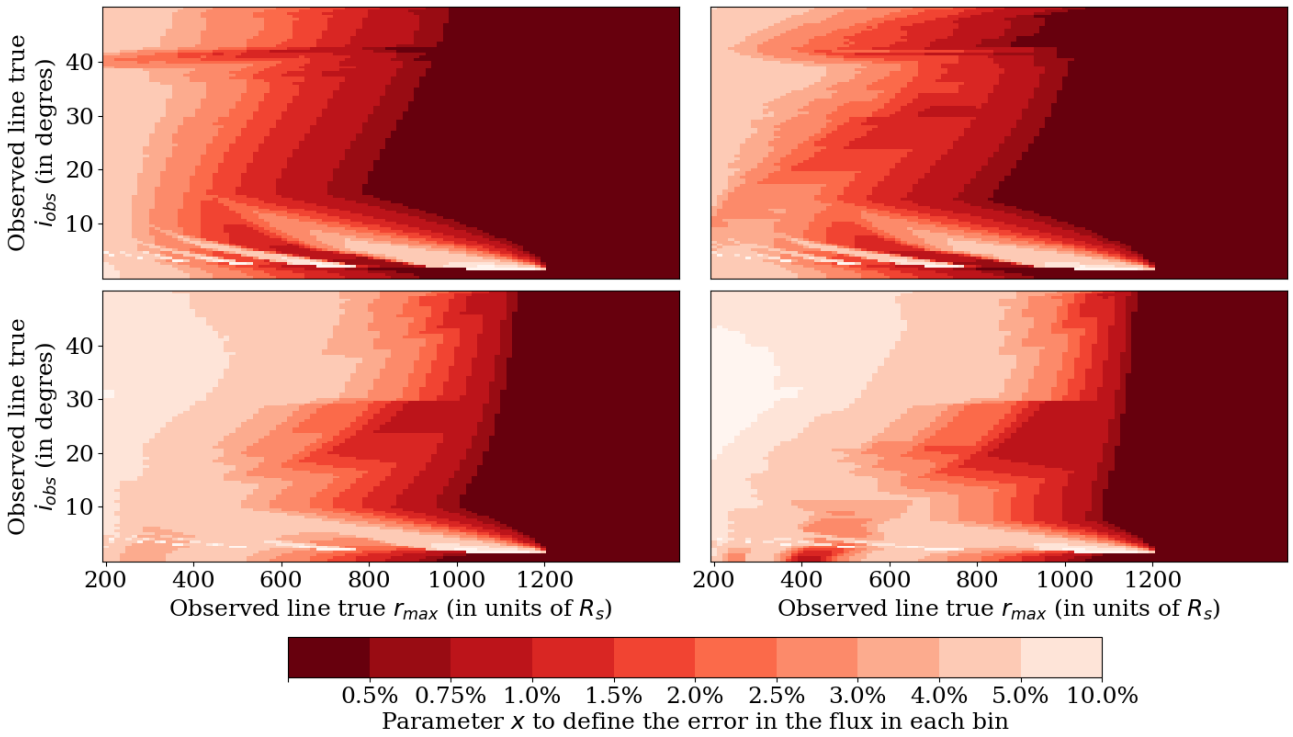

Figure 5.21: **Maximal uncertainty in the flux that X-ray facilities must reach to detect the truncation of the disc outer parts.**
The four panels display the maximal value of parameter x in equation (5.6) for which it is possible to detect the disc truncation. The x-axis represents the initial values of r_{max} used to compute the theoretical iron line profile, while the y-axis represents the initial values of i_{obs}. Each panel corresponds to a different value of h_s: $h_s = 5\ R_s$ and $h_s = 10\ R_s$ for the first line and $h_s = 50\ R_s$ and $h_s = 100\ R_s$ for the second line.
The regions colored in the darker red correspond to the observed iron lines for which it was impossible to detect the disc truncation, even with $x = 0.5\%$.

Figure 5.21 shows that detecting the truncation of the accretion disc when the outer radius is above 800 R_s would require an uncertainty in the flux in each bin below 1%. For equal mass binaries, the truncation of the disc at this outer radius corresponds to separations between 0.2 mpc if the central MBH mass is $10^6\ M_\odot$ and 0.2 pc if the central MBH mass is $10^9\ M_\odot$. For these systems, the time before the merger is comprised between 8×10^5 and 8×10^8 years.

5.5 Simulation of observations with `Xspec`

The method presented in Chapter 4 provides the Kα iron line profile, taking into account the GR effects from the central MBH (computed in the Schwarzschild metric and with a first-order expansion of the geodesic equations). The line emissivity is assumed to be proportional to the illuminating hard X-ray flux. This flux is considered to be proportional to the inverse of the square distance between the point-source corona and the emitting point and the impinging angle of X-ray photons. Therefore, the flux obtained in each bin is not in physical units. In the previous section, I presented a basic study aiming at including uncertainties in the flux in each bin to mimic realistic observations. This section aims to present a more realistic study of disc truncation detectability by future X-ray instruments. The work described below has been performed using the `Xspec` spectral-fitting software (Arnaud 1996). Simulations of realistic data from the planned cryogenic imaging spectrometer `X-IFU` onboard the `Athena` X-ray observatory have been performed.

5.5.1 `Xspec` spectral fitting tool

X-ray observations provide, in an exposure time t_{exp}, a number of photon counts C in each energy (or frequency) channel (I) of the spectrometer. It depends on the spectrum of the source ($f(E)$) through the relation:

$$C(I) = \int f(E)\ R(I,\ E)\ dE \times t_{exp} \tag{5.16}$$

where $R(I, E)$ is the instrumental response, i.e., a matrix proportional to the probability that a photon arriving with energy E at the detector entrance is detected in channel I. The instrumental response is considered with the ancillary response file (ARF) and the redistribution matrix file (RMF).
The ARF combines the effective area of the telescope, the filter efficiency, and the detector quantum efficiency. The effective area of the telescope is its geometric area corrected with different effects, including those of reflectivity and vignetting (photons that arrive with an off-axis angle have a lower probability of reaching the focal plane of the telescope). The detector quantum efficiency is a measure of the efficiency of the detector to convert incident photons into electrons. The ARF is a function of the energy of the incident photon.
The RMF is a two-dimensional matrix that relates the incident photon's energy to the energy of the associated count(s). It translates the probability that an incident photon with energy E is detected in a channel I. For a perfect system, this matrix is diagonal: an incident photon is detected in the corresponding channel. In reality, there is a spreading of the observed counts due to the fact that there is a non-zero probability that the charge detected was excited by a photon of higher energy.

In general, it is not possible to derive directly the observed spectrum $f(E)$ from the detected counts $C(I)$ because the inversion of $R(I, E)$ is not unique and sensitive to small changes in $C(I)$. Thus, to derive the physical properties of the source from its observation, parametric physical spectral models $f_p(E)$ are used. With equation (5.16), the expected number of counts $C_p(I)$ based on this specific model can be computed and fitted to the real observation $C(I)$. Here, we used a fit based on the maximization of the likelihood function. The observation $C(I)$ in each energy channel is a realization of the random variable X_I. The likelihood is defined as

$$\mathcal{L} = \prod_I \mathbb{P}\left(X_I = C(I)|p\right)$$

where $\mathbb{P}\left(X_I = C(I)|p\right)$ is the probability to observe $C(I)$ assuming that the emission of the source can be described by the model with the value of parameters $p = (p_1, ...p_m)$, where m is the number of parameters for the model. Maximizing $\mathcal{L}$ finds the values of the parameters that are the more likely to produce the observation.

The physical model that we will use to simulate the observation of an iron line is described by a power-law continuum, the iron line, and the galactic absorption. The background flux will be neglected (see below in section 5.5.3). Thus, the random variable X_I follows a Poisson distribution of parameter λ_I:

$$\mathbb{P}\left(X_I = k\right) = \frac{\lambda_I^k\ e^{-\lambda_I}}{k!}$$

If the model $f_p(E)$ produces the observation $C_p(I)$, the parameter λ_I, which is the mean of the Poisson distribution, equals $C_p(I)$. Thus, the likelihood function is

$$\mathcal{L} = \prod_I \frac{[C_p(I)]^{C(I)}\ \ e^{-C_p(I)}}{[C(I)]!}$$

In practice, in `Xspec`, it is twice the opposite of the likelihood that is minimized (Cash 1979):

$$\begin{aligned}\mathcal{S} = -2\ln\mathcal{L} &= -2\sum_I \left[C(I)\ln\left(C_p(I)\right) - C_p(I) - \ln\left(C(I)!\right)\right] \\ &= -2\sum_I \left[C(I)\left(\ln\left(C_p(I)\right) - \ln\left(C(I)\right)\right) - \left(C_p(I) - C(I)\right)\right]\end{aligned}$$

The best fit is the minimum of $p \to \mathcal{S}(p)$ and provides the value of the parameters $\widehat{p} = (\widehat{p}_1, ..., \widehat{p}_m)$. In `Xspec`, the algorithm that minimizes the statistic $\mathcal{S}$ can converge to any of the local minimum of the function. Thus, it is not guaranteed that the best fit is unique, and this is why, in the following, the quality of the fits is assessed by estimating the uncertainties on the best-fit parameters and checking whether the best-fit values are compatible with the input ones.

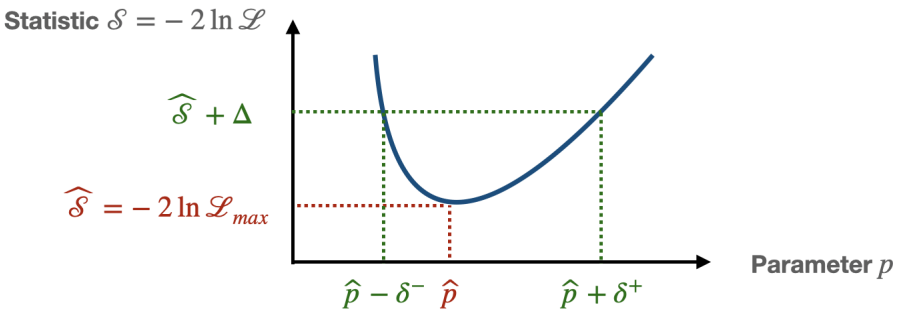

Figure 5.22: Illustration of the parameter error estimation

An important question is then to know what the uncertainty of the fitted parameters is. I do not detail all the methods available in `Xspec` to determine the parameter errors, and here, I focus on the one that is used below.
The confidence interval for each parameter is defined by varying the statistic $\mathcal{S}$ by Δ from the minimum $\widehat{\mathcal{S}}$ found at the best fit. The limits of the confidence intervals for each parameter are given by the values of parameters for which the statistic equals $\widehat{\mathcal{S}} + \Delta$. Figure 5.22 illustrates the method in one dimension: the variation of $\mathcal{S}$ is used to derive the interval for one parameter.
The question is to link the value of Δ to the desired Confidence Level (CL) for the parameter estimation. This means knowing the probability that the statistic $\mathcal{S}$ is in the range $[\widehat{\mathcal{S}};\ \widehat{\mathcal{S}} + \Delta]$. Or, said differently, determining Δ so that the probability that $\mathcal{S}$ in the range $[\mathcal{S};\ \widehat{\mathcal{S}} + \Delta]$ is above a fixed targeted CL $100 \times (1 - \alpha)\%$. This requires knowing the statistics followed by $\mathcal{S}$. In the method used here, $\mathcal{S} - \widehat{\mathcal{S}}$ is assumed to follow a χ^2 distribution and the value of Δ is such that

$$X = \mathcal{S} - \widehat{\mathcal{S}} \sim \chi^2(m)$$
$$\mathbb{P}(X \leq \Delta) = 1 - \alpha = 0.9 \Leftrightarrow P(X > \Delta) = \alpha = 0.1$$

where m is the number of degrees of freedom. These values Δ are tabulated for the χ^2 statistic (see, e.g., Avni (1976)). In the following, I use the error routine of `Xspec`, which derives the intervals independently for each parameter. Thus, for a CL of 90% and $m = 1$, $\Delta = 2.71$.

`Xspec` was used through the `Pyspec` interface.

5.5.2 Model settings

The iron line model introduced in Chapter 4 has been used to explore the capabilities of Athena/X-IFU to detect disc truncation. In the following, the inclination angle (i_{obs}) and the Lamppost height (h_s) are fixed to 30° and 5 R_s, respectively. Likewise, the disc inner radius is fixed at 3 R_s.

Iron line profiles with different values of the disc outer edge radius r_{max} have been used to create an additive table model grid with three parameters: the redshift $z_{K\alpha}$, the flux normalization $F_{K\alpha}$, and r_{max}. The latter is varied from 200 to 1500 R_s to build the model grid. The iron line profile calculated in Chapter 4 is in arbitrary units. In order to give it physical flux values, the integrated iron line flux has been rescaled to match a photon flux of $2.17 \times 10^{-4}\,\mathrm{ph\,s^{-1}\,cm^{-2}}$ equal to the typical integrated flux of the Kα iron line from the Seyfert 1 galaxy MCG-6-30-15 (Vaughan & Edelson 2001).

The iron line profile model is then summed with an absorbed power law.

As a result, the final model is written in `Xspec` terminology as: TBabs × (atable{Iron Line} + zpowerlw). Here, atable{Iron Line} is the iron line table model specifically built for this study as explained above and called in `Xspec` as an additive atable model; zpowerlw is the (possibly redshifted) photon power law model; and TBabs is the standard Tuebingen-Boulder interstellar medium absorption model.

This model eventually includes seven parameters: the hydrogen column density (N_H), r_{max}, the iron line redshift ($z_{K\alpha}$), the iron line flux normalization ($norm_{K\alpha} = F_{K\alpha}/2.17 \times 10^{-4}$, the iron line photon flux normalized to that of MCG-6-30-15), the power-law photon index (Γ), the power-law redshift (z_{PL}), which will be tied to $z_{K\alpha}$, and the power-law flux normalization at 1 keV (ϕ_{PL}).

Figure 5.23 shows the abovementioned model computed for $N_H = 10^{21}\,\mathrm{cm}^{-2}$, $r_{max} = 200\,\mathrm{R}_s$, $z_{K\alpha} = z_{PL} = 0.0077$ (redshift of MCG-6-30-15); $norm_{K\alpha} = 1$ (which means that the integrated photon flux is equal to that of MCG-6-30-15 as published in Vaughan & Edelson (2001)), $\Gamma = 1.6$, and $\phi_{PL} = 3.8 \times 10^{-3}\,\mathrm{ph\,s^{-1}\,cm^{-2}\,keV^{-1}}$. The values of Γ and ϕ_{PL} are representative of the power-law 2-10 keV continuum observed in MCG-6-30-15 soft X-ray spectra as described e.g. in Dauser et al. (2010).

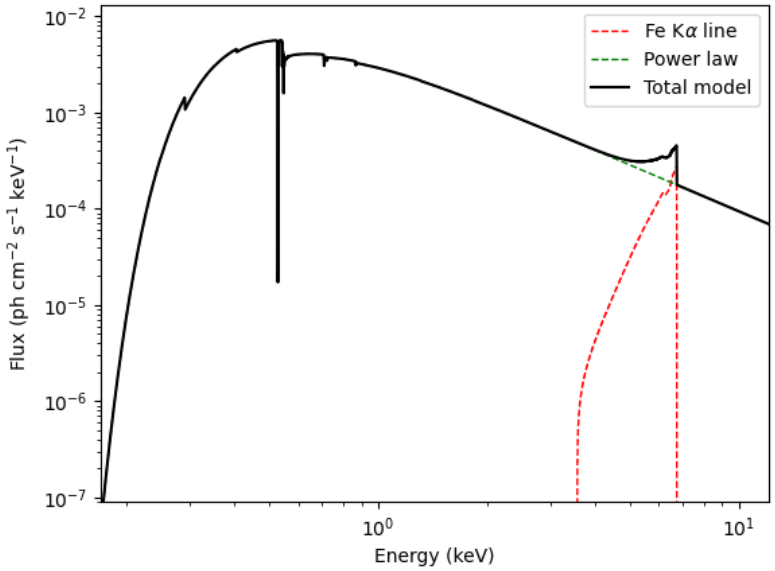

Figure 5.23: `Xspec` model (black) and its components: Iron Kα line model (in red), and absorbed power law (in green). Model parameter values considered in the plot are given in the text.

5.5.3 Simulation setups and fitting

In the simulations described below, r_{max} values are randomly drawn from a uniform distribution between 200 and 1 500 R_s. The iron line and power-law fluxes are scaled with respect to the simulated source luminosity and redshift. For the luminosity, a scaling factor is applied at the parameters $norm_{K\alpha}$ and ϕ_{PL} to rescale the model compared to the 2-10 keV luminosity of MCG-6-30-15 taken equal to $7{\times}10^{42}\,\mathrm{erg\,s^{-1}}$ (McHardy et al. 2005). The luminosity distance d_L of the source is computed from its redshift by using the `astropy.cosmology` redshift_distance module using cosmological parameters from the nine-year WMAP results. The fluxes of the redshifted iron line and power law are then rescaled by applying a factor $(d_{MCG}/d_L)^2$ where $d_{MCG} = 33.2\,\mathrm{Mpc}$ is the distance of MCG-6-30-15

(Raimundo et al. 2013).

Once the model has been defined, `Athena`/`X-IFU` data were simulated for a given exposure time t_{exp} using the `fakeit` command of `Xspec` based on the latest response matrices (ARF, RMF, and background spectrum) available on the `Athena` website.

According to Barret & Cappi (2019), the `X-IFU` background rate for a point-source with an extraction radius of 5 arcsec is less than 2×10^{-4} counts/s. In the simulations described in the following sections, when the fitted parameters are well constrained, the source count rates are generally greater than 10^{-1} count/s, and thus, the background will be considered negligible.

In addition, spectral bins in our simulations have been grouped by using the optimal binning scheme of Kaastra & Bleeker (2016) through the `ftools ftgrouppha`.

Simulated spectra were then fitted using `PyXspec` and the `cstat` statistics (see section 5.5.1). The fit was constrained to converge in 50 iterations. While the redshift of the source was fixed to the input value, all of the other parameters are left free to vary. Since, with real data, we will not know what the model parameters will be, the initial values of the parameters are not taken to the input ones (except for the redshift that we assume to be constrained independently by other multi-wavelength observations). Instead, the initial parameter values used for fitting are chosen in the following way: the N_H value is drawn randomly from a uniform distribution bounded as 1/10 and 10 times the input value; the value of r_{max} is drawn randomly from a uniform distribution between 200 and 1 500 R_s; the iron line and power-law normalizations are drawn randomly from uniform distributions varying from 0.5 to 1.5 times the input normalization values; and Γ is drawn randomly from a uniform distribution between 0 and 4.

Errors on the fitted parameters are computed using the `error` command of `PyXspec` for a CL of 90%. If a new best fit is obtained during the error computation, the error estimation stops and restarts to recalculate the uncertainties based on this newly identified best fit.

5.5.4 Results

5.5.4.1 First simulation: iron line and absorbed power-law continuum at a distance of 33.2 Mpc

In order to demonstrate the capability of `X-IFU` to constrain the value of r_{max}, the source is first assumed to be at the same distance as MCG-6-30-15 (33.2 Mpc; $z = 0.0077$), with an iron line flux of $2.17 \times 10^{-4}\,\mathrm{ph\,s^{-1}\,cm^{-2}}$ (typical photon flux of the iron line Kα observed in MCG-6-30-15). The power-law continuum parameters have been taken on power-law fits to `XMM-Newton` data from MCG-6-30-15 in a typical state (Dauser et al. 2010): 2-10 keV energy flux of $2.5 \times 10^{-11}\,\mathrm{erg\,s^{-1}\,cm^{-2}}$, and a photon index $\Gamma = 1.6$, which translate into a photon flux of $3.8 \times 10^{-3}\,\mathrm{ph\,s^{-1}\,cm^{-2}\,keV^{-1}}$ at 1 keV, absorbed by a hydrogen column density $N_H = 10^{21}\,\mathrm{cm^{-2}}$.

For one given exposure time t_{exp}, 20 simulations for different initial values of r_{max} drawn randomly in the range [200; 1500] R_s are performed. For each of these simulations, the 90% CL uncertainties on the fitted parameters are saved. One-sided errors, $\sigma_{r_{max}}$, are computed as the mean over the positive and negative errors. The mean value of the ratio $\frac{\sigma_{r_{max}}}{r_{max}}$ between the one-sided error on r_{max} and the input r_{max} value is computed by using the 20 simulations.

The same procedure is applied for different t_{exp} until the mean value of $\frac{\sigma_{r_{max}}}{r_{max}}$ is lower than 10%. Figure 5.24 shows the evolution of the mean value of $\frac{\sigma_{r_{max}}}{r_{max}}$, as a function of the exposure time t_{exp}. As we can see, on average, $\sigma_{r_{max}}$ becomes smaller than 10% of the input r_{max} value for $t_{exp} \gtrsim 5\,\mathrm{Ms}$.

Figures 5.25 and 5.26 show "observed" and unfolded spectra for $t_{exp} = 5\,\mathrm{Ms}$ respectively for r_{max}=200 Rs and 1500 Rs. It is worth noticing that the dip feature of the iron line profile around 6.4 keV (for $z \sim 0$) is

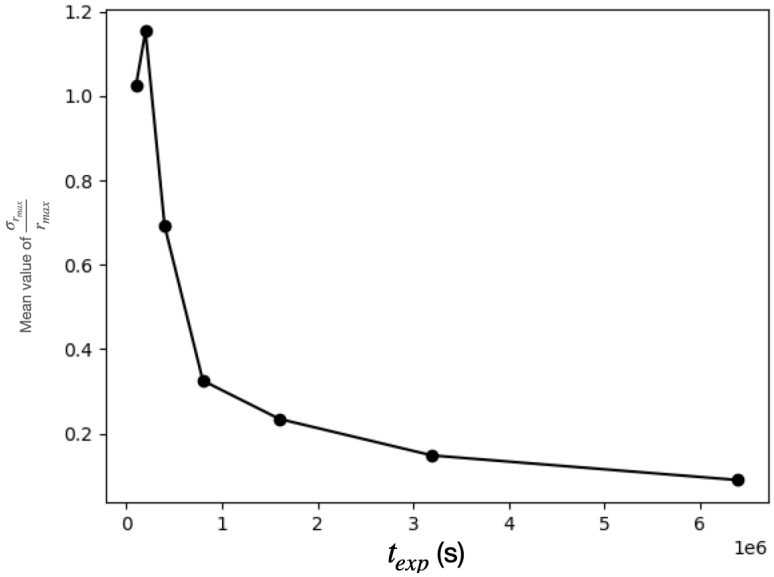

Figure 5.24: Evolution of the mean value of $\frac{\sigma_{rmax}}{r_{max}}$ (averaged over 20 simulations) as a function of t_{exp} for a source at $z = 0.0077$.

well resolved with such a large exposure time, which is certainly why the r_{max} value is well constrained by the fit.

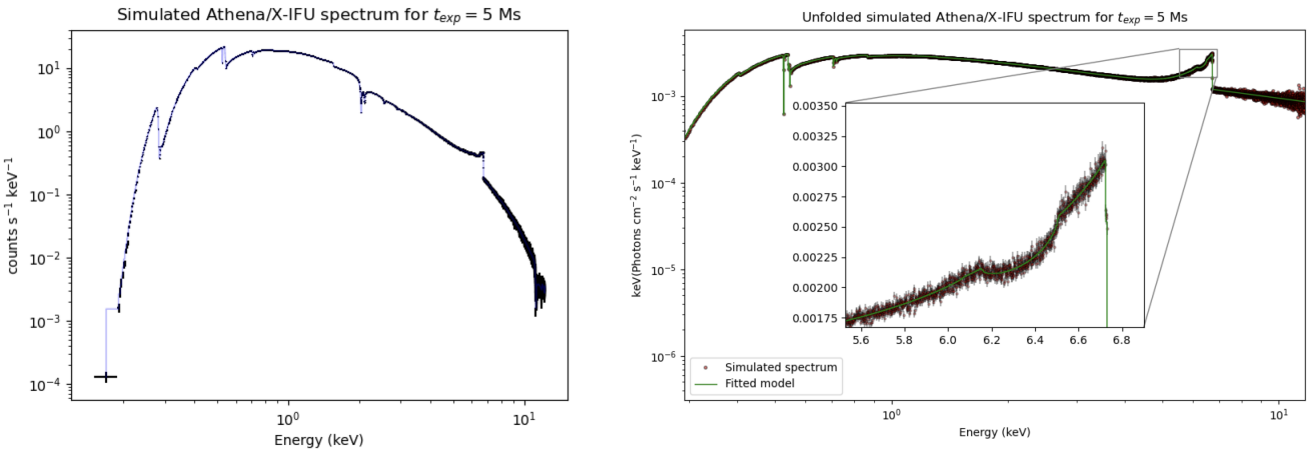

Figure 5.25: Left: observed spectrum (black points) simulated with `fakeit` for $r_{max} = 200\,\mathrm{R}_s$, an exposure time of 5 Ms and a redshift of 0.0077. The blue line shows the input model. Right: unfolded spectrum for the same input parameters.

In addition, Figure 5.27 shows the best fit r_{max} versus the input r_{max} values for the 20 simulations performed for $t_{exp} = 5\,\mathrm{Ms}$. One can see that not only are the uncertainties on the fitted r_{max} values generally small, but also that the best-fit values converge toward the input ones. As expected, a larger scattering is observed at large r_{max}, which is mostly due to the fact that the impact of the disc truncation on the iron line profile is smaller for large r_{max} values than for smaller ones (see Figures 5.1 and 5.3).

In addition, Figure 5.28 shows the ratio between the best fit and the input values for the other fitted parameters and for the 20 simulations. One can see that the values are well constrained, and the ratios fluctuate around 1, which tends to show that the fit is not biased.

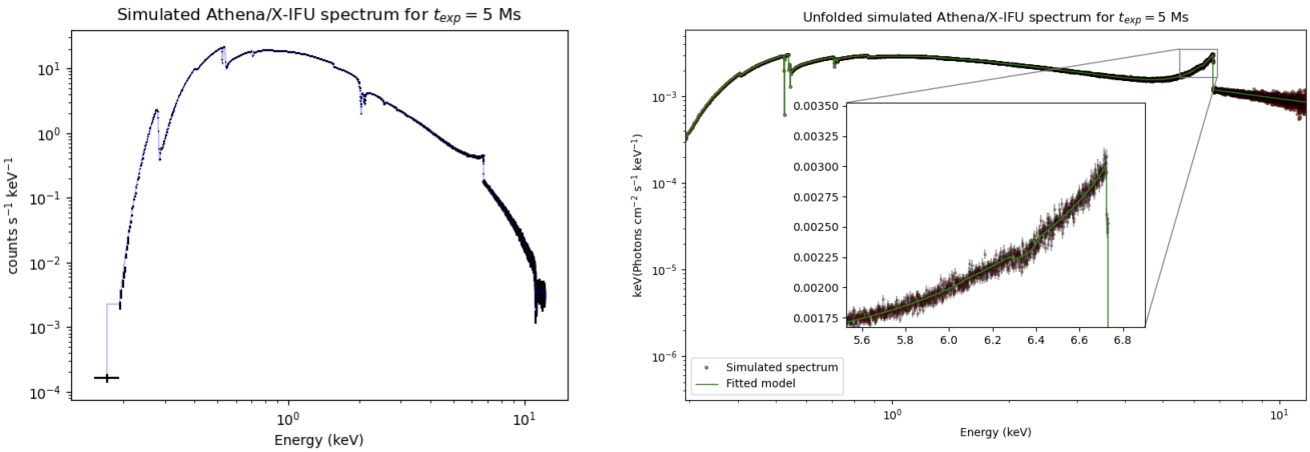

Figure 5.26: Left: observed spectrum (black points) simulated with `fakeit` for $r_{max} = 1500\,R_s$, an exposure time of 5 Ms and a redshift of 0.0077. The blue line shows the input model. Right: unfolded spectrum for the same input parameters.

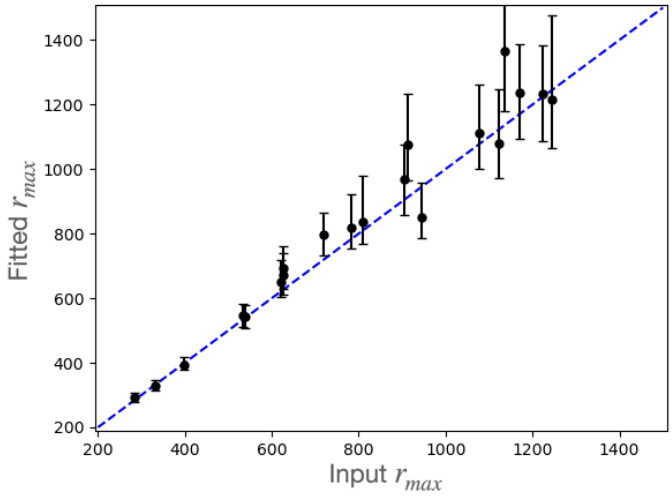

Figure 5.27: Best fit r_{max} values versus the input r_{max} values for 20 simulations performed considering $t_{exp} = 5$ Ms.

5.5.4.2 Second simulations: testing a broader range of parameters

Given the capabilities of `X-IFU` to estimate the r_{max} value as highlighted in section 5.5.4.1, it is tempting to investigate further the configurations (in terms of exposure time, source soft X-ray luminosity, redshift, and iron line intrinsic luminosity) in which `X-IFU` will be able to constrain the r_{max} value.

Varying source luminosity, redshift and exposure times

To do so, I first repeated the simulations described in section 5.5.4.1 but assuming different source luminosities $L_{[2-10]\,keV}$ in the energy range [2; 10] keV, and different redshifts. Simulations have been done for exposure times of 50 ks, 500 ks, 1 Ms and 5 Ms.

Source luminosities between 10^{40} and 10^{45} erg/s are considered based on previous work from Singh et al. (2011). Power-law and iron line flux have been rescaled by a factor equal to $\frac{L_{[2-10]\,keV}}{7\times10^{42}}$, 7×10^{42} erg/s being the [2-10] keV luminosity of MCG-6-30-15 as derived by McHardy et al. (2005).

As before, the input r_{max} values are drawn from a uniform distribution between 200 and 1 500 R_s. 20 simulations are performed for each combination of redshift and luminosity.

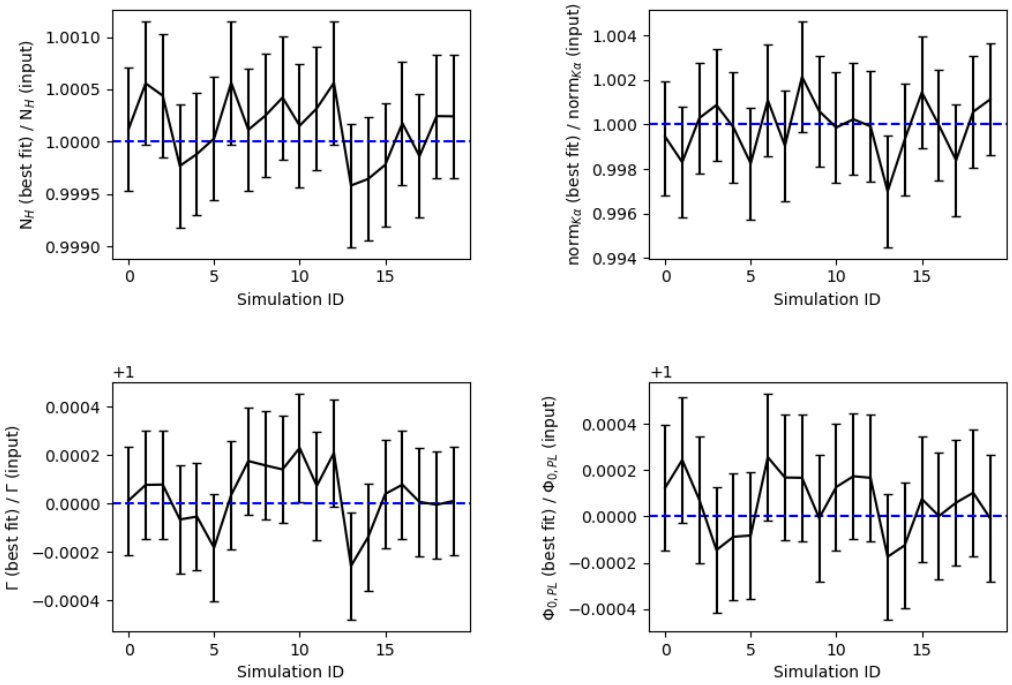

Figure 5.28: Ratio between the best fit and the input values for the other fitted parameters and for the 20 simulations.

Figure 5.30 shows the mean value of $\frac{\sigma_{r_{max}}}{r_{max}}$ (as defined in the previous section) as a function of the redshift and $L_{[2-10]\,keV}$. While not shown on the plots, it was also verified that when the value of r_{max} is properly constrained, the errors on the other fitted parameters are minor too. In addition, it was verified that the fit is not biased, meaning that the fitted values of the different parameters are still compatible with the input values.

As expected, the brightest sources are also those for which the r_{max} value can be constrained more easily. Interestingly, we can see that it will be difficult to constrain r_{max} for sources with a redshift greater than ∼0.1, even with a substantial exposure time. For more reasonable exposure times (50-500 ks), r_{max} can only be estimated for sources in the local universe unless we focus on galaxies with intrinsic luminosity greater than 10^{44} erg/s.

Varying iron line intrinsic luminosity

As a last step, the capability of `X-IFU` to constrain the r_{max} value for intrinsically weaker iron lines compared to that of MCG-6-30-15 was investigated. To do so, the same simulation setup as the one described in section 5.5.4.2 is used. Another scaling factor is applied to the iron line luminosity $L_{K\alpha}$: 1/2, 1/5, and 1/10 to simulate an iron line luminosity respectively equal to 1/2, 1/5, and 1/10 of that of MCG-6-30-15.

Figures 5.30, 5.31, and 5.32 show the results for different redshift and source luminosities and for the same exposure times as those considered before.

Again, for galaxies with intrinsic luminosities higher than $\sim 10^{44}$ erg/s, the r_{max} value can be constrained with small enough uncertainties, even if the iron line luminosity is weaker. However, the situation worsens for weaker sources with greater redshift, particularly if the line brightness is less than 0.2 times that of MCG-6-30-15.

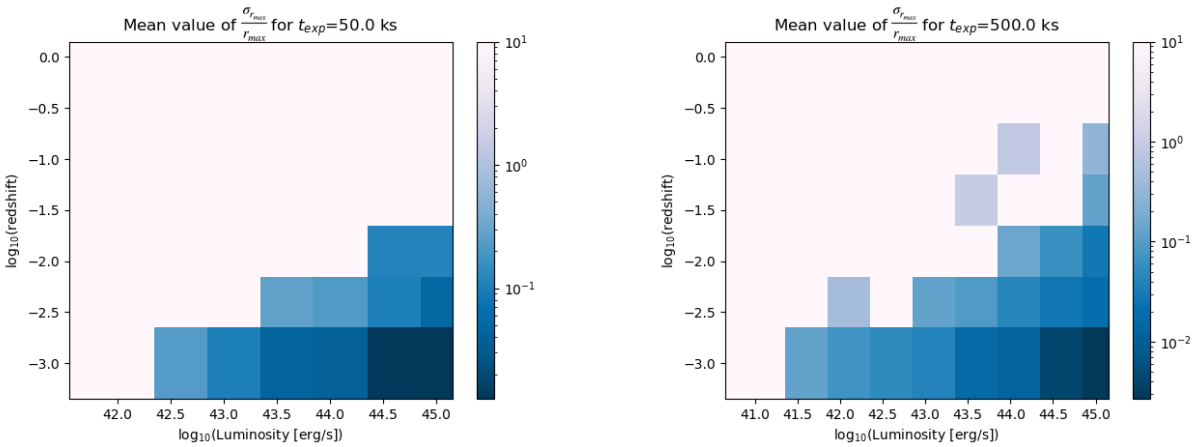

(a) $t_{exp} = 50\,\mathrm{ks}$

(b) $t_{exp} = 500\,\mathrm{ks}$

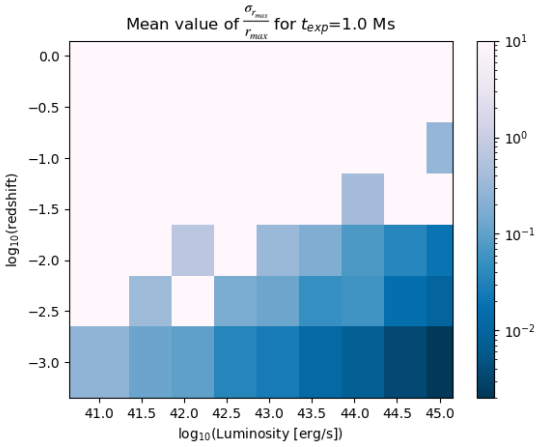

(c) $t_{exp} = 1\,\mathrm{Ms}$

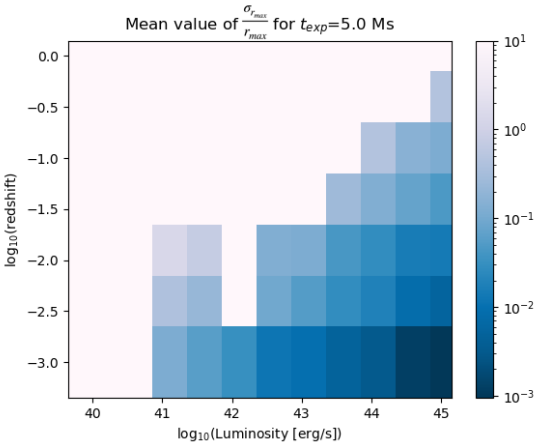

(d) $t_{exp} = 5\,\mathrm{Ms}$

Figure 5.29: Mean value of $\frac{\sigma_{rmax}}{r_{max}}$ as a function of both the redshift and the soft X-ray luminosity $L_{[2-10]\,keV}$. The reader's attention is drawn to the fact that the range of $L_{[2-10]\,keV}$ covered by the x-axis varies from case to case since, for short exposure times, the counting rate is extremely low, and spectrum fitting becomes impossible. The lowest luminosities have, therefore, not been simulated in these cases.

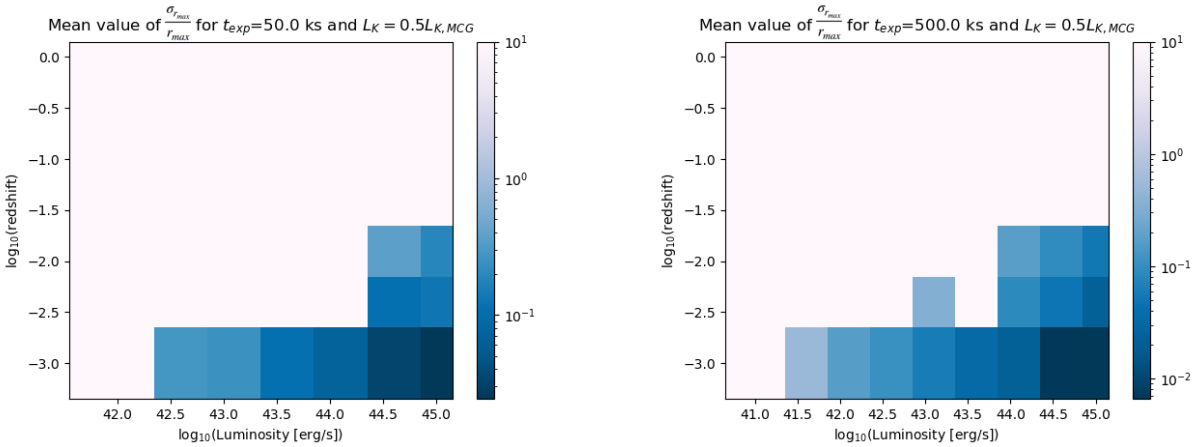

(a) $t_{exp} = 50\,\mathrm{ks}$

(b) $t_{exp} = 500\,\mathrm{ks}$

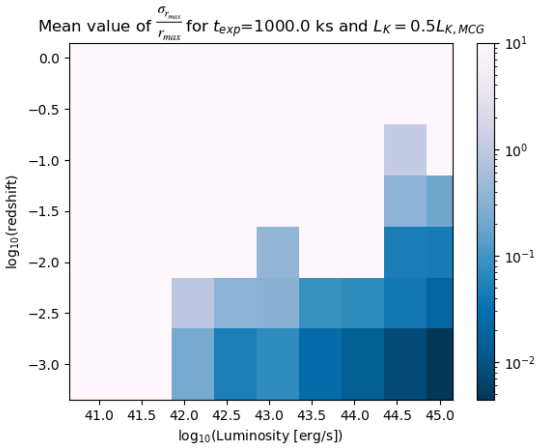

(c) $t_{exp} = 1\,\mathrm{Ms}$

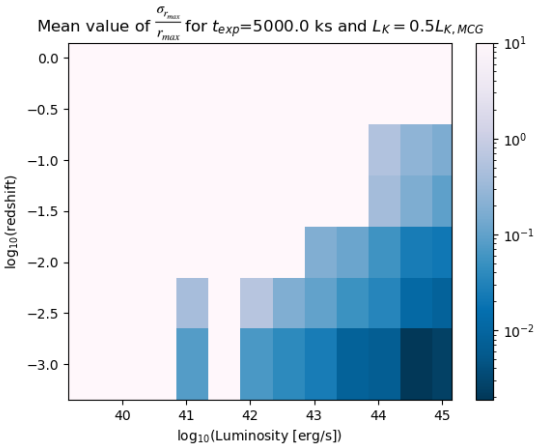

(d) $t_{exp} = 5\,\mathrm{Ms}$

Figure 5.30: Mean value of $\frac{\sigma_{rmax}}{r_{max}}$ as a function of both the redshift and the soft X-ray luminosity $L_{[2-10]\,keV}$ for a Fe Kα line luminosity twice smaller than the one of MCG-6-30-15. The reader's attention is drawn to the fact that the range of $L_{[2-10]\,keV}$ covered by the x-axis varies from case to case since, for short exposure times, the counting rate is extremely low, and spectrum fitting becomes impossible. The lowest luminosities have, therefore, not been simulated in these cases.

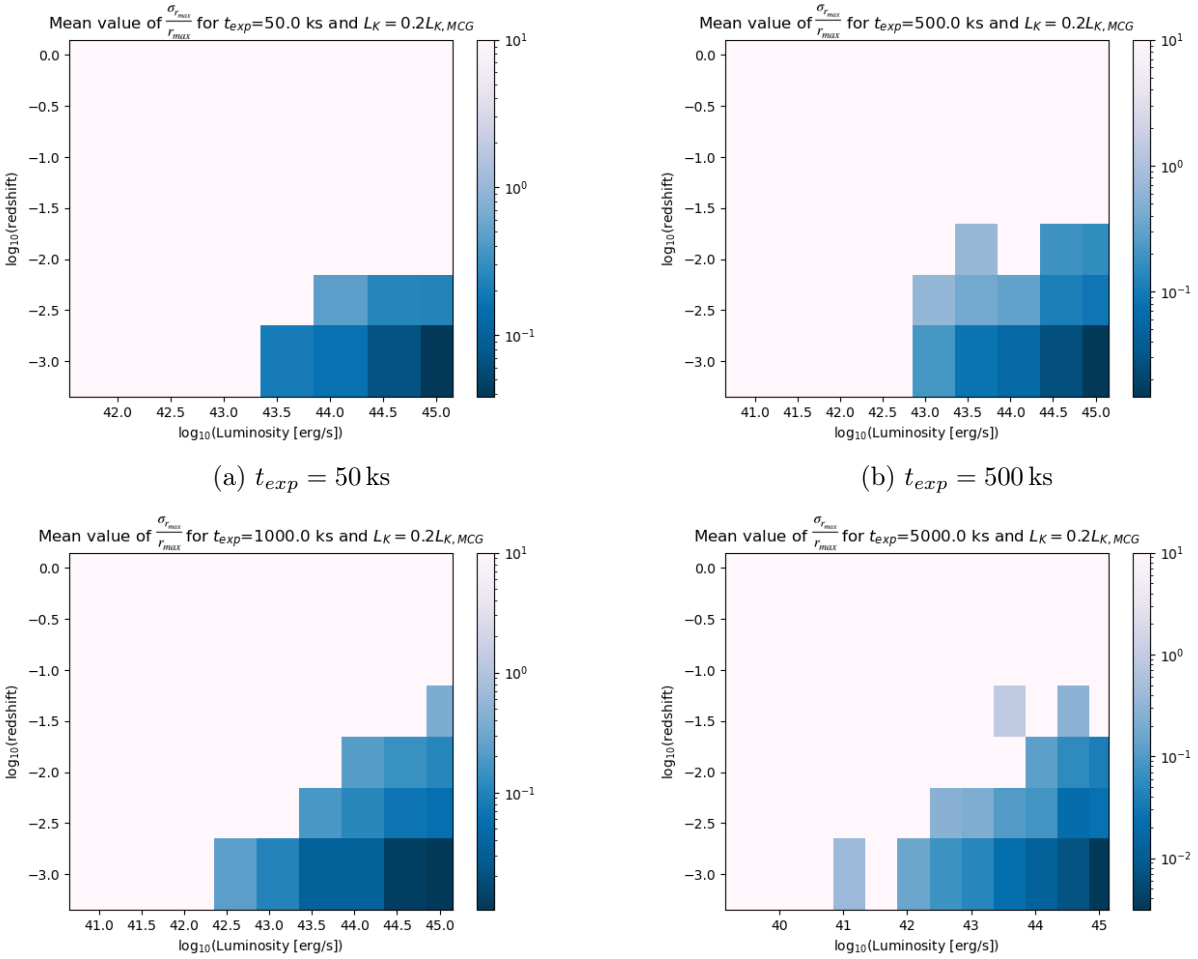

(a) $t_{exp} = 50\,\mathrm{ks}$

(b) $t_{exp} = 500\,\mathrm{ks}$

(c) $t_{exp} = 1\,\mathrm{Ms}$

(d) $t_{exp} = 5\,\mathrm{Ms}$

Figure 5.31: Mean value of $\frac{\sigma_{rmax}}{r_{max}}$ as a function of both the redshift and the soft X-ray luminosity $L_{[2-10]\,keV}$ for a Fe Kα line luminosity 5 times smaller than the one of MCG-6-30-15. The reader's attention is drawn to the fact that the range of $L_{[2-10]\,keV}$ covered by the x-axis varies from case to case since, for short exposure times, the counting rate is extremely low, and spectrum fitting becomes impossible. The lowest luminosities have, therefore, not been simulated in these cases.

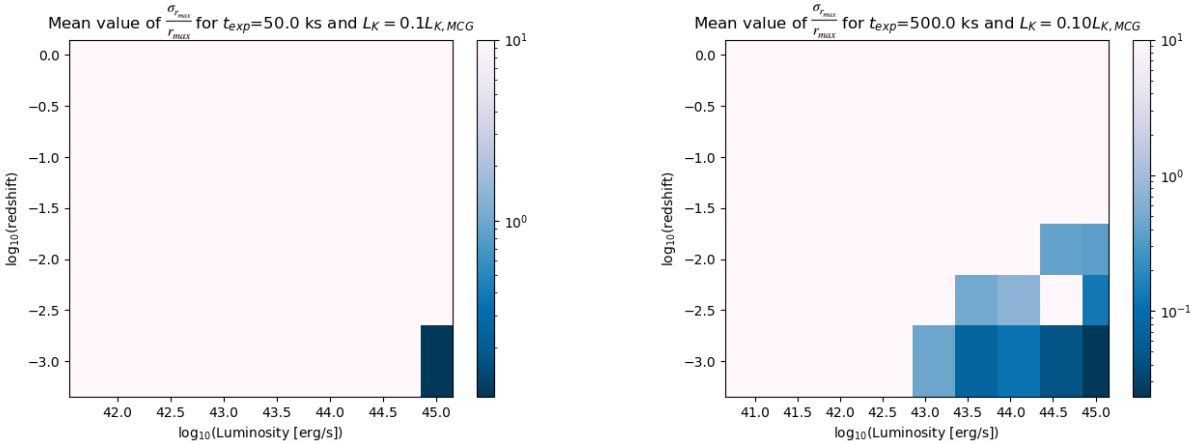

(a) $t_{exp} = 50\,\mathrm{ks}$ (b) $t_{exp} = 500\,\mathrm{ks}$

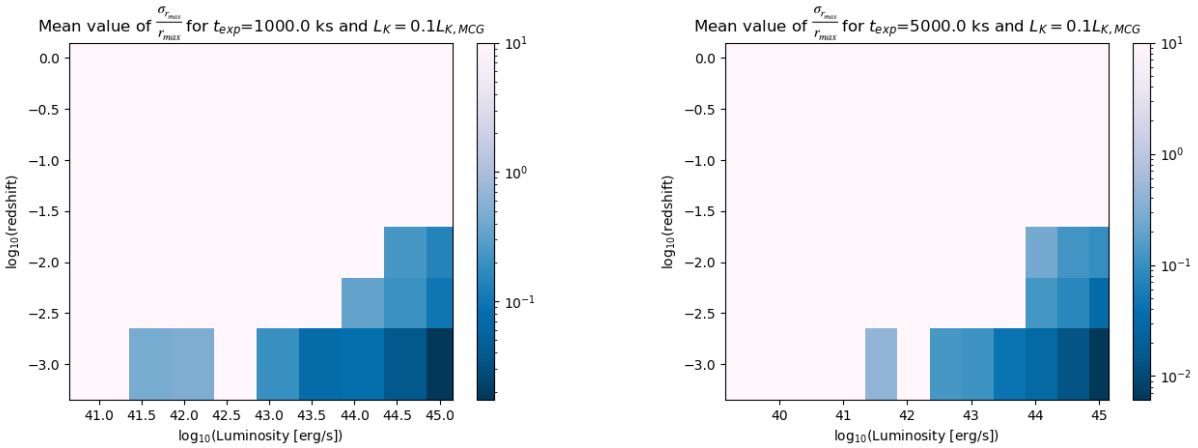

(c) $t_{exp} = 1\,\mathrm{Ms}$ (d) $t_{exp} = 5\,\mathrm{Ms}$

Figure 5.32: Mean value of $\frac{\sigma_{rmax}}{r_{max}}$ as a function of both the redshift and the soft X-ray luminosity $L_{[2-10]\,keV}$ for a Fe Kα line luminosity ten times smaller than the one of MCG-6-30-15. The reader's attention is drawn to the fact that the range of $L_{[2-10]\,keV}$ covered by the x-axis varies from case to case since, for short exposure times, the counting rate is extremely low, and spectrum fitting becomes impossible. The lowest luminosities have, therefore, not been simulated in these cases.

5.5.5 Conclusions and future work

The measure of r_{max} may have important implications on the identification of MBH binaries if this signature is used together with other possible hints of binarity (such as spiral density waves propagating in the disc, disc ellipticity, ...). Based on the simulations performed above, constraining the r_{max} value seems feasible under good conditions, which imply an exposure time long enough ($\gtrsim$ 500 ks), a galaxy in the local universe ($z \lesssim 0.1$) with a 2-10 keV luminosity above $\gtrsim 10^{41}$ erg/s. However, these results should be treated with caution. First, we did not address the capability of constraining r_{max} for other inclinations and lamp-post heights. In addition, the iron line profile simulated here only accounts for the contribution of the accretion disc. However, iron line emission from other external reflection components could also be present and will consequently impact the overall shape of the line. In another hand, if an accretion disc surrounds the secondary black hole, iron line emission from that other component will also contribute to the spectrum, making the data more complicated to interpret.

From an instrumental point of view, the simulations performed above are based on the latest response matrices of `X-IFU`, but more refined simulations that take into account the whole detection and readout chain using the end-to-end simulation tool `SIXTE` would enable to predict more accurately the expected performances of `X-IFU` based on the current knowledge of the instrument. In particular, as underlined in Barret & Cappi (2019), a high-resolution spectrometer such as `X-IFU` might be difficult to calibrate, leading to uncertainty on its effective area and, consequently to systematic errors in the spectra. Further works addressing the question of the observability of the binarity impact on the $K\alpha$ iron line will have to take this into account by allocating systematic errors in addition to the statistical ones.

As said above, the study of the detectability of disc truncation through the iron line suggests that only bright enough systems in the local Universe might be identified using this technique. However, the population of merging MBHs in the local Universe is still an active area of research. Different approaches have been developed to predict the population of merging MBH binaries and the sources detectable by GW detectors: semi-analytical models (see, e.g.Agazie et al. (2023a) and references in section 1.5 therein) and hydrodynamics cosmological simulations (`IllustrisTNG` and `Millennium` simulations, Vogelsberger et al. (2013, 2014), Genel et al. (2014), Springel et al. (2005)). Although providing estimates for the MBH binary population, uncertainties remain on the population of sources that might be detectable by PTA and LISA. The uncertainties are due to the physics at small scales inside galaxies to understand the evolution of MBHs (for instance, the processes that lead to the MBH binary coalescence following the merger of two galaxies or the AGN feedback processes and its consequences on the co-evolution of the MBHs and their host galaxies used in the model) or the initial population of seed BHs at high redshift and their initial evolution (Volonteri et al. 2021). Detections of the GW background and individual sources with PTA will allow testing of these models and predict more accurately the MBH binary population that might be detected with LISA up to high redshift ($z \sim 10$, Amaro-Seoane et al. (2023)).
Agazie et al. (2023a), tried to constrain the population of MBH binaries emitting GWs signal in the 15 years of data from `NANOGrav`. Their results are based on semi-analytical models that combine galaxy masses and merger rate, MBH masses based on the relations between MBH and their host-galaxy, and a prescription for the delay between galaxy merger and MBH merger. Assuming that the detected signal originates from a population of coalescing MBH binaries, they infer that the population is mainly composed of sources at a redshift between $\sim$0.15 and $\sim$0.9 with an orbital separation between $\sim$ 0.1 and 0.01 pc. Their results on the underlying MBH population based on the model to fit the GWs data suggest that below a redshift of 0.1, the population of MBH binary merging per `NANOGrav` GW frequency bin drops from 1000 systems to 10 at z 0.01. These values are given for the highest frequency bin and are slightly higher at lower frequencies. The peak of MBH binaries emitting GWs in the `NANOGrav` frequency bins is at a higher redshift (just below z=1), with more than 10^5 binaries per frequency bin.
Therefore, the population of binaries for which the truncation of the disc might be detected through the observation of the Kα iron line corresponds to a subsample of $\sim$2% of the binaries contributing to

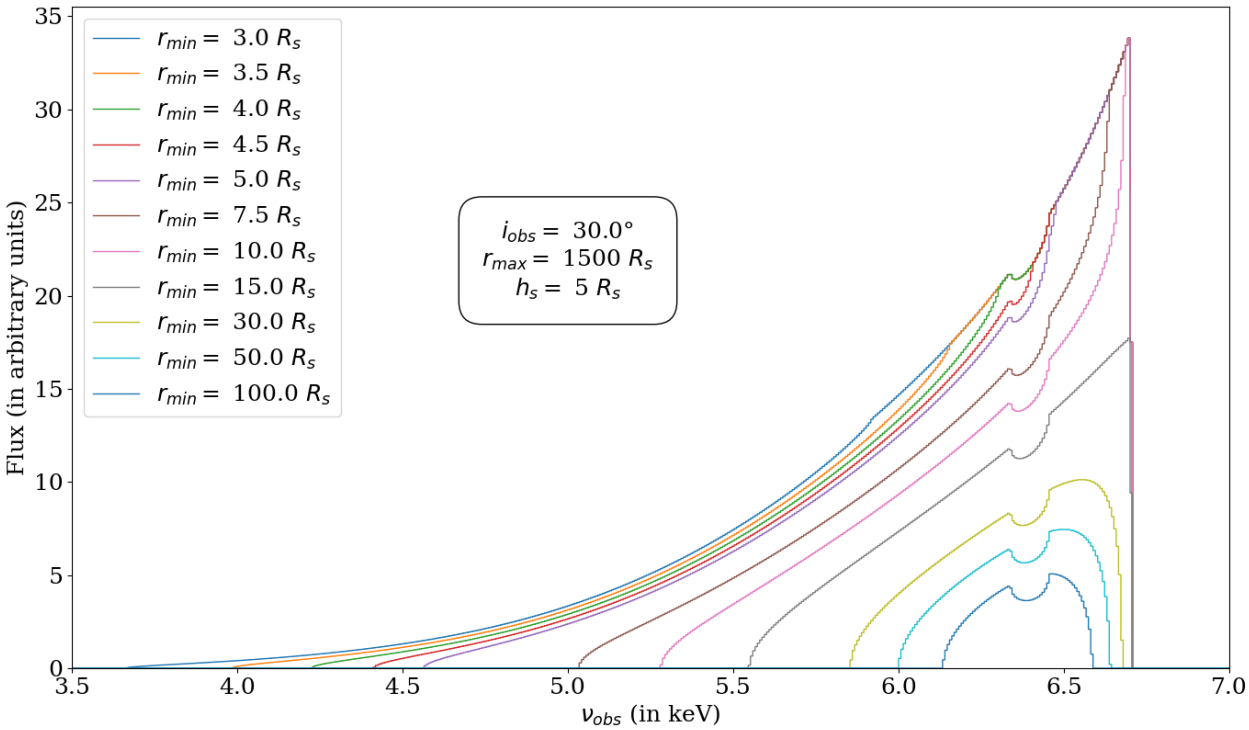

Figure 5.33: **Influence of r_{min} on the iron line profile.**
For all lines, the velocity field in the disc is Keplerian ($u_r = 0$ and $u_\phi = \sqrt{\frac{GM}{r}}$), $r_{max} = 1\ 500\ R_s$, $i_{obs} = 30°$, $q = 3$, and $h_s = 5\ R_s$. The iron line is computed with the *binning* method. There are $N_r = 200\ 000$ cells logarithmically spaced in the radial direction and $N_\phi = 6\ 000$ cells linearly spaced in the azimuthal direction. The flux is computed in $N_{bin} = 640$ bins linearly spaced between 3.2 keV and 7.68 keV ($\Delta\nu = 7$ eV).

the current `NANOGrav` signal under the hypothesis that it is indeed from astrophysical origin and that these galaxies have both a soft X-ray luminosity above $\sim 10^{41}$ erg/s and a Kα iron line intrinsically bright enough. However, the number of MBH binary expected in these parameter space is not zero, and identifying these systems through multi-wavelength observations remains an essential issue for multi-messenger follow-up of the different stages of the binary coalescence. Although constraining r_{max} can be challenging using single exposures from `Athena/X-IFU`, leveraging stacked archival data collected from the same target throughout the mission's lifespan will facilitate reaching the required exposure time for conducting such studies.

5.6 Future work

Impact of the disc inner edge radius

Another important continuation of this work would be considering the impact of r_{min} on these conclusions. Figure 5.33 displays how the iron line profile is impacted by r_{min}, considering a region that extends up to $r_{max} = 1\ 500\ R_s$. Truncating the inner parts of the disc reduces the line's red-shifted and blue-shifted wings due to the semi-relativistic Doppler, and the iron line becomes more symmetric around the emitted frequency $\nu_{em} = 6.4$ keV. This would require not using the approximation $r \gg R_s$ and eventually computing the geodesic in the Kerr metric to account for the central MBH spin.

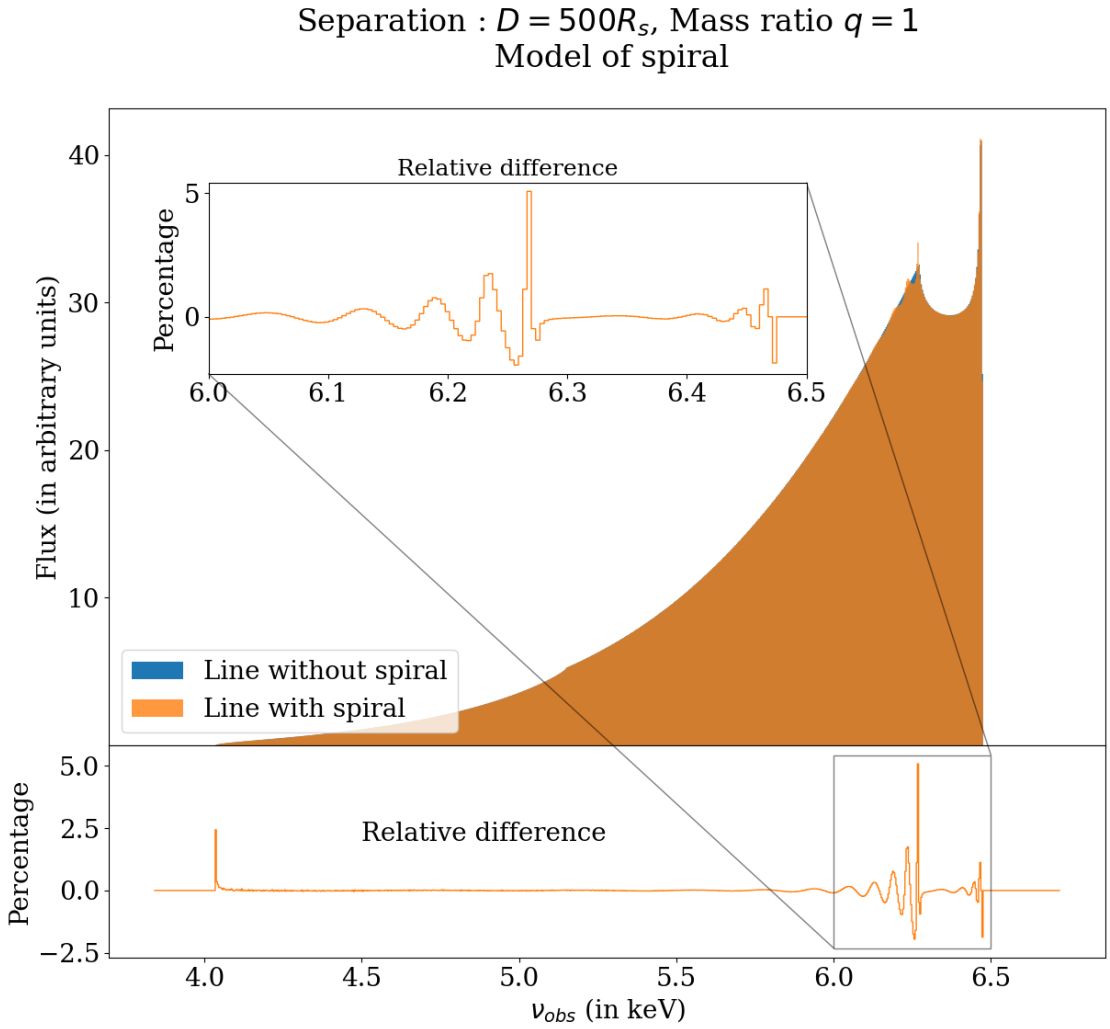

Figure 5.34: **Influence of the spiral wave modeled from the simulation outputs on the iron line profile.**

Wave spiral in the velocity field

Finally, the presence of the MBH companion can also create a density spiral within the disc. The spirals were modeled in Chapter 3. In Figure 5.34, I present the influence of the spiral on the iron line model for one of the accretion disc configurations.

CHAPTER

6

CONCLUSIONS AND PERSPECTIVES

This thesis focused on the search for observational signatures of MBH binary systems with sub-parsec separation. These binaries are observationally elusive because their projected orbital separation is well beyond the current resolution capabilities of EM observatories. Therefore, there is no way other than to use numerical simulations to gain insight into the accreting environment around MBH binaries and to predict observational signatures that can distinguish them from isolated AGNs.

During my Ph.D., I focused on studying early MBH binaries whose separation is of the same order of magnitude as the standard size of an isolated AGNs disc. Hence, one can consider that an initial accretion disc, likely orbiting around the most massive MBH, is still present in the early MBH binary. The first objective of this Ph.D. is to investigate the impact of the gravitational influence of the least massive MBH upon the accretion disc surrounding the primary MBH of the binary. The second objective is to explore how the changes in the disc structure can impact the iron Kα line profile and whether it could be distinguished from the profile emitted by the disc around an isolated AGN.

6.1 Summary

During the first part of my Ph.D., I worked on numerical simulations designed to study the accretion disc around one of the MBHs and under the gravitational influence of the MBH companion.
Chapter 2 presents the numerical setup for the simulations. The simulation grid is centered on one of the MBHs, while the companion is outside the accretion disc. During the initial stages of the inspiral phase, the binary orbital decay, caused by the emission of GWs, is slow compared to its orbital period. Therefore, the MBH companion is assumed to be in a fixed circular orbit. The impact of the MBH companion is stronger in the outer parts of the disc, where the gravitational influence of the primary MBH and, more specifically, its GR on the disc are fainter. Therefore, the disc is described with the hydrodynamic equations solved with the `MPI-AMRVAC` code (Keppens et al. 2012; van der Holst et al. 2012). The simulations are carried out in two dimensions since the accretion discs are expected to align with the binary orbital plane. To describe the gravitational influence of the primary MBH on its surrounding disc, a Paczyński & Wiita (1980) potential is used to simulate the disc down to the ISCO. However, the simulated disc does not reach the MBH companion's ISCO, so its gravitational influence on the disc is considered Newtonian in our simulations.
This numerical setup is used to explore the impact of the MBH companion on the accretion disc structure for different values of the MBH binary orbital separation and mass ratio. It starts with large separations. As the disc is truncated under the gravitational influence of the MBH companion, the

same numerical setup can be used to simulate the disc with smaller orbital separations between the two MBHs. We only considered orbital separations for which the orbital decay remains slow compared to the orbital period. Hence, the MBH companion remains in a fixed circular orbit, and only the initial conditions are adapted to study different separation values.

In the simulations, the outer parts of the disc are truncated by the gravitational influence of the MBH companion. Non-axisymmetric features, such as a two-arm spiral, appear at the beginning and remain throughout the simulation, although displaying smaller amplitude with time. The final stable shape of the disc is elliptical.
Chapter 3 discusses how the MBH binary orbital parameters affect the truncation of the disc and the two-arm spiral observed at the beginning of the simulation. The definition of the disc outer edge considers the aim to explore the influence of disc truncation on the EM emission compared to that of isolated AGNs. It thus relies on the density drop at the disc outer edge. The discussion on the spiral considers a two-arm model with a logarithmic shape. This is the self-similar solution that dominates in the disc outer parts when considering a linearized perturbation of the disc due to the tidal effect of the companion. The impact of the binary orbital parameters on the disc ellipticity has been studied by Peggy Varniere and Fabien Casse and will be presented in the forthcoming article (see the draft version in Appendix A).

The second part of my Ph.D. was dedicated to studying how the changes in the disc structure induced by the MBH companion gravitational influence can impact the Kα iron line profile. The spatial resolution required to compute the iron line is more extensive than the spatial resolution in the code `AMRVAC`. Therefore, computing the iron line would require interpolating the simulation points. To begin with, the initial aim was to explore each of the three effects mentioned above separately with analytic formulas. I only had time to examine the impact of the truncation of the disc on the iron line profile.

Chapter 4 presents the model used to compute the iron line broadening due to the central MBH's gravitational influence. The GR effects of the primary MBH on the iron line photons are considered in a Schwarzschild metric. The geodesic parameters are computed in the same approximation as in Hartnoll & Blackman (2000, 2001, 2002): a first-order expansion of the geodesic equations. This assumption simplifies the computation of the geodesic parameters and is used in our case because the effects we aim to study occur in the outer parts of the disc. The commonly used Lamppost model is considered to model the illumination of the disc by the hard X-ray source.
The numerical approach employed to compute the iron line is to divide the disc into elementary cells. The iron line flux is computed in frequency bins given as an input. The observed iron line flux in each bin is the sum of the flux contributions from each cell in which the observed frequency falls within the considered bin. The level of spatial resolution necessary to describe the disc depends on the spectral resolution used to compute the line, as described in section 4.2.1.

Chapter 5 examines how the truncation of the disc outer parts affects the iron line profile. As the iron line profiles degenerate for different configurations (disc inner and outer edge radii, inclination of the disc compared to the observer's line of sight, distance between the point-source corona and the central BH), the influence of the other parameter values is also considered.
By comparing the iron line profile with that associated with the accretion disk of a single AGN, we investigate whether the iron line profile can be used as a diagnostic to identify truncated accretion disc and, hence, candidate MBH binary systems. A preliminary study investigates the influence of the binary orbital parameters on the detectability of disc truncation using the theoretical iron line profiles computed with the method presented in Chapter 4.
The theoretical line profiles are then used with `Xspec` to model more realistic observations of iron lines involving an absorbed power-law continuum together with the iron line profiles as computed in Chapter 4 and normalized with physical values of the integrated flux between the continuum and the

line. The detectability of disc truncation is explored for different values of the source luminosity, the redshift, exposure times, and the intrinsic luminosity of the iron line.

6.2 Conclusions and perspectives

The numerical setup of the hydrodynamical simulations was designed to study the MBH binaries in the early stages of the inspiral. This corresponds to a stage of MBH binaries after the hardening phase. In this precedent phase, the interaction of the binary with its accreting environment might be crucial to shrink the orbital separation and solve the last parsec problem. In the phase studied here, the two MBHs are still sufficiently apart from each other not to be in their final steps. In this following phase, the GR effects on the binary orbital evolution and the accreting environment are primordial.
The numerical simulations focus on the accretion disc around one of the MBHs and explore the gravitational impact of the companion on the disc structure. This work completes the numerical work on MBH binaries in the inspiral phase, which mainly focused on the circumbinary disc. Due to the very large difference between the gas dynamical time at the ISCO and the binary orbital period, the simulations were challenging to design.
The interest of these simulations is that they describe the disc around a MBH with a high spatial resolution and simulate the disc down to inside its inner edge. The numerical work focusing on these stages of the merger mainly focuses on the accretion from the circumbinary disc. It does not resolve the inner edge of the disc around each MBH with high radial resolution. For instance, the binary systems targeted by our simulations are comparable with the study by Westernacher-Schneider et al. (2022). Their highest spatial resolution is about 3.1 R_s. They consider a typical binary with a separation $D = 1\ 275\ R_s$. In our case, for $D = 1\ 000\ R_s$ or $D = 1\ 500\ R_s$, the resolution at the inner edge is about 0.02 R_s. Due to the logarithmic spacing of the radial resolution, the resolution at the simulation's outer edge is 8 R_s and 13 R_s, respectively.
In this work, we focused on the impact of the MBH on the disc outer parts, where its influence is the strongest. The simulations show that the disc outer parts are truncated, a two-arm spiral pattern appears in the disc, and the overall shape of the disc becomes elliptic. The influence of the binary orbital parameters on these structural changes was explored.

The systems we are studying emit GWs in the PTA detectability waveband or have just started emitting in the LISA one. Hence, they could be detected by these GW detectors. However, these systems are far from the final merger, so the localization of the source in the sky contains thousands of AGNs. Therefore, it is crucial to distinguish the emission of such a system from the emission of an isolated AGN to identify the source of the GW detection. This will allow monitoring of the different stages of the coalescence with multi-messenger observations. The impact of the MBH companion on the disc structure can be used to explore EM signatures of its presence at different wavelengths. During the second part of my Ph.D., I focused on studying the profile of the iron Kα emission line.

The effects that we aim to study are non-axisymmetric. Therefore, using iron line models available with `Xspec` is not directly possible. We developed a model to compute the iron line and its relativistic broadening to account for the two-arm spiral pattern and the elliptic shape. Due to time constraints, I only had time to use this model to study the truncation of the disc outer parts. However, the numerical setup I have created will easily be adapted to simulate the impact of the spiral pattern as well as the disc ellipticity on the iron line profile.
A preliminary study shows that removing iron line material from the outer parts of the disc impacts the iron line profile. The maximal error in the flux in each bin associated with theoretical line profiles to detect disc truncation with the presented method depends on the system's characteristics. Typically, for an error of 2% in the flux in each bin of spectral width 7 eV, the truncation of the disc is identified up to an outer edge radius of 1 000 R_s.
A more realistic study realized with `Xspec` to model observations with `Athena/X-IFU` suggests that the detection of the disc is possible only for systems in the local universe ($z \lesssim 0.1$) with a [2-10]

keV luminosity above 10^{41} erg/s. The MBH binary population is small (e.g., Agazie et al. (2023a)), with a number of sources per `NANOGrav` frequency bins (of width 1.98nHz) comprised between 1000 at a redshift of 0.1 and 100 at a redshift of 0.01. Therefore, the population of binaries for which the truncation of the disc might be detected through the observation of the Kα iron line corresponds to a subsample of $\sim$2% of the binaries contributing to the current `NANOGrav` signal under the hypothesis that it is indeed from astrophysical origin and that these galaxies have both a soft X-ray luminosity above $\sim 10^{41}$ erg/s and a Kα iron line intrinsically bright enough.

Using equation (3.1), the orbital parameters corresponding to these systems have orbital periods and separations

$$T_{orb} \simeq (40-50) \text{ days} \times \frac{M_1}{10^6 M_\odot}$$
$$D \simeq (1-3) \times 10^{-4} \text{ pc } \frac{M_1}{10^6 \ M_\odot}$$

depending on the mass ratio value between 1 and 10^{-4}. Thus, the temporal variability of these systems could also be detected. For instance, they have the orbital parameters targeted by the search for temporal variability due to Doppler boosting, as presented in section 1.3.2. The more massive systems are also targets for optical emission line offset research or reverberation mapping studies (section 1.3.2). When considering accretion from the circumbinary disc, these systems also reveal variability due to the accretion flows (e.g., Westernacher-Schneider et al. (2022)).

6.3 Future work

Eracleous et al. (1995) studied the impact of elliptic discs on Hα lines emitted at higher distances from the central MBH. Hartnoll & Blackman (2002) present the impact of a spiral (although not due to tidal effects and thus having a structure different) on the iron line profile, and I show in the conclusion of Chapter 5 preliminary insight into the impact of the spiral model presented in Chapter 3 on the iron line profile. All these effects can be understood independently and combined to predict how they jointly impact the iron line profile. The study by Eracleous et al. (1995) considers the pericenters of the inner and outer edges of the disc at 500 R_s and 2 500 R_s, respectively. The line profile double peaks can have a relative intensity that is inverted compared lines emitting by circular discs (for which the red peak is lower than the blue peak). This effect is due to the semi-relativistic Doppler shift due to the velocity field of the emitters in the disc. In the case of the iron line, the emitting region is closer to the central MBH. Thus, the effect of eccentricity on the iron line is expected to be more noticeable.

These effects can be considered in realistic observation models using `Xspec`, as done in section 5.5 for the disc truncation. The preliminary study on the detectability of the disc truncation emphasizes the importance of the inclination angle and the corona height, which remain to be considered for the analysis with `Xspec`. The effects of the disc ellipticity and the spiral pattern in the disc can be investigated to model realistic observations of iron line profiles with `Athena/X-IFU`.

Computing the iron line without using a first-order expansion of the geodesic equations would more precisely consider the iron line flux emitted in the inner parts. As the iron line profiles degenerate with the different parameters (disc inner and outer edge radii, inclination of the disc compared to the observer's line of sight, distance between the point-source corona and the central black hole), the value of the disc inner edge might be crucial to study the detectability of the disc truncation. Initially, we did not consider this parameter, as the effects studied here occur in the disc outer region.
Furthermore, the disc inner edge radius is linked to the spin of the central MBH (the value of the ISCO in a Kerr metric varies with the spin). This was not considered when simulating the disc with the code `AMRVAC`. We focused on the impact of the MBH companion on the disc's outer parts.

The inner parts of the disc could also exhibit non-axisymmetric features that might affect the disc emission at a detectable level. Casse et al. (2017) show that studying the gas dynamics in the inner parts of the disc with a pseudo-Newtonian framework is not necessarily problematic. The emission of the disc must, however, be computed in the GR framework.
Nevertheless, in the simulations presented here, the disc inner edge extends compared to its initial position. This is because the Paczsynki-Wiita potential is used, which places the simulation inner edge close to the last stable circular orbit (2.5 R_s). A GR framework would enable simulating the disc down to a lower radius without the fluid velocity exceeding the speed of light. This would allow exploring the MBH's impact on the disc inner parts.
If interesting features are found in the disc's inner parts, computing their detectability through the iron line profile would require using an iron line model that does not consider a first-order expansion of the geodesic equations and accounts for the spin of the central MBH. Thus, one would have to solve the Kerr geodesic equations using a GR ray-tracing code as `Gyoto` (Vincent et al. 2011).

Developing a model to compute the impact of non-axisymmetric features in the disc inner parts in a Kerr metric would also allow computing iron line profiles emitted by the disc around each MBH at more advanced stages of the merger.

In Chapters 2 and 3, numerical simulations were conducted with a MBH companion orbiting in a circular motion. However, the binary orbital motion is expected to be elliptical. This elliptical orbit could affect the disc structure and, thus, the EM emission (e.g., Hayasaki & Okazaki (2004, 2006) in the context of binary stars).

BIBLIOGRAPHY

Abramowicz, M. A., Chen, X., Kato, S., Lasota, J.-P., & Regev, O. 1995, The Astrophysical Journal, 438, L37

Abramowicz, M. A., Chen, X.-M., Granath, M., & Lasota, J.-P. 1996, The Astrophysical Journal, 471, 762

Abramowicz, M. A., Czerny, B., Lasota, J. P., & Szuszkiewicz, E. 1988, The Astrophysical Journal, 332, 646

Abramowicz, M. A. & Fragile, P. C. 2013, Living Reviews in Relativity, 16, 1

Afzal, A., Agazie, G., Anumarlapudi, A., et al. 2023, The Astrophysical Journal Letters, 951, L11

Agazie, G., Anumarlapudi, A., Archibald, A. M., et al. 2023a, The NANOGrav 15-Year Data Set: Bayesian Limits on Gravitational Waves from Individual Supermassive Black Hole Binaries

Agazie, G., Anumarlapudi, A., Archibald, A. M., et al. 2023b, The Astrophysical Journal, 952, L37

Aly, H., Dehnen, W., Nixon, C., & King, A. 2015, Monthly Notices of the Royal Astronomical Society, 449, 65

Amaro-Seoane, P., Andrews, J., Arca Sedda, M., et al. 2023, Living Reviews in Relativity, 26, 2

Antoniadis, J., Arumugam, P., Arumugam, S., et al. 2023, The Second Data Release from the European Pulsar Timing Array: V. Implications for Massive Black Holes, Dark Matter and the Early Universe

Antonucci, R. 1993, Annual Review of Astronomy and Astrophysics, 31, 473

Armitage, P. J. & Murray, J. R. 1998, Monthly Notices of the Royal Astronomical Society, 297, L81

Armitage, P. J. & Natarajan, P. 2002, The Astrophysical Journal, 567, L9

Armitage, P. J. & Natarajan, P. 2005, The Astrophysical Journal, 634, 921

Arnaud, K. A. 1996, Astronomical Data Analysis Software and Systems V, 101, 17

Artemova, I. V., Bjoernsson, G., & Novikov, I. D. 1996, The Astrophysical Journal, 461, 565

Artymowicz, P. 1993a, The Astrophysical Journal, 419, 166

Artymowicz, P. 1993b, The Astrophysical Journal, 419, 155

Arzamasskiy, L. & Rafikov, R. R. 2018, The Astrophysical Journal, 854, 84

Avni, Y. 1976, The Astrophysical Journal, 210, 642

Ayzenberg, D., Blackburn, L., Brito, R., et al. 2023, Fundamental Physics Opportunities with the Next-Generation Event Horizon Telescope

Babak, S. & Sesana, A. 2012, Physical Review D, 85, 044034

Balbus, S. A. & Hawley, J. F. 1991, The Astrophysical Journal, 376, 214

Balbus, S. A. & Hawley, J. F. 1992, The Astrophysical Journal, 400, 610

Bambi, C., Cárdenas-Avendaño, A., Dauser, T., García, J. A., & Nampalliwar, S. 2017, The Astrophysical Journal, 842, 76

Bardeen, J. M. & Petterson, J. A. 1975, The Astrophysical Journal, 195, L65

Barret, D., Albouys, V., den Herder, J.-W., et al. 2023, Experimental Astronomy, 55, 373

Barret, D. & Cappi, M. 2019, Astronomy & Astrophysics, 628, A5

Barret, D., Trong, T. L., den Herder, J.-W., et al. 2016, in Space Telescopes and Instrumentation 2016: Ultraviolet to Gamma Ray, Vol. 9905 (SPIE), 714–754

Beckwith, K. & Done, C. 2004, Progress of Theoretical Physics Supplement, 155

Begelman, M. C., Blandford, R. D., & Rees, M. J. 1980, Nature, 287, 307

Begelman, M. C., McKee, C. F., & Shields, G. A. 1983, The Astrophysical Journal, 271, 70

Begelman, M. C., Volonteri, M., & Rees, M. J. 2006, Monthly Notices of the Royal Astronomical Society, 370, 289

Binney, J. & Tremaine, S. 2008, Galactic Dynamics: Second Edition, rev - revised, 2 edn. (Princeton University Press)

Bîrzan, L., Rafferty, D. A., Brüggen, M., et al. 2020, Monthly Notices of the Royal Astronomical Society, 496, 2613

Blandford, R. D., Netzer, H., Woltjer, L., Courvoisier, T. J. L., & Mayor, M. 1990, Active Galactic Nuclei, 97

Blandford, R. D. & Payne, D. G. 1982, Monthly Notices of the Royal Astronomical Society, 199, 883

Blandford, R. D. & Znajek, R. L. 1977, Monthly Notices of the Royal Astronomical Society, 179, 433

Blondin, J. M. 2000, New Astronomy, 5, 53

Blumenthal, G. R. & Gould, R. J. 1970, Reviews of Modern Physics, 42, 237

Blustin, A. J., Page, M. J., Fuerst, S. V., Branduardi-Raymont, G., & Ashton, C. E. 2005, Astronomy & Astrophysics, 431, 111

Bode, T., Bogdanović, T., Haas, R., et al. 2011, The Astrophysical Journal, 744, 45

Bode, T., Haas, R., Bogdanović, T., Laguna, P., & Shoemaker, D. 2010, The Astrophysical Journal, 715, 1117

Boffin, H. M. J. 2001, Astrotomography, Indirect Imaging Methods in Observational Astronomy, 573, 69

Bonetti, M., Sesana, A., Haardt, F., Barausse, E., & Colpi, M. 2019, Monthly Notices of the Royal Astronomical Society, 486, 4044

Bortolas, E., Mapelli, M., & Spera, M. 2018, Monthly Notices of the Royal Astronomical Society, 474, 1054

Bourne, M. A., Fiacconi, D., Sijacki, D., Piotrowska, J. M., & Koudmani, S. 2023, Dynamics and Spin Alignment in Massive, Gravito-Turbulent Circumbinary Discs around Supermassive Black Hole Binaries

Bowen, D. B., Mewes, V., Campanelli, M., et al. 2018, The Astrophysical Journal, 853, L17

Breiding, P., Burke-Spolaor, S., Eracleous, M., et al. 2021, The Astrophysical Journal, 914, 37

Bromley, B. C., Chen, K., & Miller, W. A. 1997, The Astrophysical Journal, 475, 57

Canton, T. D., Mangiagli, A., Noble, S. C., et al. 2019, The Astrophysical Journal, 886, 146

Cappi, M., Mihara, T., Matsuoka, M., et al. 1996, The Astrophysical Journal, 458, 149

Cash, W. 1979, The Astrophysical Journal, 228, 939

Casse, F., Varniere, P., & Meliani, Z. 2017, Monthly Notices of the Royal Astronomical Society, 464, 3704

Cattorini, F., Giacomazzo, B., Colpi, M., & Haardt, F. 2023, GRMHD Simulations of Accretion Flows onto Unequal-Mass, Precessing Massive Binary Black Hole Mergers

Cattorini, F., Maggioni, S., Giacomazzo, B., et al. 2022, The Astrophysical Journal Letters, 930, L1

Chandrasekhar, S. 1943, The Astrophysical Journal, 97, 255

Charisi, M., Bartos, I., Haiman, Z., et al. 2016, Monthly Notices of the Royal Astronomical Society, 463, 2145

Charisi, M., Haiman, Z., Schiminovich, D., & D'Orazio, D. J. 2018, Monthly Notices of the Royal Astronomical Society, 476, 4617

Charisi, M., Taylor, S. R., Runnoe, J., Bogdanovic, T., & Trump, J. R. 2022, Monthly Notices of the Royal Astronomical Society, 510, 5929

Collin, S. & Huré, J.-M. 2001, Astronomy & Astrophysics, 372, 50

Collin-Souffrin, S. & Dumont, A. M. 1990, Astronomy and Astrophysics, 229, 292

Colpi, M. 2014, Space Science Reviews, 183, 189

Combi, L., Armengol, F. G. L., Campanelli, M., et al. 2022, The Astrophysical Journal, 928, 187

Cornachione, M. A. & Morgan, C. W. 2020, The Astrophysical Journal, 895, 93

Cuadra, J., Armitage, P. J., Alexander, R. D., & Begelman, M. C. 2009, Monthly Notices of the Royal Astronomical Society, 393, 1423

Cunningham, C. T. 1975, The Astrophysical Journal, 202, 788

d'Ascoli, S., Noble, S. C., Bowen, D. B., et al. 2018, The Astrophysical Journal, 865, 140

Dauser, T., Garcia, J., Wilms, J., et al. 2013, Monthly Notices of the Royal Astronomical Society, 430, 1694

Dauser, T., Wilms, J., Reynolds, C. S., & Brenneman, L. W. 2010, Monthly Notices of the Royal Astronomical Society, 409, 1534

Davelaar, J. & Haiman, Z. 2022, Physical Review Letters, 128, 191101

De Rosa, A., Vignali, C., Bogdanović, T., et al. 2019, New Astronomy Reviews, 86, 101525

Decarli, R., Dotti, M., Fumagalli, M., et al. 2013, Monthly Notices of the Royal Astronomical Society, 433, 1492

Dempsey, A. M., Muñoz, D., & Lithwick, Y. 2020, The Astrophysical Journal, 892, L29

Dexter, J., Lutz, D., Shimizu, T. T., et al. 2020, The Astrophysical Journal, 905, 33

Di Matteo, T., Springel, V., & Hernquist, L. 2005, Nature, 433, 604

Dittmann, A. J. & Ryan, G. 2022, Monthly Notices of the Royal Astronomical Society, 513, 6158

Done, C., Madejski, G. M., & Życki, P. T. 2000, The Astrophysical Journal, 536, 213

D'Orazio, D. J. & Charisi, M. 2023, Observational Signatures of Supermassive Black Hole Binaries

D'Orazio, D. J. & Di Stefano, R. 2018, Monthly Notices of the Royal Astronomical Society, 474, 2975

D'Orazio, D. J. & Duffell, P. C. 2021, The Astrophysical Journal, 914, L21

D'Orazio, D. J. & Haiman, Z. 2017, Monthly Notices of the Royal Astronomical Society, 470, 1198

D'Orazio, D. J., Haiman, Z., Duffell, P., Farris, B. D., & MacFadyen, A. I. 2015, Monthly Notices of the Royal Astronomical Society, 452, 2540

D'Orazio, D. J., Haiman, Z., Duffell, P., MacFadyen, A. I., & Farris, B. D. 2016, Monthly Notices of the Royal Astronomical Society, 459, 2379

D'Orazio, D. J., Haiman, Z., & MacFadyen, A. 2013, Monthly Notices of the Royal Astronomical Society, 436, 2997

D'Orazio, D. J. & Loeb, A. 2019, Physical Review D, 100, 103016

Dotti, M., Bonetti, M., D'Orazio, D. J., Haiman, Z., & Ho, L. C. 2022, Monthly Notices of the Royal Astronomical Society, 509, 212

Dotti, M., Montuori, C., Decarli, R., et al. 2009, Monthly Notices of the Royal Astronomical Society: Letters, 398, L73

Dovčiak, M., Svoboda, J., Goosmann, R. W., et al. 2014, An XSPEC Model to Explore Spectral Features from Black-Hole Sources - II. The Relativistic Iron Line in the Lamp-Post Geometry

Duffell, P. C., D'Orazio, D., Derdzinski, A., et al. 2020, The Astrophysical Journal, 901, 25

Dunhill, A. C., Cuadra, J., & Dougados, C. 2015, Monthly Notices of the Royal Astronomical Society, 448, 3545

Eardley, D. M., Lightman, A. P., & Shapiro, S. L. 1975, The Astrophysical Journal, 199, L153

Eracleous, M., Boroson, T. A., Halpern, J. P., & Liu, J. 2012, The Astrophysical Journal Supplement Series, 201, 23

Eracleous, M., Lewis, K. T., & Flohic, H. M. L. G. 2009, New Astronomy Reviews, 53, 133

Eracleous, M., Livio, M., Halpern, J. P., & Storchi-Bergmann, T. 1995, The Astrophysical Journal, 438, 610

Event Horizon Telescope Collaboration, Akiyama, K., Alberdi, A., et al. 2022, The Astrophysical Journal Letters, 930, L12

Event Horizon Telescope Collaboration, Akiyama, K., Alberdi, A., et al. 2019, The Astrophysical Journal, 875, L1

Fabian, A. C., Iwasawa, K., Reynolds, C. S., & Young, A. J. 2000, The Publications of the Astronomical Society of the Pacific, 112, 1145

Fabian, A. C., Rees, M. J., Stella, L., & White, N. E. 1989, MNRAS

Fabian, A. C., Zoghbi, A., Wilkins, D., et al. 2012, Monthly Notices of the Royal Astronomical Society, 419, 116

Farris, B. D., Duffell, P., MacFadyen, A. I., & Haiman, Z. 2014, The Astrophysical Journal, 783, 134

Farris, B. D., Duffell, P., MacFadyen, A. I., & Haiman, Z. 2015a, Monthly Notices of the Royal Astronomical Society, 447, L80

Farris, B. D., Duffell, P., MacFadyen, A. I., & Haiman, Z. 2015b, Monthly Notices of the Royal Astronomical Society, 446, L36

Farris, B. D., Liu, Y. T., & Shapiro, S. L. 2010, Physical Review D, 81, 084008

Ferrarese, L. & Ford, H. 2005, Space Science Reviews, 116, 523

Ferrarese, L. & Merritt, D. 2000, The Astrophysical Journal, 539, L9

Franchini, A. & Martin, R. G. 2019, The Astrophysical Journal Letters, 881, L32

Frank, J., King, A., & Raine, D. 2002, Accretion Power in Astrophysics, 3rd edn. (Cambridge: Cambridge University Press)

Fromang, S. & Lesur, G. 2019, EAS Publications Series, 82, 391

García, J., Dauser, T., Lohfink, A., et al. 2014, The Astrophysical Journal, 782, 76

Genel, S., Vogelsberger, M., Springel, V., et al. 2014, Monthly Notices of the Royal Astronomical Society, 445, 175

George, I. M. & Fabian, A. C. 1991, Monthly Notices of the Royal Astronomical Society, 249, 352

Ghez, A. M., Klein, B. L., Morris, M., & Becklin, E. E. 1998, The Astrophysical Journal, 509, 678

Ghisellini, G., Haardt, F., & Matt, G. 1994, Monthly Notices of the Royal Astronomical Society, 267, 743

Giacomazzo, B., Baker, J. G., Coleman Miller, M., Reynolds, C. S., & Van Meter, J. R. 2012, The Astrophysical Journal, 752, L15

Godon, P. 1997, The Astrophysical Journal, 480, 329

Gold, R., Paschalidis, V., Etienne, Z. B., Shapiro, S. L., & Pfeiffer, H. P. 2014, Physical Review D, 89, 064060

Goldreich, P. & Tremaine, S. 1979, The Astrophysical Journal, 233, 857

Goldstein, J. M., Veitch, J., Sesana, A., & Vecchio, A. 2018, Monthly Notices of the Royal Astronomical Society, 477, 5447

Goodman, J. 2003, Monthly Notices of the Royal Astronomical Society, 339, 937

Graham, M. J., Djorgovski, S. G., Stern, D., et al. 2015, Monthly Notices of the Royal Astronomical Society, 453, 1562

Gualandris, A. & Merritt, D. 2012, The Astrophysical Journal, 744, 74

Guilet, J. & Ogilvie, G. I. 2012, Monthly Notices of the Royal Astronomical Society, 424, 2097

Gültekin, K. & Miller¨, J. M. 2012, The Astrophysical Journal, 761, 90

Guo, H., Liu, X., Shen, Y., et al. 2019, Monthly Notices of the Royal Astronomical Society, 482, 3288

Guo, H., Liu, X., Zafar, T., & Liao, W.-T. 2020, Monthly Notices of the Royal Astronomical Society, 492, 2910

Guo, W.-J., Li, Y.-R., Zhang, Z.-X., Ho, L. C., & Wang, J.-M. 2022, The Astrophysical Journal, 929, 19

Gutiérrez, E. M., Combi, L., Noble, S. C., et al. 2022, The Astrophysical Journal, 928, 137

Haardt, F. 1993, The Astrophysical Journal, 413, 680

Haardt, F. & Maraschi, L. 1991, The Astrophysical Journal, 380, L51

Haiman, Z. 2017, Physical Review D, 96, 023004

Haiman, Z. & Loeb, A. 2001, The Astrophysical Journal, 552, 459

Hartnoll, S. A. & Blackman, E. G. 2000, Monthly Notices of the Royal Astronomical Society, 317, 880

Hartnoll, S. A. & Blackman, E. G. 2001, Monthly Notices of the Royal Astronomical Society, 324, 257

Hartnoll, S. A. & Blackman, E. G. 2002, Monthly Notices of the Royal Astronomical Society, 332, L1

Hawkins, M. R. S. 2007, Astronomy & Astrophysics, 462, 581

Hawley, J. F. & Balbus, S. A. 1991, The Astrophysical Journal, 376, 223

Hawley, J. F. & Balbus, S. A. 1992, The Astrophysical Journal, 400, 595

Hayasaki, K. 2009, Publications of the Astronomical Society of Japan, 61, 65

Hayasaki, K. & Okazaki, A. T. 2004, Monthly Notices of the Royal Astronomical Society, 350, 971

Hayasaki, K. & Okazaki, A. T. 2006, Monthly Notices of the Royal Astronomical Society, 372, 1140

Heath, R. M. & Nixon, C. J. 2020, Astronomy & Astrophysics, 641, A64

Heckman, T. M. & Best, P. N. 2014, Annual Review of Astronomy and Astrophysics, 52, 589

Hees, A., Do, T., Ghez, A. M., et al. 2017, Physical Review Letters, 118, 211101

Hu, B. X., D'Orazio, D. J., Haiman, Z., et al. 2020, Monthly Notices of the Royal Astronomical Society, 495, 4061

Hughes, S. A. 2009, Annual Review of Astronomy and Astrophysics, 47, 107

Ingram, A., Motta, S., Aigrain, S., & Karastergiou, A. 2021, Monthly Notices of the Royal Astronomical Society, 503, 1703

Ji, X., Lu, Y., Ge, J., Yan, C., & Song, Z. 2021, The Astrophysical Journal, 910, 101

Jiang, J., Bambi, C., & Steiner, J. F. 2015, Journal of Cosmology and Astroparticle Physics, 2015, 025

Jovanović, P., Jovanović, V. B., Borka, D., & Bogdanović, T. 2014, Advances in Space Research, 54, 1448

Ju, W., Stone, J. M., & Zhu, Z. 2016, The Astrophysical Journal, 823, 81

Kaastra, J. S. & Bleeker, J. A. M. 2016, Astronomy and Astrophysics, 587, A151

Kallman, T. & Bautista, M. 2001, The Astrophysical Journal Supplement Series, 133, 221

Kara, E., Alston, W. N., Fabian, A. C., et al. 2016, Monthly Notices of the Royal Astronomical Society, 462, 511

Kauffmann, G. & Haehnelt, M. 2000, Monthly Notices of the Royal Astronomical Society, 311, 576

Kelley, L. Z., Blecha, L., Hernquist, L., Sesana, A., & Taylor, S. R. 2018, Monthly Notices of the Royal Astronomical Society, 477, 964

Kelley, L. Z., Haiman, Z., Sesana, A., & Hernquist, L. 2019, Monthly Notices of the Royal Astronomical Society, 485, 1579

Kelly, B. J., Baker, J. G., Etienne, Z. B., Giacomazzo, B., & Schnittman, J. 2017, Physical Review D, 96, 123003

Keppens, R., Meliani, Z., van Marle, A. J., et al. 2012, Journal of Computational Physics, 231, 718

Kerr, R. P. 1963, Physical Review Letters, 11, 237

Kewley, L. J., Nicholls, D. C., & Sutherland, R. S. 2019, Annual Review of Astronomy and Astrophysics, 57, 511

Khan, F. M., Fiacconi, D., Mayer, L., Berczik, P., & Just, A. 2016, The Astrophysical Journal, 828, 73

Khan, F. M., Just, A., & Merritt, D. 2011, The Astrophysical Journal, 732, 89

King, A. L., Lohfink, A., & Kara, E. 2017, The Astrophysical Journal, 835, 226

King, A. R., Pringle, J. E., & Livio, M. 2007, Monthly Notices of the Royal Astronomical Society, 376, 1740

Kley, W., Papaloizou, J. C. B., & Ogilvie, G. I. 2008, Astronomy & Astrophysics, 487, 671

Kocsis, B., Haiman, Z., & Loeb, A. 2012, Monthly Notices of the Royal Astronomical Society, 427, 2680

Komossa, S. 2015, Journal of High Energy Astrophysics, 7, 148

Kormendy, J. & Ho, L. C. 2013, Annual Review of Astronomy and Astrophysics, 51, 511

Kormendy, J. & Richstone, D. 1995, Annual Review of Astronomy and Astrophysics, 33, 581

Krause, M. G. H., Shabala, S. S., Hardcastle, M. J., et al. 2019, Monthly Notices of the Royal Astronomical Society, 482, 240

Laor, A. 1991, The Astrophysical Journal, 376, 90

Larwood, J. D., Nelson, R. P., Papaloizou, J. C. B., & Terquem, C. 1996, Monthly Notices of the Royal Astronomical Society, 282, 597

Leighly, K. M., Terndrup, D. M., Gallagher, S. C., & Lucy, A. B. 2016, The Astrophysical Journal, 829, 4

Liao, W.-T., Chen, Y.-C., Liu, X., et al. 2021, Monthly Notices of the Royal Astronomical Society, 500, 4025

Lightman, A. P. & White, T. R. 1988, The Astrophysical Journal, 335, 57

Liska, M., Tchekhovskoy, A., & Quataert, E. 2020, Monthly Notices of the Royal Astronomical Society, 494, 3656

Liu, B. F. & Qiao, E. 2022, iScience, 25, 103544

Liu, X., Shen, Y., Bian, F., Loeb, A., & Tremaine, S. 2014, The Astrophysical Journal, 789, 140

Lobban, A. & King, A. 2022, Monthly Notices of the Royal Astronomical Society, 511, 1992

Lodato, G. & Natarajan, P. 2006, Monthly Notices of the Royal Astronomical Society, 371, 1813

Loeb, A. & Rasio, F. A. 1994, The Astrophysical Journal, 432, 52

Lyubarskii, Yu. E. 1997, Monthly Notices of the Royal Astronomical Society, 292, 679

MacFadyen, A. I. & Milosavljević, M. 2008, The Astrophysical Journal, 672, 83

Madau, P., Haardt, F., & Dotti, M. 2014, The Astrophysical Journal, 784, L38

Madau, P. & Rees, M. J. 2001, The Astrophysical Journal, 551, L27

Magdziarz, P. & Zdziarski, A. A. 1995, Monthly Notices of the Royal Astronomical Society, 273, 837

Magorrian, J., Tremaine, S., Richstone, D., et al. 1998, The Astronomical Journal, 115, 2285

Makita, M., Miyawaki, K., & Matsuda, T. 2000, Monthly Notices of the Royal Astronomical Society, 316, 906

Matsuda, T., Makita, M., Fujiwara, H., et al. 2000, Astrophysics and Space Science, 274, 259

Matt, G., Fabian, A. C., & Reynolds, C. S. 1997, Monthly Notices of the Royal Astronomical Society, 289, 175

Matt, G., Fabian, A. C., & Ross, R. R. 1993, Monthly Notices of the Royal Astronomical Society, Vol. 262, 179-186 (1993), 262, 179

Matt, G., Fabian, A. C., & Ross, R. R. 1996, Monthly Notices of the Royal Astronomical Society, 278, 1111

McHardy, I. M., Gunn, K. F., Uttley, P., & Goad, M. R. 2005, Monthly Notices of the Royal Astronomical Society, 359, 1469

McKernan, B., Ford, K. E. S., Kocsis, B., & Haiman, Z. 2013, Monthly Notices of the Royal Astronomical Society, 432, 1468

Meheut, H., Casse, F., Varniere, P., & Tagger, M. 2010, Astronomy and Astrophysics, 516, A31

Merritt, D. & Poon, M. Y. 2004, The Astrophysical Journal, 606, 788

Meyer-Vernet, N. & Sicardy, B. 1987, Icarus, 69, 157

Mignon-Risse, R., Varniere, P., & Casse, F. 2023a, Astronomische Nachrichten, 344, e220130

Mignon-Risse, R., Varniere, P., & Casse, F. 2023b, On the Origin of the Lump in Circumbinary Discs

Milosavljević, M. & Merritt, D. 2001, The Astrophysical Journal, 563, 34

Milosavljevic, M. & Merritt, D. 2003, in AIP Conference Proceedings, Vol. 686, 201–210

Milosavljević, M. & Phinney, E. S. 2005, The Astrophysical Journal, 622, L93

Miranda, R., Muñoz, D. J., & Lai, D. 2017, Monthly Notices of the Royal Astronomical Society, 466, 1170

Moody, M. S. L., Shi, J.-M., & Stone, J. M. 2019, The Astrophysical Journal, 875, 66

Munoz, D. J. 2019, AAS/Division for Extreme Solar Systems Abstracts, 51, 324.11

Muñoz, D. J. & Lai, D. 2016, The Astrophysical Journal, 827, 43

Murray, J. R., Armitage, P. J., Ferrario, L., & Wickramasinghe, D. T. 1999, Monthly Notices of the Royal Astronomical Society, 302, 189

Nandra, K., George, I. M., Mushotzky, R. F., Turner, T. J., & Yaqoob, T. 1997, The Astrophysical Journal, 488, L91

Narayan, R. & Yi, I. 1994, The Astrophysical Journal, 428, L13

Narayan, R. & Yi, I. 1995a, The Astrophysical Journal, 444, 231

Narayan, R. & Yi, I. 1995b, The Astrophysical Journal, 452, 710

Nayakshin, S., Kazanas, D., & Kallman, T. R. 2000, The Astrophysical Journal, 537, 833

Ni, Y., Jiang, J., & Bambi, C. 2016, Journal of Cosmology and Astroparticle Physics, 2016, 014

Niedźwiecki, A., Zdziarski, A. A., & Szanecki, M. 2016, The Astrophysical Journal, 821, L1

Nightingale, J. W., Smith, R. J., He, Q., et al. 2023, Monthly Notices of the Royal Astronomical Society, 521, 3298

Nixon, C., King, A., & Price, D. 2013, Monthly Notices of the Royal Astronomical Society, 434, 1946

Noble, S. C., Krolik, J. H., Campanelli, M., et al. 2021, The Astrophysical Journal, 922, 175

Noble, S. C., Mundim, B. C., Nakano, H., et al. 2012, The Astrophysical Journal, 755, 51

Nowak, M. A., Hanke, M., Trowbridge, S. N., et al. 2011, The Astrophysical Journal, 728

Nowak, M. A. & Wagoner, R. V. 1991, The Astrophysical Journal, 378, 656

Ogiya, G., Hahn, O., Mingarelli, C. M. F., & Volonteri, M. 2020, Monthly Notices of the Royal Astronomical Society, 493, 3676

Paczyński, B. & Wiita, P. J. 1980, Astronomy and Astrophysics, 88, 23

Padovani, P., Alexander, D. M., Assef, R. J., et al. 2017, The Astronomy and Astrophysics Review, 25, 2

Papaloizou, J. & Pringle, J. E. 1977, Monthly Notices of the Royal Astronomical Society, 181, 441

Pariev, V. I. & Bromley, B. C. 1998, The Astrophysical Journal, 508, 590

Perets, H. B., Hopman, C., & Alexander, T. 2007, The Astrophysical Journal, 656, 709

Peterson, B. M. 2006, Physics of Active Galactic Nuclei at all Scales, 693, 77

Pflueger, B. J., Nguyen, K., Bogdanović, T., et al. 2018, The Astrophysical Journal, 861, 59

Piro, L., Colpi, M., Aird, J., et al. 2023, Monthly Notices of the Royal Astronomical Society, 521, 2577

Pooley, D., Blackburne, J. A., Rappaport, S., & Schechter, P. L. 2007, The Astrophysical Journal, 661, 19

Porter, K. & Fukumura, K. 2020, The Astrophysical Journal, 892, 108

Preto, M., Berentzen, I., Berczik, P., & Spurzem, R. 2011, The Astrophysical Journal, 732, L26

Pringle, J. E. 1981, Annual Review of Astronomy and Astrophysics, 19, 137

Proga, D., Stone, J. M., & Kallman, T. R. 2000, The Astrophysical Journal, 543, 686

Pudritz, R. E., Hardcastle, M. J., & Gabuzda, D. C. 2012, Space Science Reviews, 169, 27

Rafikov, R. R. 2016, The Astrophysical Journal, 827, 111

Raimundo, S. I., Davies, R. I., Gandhi, P., et al. 2013, Monthly Notices of the Royal Astronomical Society, 431, 2294

Reynolds, C. S. 1996, PhD thesis, University of Cambridge

Reynolds, C. S. & Nowak, M. A. 2003, Physics Reports, 377, 389

Rodriguez, C., Taylor, G. B., Zavala, R. T., et al. 2006, The Astrophysical Journal, 646, 49

Roedig, C., Dotti, M., Sesana, A., Cuadra, J., & Colpi, M. 2011, Monthly Notices of the Royal Astronomical Society, 415, 3033

Roedig, C., Krolik, J. H., & Miller, M. C. 2014, The Astrophysical Journal, 785, 115

Roseberry, H. H. & Bearden, J. A. 1936, Physical Review, 50, 204

Ross, R. R., Fabian, A. C., & Young, A. J. 1999, Monthly Notices of the Royal Astronomical Society, 306, 461

Rozyczka, M. & Spruit, H. C. 1993, The Astrophysical Journal, 417, 677

Runnoe, J. C., Eracleous, M., Mathes, G., et al. 2015, The Astrophysical Journal Supplement Series, 221, 7

Runnoe, J. C., Eracleous, M., Pennell, A., et al. 2017, Monthly Notices of the Royal Astronomical Society, 468, 1683

Ryan, G. & MacFadyen, A. 2017, The Astrophysical Journal, 835, 199

Rybicki, G. B. & Lightman, A. P. 1979, Radiative Processes in Astrophysics, a wiley-interscience publication edn. (A Wiley-Interscience Publication)

Saade, M. L., Stern, D., Brightman, M., et al. 2020, The Astrophysical Journal, 900, 148

Savonije, G. J., Papaloizou, J. C. B., & Lin, D. N. C. 1994, in Theory of Accretion Disks — 2, ed. W. J. Duschl, J. Frank, F. Meyer, E. Meyer-Hofmeister, & W. M. Tscharnuter (Dordrecht: Springer Netherlands), 363–374

Schwarzschild, K. 1916, Abh. Konigl. Preuss. Akad. Wissenschaften Jahre 1906,92, Berlin,1907, 1916, 189

Sesana, A. 2010, The Astrophysical Journal, 719, 851

Sesana, A., Vecchio, A., & Colacino, C. N. 2008, Monthly Notices of the Royal Astronomical Society, 390, 192

Shakura, N. I. 1972, Astronomicheskii Zhurnal, 49, 921

Shakura, N. I. & Sunyaev, R. A. 1973, Astronomy and Astrophysics, 24, 337

Sheikhnezami, S. & Fendt, C. 2018, The Astrophysical Journal, 861, 11

Shi, J.-M. & Krolik, J. H. 2015, The Astrophysical Journal, 807, 131

Shi, J.-M., Krolik, J. H., Lubow, S. H., & Hawley, J. F. 2012, The Astrophysical Journal, 749, 118

Singh, V., Shastri, P., & Risaliti, G. 2011, Astronomy and Astrophysics, 532, A84

Siwek, M., Weinberger, R., & Hernquist, L. 2023, Monthly Notices of the Royal Astronomical Society, 522, 2707

Siwek, M., Weinberger, R., Munoz, D., & Hernquist, L. 2022, Monthly Notices of the Royal Astronomical Society, 518, 5059

Springel, V., White, S. D. M., Jenkins, A., et al. 2005, Nature, 435, 629

Spruit, H. C. 1987, Astronomy and Astrophysics, 184, 173

Szanecki, M., Niedźwiecki, A., Done, C., et al. 2020, Astronomy & Astrophysics, 641, A89

Tamanini, N., Caprini, C., Barausse, E., et al. 2016, Journal of Cosmology and Astroparticle Physics, 2016, 002

Tanaka, Y., Nandra, K., Fabian, A. C., et al. 1995, Nature, 375, 659

Tang, Y., Haiman, Z., & MacFadyen, A. 2018, Monthly Notices of the Royal Astronomical Society, 476, 2249

Tang, Y., MacFadyen, A., & Haiman, Z. 2017, Monthly Notices of the Royal Astronomical Society, 469, 4258

Taylor, S. R. 2021, The Nanohertz Gravitational Wave Astronomer

The International Pulsar Timing Array Collaboration, Agazie, G., Antoniadis, J., et al. 2023, Comparing Recent PTA Results on the Nanohertz Stochastic Gravitational Wave Background

Tiede, C., Zrake, J., MacFadyen, A., & Haiman, Z. 2020, The Astrophysical Journal, 900, 43

Toro, E. F. 2009, Riemann Solvers and Numerical Methods for Fluid Dynamics: A Practical Introduction (Berlin, Heidelberg: Springer)

Urry, C. M. & Padovani, P. 1995, Publications of the Astronomical Society of the Pacific, 107, 803

Ursini, F., Dovčiak, M., Zhang, W., et al. 2020, Astronomy & Astrophysics, 644, A132

van der Holst, B., Keppens, R., Meliani, Z., et al. 2012, Astrophysics Source Code Library, ascl:1208.014

Vaughan, S. & Edelson, R. 2001, The Astrophysical Journal, 548, 694

Vincent, F. H., Meheut, H., Varniere, P., & Paumard, T. 2013, Astronomy and Astrophysics, 551, A54

Vincent, F. H., Paumard, T., Gourgoulhon, E., & Perrin, G. 2011, Classical and Quantum Gravity, 28, 225011

Virtanen, P., Gommers, R., Oliphant, T. E., et al. 2020, Nature Methods, 17, 261

Vogelsberger, M., Genel, S., Sijacki, D., et al. 2013, Monthly Notices of the Royal Astronomical Society, 436, 3031

Vogelsberger, M., Genel, S., Springel, V., et al. 2014, Monthly Notices of the Royal Astronomical Society, 444, 1518

Volonteri, M., Haardt, F., & Madau, P. 2003, The Astrophysical Journal, 582, 559

Volonteri, M., Habouzit, M., & Colpi, M. 2021, Nature Reviews Physics, 3, 732

Wang, J.-M., Songsheng, Y.-Y., Li, Y.-R., & Yu, Z. 2018, The Astrophysical Journal, 862, 171

Westernacher-Schneider, J. R., Zrake, J., MacFadyen, A., & Haiman, Z. 2022, Physical Review D, 106, 103010

White, S. D. M. & Rees, M. J. 1978, Monthly Notices of the Royal Astronomical Society, 183, 341

Wilkins, D. R. & Gallo, L. C. 2015, Monthly Notices of the Royal Astronomical Society, 448, 703

Wilms, J., Speith, R., & Reynolds, C. S. 1998, Black Holes: Theory and Observation, 514, 69

Xin, C., Charisi, M., Haiman, Z., et al. 2020, Monthly Notices of the Royal Astronomical Society, 496, 1683

Yan, C.-S., Lu, Y., Dai, X., & Yu, Q. 2015, The Astrophysical Journal, 809, 117

Yaqoob, T. & Padmanabhan, U. 2004, The Astrophysical Journal, 604, 63

Yu, Q. & Lu, Y. 2001, Astronomy & Astrophysics, 377, 17

Yu, Q. & Tremaine, S. 2002, Monthly Notices of the Royal Astronomical Society, 335, 965

Zdziarski, A. A., Fabian, A. C., Nandra, K., et al. 1994, Monthly Notices of the Royal Astronomical Society, 269, L55

Zrake, J., Tiede, C., MacFadyen, A., & Haiman, Z. 2021, The Astrophysical Journal, 909, L13

APPENDIX

A

ARTICLE ON THE NUMERICAL SIMULATIONS

The article will be submitted to MNRAS with a compagnon article on the observational consequences. This article focuses on the gravitational impact of the MBH on the accretion disc around the primary MBH. It presents the impact of the binary orbital parameters on the truncation of the disc and the elliptical shape of the disc.

MNRAS **000**, 1–8 (2022) Preprint 22 February 2024 Compiled using MNRAS LATEX style file v3.0

Sculpting the outer edge of accretion discs in early binary black hole

Fabien Casse,[1]★ Peggy Varniere,[1,2] Léna Arthur,[1] Fabrice Dodu[1]
[1]*Université Paris Cité, CNRS, Astroparticule et Cosmologie, F-75013 Paris, France*
[2]*Université Paris-Saclay, Université Paris Cité, CEA, CNRS, AIM, 91191, Gif-sur-Yvette, France*

Accepted XXX. Received YYY; in original form ZZZ

ABSTRACT

Key words: accretion, accretion discs – black holes physics – hydrodynamics

1 INTRODUCTION

For more than three decades, binary black holes have remained a conjecture in astrophysics when considering colliding galaxies hosting supermassive black holes (Begelman et al. 1980). In that context, supermassive black holes are expected to bind gravitationally and to progessively get closer until they merge. Overtime numerous studies have been performed in order to understand what are the physical processes that can preside such inspiral motion. For orbital separation beyond the parsec scale the dynamical friction of black holes with the galactic gaseous environment seems to be the leading process (Mayer et al. 2007). At orbital sepration below 10^{-2} pc, gravitational wave emission is expected to be the key phenomenon driving the inspiral motion until the fusion of the two compact objects. Between these two separation scales no clear consensus has emerged identifying the mechanism driving the inspiral motion - the 'final parsec problem' - as three-body stellar interaction (see e.g. Preto et al. (2011)) or disc gas interaction (e.g. Armitage & Natarajan (2002); Cuadra et al. (2009)) are canditates for this role.
Since the first detection of gravitational waves emitted by the fusion of a stellar binary black hole (Abbott et al. 2016), the binary black hole conjecture has become a vivid reality in the astrophysical community. Such discovery have enhanced the relevence of numerical studies devoted to the structure of the binary including the interaction of the two compact objects with their circumbinary disc (CBD) (MacFadyen & Milosavljević 2008; Ragusa et al. 2016; Muñoz et al. 2020; Siwek et al. 2023; Franchini et al. 2023), the impact of the binary upon the CBD (Noble et al. 2012; Zilhão et al. 2015; Noble et al. 2021; Mignon-Risse et al. 2023a), the presence of mini-discs around black hole (Pihajoki et al. 2018; Ingram et al. 2021; Davelaar & Haiman 2022) or the existence of the so-called 'lump' structure at the inner edge of the CBD (Shi et al. 2012; Noble et al. 2012; D'Orazio et al. 2013; Mignon-Risse et al. 2023b).
Understanding the dynamical structure of the gas orbiting within the complex gravitational field of the binary black hole is indeed the key to discriminate between single black hole and pre-merger binary black hole through the electromagnetic output of the system. So far the caracterization of electromagnetic signatures of binary black hole systems have been performed in the framework of black holes orbital separation up to a few hundreds of gravitational radii (Tanaka et al. 2012; Tang et al. 2018; d'Ascoli et al. 2018; Combi et al. 2022; Major Krauth et al. 2023; Cocchiararo et al. 2024) and suggest that electromagnetic binary black hole signature should be identifiable provided the redshift of these systems remain relatively small and the mass ratio of the binary is smaller than unity. It is noteworthy that all the aforementionned studies have been performed assuming ad-hoc initial conditions that are not supported by simulations devoted to earlier phases of the binary. In particular it is still unclear how both the CBD or mini-discs form around the binary black hole leading to uncertainties regarding inital conditions used in general relativistic fluid simulations and the electromagnetic signature of the binary in its late phases. Simulations of the early phase of the binary are then required in order to bridge the gap between early stages of the binary and the close-to-merger phase.
The goal of the present paper is to make a first step upon that bridge by studying the gravitational effects of a remote object upon the accretion disc orbiting around a central black hole binded to that object. The outcome of such simulations will lead us to assess the potential electromagnetic signatures of early binary black hole through the modifications of the disc and the related modifications of the thermal emission from the accretion disc. This can help us identifying binary patterns that can potentially lead to the detection of early binary black hole systems. Such detection would be unvaluable as it would provide observational clues on the gas structure throughout the evolution of the binary and thus to the formation of the CBD and mini-dics.
The paper is organized as follows: the second section is devoted to the numerical framework and setup of the simulations of a large accretion disc sourrounding a central black hole and prone to the gravitational influence of a second massive object orbiting beyond the outer edge of the accretion disc. The third section presents the results of the hydrodynamical simulations while the last section summarizes the results and discusses the perspectives of our work.

2 HYDRODYNAMICS SIMULATIONS OF ACCRETION DISCS IN EARLY BBH SYSTEMS

In this paper we aim at studying the effect of the presence of an external gravitational perturbator upon the accretion disc orbiting around a black hole. As we focus our study on the early phases of the BHB, namely when the distance between the black hole and the secondary object D_{12} is much larger than the size of the black hole

★ E-mail: fcasse@apc.in2p3.fr

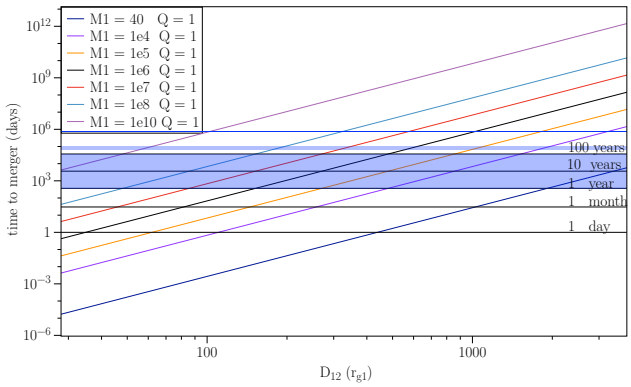

Figure 1. Time to merger as function of binary separation and masses. The horizontal band represent 100 years each.

gravitational radius $r_{g1} = GM_1/c^2$. In the previous expression G stands for the graviational constant while c is the velocity of light. The other important parameter describing the BBH is obviously the mass ratio of the two black holes that we define as $Q = M_2/M_1$.

2.1 Early stages of circular orbiting BBH

The most likely configuration for such BBH is the one where both black hole orbit a nearly circular orbit around each other until fusion in a so called inspiral motion (REF). In early stages of the system, the loss of angular momemtum induced by the production of gravitational waves is very slow so on can safely assume that the actual orbits of the black holes around the center of mass of the system are circular. If one assumes that the loss of angular momentum in the binary is mainly induced by the emission of gravitational waves, the variation of the orbital separation of the binary D_{12} occurs over a timescale dt which is provided by (Hughes 2009)

$$\frac{dD_{12}}{D_{12}} = -\frac{64G^3(M_1+M_2)^2\mu}{5c^5D_{12}^4}dt \tag{1}$$

where $\mu = M_1M_2/(M_1+M_2)$. In a circular orbit configuration, the angular frequency of the BBH is given by

$$\Omega_{\rm BBH} = \left(\frac{G(M_1+M_2)}{D_{12}^3}\right)^{1/2} \tag{2}$$

while the distances of each object from the center of mass of the system are $r_1 = D_{12}Q/(Q+1)$ and $r_2 = D_{12}/(Q+1)$ respectively. The velocity of both the black hole and the secondary object in the frame of the center of mass of the system will then be $\beta_1^2 = V_1^2/c^2 = r_{g1}Q/D_{12}$ and $\beta_2^2 = r_{g1}/D_{12}$. Early stages of the BBH will then lead to object velocities much smaller than the velocity of light, thus opening the way to a classical description of the motion of the black hole and the secondary object. In the folowing of this paper we will use the orbital period of the BBH as time reference, namely

$$P_{\rm BBH} = 2\pi\left(\frac{D_{12}^3}{GM_1(1+Q)}\right)^{1/2} = \frac{2\pi r_{g1}}{c}\left(\frac{D_{12}^3}{r_{g1}^3(1+Q)}\right)^{1/2}. \tag{3}$$

In order to fulfill the circular orbit assumption made in this paper, one has to check that the loss of angular momentum is limited over one binary period, for instance $|dD_{12}/D_{12}| \leq 0.1\%$ for $dt = P_{\rm BBH}$. The previous equations then lead to a lower limit of the binary separation D_{12}, namely

$$\left|\frac{dD_{12}}{D_{12}}\right| = \frac{128\pi Q(1+Q)^{1/2}}{5}\left(\frac{r_{g1}}{D_{12}}\right)^{5/2} \leq 0.1\% \tag{4}$$

which is verified only if $D_{12} \geq 100r_{g1}$. At such binary separation, one may consider that the formation of a potential CBD has already begun expect which is beyond the scope of this paper aiming at looking at the effects of the secondary object in the very early phase of the binary system. In order to investigate the shrinkage of the accretion disc orbiting the central black hole in phases where CBD structure are not yet formed, we will restrict ourselves to binary separations $D_{12} \geq 500r_{g1}$.

2.2 Hydrodynamics simulations of the accretion disc around black hole in BBH

The follow up of the evolution of the accretion disc prone to an external orbiting perturbator requires to perform long-term simulations of the fluid into the complex gravitational field generated by the presence of the two massive objects. As we focus on the evolution of one accretion disc in the system, the most likely black hole to host one is the most massive one. In that view we will then restrain ourself to BBH configuration where the mass ratio parameter $Q \leq 1$.

2.2.1 Simulations framework

The best frame to perform such simulations is obviously the one coinciding with the primary black hole located at the center of the accretion disc (this frame will be called $\mathcal{R}$ hereafter). In such frame the center of mass of the accretion disc remains still but one has to consider fictitious forces at work upon the fluid. Indeed, the frame associated with the primary black hole has a circular motion around the center of mass of the BBH system. In the cartesian frame associated with the center of mass, we choose to keep the axis of $\mathcal{R}$ parallel to the axis of the inertial frame of the center of mass of the system. This ensures that the frame $\mathcal{R}$ is not rotating so that no Coriolis forces has to be accounted for in this frame. As a result the second black hole of the system will have a circular motion in $\mathcal{R}$ whose radius is D_{12} and angular velocity Ω_{BH}.

2.2.2 Hydrodynamics equations

Within our set of simulations we aim at describing the long-term evolution of the entire disc orbiting around the primary black hole. In order to do so we need to include both the innermost stable circular orbit (ISCO) out to the external radius of the disc. As the gravity of the primary black hole closely matches Newtonian gravity beyond $20r_{g1}$ we choose to use a classical hydrodynamics framework. This choice enables us to keep good accuracy for our study will optimizing computing time. Moreover encompassing the gravitational effects of the second black hole will be much easier as its influence is of Newtonian nature as any massive object would do.
In order to take into account the relativistic nature of the primary black hole we use the pseudo-Newtonian description provided by Paczynsky & Wiita (1980) so that the inner edge of the disc will form near the ISCO. Early BBH systems are slow evolving systems so the approach of the two black holes and the mutual gravitational interaction is very likely to align accretion disc spin with the plane hosting the motion of the black holes. Accordingly we will consider 2D simulations within that plane.

The set of hydrodynamics equations translates the conservation of mass and momentum of the gas in the complex gravitational field of the BBH system. These conservation laws write

$$\begin{aligned} \frac{\partial \rho}{\partial t} + \nabla \cdot (\rho \mathbf{u}) &= 0 \\ \frac{\partial \rho \mathbf{u}}{\partial t} + \nabla (\rho \mathbf{u}\mathbf{u} + P\mathbb{1}) &= \mathbf{f}_{BH_1} + \mathbf{f}_{BH_2} + \mathbf{f}_{\mathcal{R}} \end{aligned} \tag{5}$$

where ρ is the gas density, $\rho\mathbf{u}$ is the gas momentum density, P is the thermal pressure and $\mathbb{1}$ is the identity matrix. The momentum conservation law takes into account the gravitational force densities generated by the central black hole using a pseudo-Newtonian prescription of the force of the central black hole

$$\mathbf{f}_{BH_1} = -\rho c^2 r_{g1} \frac{\mathbf{r}}{r(r-2r_{g1})^2} \tag{6}$$

where $\mathbf{r}$ is the position vector of a given gas element in the frame of the central black hole where $\|\mathbf{r}\| = r$. The gravitational force density originating from the second black hole $\mathbf{f}_{BH_2}$ orbiting around the primary one in the $\mathcal{R}$ frame can be described with very good accuracy by a Newtonian law as the distance between any element of gas in the simulation remains at large distances compared to the gravitational radius r_{g2} of the second black hole. This force reads

$$\mathbf{f}_{BH_2} = Q\rho c^2 r_{g1} \frac{\mathbf{D}_{12} - \mathbf{r}}{\|\mathbf{D}_{12} - \mathbf{r}\|^3} \tag{7}$$

where $\mathbf{D}_{12}$ is the position vector of the second black hole in the frame of the central black hole, namely the $\mathcal{R}$ frame. In addition to this two gravitational force densities, one also has to consider the fictitious forces due to the rotation of $\mathcal{R}$. Indeed the motion of the central black hole in the frame of the BBH center of mass frame being circular, the $\mathcal{R}$ frame is not an inertial frame. As the axis of this frame remains constant, no Coriolis force has to be considered. The only fictitious force is then

$$\mathbf{f}_{\mathcal{R}} = -Q\rho c^2 r_{g1} \frac{\mathbf{D}_{12}}{D_{12}^3} \tag{8}$$

In order to close the set of equations we use a polytropic equation of state providing the value of the thermal pressure P as a function of the density, namely $P = \kappa\rho^\gamma$ with $\gamma = 5/3$ and $\kappa = 10^{-4}$. The value of γ is chosen in agreement with monoatomic gas caracteristics while the value of κ, related to the local sound speed, is set to mimic the physics of a thin accretion disc.

2.2.3 *Numerical simulation setup*

The goal of the present paper is to study the effects of the gravitational influence of a secondary black hole orbiting around a primary black hole surrounded by its accretion disc. In contrast to single black hole systems, the presence of a second black hole in the BBH system likely create an outer edge to the accretion disc of the primary black hole. In order to quantify that effect, we setup hydrodynamics simulations solving the aforementionned equations in the 2D orbital plane. The simulation domain is designed to describe the entire accretion disc from its inner to its outer edges. The simulation domain is thus set to be $\phi \in [0, 2\pi]$ and $r \in [5r_{g1}, 0.98D_{12}]$ so that this domain contains the inner edge of the accretion disc while maintaining velocities below the speed og light. The location of the L_1 Lagrangian point of the BBH system is approximately (Plavec & Kratochvil 1964; Hameury 2001)

$$\frac{R_{L_1}}{D_{12}} = \frac{1}{2} - 0.227 \log Q \tag{9}$$

so that it lies within our simulation domain for any mass ratio $Q \geq 7 \times 10^{-3}$. The location of the L_1 Lagrangian point of the system being an helpful indicator of the upper limit of the outer radius of an accretion disc in a binary system, we thus make sure that the formation of the outer edge of the accretion disc will be captured by our simulation.

The initial conditions of the simulations are consistent with an accretion disc in balance in the gravitational field of a single non-spinning black hole, namely with an inner edge located near the innermost stable circular orbit (ISCO, $6r_{g1}$) and an outer edge located close to the outer limit of the simulation domain. The initial gas density is prescribed as

$$\rho(r) = \frac{\rho_o}{4}\left(1 + \tanh\frac{r - r_b}{\sigma_b}\right)\left(1 - \tanh\frac{r - r_{ext}}{\sigma_{ext}}\right)\left(\frac{6r_{g1}}{r}\right)^{3/2} \tag{10}$$

where $\rho_o = 10$, $r_b = 4.5r_{g1}$ and $r_{ext} = 0.7D_{12}$ (see Vincent et al. (2013)). The two constants σ_b and σ_{ext} have been set to 0.45 and $0.05D_{12}$ respectively in order for the disc to exhibit edges where density drops to a floor value ρ_{min} which is ten order of magnitude smaller than the maximal initial density value. Radial velocity is set to zero initially and the azimuthal velocity is computed in order for the gas to reach a full balance with the central black hole gravitational field and is thermal pressure.

The challenge of these simulations stems from the fact that there is a huge contrast between the dynamical timescale of the gas lying at the inner edge of the accretion disc and the timescale related to the orbit of the secondary black hole. Indeed the ratio of the velocity of gas orbiting the last stable orbit of an accretion disc orbiting a non-spinning black hole to the velocity of the secondary black hole reads

$$\frac{V_{\rm isco}}{V_{BH_2}} \simeq \sqrt{\frac{D_{12}}{6r_{g1}}} \tag{11}$$

while the spatial resolution needed to accurately describe the dynamics of the gas requires much smaller cells near the inner edge than at the outer edge of the simulation. In order to alleviate the numerical cost of these simulation we use a logarithmically radially spaced grid with 720 cells in the radial direction and 320 in the azimuthal one. The use of a logarithmic grid is an important asset to perform these simulations but however cannot prevent us from a huge temporal numerical cost. Indeed, the timestep of hydrodynamics simulations is controlled by the so-called CFL condition (Courant-Friedrish-Levy) translating the causality of hydrodynamical phenomena as

$$\Delta t < \min\left(\frac{\Delta X_i}{V_i}\right) \tag{12}$$

where ΔX_i is the size of a cell in the i^{th} direction. The dominant motion of the gas being in the azimuthal direction, such condition leads to a timestep contrast between the inner and outer border of the simulation to be

$$\frac{\Delta t_{\rm isco}}{\Delta P_{\rm BBH}} \simeq \left(\frac{D_{12}}{6r_g}\right)^{3/2} \tag{13}$$

As we wish to follow the evolution of the accretion disc over many orbits of binaries whose seperation are up to $6000r_{g1}$, the previous relation indicates that we have to perform up to 3×10^4 times more timesteps than if we were just considering the motion of the secondary object. As an example, the number of iterations required to perform the most challenging simulation is 1.04×10^9. Such computation was achieved using MPI library over 80 cores during several weeks.

In order to complete the display of our numerical steup, it is noteworthy that periodic boundary conditions have been used in the azimuthal direction while outflowing conditions are imposed at the inner radial boundary. At the outer boundary of the simulation, we do not prevent gas from inflowing in the computatinal domain as this can lead to unphysical effects such as artificial thermal pressure gradient. Instead we authorize gas to inflow into the computational domain but with a density very close to the floor density.

3 ACCRETION DISC OUTER EDGE IN EARLY BLACK HOLE BINARIES

In order to study the extent of an accretion disc orbiting around a black hole belonging to a BBH, we performed a set of simulations helping us to scan the parameter space of such binaries, namely the mass ratio Q and the separation D_{12} between the black hole and the other object. In the first part of this section, we present the outcome of one fiducial simulation displaying the typical features of the shrinked accretion disc in an equal mass BBH where the gravitational influence of the secondary object is expected to play at full strength. In the second part we will provide the results originating from our survey of the parameter space (Q, D_{12}) while in the last part, we discuss the fundamental differences in the disc structure one can expect from the presence of the secondary disruptor such as in early BBH.

3.1 Accretion disc in early equal-mass BBH

The design of our simulation, presented in the previous section, is consistent with an initial accretion disc whose extent exceeds the expected size of the Roche lobe of the primary black hole. The temporal evolution of the gas density is displayed on Fig.(2) where one can see the outer part of the initial disc being swept away by the gravitational force exerted by the secondary object located just outside of the simulation domain. The transition from the initial stage to the shrinked accretion disc lasts for approximately one BBH period before stepping into a stabilization phase where the accretion disc slowly rearranges itself under the influence of the two objects composing the BBH. It is noteworthy that the gravitational influence of the secondary massive object upon the disc is also visible through the formation of an overdense arm in the very first stages of the simulation. This arm rotates at the same angular velocity than the secondary object near the outer edge of the disc but then experiences the differential rotation of the gas which leads to the spiral shape of this overdensity. In time the spiral arm pattern slowly lessens as the disc outer edge shrinks. On Fig.(2) the disc evolution was monitored for more than 20 BBH periods where the structure of the initial axisymmetric disc evolves toward an elliptic shrinked structure which remains stable for more than ten BBH periods.

Under such circumstances, it is not straightformward to precisely assess the value of the outer edge of the accretion disc in its final stage. However it is useful to measure the azimuthally averaged radius of the outer edge in order to infer any observationnal modification due to the removed part of the disc material. We have adopted the following procedure to measure the radial extent of the disc. For any given snapshot, we first azimuthally average the azimuthal velocity and gas density of the disc so that we obtain the averaged radial profile of these two quantities. Such profiles are displayed in Fig.(3) for our fiducial simulation where both initial and final profiles of the aforementionned quantities are represented. One can see that the density profile has evolved over time since the gas density has increased inside the disc while it has significantely dropped beyond a reference point where both initial and final densities match. We use this reference point to define the average outer edge of the disc $r_{\rm out}$: $r_{\rm out}$ corresponds to the radius where the gas density is equal to one tenth of the density at the reference point. Our choice is motivated by the fact that the azimuthal velocity remains very close to the Keplerian velocity up to this radius. Beyond the measured $r_{\rm out}$, the gas is no longer displaying any dynamical behaviour in agreement with a balanced disc structure. Indeed, outside of $r_{\rm out}$, mass is very likely reacting to equivalent gravitational forces coming from the two objects composing the BBH. It is noteworthy that in all our simulations, whatever are the Q and D_{12} parameters, we recover similar profiles regarding azimuthal velocity and gas density. This ensures that the way we measure the average outer edge $r_{\rm out}$ stays coherent throughout our simulation sample.

Applying this method to determine $r_{\rm out}$ to our fiducial simulation leads us to Fig.(4) where the temporal evolution of $r_{\rm out}$ is displayed over nearly 25 $P_{\rm BBH}$. In such simulation, the initial disc whose outer edge lies at $r_{\rm out} = 1500 r_{g1}$ (beyond the Roche lobe radius of the primary black hole) rapidly skrinks to a smaller extension which remains stationnary after approximately $3P_{\rm BBH}$. The final outer edge radius of the disc in this simulation is then $\simeq 600 r_{g1}$. The general behavior of $r_{\rm out}$ in this fiducial simulation matches the general behavior of the disc in all our other simulations: a decrease of the outer edge followed by a stabilization of the outer edge. In order to understand why the disc is experiencing such rapid shrinking in this simulation, one has to keep in mind that $P_{\rm BBH}$ is large compared to the gas dynamical time as $P_{\rm BBH}$ corresponds to 6 orbiting periods of the gas near $r_{\rm out}$ and 6000 periods at the ISCO of the disc.

We have performed other equal mass BBH simulations considering various separations D_{12} ranging from $10^3 r_{g1}$ to $6\times10^3 r_{g1}$. The outcome of these computations is very similar to our fiducial simulation as displayed in Fig.(5) where we show the evolution of $r_{\rm out}/D_{12}$ as a function of time. Since the BBH separations are different in these simulation, we have normalized time with $P_{\rm BBH}$ so that Fig.(5) can provide comparison between the various simulations by considering identical relative dynamical timescale for the BBH. As one can see on Fig.(5) the variations of $r_{\rm out}/D_{12}$ are very similar throughout our equal mass BBH sample where a rapid drop of the outer radius occurs over a few $P_{\rm BBH}$ and a final value of $r_{\rm out} \simeq 0.3 D_{12}$. In order to investigate further into the dependance of the outer edge radius $r_{\rm out}$ on both Q and D_{12} we now turn our attention to non-equal BBH systems.

3.2 Accretion disc outer edge in early BBH: non-equal mass binaries versus separation

In order to go beyond the equal mass BBH framework we have performed a series of simulations where we have considered various mass ratios Q and separation D_{12}. The range of mass ratio considerd in our simulation sample is $Q \in [9\times10^{-4}, 1]$. The lower value of this interval was constrained by computational time limitation while we set the upper limit to $Q = 1$ as the most massive black hole is likely to host the accretion disc. The range of binary separation in our sample is $D_{12}/r_{g1} \in [500, 6000]$. The upper limit of $r_{\rm out}$ is consistent with the typical size of accretion discs observed around a supermassive black hole (REF) while the lower limit corresponds to a configuration where no minidisc are yet formed and the binary separation remains nearly constant during the whole simulation.

For the sake of consistency we considered the exact same hydrodynamical setting in our simulation than in the one presented in Sect.

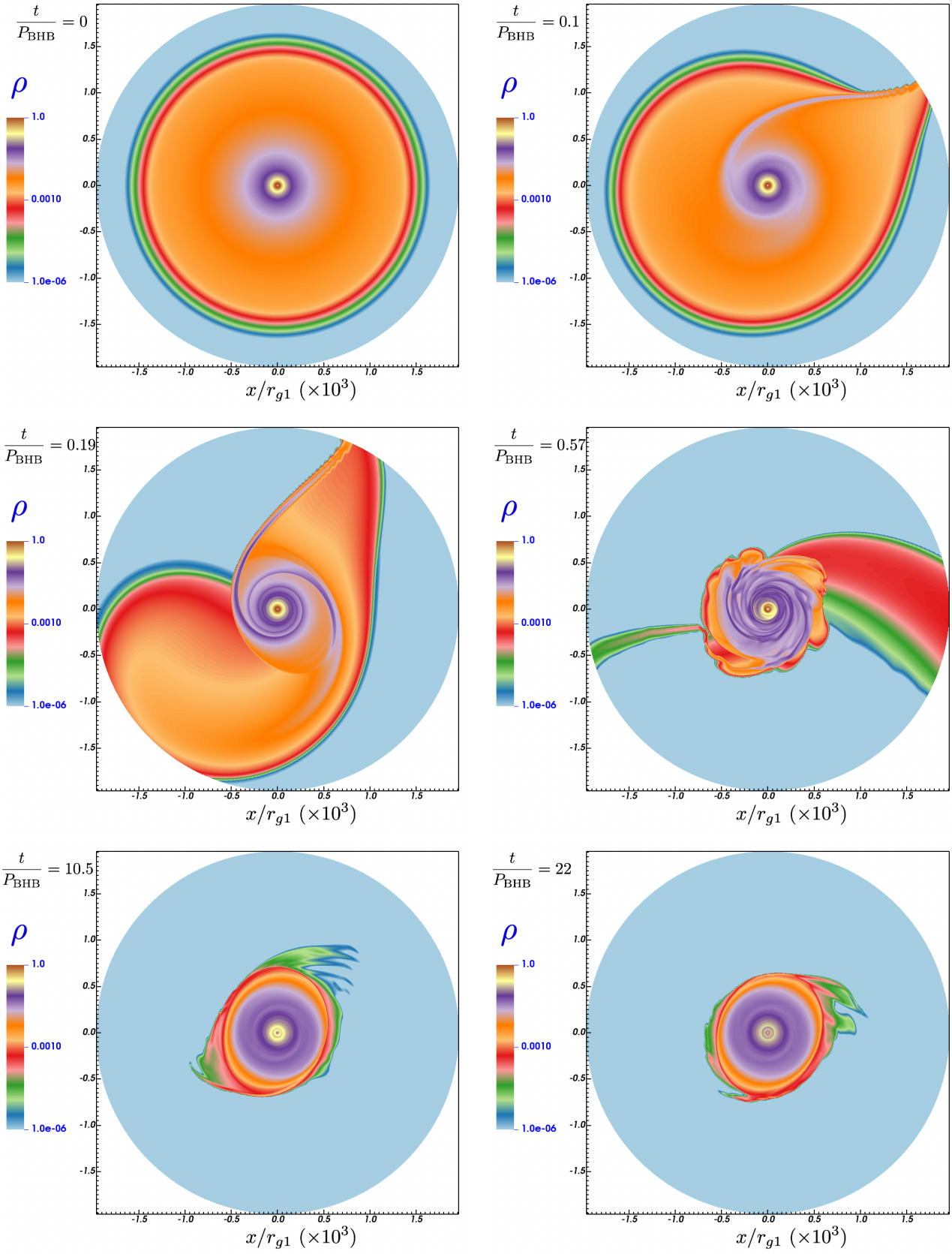

Figure 2. Snapshots of the logarithmic density of an accretion disc surrounding the primary black hole of an early BBH. The secondary black hole orbiting in a circular motion around the primary black hole has an equal mass ($Q = 1$) while been separated by $D_{12} = 2000\ r_{g1}$. Time is here normalised to the BBH period $P_{\rm BBH}$. The tidal effects induced by the presence of the secondary object leads to the removal of the outer part of the initial disc whose outer edge lies beyond the Lagrangian L_1 point of the BBH. After more than one orbital period of the BBH, the disc remains stable with an outer edge reduced to approximately 600 r_{g1} while displaying an elliptic outer edge shape whose ellipticity is approximately $e = 0.6$.

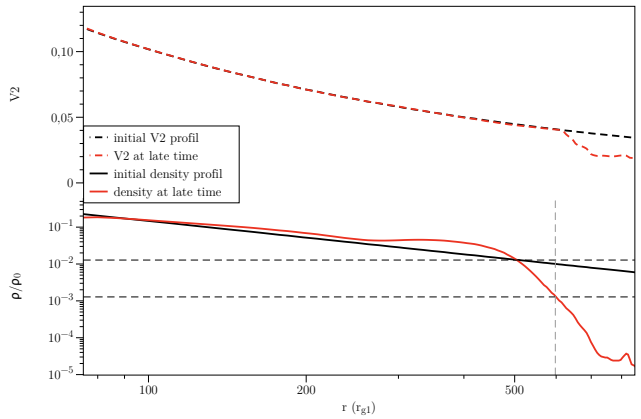

Figure 3. Comparison of the initial radial profiles of the azimuthal velocity (upper panel) and density (lower panel) of the disc with final profiles of the simulation. The profile are obtained by azimuthally averaging the corresponding snapshots.

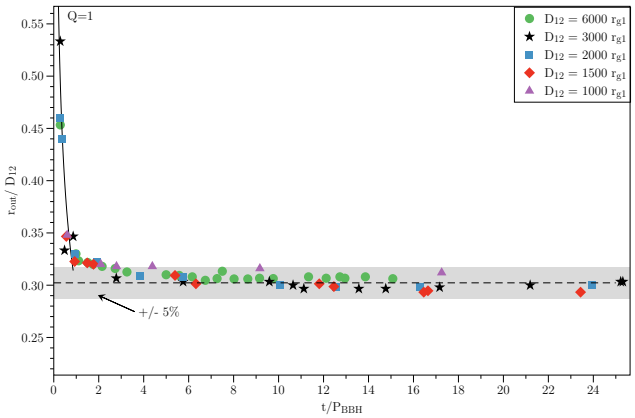

Figure 5. Temporal evolution of the outer edge of accretion discs in equal mass binaries for initial binary separation ranging from $500r_{g1}$ to $6000r_{g1}$. The outer radius of the disc is normalised to the binary separation while time is nomalised to the binary period $P_{\rm BBH}$.

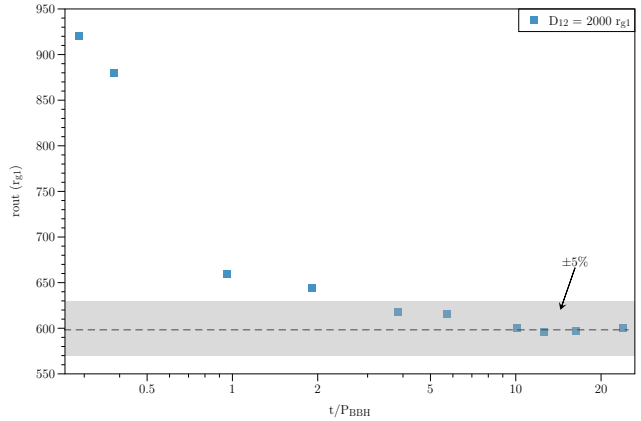

Figure 4. Temporal evolution of the averaged outer radius of the disc displayed in Fig.(2). Time is normalised to the binary period t_{BH_2}. After a fast decrease from the intial outer edge value (1550 r_{g1}), the outer edge radius stabilize to a value of approximately 600 r_{g1}.

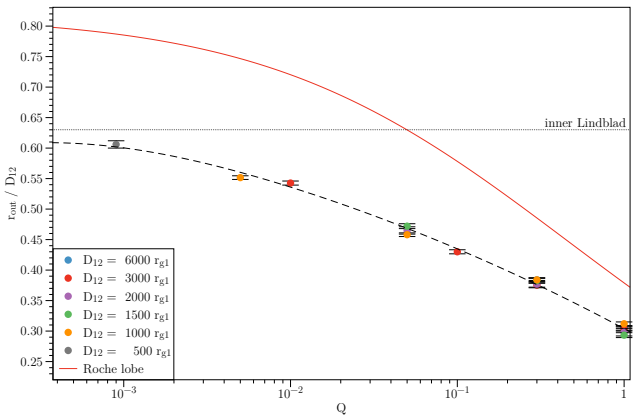

Figure 6. juste pour l'avoir sous la main! mets ou tu veux $-0.18 * log10(0.019 * x + 6.810^{-6}) * x^{0.044}$ – certains de ces params peuvent bouger sans changer le χ^2 donc a voir si une autre formule est mieux...

3.1 only varying Q and D_{12} parameters. For each simulation we measured the outer edge of the accretion disc in the exact same way than in Sect. 3.1 and compiled the results in order to infer if any univoque relationship between $r_{\rm out}$ and the two binary parameters would exit. Fig.(6) represents the value of the ratio $r_{\rm out}/D_{12}$ as a function of the mass ratio parameter Q. The main result provided by this figure is that the ratios $r_{\rm out}/D_{12}$ are remarkably similar for any given mass ratio Q. Indeed, for any given mass ratio, the final outer edge radius in each simulation is equal to the same fraction of D_{12}, whatever is the BBH separation D_{12}. Scanning the various values of BBH mass ratio, we find that this fraction is however dependent on Q as its value increases as Q decreases. In order to check the consistency of our simulations, we have represented on Fig.(6) the distance from the primary black hole to the L_1 point of the BBH system as well as the location of the inner Lindblad resonance. All the values of $r_{\rm out}$ found in our sample are smaller than these two quantities ensuring the stability of the final structure of the accretion flow around the primary black hole of the BBH. At high mass ratio, the location of the L_1 is the main limitation while at low mass ratio, the Lindblad inner resonance is dominating the extent of the accretion disc. We provide here an empirical formula that fits the results arising from our computations as

$$\frac{r_{\rm out}}{D_{12}} = -0.18 Q^{0.044} \log\left(0.019Q + 6.8 \times 10^{-6}\right) \quad (14)$$

The coefficients of this formula were derived by minimizing a standard χ^2 test based on the values provided by our simulations (with a $\chi^2 = 0.99$ and residus below 1%).

3.3 Ellipticity of the disc in early BBH

As previously mentionned in Sect.3.1 the final shape of the primary black hole accretion discs no longer exhibit an axisymmetric structure as the outer edge of the accretion discs appear to be elliptical. Inferring the ellipticity of the outer part of the resulting disc was done using the flollwing procedure. First, we calculate the contour of the gas density ρ in the outer disc (where values of the density is much smaller than unity but larger than the floor density). In a second step, we remove the spiral arms from this contours and finally we evaluate

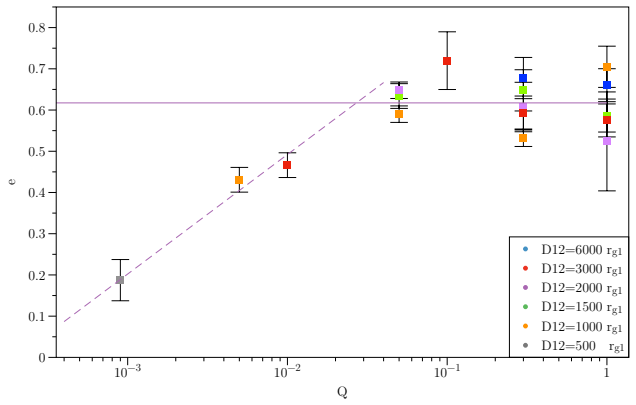

Figure 7. Eccentricity of the outer disc as a function of the binary mass ratio Q. The eccentricity only depends on the mass ratio parameter and not on the orbital separation.

the approximation of this contour by an ellipse. The fitting algorithm is built from algebraic equations of an ellipse. All elliptical fits were obtained from the object-oriented tools for fitting conics and quadrics developed by Matt (2023) within the Maple library.
The results obtained from the fitting of the shape of the outer edge of the accretion disc orbitting around the primary black hole are displayed on Fig.7 along with the associated uncertainties. As expected we can see that for the smallest values of the mass ratio between the black hole and the secondary gravitational disruptor Q, the ellipticity e is small and increases with Q. On the other hand we also find that the value of ellipticity reaches a plateau where $e \sim 0.6$ provided the mass ratio $Q > 10^{-2}$. It is noteworthy that such ellipticity is significant even with moderate mass ratio and that the cumulative gravitational effects of the secondary object over many orbits around the primary black hole will result in a identical value of the ellipticity of the order of 0.6 as illustrated in the final snapshots of Fig.2. Such result is likely to prevent ellipticity to be a reliable indicator of the mass ratio of any potential BBH as being able to measure e will only indicate if Q is smaller or larger than some reference value around 10^{-2}.

4 CONCLUSIONS

In the preent paper we adressed the topic of the gravitational influence of a secondary massive object upon the accretion disc surrounding a black hole. The secondary object is graviationally binded to the black hole and forms a binary system with it whose orbital separation is larger than a few hundreds graviational radii. At that distance, the decay of the orbital separation is very slow so one can assume the trajectory of the secondary to be circular. Such framework is consistent with the early stages of binary black hole systems when the secondary black hole slowing influence the structure of the accretion disc orbiting around the primary black hole.
We perfomed 2D hydrodynamical simulations over a very large number of dynamical timesteps leading to the description of the sculpting of the outer edge of the accretion disc by the secondary object. We report three main effects of such influence on the accretion disc:

- the disc outer edge radius, delibarately set at an initial value exceeding both the Roche lobe size and the innermost Lindblad resonance, first decreases and then reaches, over a few orbital periods, a stationnary value. Scanning various binary mass ratio we have demonstrated that the value of the outer edge of the disc is proportional to the orbital separation, the coefficient factor being only dependant on the binary mass ratio Q (see Eq.14).
- the gravitational influence of the secondary black hole is also visible through the existence of an overdense arm in the disc. This spiral arm appears at the beginning of the simulation but is rapidly twisted by the differential rotation of the disc leading to a spiral shape rotating at the same angular velocity than the secondary object. The amplitude of the overdensity slowly decreases with time but remains present throughout the whole simulation.
- the reduced accretion disc, once it has reached its final size, exhibits an outer edge whose shape is elliptical with an eccentricity e that only depends on the binary mass ratio Q (see Fig.7). The eccentricity of the outer edge varies from $e = 0.2$ for $Q = 9 \times 10^{-4}$ to $e = 0.6$ for mass ratio $Q > 0.05$. It is noteworthy that the elliptical enveloppe of the outer part of the disc rotates at the same angular velocity than the secondary object.

It is noteworthy that the observational implications of these three features do not stand on the same timescale. Indeed the reduced size of the accretion disc, once noticed, have to be monitored over many binary orbital periods in order to check if the outer radius is indeed decreasing with time, following the timescale associated with the inspiral motion of the binary. On the other hand, the presence of spiral arms and elliptical outer edge will generate light-curve modulation over the orbital period of the binary as these features rotate with the same angular velocity than the binary.
The first two features are not specific to the presence of a gravitational disruptor in the system. Indeed one can explain a reduced outer radius of the disc by the absence of a large reservoir of gas in the vicinity of the black hole. The presence of spiral arms in the accretion disc is also quite common in astrophysics and can find its origin in fluid instabilities. On the other end, the elliptical shape of the outer part of the accretion disc points toward the presence of a secondary massive object. Observing a system where all three features are identified altogether would hint toward the existence of a binary system. Assessing the detectability of these features is not in the scope of this paper and we refer the reader to a companion paper devoted to the observational implications of the findings of the present paper.

ACKNOWLEDGEMENTS

The numerical simulations we have presented in this paper were produced on the DANTE platform (APC, France), and on the HPC resources from GENCI-CINES (Grant A0100412463). Part of this study was supported by the LabEx UnivEarthS, ANR-10-LABX-0023 and ANR-18-IDEX-0001.

DATA AVAILABILITY

The data that support the findings of this study are available from the corresponding author, FC, upon request.

REFERENCES

Abbott B. P. e. a., LIGO Scientific Collaboration Virgo Collaboration 2016, Phys. Rev. Lett., 116, 061102
Armitage P. J., Natarajan P., 2002, ApJ, 567, L9
Begelman M. C., Blandford R. D., Rees M. J., 1980, Nature, 287, 307
Cocchiararo F., Franchini A., Lupi A., Sesana A., 2024, arXiv e-prints, p. arXiv:2402.05175

Combi L., Lopez Armengol F. G., Campanelli M., Noble S. C., Avara M., Krolik J. H., Bowen D., 2022, ApJ, 928, 187
Cuadra J., Armitage P. J., Alexander R. D., Begelman M. C., 2009, MNRAS, 393, 1423
D'Orazio D. J., Haiman Z., MacFadyen A., 2013, MNRAS, 436, 2997
Davelaar J., Haiman Z., 2022, Phys. Rev. D, 105, 103010
Franchini A., Lupi A., Sesana A., Haiman Z., 2023, MNRAS, 522, 1569
Hameury J.-M., 2001, Ecole de Goutelas, 23, 57
Hughes S. A., 2009, in American Astronomical Society Meeting Abstracts #213. p. 230.01
Ingram A., Motta S. E., Aigrain S., Karastergiou A., 2021, MNRAS, 503, 1703
MacFadyen A. I., Milosavljević M., 2008, ApJ, 672, 83
Major Krauth L., Davelaar J., Haiman Z., Westernacher-Schneider J. R., Zrake J., MacFadyen A., 2023, arXiv e-prints, p. arXiv:2310.19766
Matt J., 2023, Object-oriented tools for fitting conics and quadrics (https://www.mathworks.com/matlabcentral/fileexchange/87584-object-oriented-tools-for-fitting-conics-and-quadrics), MATLAB Central File Exchange.
Mayer L., Kazantzidis S., Madau P., Colpi M., Quinn T., Wadsley J., 2007, Science, 316, 1874
Mignon-Risse R., Varniere P., Casse F., 2023a, MNRAS, 519, 2848
Mignon-Risse R., Varniere P., Casse F., 2023b, MNRAS, 520, 1285
Muñoz D. J., Lai D., Kratter K., Miranda R., 2020, ApJ, 889, 114
Noble S. C., Mundim B. C., Nakano H., Krolik J. H., Campanelli M., Zlochower Y., Yunes N., 2012, ApJ, 755, 51
Noble S. C., Krolik J. H., Campanelli M., Zlochower Y., Mundim B. C., Nakano H., Zilhão M., 2021, ApJ, 922, 175
Paczynsky B., Wiita P. J., 1980, A&A, 88, 23
Pihajoki P., Mannerkoski M., Nättilä J., Johansson P. H., 2018, ApJ, 863, 8
Plavec M., Kratochvil P., 1964, Bulletin of the Astronomical Institutes of Czechoslovakia, 15, 165
Preto M., Berentzen I., Berczik P., Spurzem R., 2011, ApJ, 732, L26
Ragusa E., Lodato G., Price D. J., 2016, MNRAS, 460, 1243
Shi J.-M., Krolik J. H., Lubow S. H., Hawley J. F., 2012, ApJ, 749, 118
Siwek M., Weinberger R., Hernquist L., 2023, MNRAS, 522, 2707
Tanaka T., Perna R., Haiman Z., 2012, MNRAS, 425, 2974
Tang Y., Haiman Z., MacFadyen A., 2018, MNRAS, 476, 2249
Vincent F. H., Meheut H., Varniere P., Paumard T., 2013, A&A, 551, A54
Zilhão M., Noble S. C., Campanelli M., Zlochower Y., 2015, Phys. Rev. D, 91, 024034
d'Ascoli S., Noble S. C., Bowen D. B., Campanelli M., Krolik J. H., Mewes V., 2018, ApJ, 865, 140

This paper has been typeset from a TEX/LATEX file prepared by the author.

APPENDIX

B

RESULTS OF THE SPIRAL FIT

This appendix reproduces the Figure 3.13 for all the simulations presented in Table 3.1.

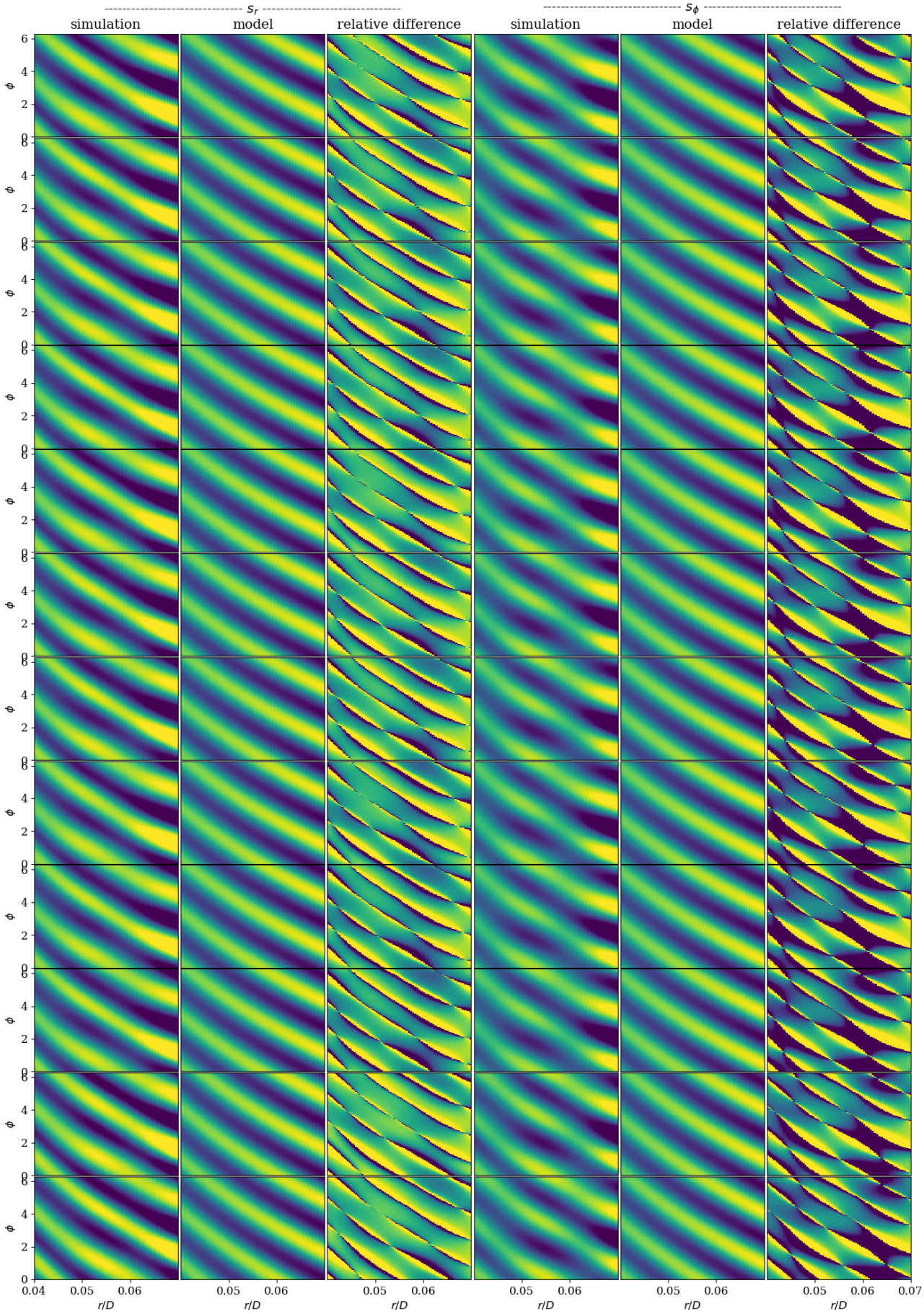

Figure B.1: **Result of the method to find the spiral parameters applied on the simulation of Table 3.1**
The spiral are fitted with the model 3.11 and the method presented in section 3.2.

APPENDIX

C

DERIVATION OF THE IRON LINE PHOTON GEODESICS

This appendix details the derivation of the iron line photons geodesic from the emitting point in the disc to the observer at infinity.

C.1 Coordinates substitution

C.1.1 Definition of the coordinate substitution

Figure 4.2 illustrates the substitution between the coordinate system in which the accretion disc lies in the equatorial plane to the corrdinate system in which the photon's geodesic lies in the equatorial plane.

$$\begin{cases} t' &= t \\ r' &= r \\ \theta' &= f_{\theta'}(\theta, \phi) \\ \phi' &= f_{\phi'}(\theta, \phi) \end{cases}$$

This coordinate substitution is composed of two rotations around the central black hole. First an intermediate coordinate system is obtained by a rotation around the (Oy) axis so that the (Ox) axis is in the direction of the observer. The associated rotation matrix is

$$R_1 = \begin{pmatrix} \sin i_{obs} & 0 & -\cos i_{obs} \\ 0 & 1 & 0 \\ \cos i_{obs} & 0 & \sin i_{obs} \end{pmatrix}$$

From this intermediate coordinate system a rotation around the (Oz) axis places the emitting point in the disc (r_{em}, ϕ_{em}) in the equatorial plane. The rotation matrix is

$$R_2 = \begin{pmatrix} 1 & 0 & 0 \\ 0 & \cos\alpha & \sin\alpha \\ 0 & -\sin\alpha & \cos\alpha \end{pmatrix} \tag{C.1}$$

where α is the rotation angle to determine.

Thus, the complete coordinate substitution is defined by

$$\begin{pmatrix} x' \\ y' \\ z' \end{pmatrix} = R_2 R_2 \begin{pmatrix} x \\ y \\ 0 \end{pmatrix} = \begin{pmatrix} x \sin i_{obs} \\ y\cos\alpha - x\cos i_{obs}\sin\alpha \\ -y\sin\alpha - x\cos i_{obs}\cos\alpha \end{pmatrix} \tag{C.2}$$

The value of the angle α for the second rotation (C.1) place the emitting point in equatorial plane of the coordinate system $(Ox'y')$ with $y' = 0$. The exact value of α does not appear directly in the equation that we need to compute the iron line profile.

From the first line in the coordinate substitution

$$\cos\phi' = cos\phi \sin i_{obs} \tag{C.3}$$

C.1.2 Derivation of $[\partial\phi'/\partial\phi]_{em}$

The substitution in spherical coordinates is

$$\begin{aligned}
&\left\{ \begin{array}{ll} x' & = x\sin i_{obs} + z\cos i_{obs} \\ y' & = y\cos\alpha - x\cos i_{obs}\sin\alpha + z\sin i_{obs}\sin\alpha \end{array} \right. \\
\Leftrightarrow &\left\{ \begin{array}{ll} r'\sin\theta'\cos\phi' & = r\sin\theta\cos\phi\sin i_{obs} + r\cos\theta\cos i_{obs} \\ r'\sin\theta'\sin\phi' & = r\sin\theta\sin\phi\cos\alpha - r\sin\theta\cos\phi\cos i_{obs}\sin\alpha + r\cos\theta\sin i_{obs}\sin\alpha \end{array} \right. \\
\Leftrightarrow &\left\{ \begin{array}{ll} \sin\theta'\cos\phi' & = \sin\theta\cos\phi\sin i_{obs} + \cos\theta\cos i_{obs} \\ \sin\theta'\sin\phi' & = \sin\theta\sin\phi\cos\alpha - \sin\theta\cos\phi\cos i_{obs}\sin\alpha + \cos\theta\sin i_{obs}\sin\alpha \end{array} \right.
\end{aligned}$$

Therefore,

$$\frac{\sin\phi'}{\cos\phi'} = \frac{f_{num}(\theta,\phi)}{f_{denom}(\theta,\phi)} \tag{C.4}$$

where

$$\begin{aligned}
f_{num}(\theta,\phi) &= \sin\theta\sin\phi\cos\alpha - \sin\theta\cos\phi\cos i_{obs}\sin\alpha + \cos\theta\sin i_{obs}\sin\alpha \\
f_{denom}(\theta,\phi) &= \sin\theta\cos\phi\sin i_{obs} + \cos\theta\cos i_{obs}
\end{aligned}$$

The differential form of equation (C.4) is

$$\frac{1}{(\cos\phi')^2}d\phi' = \frac{\partial}{\partial\theta}\left(\frac{f_{num}}{f_{denom}}\right)d\theta + \frac{\partial}{\partial\phi}\left(\frac{f_{num}}{f_{denom}}\right)d\phi$$

Therefore

$$\left(\frac{\partial\phi'}{\partial\phi}\right)_{em} = (\cos\phi')^2\left(\frac{\partial}{\partial\phi}\left[\frac{f_{num}}{f_{denom}}\right]\right)_{em} = (\cos\phi')^2\left(\frac{\frac{\partial f_{num}}{\partial\phi}f_{denom} - \frac{\partial f_{denom}}{\partial\phi}f_{num}}{f_{denom}^2}\right)_{em}$$

In this expression:

- From the change of coordinate system in the spherical coordinate system: $\cos\phi' = \sin i_{obs}\cos\phi$.
- The partial derivative of f_{denom} at the position of the emitter is:

$$\frac{\partial f_{denom}}{\partial\phi}(\theta = \pi/2) = -\sin\phi\sin i_{obs}$$

- The partial derivative of f_{num} at the position of the emitter is:

$$\frac{\partial f_{num}}{\partial\phi}(\theta = \pi/2) = \cos\phi\cos\alpha + \cos i_{obs}\sin\phi\sin\alpha - \frac{\partial\alpha}{\partial\phi}(\sin\phi\sin\alpha + \cos i_{obs}\cos\phi\cos\alpha)$$

  As the photon's geodesic lies in the equatorial plane:

$$\theta' = \pi/2 \Leftrightarrow z' = 0 \Leftrightarrow -y\sin\alpha - x\cos i_{obs}\cos\alpha \Rightarrow \left\{ \begin{array}{ll} \alpha & = \pi/2 \quad \text{if } y = 0 \\ \tan\alpha & = -\frac{x\cos i_{obs}}{y} \quad \text{otherwise} \end{array} \right.$$

  – if $y = 0 \Leftrightarrow \sin\phi = 0$, then $\alpha = \pi/2$ and thus $\cos\alpha = 0$

– otherwise

$$\tan\alpha = -\frac{x\cos i_{obs}}{y} \Leftrightarrow \frac{\sin\alpha}{\cos\alpha} \underset{(\theta=pi/2)}{=} -\frac{r\cos\phi\cos i_{obs}}{r\sin\phi}$$

Thus, in any case:

$$\sin\phi\sin\alpha + \cos i_{obs}\cos\phi\cos\alpha = 0$$

and

$$\frac{\partial f_{num}}{\partial\phi}(\theta=\pi/2) = \cos\phi\cos\alpha + \cos i_{obs}\sin\phi\sin\alpha$$

Using the expression of cos(arctan(x)) and sin(arctan(x)):

$$\frac{\partial f_{num}}{\partial\phi}(\theta=\pi/2) = \frac{\sin\phi\cos\phi}{\sqrt{(\sin\phi)^2+(\cos\phi)^2(\cos i_{obs})^2}}(\sin i_{obs})^2$$

Finally

$$\left(\frac{\partial\phi'}{\partial\phi}\right)_{em} = \frac{\sin\phi_0\sin i_{obs}}{\sqrt{(\sin\phi_0)^2+(\cos\phi_0)^2(\cos i_{obs})^2}} \tag{C.5}$$

C.2 Derivation of the observed frequency

The metric elements of the Schwarzschild metric (equation (4.3)) are

$$g_{\mu\nu} = \begin{pmatrix} -\left(1-\frac{R_s}{r}\right) & 0 & 0 & 0 \\ 0 & \frac{1}{1-\frac{R_s}{r}} & 0 & 0 \\ 0 & 0 & r^2 & 0 \\ 0 & 0 & 0 & r^2\sin^2\theta \end{pmatrix}$$

The observed frequency of a photon emitted at the position x in the disc for an observer at infinity in the direction ν_{obs} is

$$\frac{\nu_{obs}(\vec{n}_{obs};\vec{x})}{\nu_{em}} = \frac{(\mathbf{p}\cdot\mathbf{v})_{obs}}{(\mathbf{p}\cdot\mathbf{u})_{em}} \tag{C.6}$$

where $\mathbf{p}$ is the photon 4-momentum along its geodesic, $\mathbf{u}$ is the iron line emitters 4-velocity in the disc, and $\mathbf{v}$ is the observer 4-velocity.

Derivation of $(\mathbf{p}\cdot\mathbf{v})_{obs}$ in equation (C.6)

For a motionless observer at infinity, v can be written as

$$\mathbf{v}^\mu = \left(c\frac{dt_{obs}}{d\lambda_{obs}}, \vec{0}\right)$$

As the observer is on a time like geodesic:

$$-1 = \mathbf{v}\cdot\mathbf{v} = g_{\mu\nu}\mathbf{v}^\mu\mathbf{v}^\nu = -\left(1-\frac{R_s}{r}\right)\left(c\frac{dt_{obs}}{d\lambda_{obs}}\right)^2$$

Thus

$$\mathbf{v}^\mu == \left(\frac{1}{\sqrt{1-\frac{R_s}{r}}}, \vec{0}\right) \underset{r\to+\infty}{\longrightarrow} (1,\vec{0})$$

Therefore

$$(\mathbf{p}\cdot\mathbf{v})_{obs} = \mathbf{p}_\mu\mathbf{v}^\mu = p_t \tag{C.7}$$

the first covariant coordinate of the photon 4-momentum.

Derivation of $(\mathbf{p}\cdot\mathbf{u})_{em}$ in equation (C.6)

At the emitting point,

$$(\mathbf{p}\cdot\mathbf{u})_{em} = \mathbf{p}^{\mu'}\underline{\mathbf{e}}_{\mu'}\cdot\mathbf{u}^{\nu}\underline{\mathbf{e}}_{\nu} = \mathbf{p}^{\mu'}\mathbf{u}^{\nu}\ P^{\nu'}{}_{\nu}\ \underline{\mathbf{e}}_{\mu'}\cdot\underline{\mathbf{e}}_{\nu'} = \mathbf{p}^{\mu'}\mathbf{u}^{\nu}\ P^{\nu'}{}_{\nu}\ g_{\mu'\nu'} \tag{C.8}$$

where $P^{\nu'}{}_{\nu}$ is the change of coordinates from the coordinates in which the disc lies in the equatorial plane to the coordinates in which the photon trajectory lies in the equatorial plane, and the x-axis is aligned with the observer line of sight.

$$P^{\nu'}{}_{\nu} = \frac{\partial x^{\nu'}}{\partial x^{\nu}} \tag{C.9}$$

In the Schwarzschild metric, spherical symmetry implies that the photon trajectories lie in a plane. Coordinates can be chosen so that they belong to the equatorial plane $\theta' = \pi/2$. Since the metric elements do not explicitly depend on the coordinates t and phi, two constants of the movement result from the Killing 4-vectors $\xi = (1,0,0,0)$ and $\eta = (0,0,1,0)$: the specific energy

$$e = -\boldsymbol{\xi}\cdot\mathbf{p} = -g_{\mu\nu}\xi^{\mu}p^{\nu} = \left(1-\frac{R_s}{r}\right)c\frac{dt}{d\lambda} \tag{C.10}$$

and the specific angular momentum

$$\ell = \boldsymbol{\eta}\cdot\mathbf{p} = -g_{\mu\nu}\eta^{\mu}p^{\nu} = r^2\sin^2\theta\frac{d\phi_{Ph}}{d\lambda_{Ph}} = r^2\frac{d\phi}{d\lambda}$$

Thus, the 4-momentum of photons in the spherical coordinates $x' = (t', r', theta' = pi/2, phi')$ in which the photon trajectory lies in the equatorial plane $\theta' = \pi/2$ is:

$$\mathbf{p}^{\mu'} = \left(c\frac{dt'}{d\lambda'}, \frac{dr'}{d\lambda'}, 0, \frac{d\phi'}{d\lambda'}\right) = e\left(\frac{1}{1-\frac{R_s}{r'}}, \frac{b}{r'^2}\frac{dr'}{d\phi'}, 0, \frac{b}{r'^2}\right) \tag{C.11}$$

where b is the impact parameter:

$$b = \frac{\ell}{e} \tag{C.12}$$

In the system of coordinates in which the accretion disc lies in the equatorial plane x^{μ}, the contravariant components of the emitters' 4-velocity are

$$\mathbf{u}^{\nu} = \left(c\frac{dt_{em}}{d\lambda_{em}}, \frac{dr_{em}}{d\lambda_{em}}, \frac{d\theta_{em}}{d\lambda_{em}}, \frac{d\phi_{em}}{d\lambda_{em}}\right) = c\frac{dt_{em}}{d\lambda_{em}}\left(1, \frac{u_r}{c}, 0, \frac{1}{r}\frac{u_{\phi}}{c}\right)$$

Since emitters are on time-like geodesics:

$$-1 = \mathbf{u}\cdot\mathbf{u}$$

And the contravariant components of the emitters' 4-velocity in equation

$$\mathbf{u}^{\nu} = \frac{1}{\sqrt{1-\frac{R_s}{r}-\frac{1}{1-\frac{R_s}{r}}\frac{u_r^2}{c^2}-\frac{u_{\phi}^2}{c^2}}}\left(1, \frac{u_r}{c}, 0, \frac{1}{r}\frac{u_{\phi}}{c}\right) \tag{C.13}$$

Therefore, using equations (C.9), (C.11), and (C.13) in equation (C.8)

$$\begin{aligned}(\mathbf{p}\cdot\mathbf{u})_{em} =& \frac{1}{\sqrt{1-\frac{R_s}{r_{em}}-\frac{1}{1-\frac{R_s}{r_{em}}}\frac{u_r^2}{c^2}-\frac{u_{\phi}^2}{c^2}}}\ e\times \\ & \left[-\left(1-\frac{R_s}{r_{em}}\right)\frac{1}{1-\frac{R_s}{r_{em}}} + \frac{1}{1-\frac{R_s}{r_{em}}}\frac{b}{r_{em}^2}\left[\frac{dr'}{d\phi'}\right]_{em}\frac{u_r}{c} + r^2\left[\frac{d\phi'}{d\phi}\right]_{em}\frac{b}{r_{em}^2}\frac{1}{r_{em}}\frac{u_{\phi}}{c}\right]\end{aligned} \tag{C.14}$$

As $e = -\mathbf{p}_t$ equation (C.6) is

$$\frac{\nu_{obs}(\vec{n}_{obs};\vec{x})}{\nu_{em}} = \frac{\sqrt{1-\frac{R_s}{r_{em}}-\frac{1}{1-\frac{R_s}{r_{em}}}\frac{u_r^2}{c^2}-\frac{u_\phi^2}{c^2}}}{1-\frac{1}{1-\frac{R_s}{r_{em}}}\frac{b}{r_{em}^2}\left[\frac{dr'}{d\phi'}\right]_{em}\frac{u_r}{c}-\frac{b}{r_{em}}\left[\frac{d\phi'}{d\phi}\right]_{em}\frac{u_\phi}{c}} \tag{C.15}$$

$\left[\frac{d\phi'}{d\phi}\right]_{em}$ is derived in section C.1.2.

As the photons geodesic are null geodesic:

$$0 = \mathbf{p}\cdot\mathbf{p} = e\left(-\frac{1}{1-\frac{R_s}{r}}+\frac{1}{1-\frac{R_s}{r}}\frac{b^2}{r^4}\left(\frac{dr}{d\phi'}\right)^2+r^2\frac{b^2}{r^4}\right) \tag{C.16}$$

Solving this equation between the emitting point in the disc and the observer at infinity constraint the value of the impact parameter b, and

$$\left[\frac{dr'}{d\phi'}\right]_{em} = \frac{r_{em}^2}{b}\sqrt{1-\frac{b^2}{r_{em}}^2\frac{1}{1-\frac{R_s}{r_{em}}}} \tag{C.17}$$

C.3 Initial direction of emission of photons

The initial direction of emission of photons is defined through the spatial component of the photon 4-momentum $\frac{d\vec{r'}}{d\lambda}$:

$$\widehat{c} = -\left[\frac{\frac{d\vec{r'}}{d\lambda}}{\left\|\frac{d\vec{r'}}{d\lambda}\right\|}\right]_{\lambda=\lambda_{em}} = -\left[\frac{\frac{d\vec{r}}{d\phi'}}{\left\|\frac{d\vec{r}}{d\phi'}\right\|}\right]_{\phi'=\phi'em}$$

The minus sign translates the fact that ϕ' decreases and r increases along the geodesic. Due to the coordinate substitution associated with each geodesic (presented in section C.1), the photon's geodesic is in the equatorial plane $(Ox'y')$ and the direction of the observer at infinity coincides with the x'-axis. Therefore, the spatial components can be written

$$\vec{r} = r(\phi')\left(\cos\phi'\ \vec{n}_{obs}+\sin\phi'\ \vec{e}_{y'}\right)$$

The vector $\vec{e}_{y'}$ can be expressed with the initial condition:

$$\vec{e}_{y'} = \frac{\vec{r}_{em}-r_{em}\cos\phi'_{em}\vec{n}_{obs}}{r_{em}\sin\phi'_{em}}$$

With this fixed orthonormal basis

$$\frac{d\vec{r}}{d\phi'} = \frac{dr}{d\phi'}\left(\cos\phi'\ \vec{n}_{obs}+\sin\phi'\ \vec{e}_{y'}\right)+r(\phi')\left(-\sin\phi'\ \vec{n}_{obs}+\cos\phi'\ \vec{e}_{y'}\right)$$

Thus the initial direction of photons is

$$\widehat{c} = \frac{1}{\sqrt{\left[\frac{dr}{d\phi'}\right]_{em}+r_{em}^2}}\left(\left[\frac{dr}{d\phi'}\right]_{em}+r_{em}\right)\left(\left(\cos\phi'-\sin\phi'\right)\vec{n}_{obs}+\left(\cos\phi'+\sin\phi'\right)\vec{e'}_y\right)$$

Since

$$\vec{n}_{obs}\cdot\vec{n}_d = \cos i_{obs}$$

and

$$\vec{e'}_y\cdot\vec{n}_d = -\frac{\cos\phi'_{em}}{\sin\phi'_{em}}\cos i_{obs}$$

the scalar product between the initial direction of emission of photons and the normal to the disc is

$$\widehat{c}(\vec{n}_{obs};r_{em},\phi_{em})\cdot\vec{n}_d = \frac{1}{\sqrt{\left[\frac{dr}{d\phi'}\right]_{em}+r^2}}\frac{\cos i_{obs}}{\sin\phi'_{em}}\ r_{em}$$

C.4 First-order expansion of the geodesic equation

C.4.1 Resolution at zero-order

The geodesic equation at the zero-order (equation (4.13)) is

$$\frac{d^2x_0}{d\phi'^2} = -x_0.$$

The general form of the solution is

$$x_0 = A_0 \sin(\phi' + \alpha_0)$$

As the observer is at infinity ($x_0 \to 0$) on the x-axis ($\phi' = 0$),

$$x_0(\phi' = 0) = 0$$

Thus

$$\alpha_0 = 0$$

The geodesic equation (4.9) is

$$\frac{1}{b^2} = \left(\frac{dx}{d\phi'}\right)^2 + x^2\left(1 - R_s x\right)$$

At the zero-order $R_s \times x \ll 1$, it is

$$\frac{1}{b^2} = \left(\frac{dx_0}{d\phi'}\right)^2 + x_0^2$$

The constant A_0 can be determined using this geodesic at the emitting point:

$$\frac{1}{b^2} = \left(A_0\cos(\phi'_{em})\right)^2 + A_0^2\sin^2(\phi'_{em})^2 = A_0^2$$

Therefore, the solution at the zero-order is

$$x_0 = \frac{\sin(\phi')}{b} \tag{C.18}$$

C.4.2 Resolution at first order

The equation at first order is

$$\frac{d^2x_1}{d\phi^2} = -x_1 + \frac{3}{2}R_s x_0^2 \tag{C.19}$$

The general form of the solution is

$$x_1(\phi') = A_1\sin(\phi' + \alpha_1) + x_1^p(\phi') \tag{C.20}$$

where the first term $A_1\sin(\phi' + \alpha_1)$ is called the homogeneous part, in which the constants A_1 and α_1 will be determined with the initial and final conditions, and $x_1^p(\phi')$ is a peculiar solution of equation (C.19).

The peculiar solution x_1^p is found with the variation method. For this method, x_1^p is written

$$x_1^p(\phi') = A_1^p(\phi')\sin(\phi' + \alpha_1^p). \tag{C.21}$$

where α_1^p is a constant and $A_1^p(\phi')$ is a function of ϕ. As this peculiar solution is just one among many possible solutions equation (C.19), I can chose $\alpha_1^p = 0$ so that the following development is less complex.
With the general form of the solution given in equation (C.20), equation (C.19) can be written

$$\frac{d^2(A_1\sin(\phi' + \alpha_1) + x_1^p(\phi'))}{d\phi^2} = -A_1\sin(\phi' + \alpha_1) - x_1^p(\phi') + \frac{3}{2}R_s x_0^2(\phi')$$

The homogeneous terms simplify on both side of the equation. Replacing x_1^p by its expression (C.21) gives

$$\frac{d^2A_1^p}{d\phi^2}(\phi')\sin(\phi') + 2\frac{dA_1^p}{d\phi'}(\phi')\cos(\phi') - A_1^p(\phi')\sin(\phi') = -A_1^p(\phi')\sin(\phi') + \frac{3}{2}R_s x_0^2(\phi')$$

Using the expression of x_0 given in (C.18), this equation can be written:

$$\frac{d^2A_1^p}{d\phi^2}(\phi') + \frac{2}{\tan\phi'}\frac{dA_1^p}{d\phi'}(\phi') = \frac{3R_s}{2b^2}\sin\phi \tag{C.22}$$

This is an equation of the first order in $\frac{dA_1^p}{d\phi'}$ with a second member. The general solution of this equation can be written

$$\frac{dA_1^p}{d\phi'}(\phi') = B_0(\phi') + B_p(\phi') \tag{C.23}$$

Where

- B_0 is the general solution of the homogeneous equation

  $$B_0' + \frac{2}{\tan\phi'}B_0(\phi') = 0$$

  which is

  $$B_0(\phi') = C_0\exp\left(-2\ln|\sin\phi|\right) = \frac{C_0}{(\sin\phi)^2} \tag{C.24}$$

  where C_0 is a constant that can be determined with the limit conditions.

- B_p is a peculiar solution of equation (C.22) found with the variation method. For this method, B_p is written

  $$B_p(\phi') = \frac{C(\phi')}{\sin^2\phi'}$$

  where C is a function of ϕ. It satisfies equation (C.22):

  $$B_0'(\phi') + B_p'(\phi') + \frac{2}{\tan\phi'}\left(B_0(\phi') + B_p(\phi')\right) = \frac{3R_s}{2b^2}\sin\phi$$

  The homogeneous terms simplify in the equation. Thus, B_p is solution of the equation

  $$B_p'(\phi') + \frac{2}{\tan\phi'}B_p(\phi') = \frac{3R_s}{2b^2}\sin\phi \tag{C.25}$$

  The first derivative of B_p is given by

  $$B_p'(\phi') = \frac{d}{d\phi'}\left(\frac{C(\phi')}{\sin^2\phi'}\right) = \frac{C'(\phi')\sin^2\phi - 2C(\phi')\sin\phi\cos\phi'}{\sin^4\phi'} = \frac{C'(\phi')}{\sin^2\phi'} - \frac{2C(\phi')}{\sin^2\phi\tan\phi'}$$

  so that equation (C.25) can be written:

  $$\frac{C'(\phi')}{\sin^2\phi'} - \frac{2C(\phi')}{\sin^2\phi\tan\phi'} + \frac{2}{\tan\phi'}\frac{C(\phi')}{\sin^2\phi'} = \frac{3R_s}{2b^2}\sin\phi \tag{C.26}$$

  The function C satisfies the equation

  $$C'(\phi') = \frac{3R_s}{2b^2}\sin^3\phi$$

To find the expression of $C(\phi')$ the next step is to compute the primitive of $x \mapsto (\sin\phi)^3$

$$\begin{aligned} I_1 &= \int (\sin\phi)^3 \, d\phi \\ &= \int (\sin\phi)^2 \sin\phi \; d\phi \\ &= \int \left[1 - (\cos\phi)^2\right] \sin\phi \; d\phi \\ &= \int \sin\phi \; d\phi - \int (\cos\phi)^2 \sin\phi \; d\phi \\ &= -\cos\phi + \frac{(\cos\phi)^3}{3} \end{aligned}$$

Thus,

$$C(\phi') = \frac{3R_s}{2b^2}\left(\frac{(\cos\phi)^3}{3} - \cos\phi\right) + D$$

where D is a constant. As the peculiar solution B_p is just one among many possible solutions of equation (C.22), I can chose $D = 0$ so that the following development is less complicated.

$$B_p(\phi') = \frac{R_s}{2b^2} \, \frac{(\cos\phi)^3 - 3\cos\phi'}{(\sin\phi)^2} \tag{C.27}$$

Using equations (C.24) and (C.27), the general solution of equation (C.22) whose form was given in equation (C.23) is:

$$\frac{dA_1^p}{d\phi'}(\phi') = \frac{C_0}{(\sin\phi)^2} + \frac{R_s}{2b^2} \, \frac{(\cos\phi)^3 - 3\cos\phi'}{(\sin\phi)^2} \tag{C.28}$$

where C_0 is a constant. As the peculiar solution A_1^p is just one among many possible solutions of equation (C.19), I can chose $C_0 = 0$ so that the following development is not unnecessarily complicated. To find the expression of $A_p(\phi')$ the last step is to compute the primitive of $x \mapsto \frac{(\cos\phi)^3 - 3\cos\phi'}{(\sin\phi)^2}$

$$\begin{aligned} I_2 &= \int \frac{(\cos\phi)^3 - 3\cos\phi'}{(\sin\phi)^2} \; d\phi \\ &= \int \frac{(\cos\phi)^2 \cos\phi - 3\cos\phi'}{(\sin\phi)^2} \; d\phi \\ &= \int \frac{\left[1 - (\sin\phi)^2\right] \cos\phi - 3\cos\phi'}{(\sin\phi)^2} \; d\phi \\ &= -\int \cos\phi \; d\phi - 2\int \frac{\cos\phi}{(\sin\phi)^2} \; d\phi \\ &= -\sin\phi' + \frac{2}{\sin\phi'} + E \end{aligned}$$

Where E is a constant. As the peculiar solution A_1^p is just one among many possible solutions of equation (C.19), I can chose $E = 0$ so that the following development is less complex.
Finaly a peculiar solution to equation (C.22) is

$$A_1^p(\phi') = \frac{R_s}{2b^2}\left(\frac{2}{\sin\phi'} - \sin\phi\right)$$

Thus, the peculiar solution of equation (C.19) defined in equation (C.21) is

$$x_1^p(\phi') = \frac{R_s}{2b^2}\left(2 - (\sin\phi)^2\right)$$

And the solution to the photon equation of motion at the first order is:

$$x_1(\phi') = A_1 \sin(\phi' + \alpha_1) + \frac{R_s}{2b^2}\left(2 - (\sin\phi)^2\right) \tag{C.29}$$

where A_1 and α_1 are two constants that can be determined with the limit conditions, which I will do now.

- At the first order, the radial equation of motion (4.9) is

$$0 = 2\frac{dx_0}{d\phi'}\frac{dx_1}{d\phi'} + 2x_0x_1 - R_s x_0^3 \tag{C.30}$$

  Using equations (C.18) and (C.29) for the expressions of x_0 and x_1:

  – the first term of equation (C.30) is

$$\begin{aligned}\frac{1}{2b}\left(2\frac{dx_0}{d\phi'}\frac{dx_1}{d\phi'}\right) &= \cos\phi\left(A_1\cos(\phi'+\alpha_1) - \frac{R_s}{b^2}\sin\phi\cos\phi\right)\\ &= A_1\left[(\cos\phi)^2\cos\alpha_1 - \cos\phi\sin\phi\sin\alpha_1\right] - \frac{R_s}{b^2}\sin\phi\,(\cos\phi)^2\end{aligned}$$

  – the second term of equation (C.30) is

$$\begin{aligned}\frac{1}{2b}\left(2x_0x_1\right) &= \sin\phi\left(A_1\sin(\phi'+\alpha_1) + \frac{R_s}{2b^2}\left(2-(\sin\phi)^2\right)\right)\\ &= A_1\left[(\sin\phi)^2\cos\alpha_1 + \cos\phi\sin\phi\sin\alpha_1\right] + \frac{R_s}{b^2}\sin\phi\left(1 - \frac{(\sin\phi)^2}{2}\right)\end{aligned}$$

  – the third term of equation (C.30) is

$$\frac{1}{2b}\left(-R_s x_0^3\right) = -\frac{R_s}{b^2}\sin\phi\left(\frac{(\sin\phi)^2}{2}\right)$$

  Thus, equation (C.30) gives

$$0 = A_1\left[\left((\sin\phi)^2 + (\cos\phi)^2\right)\cos\alpha_1 + 0\times\sin\alpha_1\right] + \frac{R_s}{b^2}\sin\phi\left[-(\cos\phi)^2 + 1 - \frac{(\sin\phi)^2}{2} - \frac{(\sin\phi)^2}{2}\right]$$

  $\Leftrightarrow 0 = A_1\cos\alpha_1$

  The constant α_1 is

$$\alpha_1 = \pi/2 \tag{C.31}$$

- The observer is at ($r_{obs} \to +\infty$; $\phi_{obs} = 0$). The solution given by (C.29) has to satisfy this condition:

$$\frac{1}{r_{obs}} = 0 = x_1(\phi_{obs}=0) = A_1\sin(0+\alpha_1) + \frac{R_s}{2b^2}(2-0) = A_1\sin(\pi/2) + \frac{R_s}{b^2}$$

  Thus

$$A_1 = -\frac{R_s}{b^2} \tag{C.32}$$

Finally using the equations (C.31) and (C.32) to replace the values of the constants in equation (C.29), the solution at the first order of the equations of motion is:

$$x_1(\phi') = \frac{R_s}{2b^2}\left[1 - 2\cos\phi' + (\cos\phi)^2\right] \tag{C.33}$$

And to conclude all this computation, the complete solution of the perturbation expansion at the first order of the equation of motion is

$$\frac{1}{r(\phi')} = x(\phi') = \frac{\sin\phi'}{b} + \frac{R_s}{2b^2}\left[1 - 2\cos\phi' + (\cos\phi)^2\right] \tag{C.34}$$

This is equations (9) and (10) in Hartnoll & Blackman (2002) with the impact parameter that I write b that is equal to $2R$ in their notation. The impact parameter b can be derived writing equation (C.34) for the initial condition

$$\frac{1}{r_{em}} = x_{em} = \frac{\sin\phi'}{b} + \frac{R_s}{2b^2}\left[1 - 2\cos\phi'_{em} + \left(\cos\phi'_{em}\right)^2\right]$$

b is the solution of the quadratic equation:

$$0 = b^2 - \frac{\sin\phi'_{em}}{x_{em}}b + \frac{R_s}{2x_{em}}(1 - \cos\phi'_{em})^2$$

whose discriminant is

$$\Delta = \frac{(\sin\phi'_{em})^2}{x_{em}^2} - \frac{2R_s}{x_{em}}(1 - \cos\phi'_{em})^2$$

Thus, the impact parameter is given by

$$b = \frac{r_{em}}{2}\sin\phi_0 \pm \frac{r_{em}}{2}\sqrt{(\sin\phi'_{em})^2 + \frac{2R_s}{r_0}(1 - \cos\phi'_{em})^2}$$

The physical solution is the one with the + whether than the − so that $b \geq 0$. This is equation (11) in Hartnoll & Blackman (2002).

APPENDIX

D

SUBSTITUTION IN THE DOUBLE INTEGRAL FOR THE SECOND METHOD (SECTION 4.3.2)

For the subsitution Ψ_1 in equation (4.30) to be valid, function $r \to \nu_{obs}(r, \phi_\star)$ must be bijective. Figure 4.9 shows a Keplerian disc's observed frequency radial evolution for different inclination (i_{obs}) and azimuthal (ϕ) angle values. These radial profiles are only sometimes bijective, depending on the values of (i_{obs}, ϕ). The other cases can be taken into account using Fubini's theorem:

$$\begin{aligned} F(\tilde{\nu}, \vec{n}_{obs}) &= \iint_{\vec{x}\in\mathcal{D}} \delta\left(\tilde{\nu} - \nu_{obs}(\vec{n}_{obs}; \vec{x})\right)\ f\left(\vec{n}_{obs}; \vec{x}\right)\ d^2x \\ &= \iint_{(r,\phi)\in]r_{min};r_{max}[\ \times\ ]0;2\pi[} \delta\left(\tilde{\nu} - \nu_{obs}(\vec{n}_{obs}; r, \phi)\right)\ f\left(\vec{n}_{obs}; r, \phi\right)\ dr d\phi \\ &= \int_{\phi\in]0;2\pi[} \left[\int_{r\in]r_{min};r_{max}[} \delta\left(\tilde{\nu} - \nu_{obs}(\vec{n}_{obs}; r, \phi)\right)\ f\left(\vec{n}_{obs}; r, \phi\right)\ dr \right] d\phi \end{aligned}$$

The integration domain of the inner integral is cut into several sub-intervals on which the function $r \to \nu_{obs}(r, \phi_\star)$ is bijective. In the case of a Keplerian velocity field, Figure 4.9 shows that there are at most two intervals to define bijections of the observed frequency. The general formula is

$$\begin{aligned} F(\tilde{\nu}) &= \int_{\phi\in]0;2\pi[} \left[\int_{r\in]r_{min};r_{max}[} \delta\left(\tilde{\nu} - \nu_{obs}(\vec{n}_{obs}; r, \phi)\right)\ f\left(\vec{n}_{obs}; r, \phi\right)\ dr \right] d\phi \\ &= \int_{\phi\in]0;2\pi[} \sum_i \left[\int_{r\in I_i^r} \delta\left(\tilde{\nu} - \nu_{obs}(\vec{n}_{obs}; r, \phi)\right)\ f\left(\vec{n}_{obs}; r, \phi\right)\ dr \right] d\phi \end{aligned}$$

In this last expression, the sum over i is the sum over the sub-intervals I_i^r of $]r_{min}; r_{max}[$ in which the function $r \to \nu_{obs}(r, \phi_\star)$ is bijective. The union of these intervals covers the accretion disc's radial domain $\bigcup_i I_i^r =]r_{min};\ r_{max}[$, and there is no intersection between them.

The radial polar coordinate r is substituted by the coordinate ν in each integral of the sum. This substitution is defined by:

$$\begin{aligned} \Psi_{\phi_\star,i} : \Lambda_{\phi_\star,i} &\to I_i^r \\ \nu &\to R_{\phi_\star,i}(\nu) \end{aligned} \tag{D.3}$$

where $\Lambda_{\phi_\star,i}$ is the interval of values for the observed frequency emitted by the disc portion in I_i^r for the azimuthal angle $\phi_\star$. $\nu \to R_{\phi_\star,i}(\nu)$ is the inverse function of $r \to \nu_{obs}(r, \phi_\star)$, with the values of the

radius restricted to I_i^r. With the change of coordinates, the inner integral defined by

$$\mathcal{I}_{\phi_\star,i} = \int_{r\in I_i^r} \delta\left(\tilde{\nu} - \nu_{obs}(\vec{n}_{obs}; r, \phi)\right)\ f\left(\vec{n}_{obs}; r, \phi\right)\ dr$$

becomes

$$\mathcal{I}_{\phi_\star,i} = \int_{\nu\in\Lambda_{\phi_\star,i}} \delta\left(\tilde{\nu} - \nu_{obs}(\vec{n}_{obs}; R_{\phi_\star,i}(\nu), \phi)\right)\ \frac{f\left(\vec{n}_{obs}; R_{\phi_\star,i}(\nu), \phi\right)}{\left|\frac{\partial \nu_{obs}}{\partial r}(\vec{n}_{obs}; R_{\phi_\star,i}(\nu), \phi_\star)\right|}\ d\nu \tag{D.4}$$

As $\nu_{obs}(\vec{n}_{obs}; R_{\phi_\star,i}(\nu), \phi) = \nu$, the Dirac delta distribution simplifies the integral. The integral is null if $\tilde{\nu}$ is not in $\Lambda_{\phi_\star,i}$, which is equivalent to saying that the function $r \to \nu_{obs}(\vec{n}_{obs}; r, \phi_\star) - \tilde{\nu}$ has no roots in I_i^r.

$$\mathcal{I}_{\phi_\star,i} = \begin{cases} \frac{f\left(\vec{n}_{obs}; R_{\phi_\star,i}(\tilde{\nu}), \phi_\star\right)}{\left|\frac{\partial \nu_{obs}}{\partial r}(\vec{n}_{obs}; R_{\phi_\star,i}(\tilde{\nu}), \phi_\star)\right|} & \text{if } \tilde{\nu} \in \Lambda_{\phi_\star,i} \\ 0 & \text{otherwise} \end{cases} \tag{D.5}$$

$R_{\phi_\star,i}(\tilde{\nu})$ is the root of the function $r \to \nu_{obs}(\vec{n}_{obs}; r, \phi_\star) - \tilde{\nu}$ restricted to the intervals I_i^r where it cancels.

One-dimensional integral to compute the iron line flux

Finally, the integral on the azimuthal angle ϕ to compute the flux $F(\tilde{\nu})$ is

$$\begin{aligned} F(\tilde{\nu}) &= \int_{\phi\in]0;2\pi[} \sum_{i_{root}} \mathcal{I}_{\phi,i_{root}}\ d\phi \\ &= \int_{\phi\in]0;2\pi[} \sum_{i_{root}} \frac{f\left(\vec{n}_{obs}; R_{\phi_\star,i_{root}}(\tilde{\nu}), \phi\right)}{\left|\frac{\partial \nu_{obs}}{\partial r}(\vec{n}_{obs}; R_{\phi_\star,i_{root}}(\tilde{\nu}))\right|} d\phi \end{aligned} \tag{D.6}$$

where the sum over i_{root} is the sum over the roots of $r \to \nu_{obs}(\vec{n}_{obs}, r, \phi_\star) - \tilde{\nu}$ for each value of $\phi_\star$, written $R_{\phi_\star,i_{root}}(\tilde{\nu})$. The sum over the intervals on which $r \to \nu_{obs}(\vec{n}_{obs}, r, \phi_\star)$ is bijective is not relevant anymore and was only a calculation intermediary.

APPENDIX

E

STUDY OF THE TRUNCATION OF THE OUTER PARTS WITH GAUSSIAN NOISE

Using the binning method on the model developed by Hartnoll & Blackman (2000, 2001, 2002) prevents us from directly obtaining an observed iron line model with a realistic noise (see section 5.6). The 'fluxes' computed by the model at the entrance of the detector are not in physical units. This work's iron line observation model will be much simpler. Section 5.4 presents the results of the method based on the observed iron line profiles obtained from the theoretical iron line profiles to which observational uncertainty in the flux in each bin is added. In this section, we explore how fluctuations around the theoretical values of the flux in each bin can impact the detection of the accretion disc truncation due to the gravitational influence of a MBH companion.

We chose to add fluctuations to the flux value in each bin with a Gaussian drawn. The mean of the distribution μ_i is set to the theoretical value of the flux in each bin, while the standard deviation σ_i is a fixed fraction of the flux in each bin.

$$\mu^i = f^i \tag{E.1a}$$

$$\sigma^i = x_\sigma \times f^i \tag{E.1b}$$

Each bin has a unique Gaussian distribution, but the value of x_σ remains constant for each Gaussian used to determine the observed flux. Figure E.1 displays observed iron line profiles obtained by Gaussian drawn with different values of parameter x_σ.
Using a Gaussian distribution to add fluctuations to the flux value in each bin might seem unusual, as a Poisson distribution is usually used for this purpose. However, this choice is because the flux is not measured in physical units and cannot be converted into a number of photons per unit of time.

The error in the flux in each bin is the standard deviation. Thus, the observational value of the flux in each bin is

$$f^i_\star \pm \sigma^i \tag{E.2}$$

where $f^i_\star$ is the result of the Gaussian drawn defined in equation (E.1).

To compute the flux in a frequency band, the same procedure used for the theoretical iron line profile can be followed, with the only difference being the replacement of f^i with $f^i_\star$ in equation (5.8). As the error in each bin is $\sigma^i = x_\sigma \times f^i$, the relative error in the flux in a frequency band is the same as in

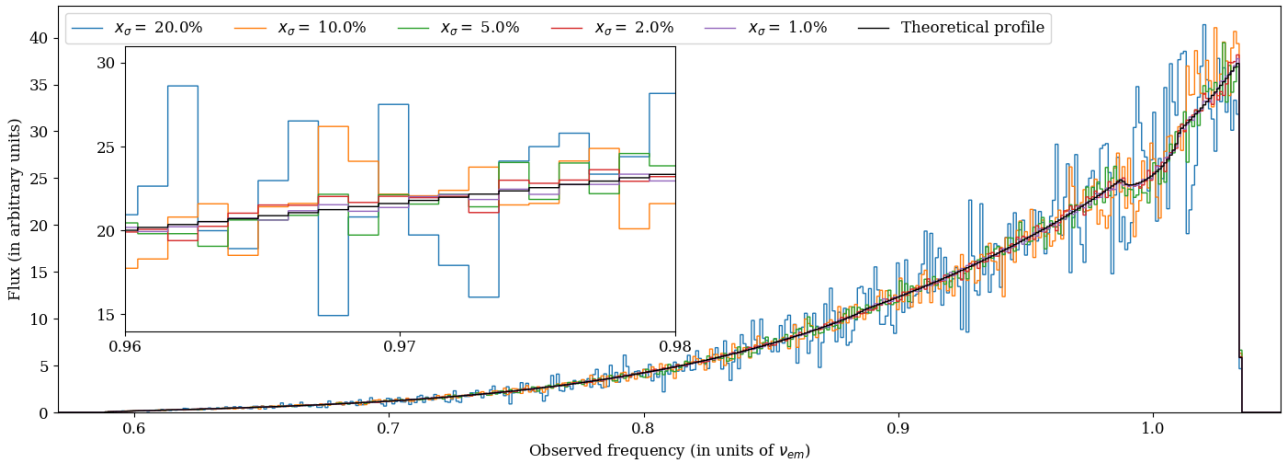

Figure E.1: **Observed iron line model with a Gaussian drawn for the flux in each bin.**
Each curve represents an observed iron line profile. The flux in each bin results from the Gaussian drawn defined in equation (E.1). Each curve corresponds to a different value of the parameter x_σ in this equation.
To compute the theoretical iron line profile with the *binning* method, the velocity field in the disc is Keplerian, $r_{min} = 3\ R_s$, $r_{max} = 751.5\ R_s$, $i_{obs} = 25.5°$, $q = 3$, and $h_s = 5\ R_s$. There are 200 000 cells logarithmically spaced in the radial direction and 6 000 cells linearly spaced in the azimuthal direction. The flux is computed in 640 bins linearly distributed between 3.2 and 7.68.

equation (5.9), but x is now x_σ defined in equation (E.1). Therefore, the compatible theoretical iron line profiles from the catalog are the ones for which the considered flux ratio falls within the interval:

$$I^\star_{comp} = [r^\star(1 - \sqrt{2}x_\sigma);\ r^\star(1 + \sqrt{2}x_\sigma)] \tag{E.3}$$

where $r^\star$ is the flux ratio computed with the fluxes resulting from the Gaussian draw (E.1).

Figure E.2 shows the amplitude constraints for the three parameters (r_{max}, i_{obs}, h_s) under various values of (r_{max}, i_{obs}). These parameters are used to calculate theoretical iron line profiles. The first row of Figure E.2 uses these profiles to compute observed line profiles using the Gaussian draw defined in equation (E.1). The observation uncertainty of the flux in each bin is the Gaussian distribution's standard deviation. The second row presents the theoretical results obtained in section 5.4: the observed line is the theoretical iron line profile, and the flux error in each bin is a constant fraction of this flux. Both rows have the same error in the flux in each bin set to 1%. The figure aims to study the impact of the Gaussian fluctuations of the flux values on the constraint amplitudes.

First, the constraint amplitude 2D colormaps appear grainy. This is due to the flux fluctuations within each bin, which causes variations in the flux ratios. As a result, the theoretical lines obtained from each flux ratio are slightly modified, leading to variations in the constraint amplitude. To illustrate this, Figure E.3 shows the constraint amplitude on r_{max} as defined in Figure E.2 for different standard deviation values. To keep the error in the flux in each bin constant, the error in the flux is not the standard deviation but a multiple of the standard deviation. The observed flux in each bin is still obtained with the Gaussian drawn defined in equation (E.1), but the observational value of the flux in each bin is

$$f^i_\star \pm n \times \sigma_i \tag{E.4}$$

It shows that as the Gaussian fluctuations decrease, the final constrain map converges towards the theoretical one obtained in section 5.4.

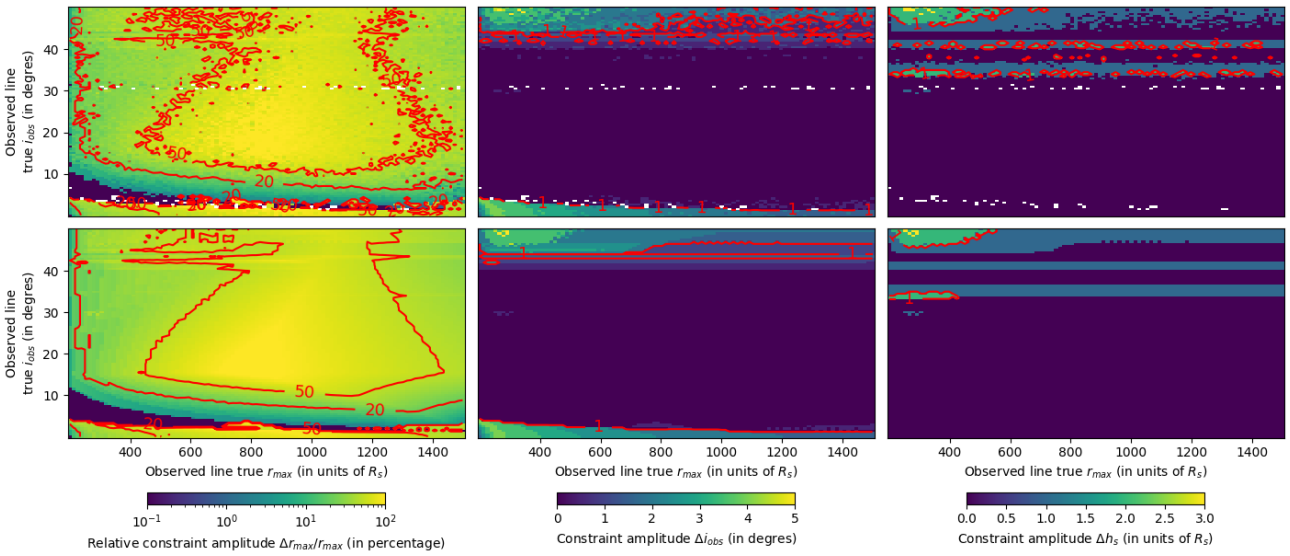

Figure E.2: **Comparison of the constrain amplitude of (r_{max}, i_{obs}, h_s) for observed iron lines defined with a Gaussian draw of the observed flux in each bin (equation (E.1) and the theoretical results.**
The x-axis is the initial value of r_{max} used to compute the theoretical iron line profiles, while the y-axis is the initial value of i_{obs}. All the theoretical iron line profiles were computed with a fixed value of $h_s = 5\ R_s$. All the other parameters used to compute the theoretical iron line profile with the binning method are the same as in Figure E.1. The flux error in each bin is the Gaussian distribution's standard deviation (E.1b).
The first raw presents the constraint amplitude for the observed iron line profiles computed with a Gaussian draw of the flux in each bin defined in equation (E.1) with a constant parameter $x_\sigma = 1\%$.
The second raw presents the constraint amplitude for observed lines defined by the theoretical profile and a flux error in each bin of $x = 1\%$, as done in section 5.4.

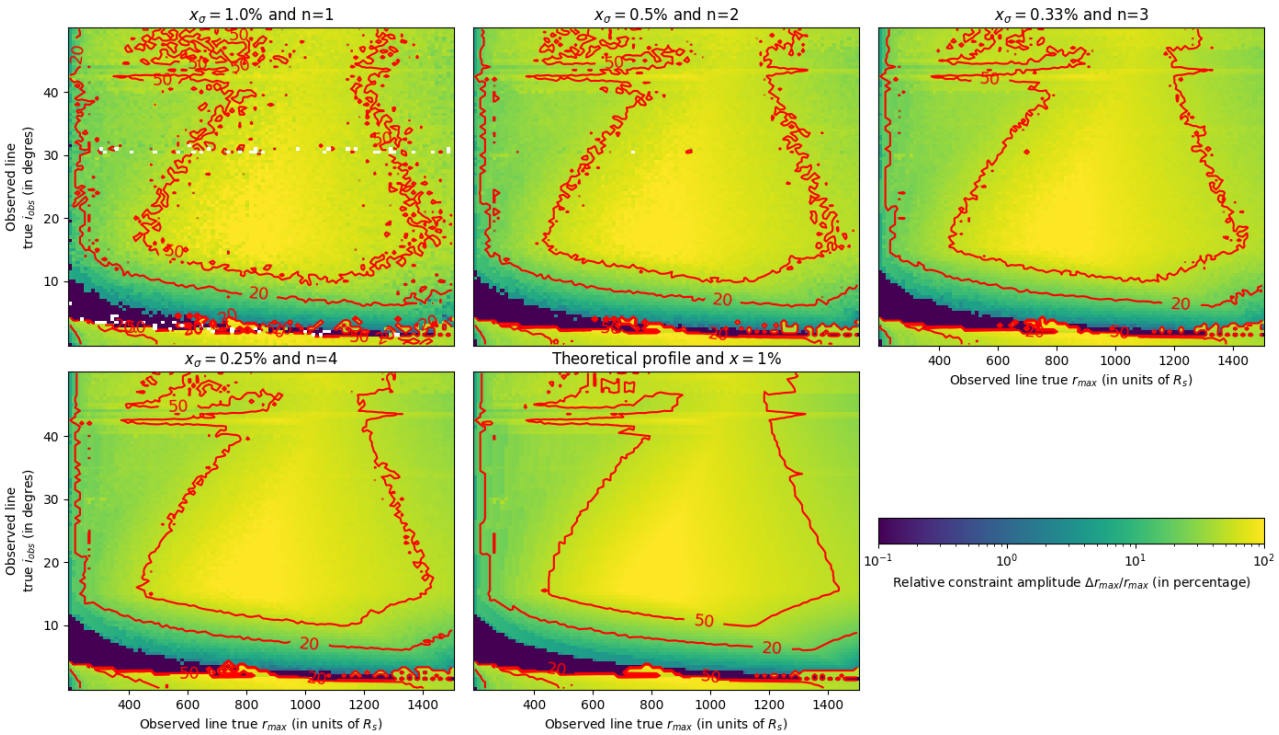

Figure E.3: **Comparison of the constrain amplitude of (r_{max}) for a constant observational error in each bin and different values of the standard deviation.** The different panels present the constraint amplitude on r_{max}, similar to Figure 2. The last panel is exactly the same as the lower left panel in Figure E.2. The first four panels are obtained with observed iron lines for which the flux in each bin is obtained by a Gaussian draw as defined in equation (E.1) and the observational uncertainty on the flux in each bin is given in equation (E.4). Each panel correspond to different values of the parameter x_σ to define the Gaussian distribution's standard deviation in equation (E.1b) and different values of the parameter n to define the error in the flux in each bin in equation (E.4).

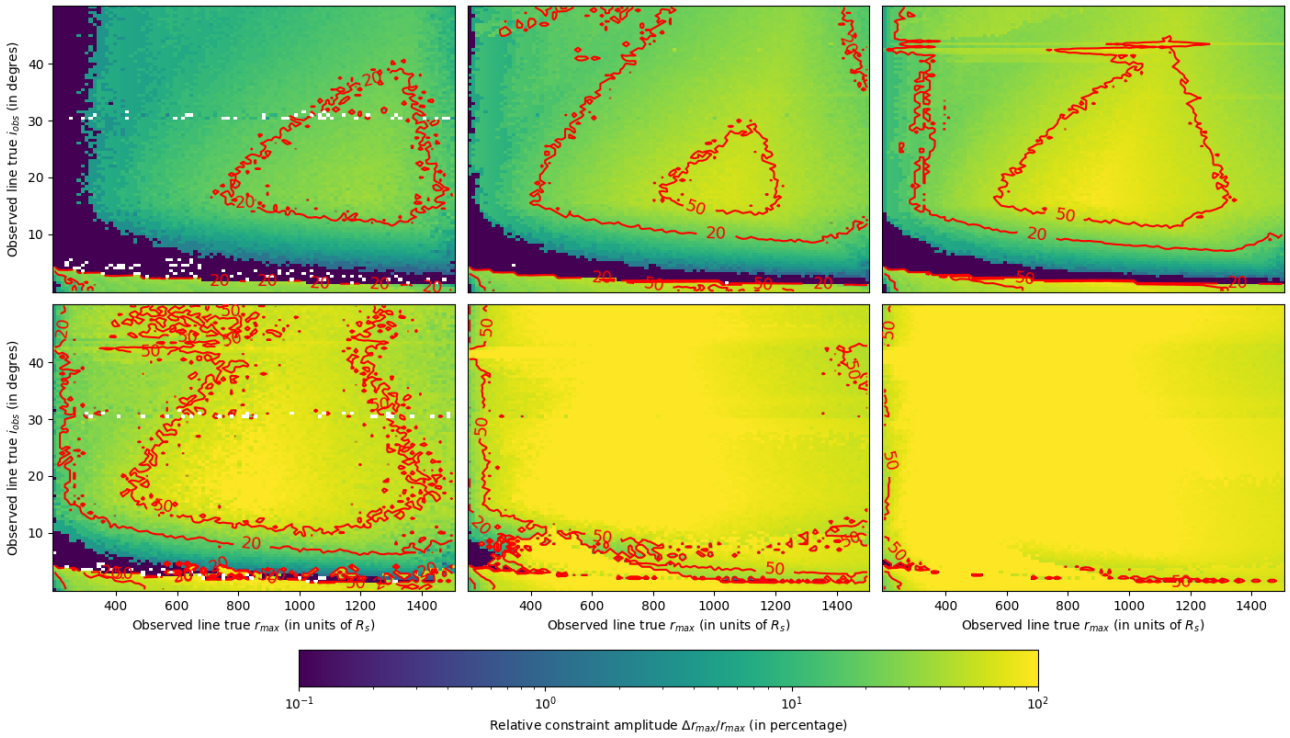

Figure E.4: **Evolution of the constrain with the multiple used to define the error in the flux in each bin from the standard deviation.**
The plots are the same as the plots in Figure E.3. In the first row the standard deviation is $x_\sigma = 0.25\%$, while in the second row the standard deviation is $x_\sigma = 1\%$. Each column correspond to a different value of parameter n in equation (E.4) to define the error in the flux in each bin: from left to right $n = 1$, $n = 2$, and $n = 3$.

Second, there is no solution for some of the observed lines tested. They are represented by white squares in Figure E.2. This occurs when at least two groups of theoretical lines defined by their compatibility to one flux ratio are disjoint. This configuration could not happen without fluctuation since, for each flux ratio, the theoretical flux ratio always stands at the middle of the observed flux ratio interval $[r(1-\sqrt{2}x), r(1+\sqrt{2}x)]$ defined in equation (5.11) (page 109. Thus, all groups of theoretical lines compatible with each flux ratio always have the initial theoretical line in common and cannot be disjoint. Assigning the error in the flux in each bin equal to the standard deviation means that, on average, approximately 68% of the flux values observed in the bins will be consistent with the expected theoretical value. This value increases if the error is set to two or three times the standard deviation. Figure E.4 illustrates this and shows that increasing the error in the flux in each bin allows for finding compatible values of the iron line parameters. Of course, it also results in weaker constraints in the accretion disc.

The study, particularly Figure E.3, reveals that introducing fluctuations to the flux values in each bin does not significantly affect the configurations of accretion discs that can be used to detect the truncation of the disc outer edge. Thus, to conclude this chapter I will use observed iron line models defined by the theoretical iron line profile to which an observed flux uncertainty is added in each bin, as done in section 5.4.